

**Mineralogical analysis and iron  
abundance estimation of the Moon  
using the SIR-2, HySI and M<sup>3</sup>  
spectrometers on-board the lunar  
orbiter Chandrayaan-1**

**Doctoral Thesis  
(Dissertation)**

**to be awarded the degree of  
Doctor rerum naturalium (Dr. rer. nat.)**

submitted by  
**Megha Upendra Bhatt**  
from Kymore, India

Approved by the Faculty of Energy and Management Sciences  
Clausthal University of Technology

Date of oral examination  
8 May 2012

**Chairperson of the Board of Examiners**

Prof. Dr. -Ing. Norbert Meyer

**Chief Reviewer**

Prof. Dr. Bernd Lehmann

**Reviewer**

Prof. Dr. Christian Wöhler

## **Bibliografische Information der Deutschen Nationalbibliothek**

Die Deutsche Nationalbibliothek verzeichnet diese Publikation in der Deutschen Nationalbibliografie; detaillierte bibliografische Daten sind im Internet über <http://dnb.d-nb.de> abrufbar.

D 104

ISBN 978-3-942171-69-4

uni-edition GmbH 2012

<http://www.uni-edition.de>

© Megha Upendra Bhatt



This work is distributed under a  
Creative Commons Attribution 3.0 License

Cover image: Left side - The SIR-2 tracks plotted on the Clementine UVVIS image of the Moon. Background image credit: NASA/USGS.  
Right side - The FeO wt.% map of the western nearside of the Moon derived for the SIR-2 tracks shown in left side image.

Printed in Germany

# Contents

<b>Summary</b>	<b>13</b>
<b>1 Introduction</b>	<b>15</b>
1.1 Space missions to the Moon . . . . .	15
1.2 Lunar geology at a glance . . . . .	18
1.2.1 Origin and evolution of the Moon . . . . .	18
1.2.2 Lunar terrains . . . . .	20
1.2.3 Lunar regolith . . . . .	23
1.2.4 Space weathering and maturity . . . . .	25
1.3 Reflectance spectra of lunar minerals . . . . .	27
1.3.1 Olivine group . . . . .	29
1.3.2 Pyroxene group . . . . .	31
1.3.3 Feldspars . . . . .	33
1.3.4 Oxides . . . . .	35
1.4 Spectrometers on-board Chandrayaan-1 . . . . .	37
1.4.1 SIR-2 instrument description . . . . .	37
1.4.2 HySI instrument description . . . . .	38
1.4.3 M <sup>3</sup> instrument description . . . . .	39
1.5 Outline and thesis structure . . . . .	40
<b>2 SIR-2 instrument, calibration and data reduction</b>	<b>41</b>
2.1 SIR-2 instrument working principle . . . . .	41
2.2 Preflight calibration . . . . .	43
2.2.1 Preflight calibration set-up . . . . .	45
2.2.1.1 Spectral calibration set-up . . . . .	45
2.2.1.2 Radiometric calibration set-up . . . . .	46
2.2.2 Bias and Dark count rate detection . . . . .	46
2.2.3 Spectral calibration . . . . .	48
2.2.3.1 Spectral position and wavelength coverage determination	50
2.2.3.2 Point Spread Function (PSF) . . . . .	52
2.2.4 Radiometric calibration . . . . .	53
2.3 Data reduction steps . . . . .	57
2.4 In-flight calibration . . . . .	58
2.5 Application of in-flight calibration to Apollo 12 and 15 landing sites . . .	60
2.6 Spectral parameters definition . . . . .	62

<b>3</b>	<b>Comparing the SIR-2 response with HySI and M<sup>3</sup></b>	<b>63</b>
3.1	Radiance to reflectance conversion of HySI and M <sup>3</sup> datasets . . . . .	63
3.2	HySI and SIR-2 combined response at the Apollo 15 landing site . . . . .	64
3.3	Comparing SIR-2, HySI, and M <sup>3</sup> responses: Mare Moscoviense . . . . .	66
3.3.1	Regional setting . . . . .	66
3.3.2	Data sets . . . . .	66
3.3.3	Alignment of SIR-2 tracks over HySI and M <sup>3</sup> . . . . .	68
3.3.4	Spectral analysis of Mare Moscoviense region . . . . .	71
3.4	Summary . . . . .	78
<b>4</b>	<b>Iron mapping algorithm based on SIR-2 band parameters</b>	<b>79</b>
4.1	Direct and indirect measurement techniques of iron abundance estimations	79
4.2	Iron abundance estimation methods: background . . . . .	80
4.3	Data-sets and data preparation . . . . .	81
4.4	Band depth comparison between SIR-2 and M <sup>3</sup> orbits from Bonpland D and surroundings . . . . .	83
4.5	Correlation between continuum slope and concentration of nanophase metallic iron . . . . .	83
4.6	Comparison of SIR-2 and M <sup>3</sup> spectra from Bonpland D . . . . .	85
4.7	Method . . . . .	86
4.8	Derivation of the absolute slope coefficient for SIR-2 and M <sup>3</sup> data-sets . .	87
4.9	Empirical calibration based on the lunar returned samples . . . . .	90
4.9.1	Iron abundance estimation based on 1- $\mu$ m absorption band parameters . . . . .	90
4.9.2	Iron abundance estimation based on 2- $\mu$ m absorption band parameters . . . . .	92
4.9.3	Limitations of the proposed iron abundance method based on 2- $\mu$ m absorption band . . . . .	93
4.10	Iron map of calibration site . . . . .	94
<b>5</b>	<b>Application of the iron mapping algorithm</b>	<b>97</b>
5.1	Crater Tycho . . . . .	97
5.1.1	2- $\mu$ m absorption band depth variations . . . . .	98
5.1.2	SIR-2 and M <sup>3</sup> spectra from central peak region of Tycho . . . . .	99
5.1.3	The FeO abundance map of crater Tycho . . . . .	101
5.2	Crater Copernicus . . . . .	102
5.2.1	SIR-2 and M <sup>3</sup> spectra from central peak region of Copernicus . .	102
5.2.2	Band depth variation comparison between SIR-2 orbit 1095 and corresponding M <sup>3</sup> orbit . . . . .	102
5.2.3	FeO map of crater Copernicus . . . . .	106
5.3	Mare Moscoviense . . . . .	106
5.3.1	FeO maps of Mare Moscoviense . . . . .	107
5.4	Western nearside FeO abundance map of the Moon . . . . .	107
<b>6</b>	<b>Conclusion and future work</b>	<b>115</b>

<b>A Preflight calibration: List of the SIR-2 files recorded</b>	<b>117</b>
A.1 Dark current measurements . . . . .	117
A.2 Spectral calibration measurements . . . . .	118
A.3 Point Spread Function (PSF) measurement files . . . . .	119
A.4 Radiometric calibration measurement files . . . . .	119
<b>B Lunar samples used for iron mapping method</b>	<b>123</b>
<b>Bibliography</b>	<b>125</b>
<b>Publications</b>	<b>137</b>
<b>Acknowledgements</b>	<b>139</b>
<b>Curriculum Vitae</b>	<b>141</b>



# List of Figures

1.1	Chandrayaan-1 spacecraft with the location of the SIR-2 and other payloads.	17
1.2	Evolution of lunar magma ocean, formation of crust and mantle as a function of time. . . . .	19
1.3	Global view of the Moon, centered at 300 °E. . . . .	21
1.4	Reflectance spectra (downloaded from RELAB) of lunar soils measured in laboratory. . . . .	22
1.5	Lunar regolith and various components of the lunar soil. . . . .	24
1.6	Comparison for freshly exposed and space weathered spectra in absolute level and after removing continuum. . . . .	26
1.7	Bidirectional reflectance spectra of the main lunar minerals (RELAB data).	28
1.8	Olivines. . . . .	30
1.9	Pyroxenes. . . . .	32
1.10	Feldspars. . . . .	34
1.11	Ilmenites and Spinel. . . . .	36
1.12	Instrument flight model of SIR-2, HySI and M <sup>3</sup> . . . . .	38
1.13	Schematic of HySI. . . . .	38
1.14	Cross section of the M <sup>3</sup> imaging spectrometer with telescope. . . . .	39
2.1	A schematic view of the SIR-2. . . . .	42
2.2	The SIR-2 subunits mounted on the thermal vacuum chamber's turn table.	43
2.3	Temperatures of the SHRU's cooling console, O-Box, and E-Box at the time of on-ground calibration. . . . .	44
2.4	Spectral calibration test set-up for the SIR-2 FS model . . . . .	45
2.5	Radiometric calibration test set-up for the SIR-2 FS model . . . . .	46
2.6	Dark and bias analysis results. . . . .	47
2.7	Spectral calibration of the SIR-2 instrument. . . . .	49
2.8	Pixel to wavelength relation and spectral resolution computed for on-ground spectral calibration of the SIR-2. . . . .	51
2.9	PSF plots for Pixel No. 14 and 226 measured at -50° and -65° detector temperatures (Table A.3). . . . .	53
2.10	Stepwise description of the radiometric calibration of the SIR-2 instrument.	55
2.11	Linearity check at detector temperature -50 °C. . . . .	56
2.12	The SIR-2 orbit 1095 raw data plotted for channel number 200 ( $\lambda = 2.1 \mu\text{m}$ ). The average dark signal is compared from preflight and in-flight measurements and plotted along with the average raw SIR-2 spectrum. . . . .	58
2.13	Preflight and in-flight calibration comparison. . . . .	59

---

2.14	Apollo 12 and 15 landing sites and comparison of RELAB and the SIR-2 reflectance spectra after apply in-flight calibration. . . . .	61
3.1	SIR-2 orbit number 740 plotted on HySI and Clementine for a comparison.	64
3.2	SIR-2 and HySI spectra extracted from locations marked in Figure 3.1. . .	65
3.3	SIR-2 orbits 606, 610 and 614 and corresponding M <sup>3</sup> orbits (bounded by yellow box) superposed over Clementine image. . . . .	67
3.4	SIR-2 orbits plotted on HySI and M <sup>3</sup> products based on the given latitude longitude informations. . . . .	69
3.5	A subsection of HySI image corresponding to SIR-2 orbit 611 and scaled radiance profile comparison before and after applying UTC shift. . . . .	70
3.6	Optimization of geographic coordinates of SIR-2 orbit 1173 based on scaled radiance profiles comparison between SIR-2 and corresponding HySI data. . . . .	72
3.7	M <sup>3</sup> 2- $\mu$ m IBD images and corresponding SIR-2 track position. . . . .	73
3.8	Representative spectra of SIR-2 orbits 606, 610 and 614 and corresponding M <sup>3</sup> and HySI spectra extracted from the location marked as square in Figure 3.7. . . . .	74
3.9	FeO distribution derived from the Clementine data using Lucey et al. (1998a) algorithm for Mare Moscoviense and surroundings. . . . .	75
3.10	Scatter plot between 2- $\mu$ m absorption band depth and continuum slope for M <sup>3</sup> image subsets shown in Figure 3.3. . . . .	77
4.1	SIR-2 orbit 1093 sampled Bonpland D crater which is considered as a calibration site for mafic iron estimation method. . . . .	81
4.2	The continuum line for the SIR-2 and M <sup>3</sup> reflectance spectra is segments of straight line to the normalized reflectance spectra. The reflectance spectra are extracted from the crater floor region from the square area drawn in Figure 4.1. . . . .	82
4.3	Band II depth comparison between SIR-2 and M <sup>3</sup> . . . . .	84
4.4	Band II depth mosaic from M <sup>3</sup> product IDs given in Table 4.1. . . . .	85
4.5	Correlation plots of the continuum slope and the parameter $I_s$ for the 68 samples listed in Table B.1. . . . .	86
4.6	A comparison of SIR-2 and M <sup>3</sup> spectra extracted from the square marked in Figure 4.1. . . . .	87
4.7	Conceptual band depth and continuum slope relationship for sample series with particular FeO content and varying maturity. . . . .	88
4.8	Correlation plots of the continuum slope versus the 2- $\mu$ m absorption band depth for Bonpland D crater and its surrounding areas for the SIR-2 and M <sup>3</sup> data. . . . .	89
4.9	Empirical calibration of FeO wt% for the 1- $\mu$ m absorption band parameters from Table B.1. . . . .	91
4.10	Empirical calibration of FeO wt% for the 2- $\mu$ m absorption band parameters from Table B.1. . . . .	93
4.11	Iron abundance maps for crater Bonpland D and surroundings. . . . .	95



---

5.1	SIR-2 orbit position and the summed reflectance profiles plotted on M <sup>3</sup> mosaics. . . . .	98
5.2	2- $\mu$ m absorption band depth for M <sup>3</sup> orbits from Tycho region with SIR-2 orbit's positions. . . . .	99
5.3	SIR-2 orbit 1086 sampled the central peak of Tycho and representative SIR-2 spectra from this region. . . . .	100
5.4	A comparison of SIR-2 and M <sup>3</sup> spectra extracted from the area marked as ECF, WCF and CP in Figure 5.2. . . . .	101
5.5	The FeO abundance maps for Tycho . . . . .	103
5.6	Summed reflectance of SIR-2 orbits 1095 and 1096 plotted on M <sup>3</sup> images from the crater Copernicus. . . . .	104
5.7	Representative SIR-2 and M <sup>3</sup> spectra from the crater Copernicus. . . . .	105
5.8	Band depth variation comparison from Copernicus region. . . . .	109
5.9	The FeO abundance maps for Copernicus. . . . .	110
5.10	FeO abundance maps for the Mare Moscoviense and surroundings, derived from SIR-2 and M <sup>3</sup> orbits from Table 3.1. . . . .	111
5.11	The SIR-2 tracks plotted on the Clementine image of the west nearside of the Moon between 55°N – 55°S, 3°E – 50°W. . . . .	112
5.12	The FeO abundance maps of western nearside of the Moon. . . . .	113



# List of Tables

1.1	Major lunar minerals . . . . .	27
1.2	Key features of SIR-2, HySI and M <sup>3</sup> for 100 km lunar polar orbit. . . . .	37
3.1	SIR-2, HySI, and M <sup>3</sup> product IDs considered to analyse Mare Moscoviense region. . . . .	68
3.2	SIR-2 track alignment on corresponding HySI images. . . . .	71
4.1	SIR-2 and M <sup>3</sup> product IDs used from calibration site and the geometric coordinate shifts calculated by comparing their scaled radiance profiles. . . . .	83
5.1	SIR-2 and M <sup>3</sup> files used for Tycho, Copernicus and Mare Moscoviense regions. . . . .	97
A.1	Dark measurement files recorded during preflight calibration of the SIR-2 Flight Spare (FS) model. . . . .	117
A.2	Spectral calibration measurement files . . . . .	118
A.3	Point Spread Function measurement files . . . . .	119
A.4	Radiometric calibration measurement files . . . . .	119
B.1	List of the lunar samples used in iron mapping algorithm. . . . .	123



# Summary

The work presented in this thesis is focused on mineralogical studies of the Moon aiming to create maps of iron abundances. We used the data from visible to near-infrared (VIS-NIR) spectrometers on-board Chandrayaan-1 spacecraft, with our major concentration on the Spectrometer InfraRed-2 (SIR-2) data. The SIR-2 on-ground and in-flight calibrations are discussed. The location of the SIR-2 tracks on the imaging spectrometers, Moon Mineralogy Mapper ( $M^3$ ), and Hyper-Spectral Imager (HySI) is determined by comparing the radiance profiles of the three instruments measured at the same Coordinated Universal Time (UTC) and the same photometric conditions.

We investigated the Moon surface mineralogy based on mineral absorption features. For this purpose, we have combined the SIR-2 and HySI reflectance spectra in order to get a spectral range coverage between 0.4 and 2.4  $\mu\text{m}$ . It is shown through the case study of the Mare Moscoviense, that the combined analysis of these two spectrometers requires inter-calibration in order to be comparable at absolute reflectance level.

We focused on the consistent lunar surface measurements collected by the SIR-2 instrument at a steady detector temperature of  $-55 \pm 0.5^\circ\text{C}$ . We used the SIR-2 data for the first time to derive the iron content of the Moon's surface utilizing 2- $\mu\text{m}$  absorption band parameters. Our method is based on the algorithm originally developed by Le Mouélic et al. (2000) for assessing FeO weight percent (wt%) in lunar surface materials analyzing Clementine mission's UVVIS and NIR data. Using both 1- $\mu\text{m}$  and 2- $\mu\text{m}$  absorption band parameters we found a correlation of about 90% between iron abundances estimated by our method and actual laboratory-measured values (from Apollo and Luna datasets). The  $M^3$  data measured at the same UTC as the SIR-2 data are used for a comparative study. Our indirect approach of estimating FeO wt% is compared with the Clementine iron abundance maps produced by the algorithm developed by Lucey et al. (1998a, 2000). The iron abundance maps generated using three different instruments are in a good agreement in terms of the FeO wt% range but some discrepancies in the FeO distribution are also noticed.

This study confirms that the 2- $\mu\text{m}$  absorption band can be used effectively to estimate the FeO wt% content of lunar surface materials through their NIR reflectance characteristics. Applications of this method would potentially be of great interest to those missions to the Moon and other planetary bodies carrying spectrometers ranging above the 0.9  $\mu\text{m}$  point.



# 1 Introduction

The Moon, the only satellite of the Earth, is the most familiar and well-studied celestial body in our solar system. It is an unusual planetary object in terms of its bulk density, size, and origin. The Moon presents pristine information of geologic processes of early planetary evolution because its surface has not been affected by plate recycling, atmosphere, water or life (Hiesinger and Head III 2006). The Moon's surface provides a continuous record of the solar-terrestrial processes for which the evidence on Earth has long been erased. Impact cratering, an exterior process, is the most important surface process on the Moon. In terms of composition, the lunar materials both resemble and differ from terrestrial mantle materials. One notable difference is that the Moon is more depleted in volatile elements and enriched in refractory elements than the Earth. The Moon has a composition that cannot be made by any single-stage process from the primordial solar nebula material suggesting that it was subject to additional thermal processing.

Data analysis from orbital remote sensing delivers global lunar maps as compared to the relatively small areas sampled by Apollo and Luna missions. Remote sensing missions launched in the past two decades have helped us to have a first estimate of the global distribution of lunar minerals and to examine the diverse regions across the Moon. The sunlight reflected by the lunar surface in the visible to near-infrared (VIS-NIR) wavelength range carries the information of minerals present on the top most layer of the lunar surface. The study of the mineral composition can provide information on a record of the thermal and chemical evolution of a planetary body because various processes like differentiation and volcanism produce distinct mineral signatures. Therefore, the mineralogical composition studies are known as powerful tools for unravelling the geologic history of a planetary body.

## 1.1 Space missions to the Moon

Lunar exploration through the spacecraft missions that began in 1959 has generated valuable experience and knowledge. Subsequently substantial analysis of the samples returned from the Apollo and Luna missions (1969-1976) have improved our understanding about Earth's only satellite. The collected samples revealed the formation ages and helped in deriving a new model for the origin of the Moon (Section 1.2.1). The data-set gathered from lunar returned samples served as "ground-truth" for analysing remotely sensed datasets and provided a baseline for our knowledge of lunar materials. However, these data-sets were limited to a small number of sites located on the equatorial regions of the Moon. Another source of samples is lunar meteorites but they lack geologic context, therefore their usability in forming a global picture of the lunar geology is limited. In 1990, the

Galileo spacecraft, on its way to Jupiter, captured some new images of the Moon which were not only helpful to map the lunar surface but also to test the instrument's response on-board. In that sense the Moon is a "reference body" that can be used for calibration purposes. Two very different missions, Clementine and Lunar Prospector were launched in 1994 and 1998, respectively. The Clementine spacecraft was placed in a lunar polar orbit for two months (Nozette et al. 1994). The Clementine mission mapped the lunar surface in 11 spectral bands including 5 bands in ultraviolet-visible (UV-VIS) and 6 bands in near-infrared (NIR). One of the important discoveries from this mission indicated the possibility of water-ice at the lunar poles. A main limitation for multispectral data such as Galileo and Clementine is the limited number of filters which result in the low spectral resolution, and that a continuous UV-VIS-NIR spectrum had to be measured by two cameras. The Lunar Prospector (LP) satellite carried five scientific instruments (Binder 1998) to map gravity, magnetic fields and lunar compositions. Clementine and LP provided the first set of data on lunar mineralogy and chemistry on a global scale. The laboratory analysis of lunar returned samples and analysis of remotely detected data using Clementine and LP missions pointed to vastly different hypotheses and theories from the one we had before the Apollo missions. For example, the Moon was thought to be undifferentiated before the Apollo missions. However, seismic and remotely sensed data, and the lunar samples analysis suggested, that the Moon is a differentiated body with a crust, mantle and possibly a small core.

The next in series was European Space Agency's (ESA) first spacecraft to the Moon, Small Mission for Advanced Research and Technology (SMART-1) spacecraft launched in September 2003 (Foing et al. 2001). The SMART-1 mission was designed to test spacecraft technologies for future missions. This mission carried seven instruments including a high resolution NIR point spectrometer, called SMART-1 infrared spectrometer (SIR). The SIR instrument collected reflectance spectra of the lunar surface in the wavelength range 0.93 to 2.4  $\mu\text{m}$ . The SIR instrument had significantly better capabilities to discriminate between different mineralogies compared to the 6 filters of Clementine in the same wavelength range. The instrument's calibration and mineralogy analysis using the SIR data are presented by Vilenius (2009) and Wiese (2009), respectively in their PhD thesis.

In 2007, Japan and China successfully launched lunar exploration spacecraft Kaguya and Chang'e-1, respectively. Kaguya or often called as Selenological and Engineering Explorer (SELENE) consisted of an orbiter and two sub-spacecrafts. The spacecraft carried a total of thirteen scientific instruments including a terrain camera (TC), multi-band imager (MI) and a spectral profiler (SP) to determine the topography and mineralogy of the lunar surface (Kato et al. 2010). SELENE mapped the Moon surface from a 100 km polar orbit. Major scientific achievements from SELENE are the identification of ubiquitous pure anorthosite in outcrops of central peaks of large craters by MI and SP and re-estimation of the crustal thickness and formation ages of farside mares by crater counting using TC data. Chang'e-1 was the first step of the three-phase Chinese Lunar Exploration Program. It had eight scientific instruments including an interference imaging spectrometer (IIM) and a three line array CCD stereo camera. The spacecraft mapped the lunar surface from a 200 km polar orbit (Zheng et al. 2008). The main scientific goals of this mission were to obtain three dimensional images of the Moon surface, estimate the regolith thickness, and the amount of Helium-3.

Indian Space Research Organization (ISRO) entered the field of planetary exploration



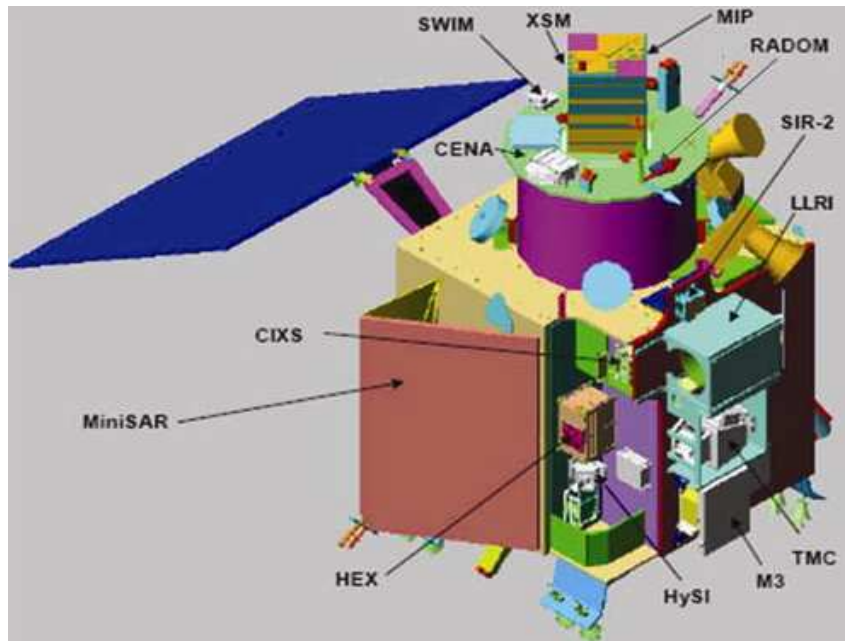


Figure 1.1: Chandrayaan-1 spacecraft with the location of the SIR-2 and other payloads (Goswami and Annadurai 2009). SIR-2 Optical-Box (O-Box) is visible.

by launching its first mission to the Moon, Chandrayaan-1 in October 2008 (Goswami and Annadurai 2009). It carried five Indian and six foreign scientific instruments. The spacecraft carried three spectrometers in UV-VIS-NIR wavelength region; the Hyper-Spectral Imager (HySI), the Spectrometer InfraRed-2 (SIR-2), and the Moon Mineralogy Mapper ( $M^3$ ) to investigate the Moon mineralogy. A suite of payloads with high spectral and spatial resolution provided remote sensing observations over a wide range of the electromagnetic spectrum for mineralogical, chemical, and photo-geological mapping of the lunar surface. The other instruments included along with the three spectrometers are listed here: The Terrain Mapping Camera (TMC), Lunar Laser Ranging Instrument (LLRI), High Energy X-ray spectrometer (HEX), Moon Impact Probe (MIP), Chandrayaan-1 X-ray Spectrometer (CIXS), Sub-KeV Atom Reflecting Analyser (SARA), Mini-Synthetic Aperture Radar (miniSAR) and Radiation Dose Monitor (RADOM). Figure 1.1 shows the nominal configuration of the Chandrayaan-1 spacecraft. The main objective of the Chandrayaan-1 mission was to upgrade and test India's technological capabilities in space and transmit back the scientific information on the lunar surface (Goswami and Annadurai 2009). The spacecraft was integrated with the Polar Satellite Launch Vehicle (PSLV) C11 and was launched successfully from Satish Dhawan Space Center in Sriharikota on 22 October 2008 at 6:22 a.m. local time. On 8 November 2008 Chandrayaan-1 was placed into a 7502x504 km lunar polar orbit, and was finally placed in the nominal 100 km circular polar orbit on 12 November 2008. The spacecraft operated at 100 km altitude for initial five months and raised to an altitude of 200 km on 16 May 2009. The mission was planned for two years, however, on 29 August 2009 the mission ended due to communication loss with the spacecraft. Important results from this mission include, indication of hydroxyl and water molecules in the sunlit lunar surface region around the poles (Pieters

et al. 2009) and the signature of sub surface ice layers in permanently shadowed regions near the lunar north pole (Spudis et al. 2010).

The National Aeronautics and Space Administration (NASA) launched the Lunar Reconnaissance Orbiter (LRO) in 2009. LRO is the first satellite of NASA's Lunar Precursor Robotic Program (LPRP) (Chin et al. 2007). It has been placed in a 50 km polar orbit. Its suite of seven instruments has taken detailed measurements of the lunar environment. The Lunar Orbiter Laser Altimeter (LOLA) has produced a detailed three dimensional map of the lunar surface which is assisting the development of better topographic maps of the surface. The Lunar Reconnaissance Orbiter Camera (LROC) with a spatial resolution of about 0.5 m is providing high resolution imagery of the whole surface with a main focus on the polar regions. China's Chang'e-2 was launched on October 2010 as a follow-on of Chang'e-1 mission. NASA has launched the Gravity Recovery and Interior Laboratory (GRAIL) mission in September 2011 to the Moon with the objective of mapping the lunar gravity and using that information to increase understanding of the Moon's interior and thermal history. Many new missions are already planned and under development by Japan, China, India, Russia and the USA. These missions are likely to answer some of the unsolved questions; (1) What are the rock types and age of the South Pole Aitken (SPA) basin? (2) Is the mantle of the Moon differentiated throughout its depth? (3) What is the vertical extent and structure of the megaregolith? (4) What are the sources for lunar polar volatiles? (5) What are the characteristics of the ancient regolith?

## 1.2 Lunar geology at a glance

### 1.2.1 Origin and evolution of the Moon

Four main scientific hypotheses have been proposed about the origin of the Moon: fission, co-accretion, capture, and giant impact. A detailed overview of these hypotheses is given by Wood (1986) and Boss (1986). The fission hypothesis, first proposed by Darwin (1878) argued that the Moon formed from the early Earth by splitting it into two due to the tidal forces. This hypothesis requires that the Moon existed only as a ring of debris around Earth because the Moon could not reside as a solid body inside the "Roche limit". The Roche limit defines a physical limit on how close the Moon could have been to Earth being a solid body and is approximately two planetary radii. According to the co-accretion hypothesis, the Moon accreted as a companion to the Earth in the same neighbourhood of the solar system (Schmidt and Hanna 1959). Co-accretion hypothesis could not explain the orbital relationship between Earth and the Moon and their different densities. The capture hypothesis (e.g., Singer 1986, Urey 1966) suggested that a relatively undifferentiated and cool Moon was formed elsewhere in the solar system and was captured during the very early history of the Earth. The capture hypothesis could successfully explain a difference in chemical compositions between the Moon and other terrestrial planets. However, captured hypothesis failed to justify Moon's capture into its present orbit.

A new hypothesis known as planetesimal impact hypothesis or giant impact hypothesis (Hartmann and Davis 1975, Cameron and Ward 1976) was formed after the lunar exploration in 1960s. The giant impact hypothesis combines salient features of all the three hypotheses briefly discussed in the previous paragraph. According to the giant

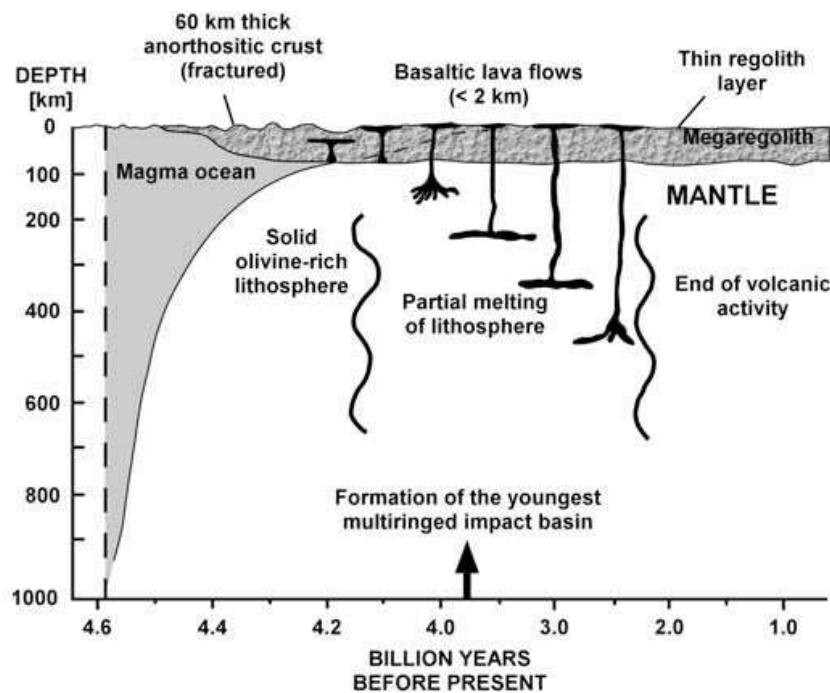


Figure 1.2: Evolution of lunar magma ocean, formation of crust and mantle as a function of time. Figure from Hiesinger and Head III (2006), pp. 7.

impact hypothesis, a Mars-sized object collided with the proto-Earth (capture hypothesis) before 4.5 Ga ago. The impact expelled large amounts of material (fission hypothesis) that eventually condensed into the Moon (co-accretion hypothesis). This new hypothesis could solve problems associated to any of the individual classical hypotheses; such as early lunar dynamics, composition, initial thermal state and timing of formation. According to the giant impact hypothesis, the Moon is derived from the outer portions of the proto-Earth and the impactor and would be iron-poor if the impactor and proto-Earth already had differentiated (e.g., Melosh and Sonett 1986, Cameron 1997). This assumption may justify the Moon's low mean density of  $3.34 \text{ g cm}^{-3}$  compared to Earth's mean density of  $5.51 \text{ g cm}^{-3}$ . The giant impact would have generated intense heat that could have caused volatiles to evaporate and be lost to space before it condenses to form the Moon (e.g., Wood 1986, Melosh and Sonett 1986). This may explain why the Moon is more depleted in volatile elements than the Earth.

The giant impact hypothesis suggests that the Moon was completely or at least partially molten to a depth of approximately 400 km in its early stage, known as the Lunar Magma Ocean (LMO) (Warren 1985, Wood et al. 1970). Warren (1985) suggested that the chemical evolution began with differentiation through solidification of the LMO and produced a wide variety of mafic lithologies in a deep layer (mantle) characterized by olivine and pyroxenes. Plagioclase began to crystallize late when roughly 75% of the LMO was solid and formed the lunar primary crust via flotation due to its lower density. As crystallization reached about 95%, the complementary mafic cumulates became more Fe-rich and formed a dense layer of ilmenite. The residual melt was enriched in potassium (K), rare earth elements (REE), and phosphorus (P), among other incompatibles and

constituted about 2% of the volume of the LMO. Figure 1.2 shows evolution of the LMO by formation of olivine-rich residual mantle and plagioclase-rich flotation crust.

Gravitational instability in the mantle caused resurfacing of the Moon approximately 500,000 years after the solidification of the anorthositic crust. The chemical diversity of mare basalts demonstrates varying degrees of mixing and relocation of early and late stage LMO cumulates. Several models (e.g., Tonks and Melosh 1990, Longhi 1980) have been proposed to describe the compositional and structural evolution of crystallizing magma ocean in a great detail. However, many uncertainties about magmatic evolution and internal structure of the Moon still persist. Some of the uncertainties are listed here: The extent of initial lunar melting, the structure of lunar mantle, compositional distribution of the minerals in polar regions, the vertical extent and structure of the mega regolith. These unanswered questions are a good motivation to study the lunar evolution in detail by utilizing high resolution data from the current and previous lunar remote sensing orbiters.

The LMO hypothesis requires the fundamental assumption that the Fe-bearing plagioclase-rich rocks (Anorthosite) globally exist in the lunar crust. Some parts of the lunar crust are observed as pure anorthositic with >90% plagioclase (ferroan anorthosite FANs) based on the laboratory studies of the returned samples (Warren 1985). However, global mapping of plagioclase is essential to test the LMO hypothesis. The first inspection of the global distribution of impact central peaks was done by ultraviolet and visible multi-spectral Clementine images. The spectral analysis of 109 crater peaks by Tompkins and Pieters (1999) showed an unprecedented amount of compositional heterogeneity in the crust, but yielded no clear vertical or lateral patterns in lithology. The results from the MI and SP on SELENE indicated the presence of anorthosite with plagioclase abundance more than 98% in the central peaks of lunar craters (Ohtake et al. 2009a). They estimated 10% higher aluminium (Al) in lunar crust than previously estimated. The occurrence of ~98% pure anorthosite raises the question whether plagioclase segregation in the LMO can produce lithologies that are almost free of mafic minerals? If possible which conditions are required for their occurrences? Other opinion is that lunar anorthosites do not derive from a single source and they are not all products of LMO. The process of establishing an anorthosite rich crust is a complicated and a two stage process (Korotev et al. 2010). Initially anorthosite rich crust was formed by buoyant concentrations in the zone of crystallization and subsequently by rising diapirically to shallower depths coupled with the dynamic expulsion of mafic trapped melt. This process could give rise to very pure near surface anorthosite massifs in the upper crust and other more mafic constituents in the form of basin derived impact melt products and igneous intrusive rocks. Chronological study of the mafic-mineral-rich sample of FAN 60025 (Apollo 16 sample) yields the age of crystallization to be  $4,360 \pm 3$  Ma in a recent approach by Borg et al. (2011). This extraordinary young age requires that either the Moon solidified significantly later than most previous estimates or the primary assumption of anorthositic crust needs to be revised.

### 1.2.2 Lunar terrains

The Moon is divided into two terrains on the basis of albedo and surface texture: the mares (smooth and low albedo) and the highlands (rugged and higher albedo). The contrast in

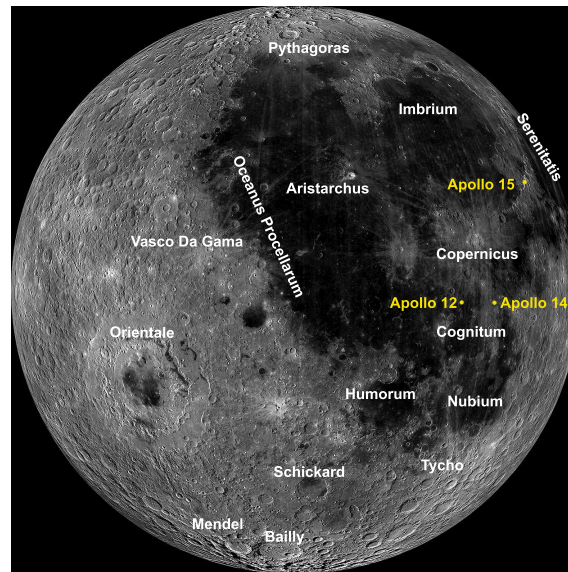


Figure 1.3: Global view of the Moon, centered at 300 °E showing locations of Apollo landing sites, basins, mares and craters in highland region of near and far sides of the Moon (LROC Wide Angel Camera (WAC) mosaic).

albedo in mare and highland is a result of their distinct compositions. The highlands are mainly composed of anorthosite material (e.g., plagioclase which is high in alumina and low in iron) while the mares are richer in iron bearing silicates (e.g., pyroxene and olivine). The far side of the Moon is mainly highlands whereas the near side is dominated by mares. The mares occupy about 17% of the lunar surface area, mostly appearing on the near side (32% of the near side and 2% of the far side). Figure 1.3 shows partly the far and near sides of the Moon for comparison. The highlands formed early in the Moon's evolution and represent the primary crust whereas mares represent the secondary crust that originated from remelting of mantle cumulates produced in the early differentiation of the Moon. The lava flow took place in impact basins or craters where the crust was shattered and cracked. The nature of mares was confirmed as being basaltic by studying the samples returned by the Apollo missions. Prior to the Apollo missions, some scientists postulated that the mares consisted of sediments, dried-up lake beds or impact-induced pyroclastic flows. Samples from the mares were returned from the nearside of the Moon during six Apollo missions (location of Apollo 12, 14 and 15 is shown in Figure 1.3).

Chemical and mineralogical analysis of basaltic samples showed that the mare basalts are heterogeneous in composition. Lunar mare basalts are classified based on their petrography, mineralogy and chemistry. The lunar mare basalts are divided into three major compositional groups based on their  $\text{TiO}_2$  contents: high-Ti basalts ( $> 9 \text{ wt\% TiO}_2$ ), low-Ti basalts ( $1.5\text{-}9 \text{ wt\% TiO}_2$ ), and very low-Ti basalts ( $< 1.5 \text{ wt\% TiO}_2$ ). The major minerals in the mare basalts are pyroxene, olivine, plagioclase and opaques, mainly ilmenite. Highland rocks can be described as either pristine (igneous) or as polymict (impact-mixed) rocks based on lunar returned samples studies. Pristine highland rocks have solidified from the LMO and have preserved components of the primary lunar crust. However, there is no simple method to discriminate pristine rocks from polymict because

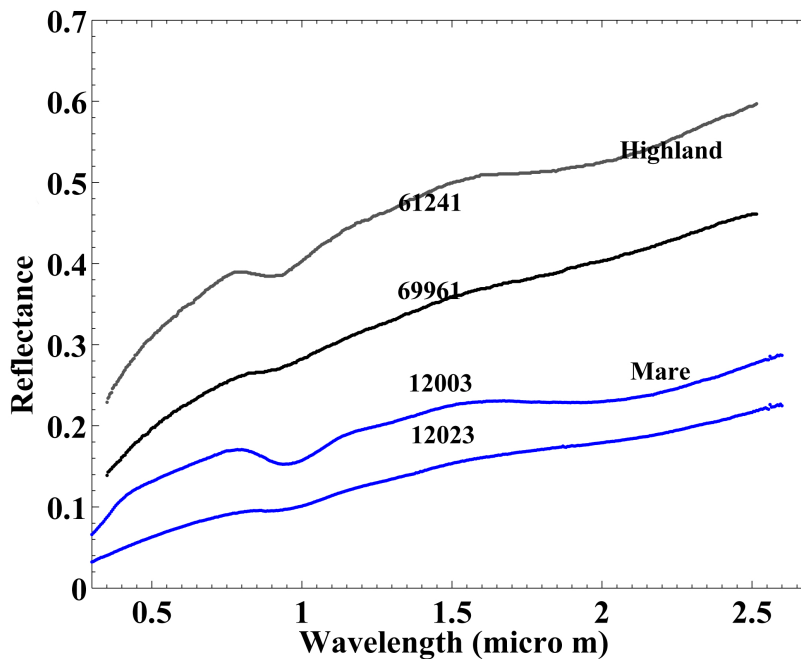


Figure 1.4: Reflectance spectra of lunar soils measured in laboratory from highland (plotted in black) and mare (plotted in blue).

it is difficult to identify differences between a pristine igneous texture from a relatively coarse-grained impact melt. Pristine highland rocks can be subdivided into three major groups: KREEP (K-REE-P rich) rocks, ferroan anorthosites and Mg-rich rocks. Please refer to Papike et al. (1998) and Heiken et al. (1991) for more details on highland rock types.

Typical NIR spectra of lunar rocks and soils returned from a feldspathic highland (Apollo 16) and a basaltic mare (Apollo 12) site are shown in Figure 1.4. Highland materials are brighter than the mare materials due to their higher plagioclase contents whereas mare materials are rich in mafic silicates and ilmenite and are darker than the highland materials.

The mare region is interpreted as having a thin, compositionally evolved crust in comparison with the massive feldspathic highlands. The variation in crustal thickness between the nearside and farside of the Moon is not well understood. The reason can be internal effects like asymmetric crystallization of the magma ocean, spatial variations on tidal heating or external effects such as asymmetric cratering. A recent model proposed by Jutzi and Asphaug (2011) suggests that a collision by a lunar companion that was created in the Moon-forming giant impact may have produced a crustal thickness consistent with the dimensions of the far side highlands. The collision would have redistributed the underlying magma ocean to the near side, explaining the observed enrichment in incompatible heat-producing elements (KREEP).

The highlands are completely covered by large craters (>40 km diameter) while the crater size in mare regions is much smaller representing the younger age of the mares as compared to highlands. The craters with diameter 30-40 km show central peaks and wall

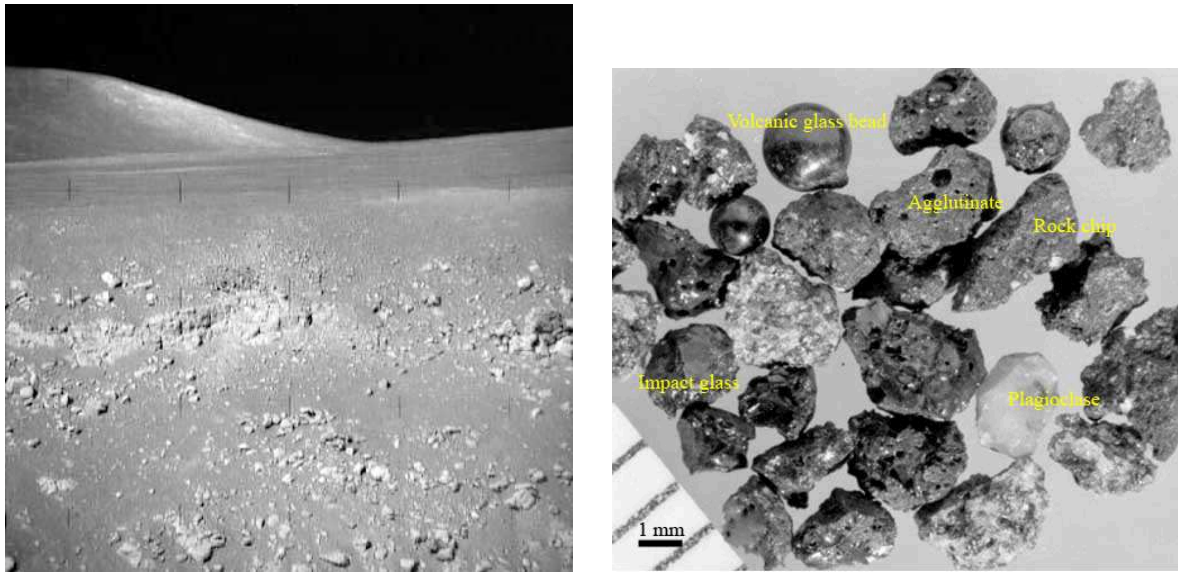
terraces. The central peak material may come from depth (10-20 km) and therefore offers a unique opportunity to remotely examine the composition of the lunar crust at a depth. The largest craters on the Moon are the multiring basins; some of them are about 2000 km in diameter. Impact basins excavate deeper levels of the lunar crust (about 20-50 km deep), bringing rocks from great depths up to the surface. Analysis of the composition of basin ejecta deposits has allowed to study the compositional structure and evolution of the Moon's lower crust/mantle. The impact melt deposits appear to extend to great distances for the basin scale events. Over 40 basins have been recognized and mapped on the Moon (Spudis 2005). The impact basins have been subdivided into three morphologic types: Central peak basins (diameter:140-175 km, example:Compton), Peak-ring basins (diameter:175-450 km, example:Schrödinger), and Multi-ring basins (diameter:more than 400 km, example:Orientale). Orientale (Figure 1.3) is the youngest basin on the Moon, and South Pole-Aitken (SPA) basin is the oldest. These basins are partly filled by lava flow; compositional variations within a basin can provide an essential tool to understand the structure of the lunar crust and the formation mechanism of these large impact basins.

### 1.2.3 Lunar regolith

Regolith is the result of continuous impact of large and small meteoroids on the lunar surface. The steady bombardment of the charged atomic particles from the sun and stars on the lunar surface also results in regolith formation (Papike et al. 1998). Regolith consists of all kind of debris ranging from boulder-sized rocks to tiny specks (Figure 1.5). The regolith has been exposed to solar wind and galactic cosmic rays for billions of years. This interaction causes the physical state of the regolith to evolve with space exposure. The data collected from the lunar returned samples suggest that the lunar surface is totally covered with the regolith. All the samples collected from Apollo and Luna missions belong to the regolith. At Apollo sites, the regolith thickness estimates based on grain size distribution suggest that the maximum thickness of regolith may not be more than 20 m (McKay et al. 1974). The thickness of the regolith is a function of surface age, because it is formed by exposure to bombardments from space. The regolith is estimated to be 10 to 15 m thick in highlands and 2 to 8 m in mare regions. However, the regolith layer is very thin (approximately few centimetres) for young surfaces of the Moon such as the floor of Tycho crater. Remotely sensed X-ray, infra-red and gamma-ray signals can penetrate at the most to a depth of 10 to 30 cm. Therefore all our information about the Moon virtually depends on the study of the regolith properties.

The regolith has been imaged by the orbiters, sieved in the laboratories, modelled, studied in detail, yet its structure and depth are not well understood. Some of the several reasons of studying regolith are listed below (Lucey et al. 2006):

- Lunar regolith provides a record of the Sun's composition and early history.
- Lunar regolith provides information about the rate at which meteoroids and cosmic dust have bombarded the Moon and, by inference, the Earth.
- Remote sensing studies in the VIS-NIR wavelength range can only measure the first few centimeters of the regolith and therefore the relation between bedrock and the overlying regolith must be understood.



(a) Apollo 15 image AS15-89-12115 showing the upper layer of regolith (image courtesy Lunar and Planetary Institute). (b) Lunar soil showing the fragments of rock and glass that constitute a typical soil (image courtesy Larry Taylor, Univ of TN Knoxville).

Figure 1.5: Lunar regolith and various components of the lunar soil.

- An understanding of the lunar regolith formation processes, physical properties, and compositions, may provide a base for studies of evolution of the regolith in other planetary bodies.

The lunar regolith formation and evolution is a complex process and can be divided into two mechanisms. First, the excavation of fresh bedrock by impacts which can penetrate the existing thin regolith layer. In this stage the regolith layer builds up rapidly. Only the larger impacts can penetrate the regolith after its thickness exceeds more than a meter, the smaller impacts only remix and redistribute the already existing regolith layer. This process of redistribution of existing regolith is called “gardening”. The regolith thickness increases slowly in this stage. Gardening brings young, buried regolith to the surface. This newly exposed surface is again subject to smaller impacts and this process continues mixing of several layers of the regolith. Second, addition of the effects of solar and cosmic particles to the regolith upper layer. These two processes are working simultaneously and combinedly produce the regolith whose structure, stratigraphy and history may vary widely in local scale. The region below regolith is a region of large blocks of material, large-scale ejecta and brecciated bedrock, often referred as the “megaregolith”. Detailed properties of the megaregolith are unknown because all the lunar samples are collected from the upper layers of the regolith.

Lunar regolith is a mixture of fine soil particles, rock chips, mineral fragments, impact and volcanic glasses, blobs of pure metal (mostly iron), breccias of many types of rocks and agglutinates (Figure 1.5(b)). Lunar soil usually refers to the subcentimeter fraction of the regolith. It is fine grained, loose, clastic material derived primarily from the mechanical disintegration of lunar rocks (McKay et al. 1991, Lucey et al. 2006). Lunar soils show



variety of chemical compositions ranging from basaltic to anorthositic. However physical properties such as grain size, density, packing and compressibility are rather uniform. Agglutinates are the intimate mixture of glasses, mineral crystals and tiny rock fragments bonded together by vesicular, flow-banded glass. Agglutinate particles can have a size ranging from millimeter to sub-micron in diameter. They may have formed by the melting and mixing produced by micrometeoritic bombardment of the regolith (McKay et al. 1991). The regolith becomes richer in agglutinates with continued exposure to space. Agglutinates are present everywhere on the Moon surface covering about 20-30% of the lunar soils. They contain pure Fe<sup>0</sup> (metallic Fe), solar wind gases and have extremely fine grains. These unique properties of agglutinates make them distinguishable to the lunar impact glasses. Agglutinates tend to mimic the composition of the soils from which they formed. The presence of agglutinates and the glass in the lunar soil obscure and modify infrared and X-ray signals from the other soil phases, thereby complicating the mapping of the lunar surface using remote sensing techniques.

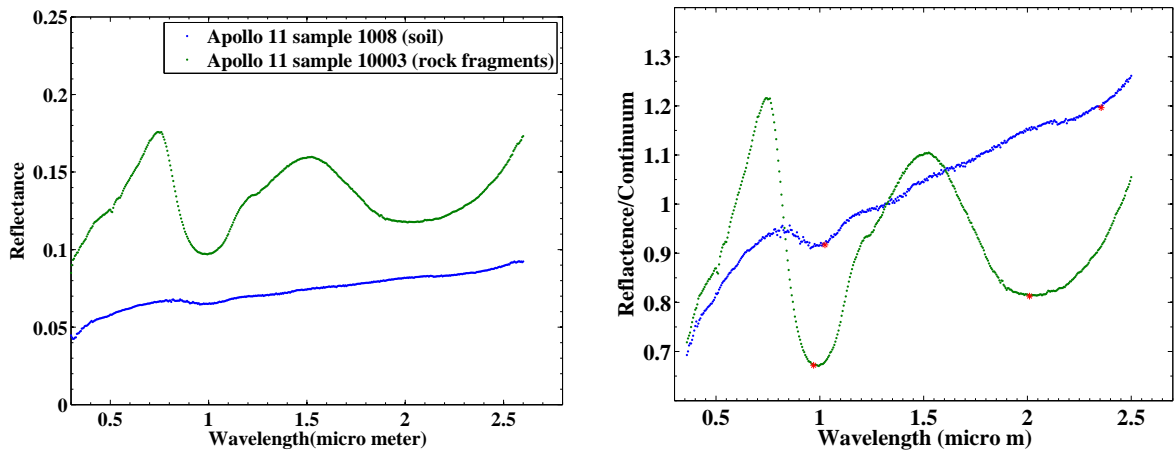
The majority of rock fragments (breccias) that makes regolith are locally derived from the bedrock underlying the regolith. However, some fractions have been transported from distant areas by large impacts. Mare area regolith is found to contain fraction of highland material in the range of 10 to 60% whereas mixing of the mare material in the highland areas is very low, in the range of 1 to 4%.

#### 1.2.4 Space weathering and maturity

Space weathering is a general term for the surface modification processes due to micrometeorite impacts and solar wind interaction that modify the optical properties of surfaces of airless bodies when exposed for a protracted period to the space (Gaffey 2010). Space weathering effects on the Moon are well studied by examination of returned samples from Apollo and Luna missions. Space weathering processes modify the spectral shape by weakening the mineral absorption features and reddening (increase in reflectance with increase in wavelength in near-infrared range) the spectral slope than the bedrock lithologies from which they were derived. Figure 1.6 demonstrates the space weathering effects on the reflectance spectra collected from the Apollo 11 mission. Figure 1.6(a) shows that the Apollo soil sample 1008 is darker with weaker absorption bands and redder continuum slope (increase in continuum slope at longer wavelengths) compared to the Apollo rock sample 10003. A straight line continuum is applied and plotted in Figure 1.6(b). Although the band parameters like spectral slope, band depth and albedo show dependency on space weathering effects, band center position can be identified from Figure 1.6(b). However, it is difficult to determine the band center position accurately in the 2  $\mu\text{m}$  region due to presence of steep spectral slope.

The changes in the spectral shape of a reflectance spectrum are due to the production of submicroscopic metallic iron (SMFe) or “nanophase metallic iron” (npFe<sup>0</sup>) in the regolith by deposition of vapours created by micrometeorite impact and solar wind sputtering. Sputtering is a process in which high energy ions from the solar wind and cosmic rays can penetrate up to 150 nm and can interact with the atoms in target grains. These trapped solar wind elements (mainly H) gradually accumulate in exposed grains, causing a reduction reaction of FeO in the silicate minerals to Fe<sup>0</sup>+H<sub>2</sub>O.

The result of space weathering effects on the lunar regolith (or samples collected from



(a) Spectrum of bedrock fragments and a mature soil (b) Spectra after removing continuum, red stars are the sample from the Apollo 11 landing site.

Figure 1.6: Comparison for freshly exposed and space weathered spectra in absolute level and after removing continuum.

regolith) is “maturation”. The exposure of the regolith to the space can alter regolith’s physical and chemical properties. For example, it may cause a decrease in the mean grain size, increase in the abundance of nanophase iron, increase in the agglutinate particles (McKay et al. 1991). The processes causing these changes are combinedly called “maturation” and the measure of degree of surface exposure is called “maturity”. The use of the word maturity is confusing with the term “ageing”, maturity term is only associated with the upper few millimeter layer of regolith. The term age can be associated with exposure in upper few meters of the regolith (Morris 1978, McKay et al. 1991). The lunar soil properties show a systematic change with increasing exposure and are highly correlated. Therefore, it is possible to determine the relative amount of surface exposure by measuring the abundance or density of the space weathering produced attributes. However, several of these key attributes reach a steady-state when exposed for an extended period of time, like formation of agglutinates (McKay et al. 1974, McKay et al. 1991). At this steady-state a soil is considered to be mature.

The surface exposure (maturity) index  $I_s/\text{FeO}$  has become the standard measure of the regolith maturity since it accurately indicates the evolutionary state of the lunar soil. Also, it is much easier to measure in laboratory than using other indices of maturity.  $I_s/\text{FeO}$  maturity index data base is large, this index has been determined for a total of 164 lunar soil samples (Morris 1978). The maturity index  $I_s/\text{FeO}$  has been obtained by measuring the relative concentration of nanophase metallic Fe with ferromagnetic resonance (FMR),  $I_s$  in the wavelength range 4 to 33 nm. Division of  $I_s$  by the concentration of total Fe, expressed as FeO, gives the maturity index  $I_s/\text{FeO}$  (Morris 1978). It is necessary to normalize  $I_s$  to the FeO content of the soil in order to obtain a maturity index because  $I_s$  is proportional to both the amount of surface exposure and the amount of Fe available for reduction in the soil (Morris 1978).  $I_s/\text{FeO}$  is a dimensionless quantity ranging from zero in rocks and soils with no surface exposure to about 100 in highly mature regolith. An

Table 1.1: Major lunar minerals

Mineral	Characteristic
Olivine	Exposed largely in and around the rims of large lunar impact basins Major cations: Fe <sup>2+</sup> and Mg <sup>2+</sup> . Mostly Mg rich Spectral features: Complex absorption feature near 1.05 – 1.1 $\mu\text{m}$
Pyroxene	One of the most common minerals in the solar system Belong to either the orthorhombic (ortho) or monoclinic (clino) symmetry groups Major cations: Fe <sup>2+</sup> , Mg <sup>2+</sup> and Ca <sup>2+</sup> Spectral features: 1 and 2 $\mu\text{m}$ absorption bands
Feldspars	Most common mineral in the lunar crust Belongs to the plagioclase series, between albite and anorthite Spectral features: Weak absorption band near 1.2 $\mu\text{m}$ for relatively pure crystalline anorthosite
Oxides	Retain signatures of critical condition of formation Main oxide minerals: Ilmenite and spinels Spectral features: Prominent broad absorption band near 2 $\mu\text{m}$ for spinel, ilmenite reduces the overall reflectance of the material

$I_s/\text{FeO}$  value of less than 30 is considered as immature whereas mature soils are characterized by  $I_s/\text{FeO}$  greater than 60 (Morris 1976). Any values in-between immature and mature soils are considered as submature soils. The maturity index of 68 lunar samples are listed in Appendix B. The relationship between  $I_s/\text{FeO}$  and continuum slope for 1 and 2  $\mu\text{m}$  absorption bands is described in Chapter 4 in detail.

### 1.3 Reflectance spectra of lunar minerals

Reflectance spectroscopy is the study of light that has been reflected or emitted by materials. The reflectance spectrum carries the information about the mineralogical composition of the surface area. However, many other factors, like the grain size distribution and the viewing geometry affect the reflectance spectrum which increases mineral detection complexities through remote sensing. Relating a spectral feature to actual mineral abundance is a challenging task because different combination of grain sizes, viewing geometry and mixture of minerals may give similar results which are not easily distinguishable by remote sensing. Therefore, the interpretation of the remotely measured reflectance spectra require laboratory based study of reflectance spectra measured in different conditions to derive empirical trends (Clark and Roush 1984). The study of the terrestrial samples have provided valuable information on the relation between the mineral composition, structure and spectral variations. Samples collected from the Apollo and Luna missions have provided detailed information about the mineralogical composition and space weathering effects on the spectral shape of reflectance spectra. The purpose of this section is to

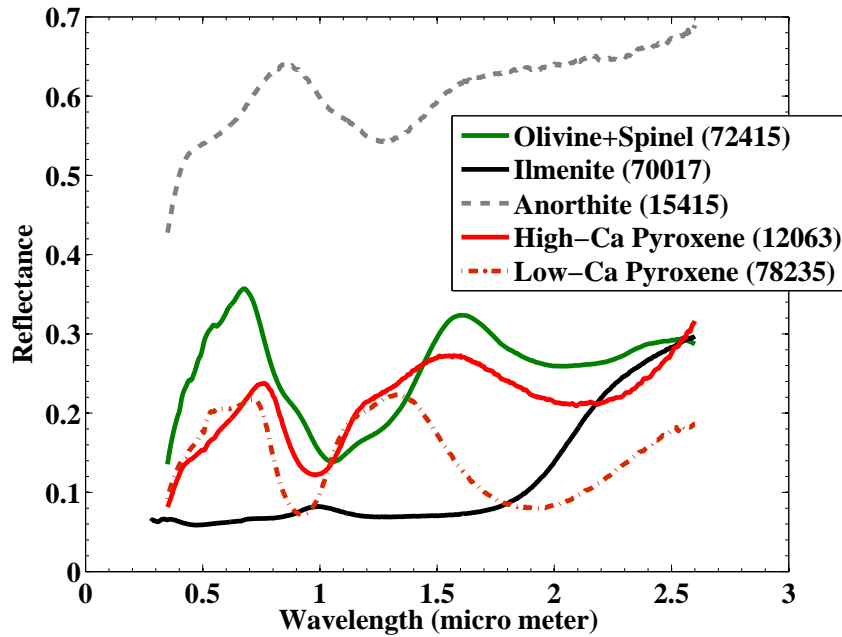


Figure 1.7: Bidirectional reflectance spectra of the main lunar minerals (RELAB data).

discuss the shape of the reflectance spectra of common lunar rock-forming minerals in the VIS-NIR region. It is important to understand the relationship between the crystal structure of the common lunar minerals and the shape of their reflectance spectra because the position, shape and strength of the absorption bands of a mineral give the information about its crystal structure and composition. We will discuss the crystal structure of the main lunar minerals, along with main mineral groups in subsequent subsections.

The spectra from the Moon's surface are measured as bidirectional reflectance. The observing (viewing) geometry is important to take into consideration for the bidirectional reflectance measurements because a viewing angle may change the spectral shape of a reflectance spectrum. The Bidirectional Reflectance factor is defined as the ratio of the brightness of the surface in consideration and a Lambert surface ideally illuminated. The Sun illuminates the surface with an angle of incidence  $i$  from the surface normal and the surface is viewed from a spacecraft at the angle of emission  $e$ , and phase angle  $g$  between the Sun, surface, and the spacecraft. The surface under consideration is assumed as a perfect sphere; however, this is not the case for planetary bodies with topographic features and may introduce errors in converting the reflectance to a standard viewing geometry ( $i=g=30^\circ$ ,  $e=0^\circ$ ).

The mineralogy of the Moon is simple compared to that on Earth. The Moon has only few hundreds of minerals with no hydrous minerals other than apatite, and with all rock types exhibiting low oxygen fugacity, restricting Fe-bearing mineralogy to  $\text{Fe}^0$  and  $\text{Fe}^{2+}$  species. Four main lunar mineral groups dominate most lunar rocks and are listed in Table 1.1. Bidirectional reflectance spectra of common lunar minerals are shown in Figure 1.7 with the lunar sample number and mineral names in legend. The principle absorption characteristics of lunar reflectance spectra are due to the ferrous iron ( $\text{Fe}^{+2}$ )

transition at different crystallographic sites of the minerals (Burns 1993). The most common iron-bearing material in lunar soils is pyroxene, which shows absorption bands between 0.9 and 1.03  $\mu\text{m}$  (“1- $\mu\text{m}$ ” absorption band) and between 1.6 and 2.3  $\mu\text{m}$  (“2- $\mu\text{m}$ ” absorption band) (Adams 1974). The band center position of absorption bands is sensitive to the presence of  $\text{Fe}^{+2}$  and moves to longer wavelengths with increasing contents of  $\text{Fe}^{+2}$  and/or  $\text{Ca}^{+2}$ . The second most common iron-bearing mineral on the lunar surface is olivine, which exhibits absorption bands in the 1- $\mu\text{m}$  region. Oxide minerals (mainly ilmenite and spinel, also major carriers of Fe) are next in abundance in the lunar rocks and mostly concentrated in mare basalts. Ilmenite is spectrally opaque at visible wavelengths and its presence reduces the overall reflectance of the surface material.

The reflectance spectra of the returned samples and man made mineral samples are taken from the Reflectance Experiment Laboratory (RELAB) <sup>1</sup>.

### 1.3.1 Olivine group

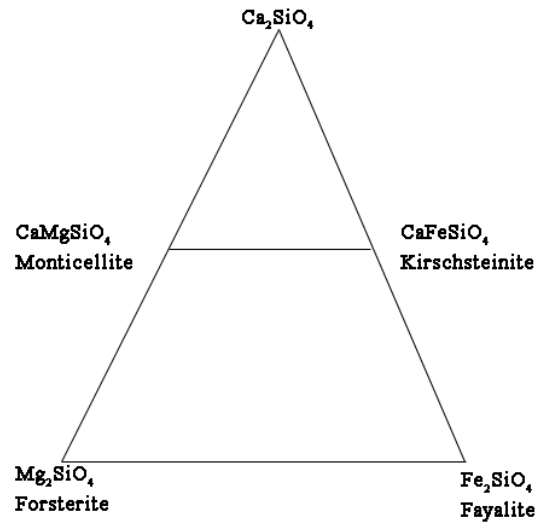
The olivine group has general formula  $\text{M}_2\text{SiO}_4$  where M is  $\text{Fe}^{2+}$ , Mg or Ca. Olivine has an orthorhombic crystal structure ( Figure 1.8(c)). It is structurally classified as an orthosilicate in which isolated  $\text{SiO}_4$  tetrahedra are linked and charge-balanced by two metal cations in M1 and M2 sites which are both distorted from octahedral symmetry (Burns 1993). Most natural olivines have compositions in the range of forsterite to fayalite (Figure 1.8(b)). Forsterite to fayalite is a complete solid solution series in which the structure shows no energetic preference for either Mg or  $\text{Fe}^{2+}$ . Therefore, one end member of olivine can have 100%  $\text{Fe}_2\text{SiO}_4$  ( $\text{Fa}_{100}$ ), and the other can be pure  $\text{Mg}_2\text{SiO}_4$  ( $\text{Fo}_{100}$ ). Any ratio is possible between end members forsterite and fayalite, giving rise to a range of olivine compositions. The solid solution between monticellite and krischsteinite involves random mixing of Mg and  $\text{Fe}^{2+}$  over M1 site. There is no solid solution between the Ca-bearing olivines and Mg, Fe olivines under normal geological conditions. Under higher pressures like Earth’s mantle, Fe, Mg olivine transforms into a variety of distorted spinel phases. The olivine analysis from the Apollo returned samples shows that most mare basalt olivines have compositions in the range  $\text{Fa}_{20}$ – $\text{Fa}_{70}$  (Heiken et al. 1991). Sample 72415 is shown in Figure 1.8(a) as an example of olivine rich rock. Sample 72415 is a cataclastic dunite made up of 93% olivine ( $\text{Fo}_{86-89}$ ).

Olivine is typically one of the first minerals to crystallize from a mafic magma, and its composition is indicative of the composition and degree of evolution of the source region in the case of a primary magma. Therefore, identifying the presence of olivine on the various solar system bodies like the Moon and asteroids can help us in understanding their petrologic history and thermal evolution. Figure 1.8(d) shows some examples of synthetic and lunar olivine spectra in the VIS-NIR wavelength range. The VIS-NIR spectrum of olivine exhibits a broad complex absorption feature near 1  $\mu\text{m}$ . This absorption band consists of three overlapping absorption bands caused by electronic transitions in  $\text{Fe}^{2+}$  ions located in distorted octahedral crystal lattice sites (Burns 1993). Olivine band centers shift to longer wavelength as  $\text{Fe}^{2+}$  increases (Burns 1993, King and Ridley 1987, Sunshine and Pieters 1998). This characteristic of olivine absorption bands can be utilized for determining the olivine composition by remote sensing.

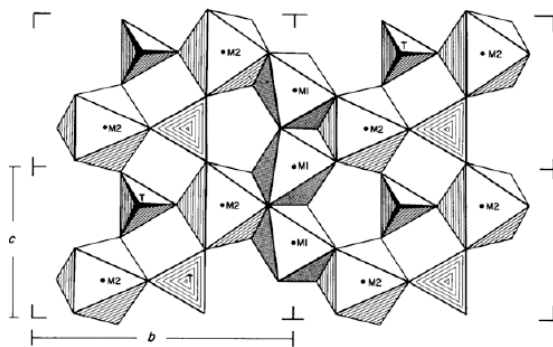
<sup>1</sup><http://www.planetary.brown.edu/rehab/>



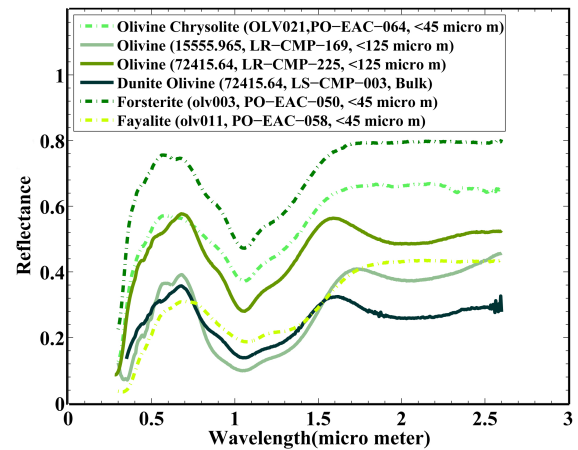
(a) Sample 72415 has 93% olivine (Fo86-89) and was collected at station 2 of Apollo 17 mission, South Massif, Taurus-Littrow (image courtesy Lunar and Planetary Institute).



(b) Ca-Fe-Mg ternary showing the solid solution series between the olivine end members forsterite (pure Mg end member) and fayalite (pure Fe end member).



(c) Crystal structure of olivine (Heiken et al. 1991). The b and c are the axis of the unit cell.



(d) Reflectance spectra of lunar samples measured in laboratory (RELAB data) containing olivine as one of the main minerals (solid lines) and synthetic olivines (dashed lines). The change in reflectance level based on the grain size is shown for the lunar sample 72415.

Figure 1.8: Olivines.

Reflectance spectra of the olivines from the lunar samples significantly differ from those of the terrestrial and synthetic olivines (Figure 1.8(d)). Lunar olivines often contain traces of  $\text{Cr}^{3+}$  in form of fine Cr-spinel (Explained in subsection 1.3.4). The complexity further increases with the presence of other absorbing species like pyroxene. Olivine

and pyroxene mixtures were analysed by Singer (1981) in detail. Singer (1981) showed that the pyroxene characteristics are dominated in the reflectance spectra of mixtures of pyroxene and olivine but the olivine is detectable as it remains apparent around 1.3  $\mu\text{m}$ .

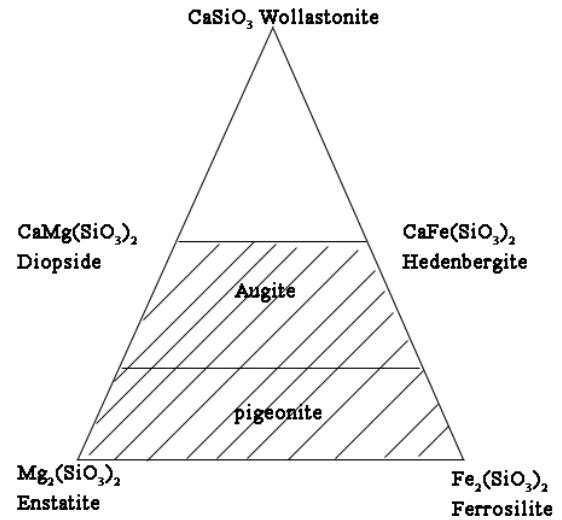
Olivine has been identified by Earth-based telescopic observations at two craters on the near side of the Moon, Aristarchus and Copernicus (Pieters 1982, Lucey et al. 1986). A global survey of the lunar surface using the Spectral Profiler on-board Kaguya found the exposures of olivine on the Moon located in and around the rims of large lunar impact basins like the South Pole-Aitken, Imbrium and Moscoviense impact basins (Yamamoto et al. 2012). Isaacson et al. (2011a) detected olivine dominated reflectance spectra from a small crater near Mare Moscoviense, the Copernicus central peak, Aristarchus, and the crater Marius in the Marius Hills using  $M^3$  data. Olivine signatures are also identified using the SIR-2 data on the Copernicus central peak (Bugiolacchi et al. 2011).

### 1.3.2 Pyroxene group

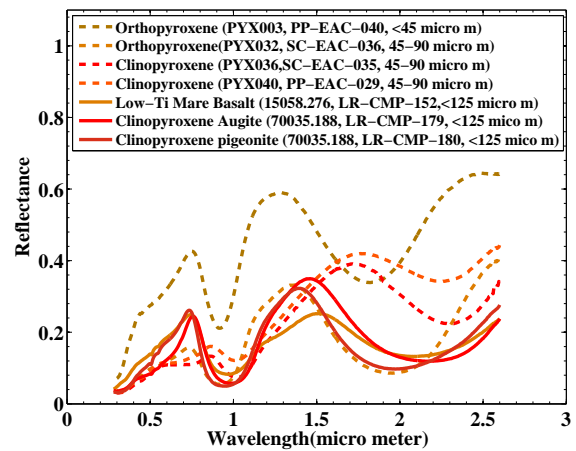
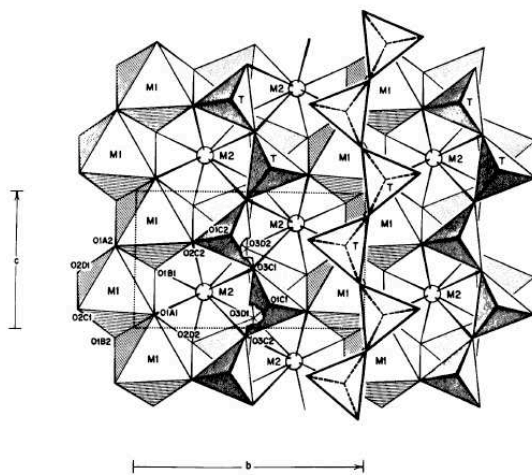
Pyroxene group has general formula  $(\text{Ca}^{2+}, \text{Fe}^{2+}, \text{Mg}^{2+})_2\text{Si}_2\text{O}_6$ . Pyroxenes are the most important group of minerals as they are abundant in terrestrial planets, meteorites, and asteroids. Their characterization allows us to address questions about the magmatic evolution and cooling history. Pyroxenes are compositionally variable solid solutions, and they contain most of the major elements present in the host rocks. Pyroxene quadrilateral is shown in Figure 1.9(b) formed by four end members of the pyroxene group. The pyroxene quadrilateral is covered by the solid lines in a complete pyroxene triangular plot. All pyroxenes are composed of infinite chains of edge-sharing M1 octahedra that are connected and extend along the c-direction of the unit cells as shown in Figure 1.9(c). These chains are cross-linked by distorted six cornered M2 sites. The M1 sites are smaller and are almost regular octahedra whereas M2 sites are larger and more distorted. The M sites form edge sharing chains which run parallel to the silicate chains. The b-direction in Figure 1.9(c) shows the orientation of back to back pyroxene forming layers. The structure shown in Figure 1.9(c) is common to all pyroxenes. But it does not show how the chains are arranged parallel to their length and if any differences between the chains are present. These two important features define different pyroxene structural groups (Burns 1993).

Pyroxenes fall into two broad categories named as orthopyroxenes and clinopyroxenes depending on their atomic arrangement and crystal shapes. Orthopyroxenes have an orthorhombic structure and form a solid solution series between ferrosilite( $(\text{Fe}^{2+})_2\text{Si}_2\text{O}_6$ ) and enstatite( $(\text{Mg}^{2+})_2\text{Si}_2\text{O}_6$ ). The M1 and M2 octahedral sites in orthopyroxenes contain primarily  $\text{Fe}^{2+}$  and  $\text{Mg}^{2+}$ , but may also contain  $\text{Ti}^{4+}$ ,  $\text{Cr}^{3+}$ ,  $\text{Fe}^{3+}$ ,  $\text{Al}^{3+}$ , and small amounts of Ca and Na. Clinopyroxenes have a monoclinic structure and mostly form a solid solution series between diopside (Ca, Mg)  $\text{Si}_2\text{O}_6$  and hedenbergite (Ca, Fe) $\text{Si}_2\text{O}_6$ . Apart from Fe, Mg, and Ca, some clinopyroxenes like augite  $(\text{CaMgFeNa})(\text{MgFeAl})(\text{SiAl})_2\text{O}_6$  contain other cations such as  $\text{Na}^+$  and  $\text{Al}^{3+}$ . Figure 1.9(a) shows a clinopyroxene rich rock collected from Apollo 15 landing site.

Near-infrared spectra of four synthetic pyroxenes and three pyroxene separates from lunar samples are presented in Figure 1.9(d). Pyroxene spectra exhibit two absorption bands in 1  $\mu\text{m}$  and 2  $\mu\text{m}$  regions due to the presence of  $\text{Fe}^{2+}$ . The strong absorption feature near 2  $\mu\text{m}$  in all the spectra of Figure 1.9(d) is caused by  $\text{Fe}^{2+}$  in the M2 pyroxene site. In contrast, the observed 1  $\mu\text{m}$  absorption is due to  $\text{Fe}^{2+}$  in both the M2 and M1 sites. This



- (a) Sample 15499 is composed of 42% of clinopyroxene and was collected at station 4 on the rim of Dune Crater of Apollo 15 mission (image courtesy Lunar and Planetary Institute). (b) The pyroxene quadrilateral part of the triangular diagram is highlighted that includes all possible pyroxene Ca:Mg:Fe compositions.



- (c) Crystal structure of pyroxene (Heiken et al. 1991). The b and c are the axis of the unit cell (dotted out-line). (d) Reflectance spectra of the Apollo rock samples (RELAB data) containing pyroxenes as one of the main minerals (solid lines) and synthetic pyroxenes (dashed lines).

Figure 1.9: Pyroxenes.

explains the difference in band depth between the 1 and 2  $\mu\text{m}$  bands, as the deeper 1  $\mu\text{m}$  absorption is actually a composite of two nested absorptions from the M1 and M2 sites, while the 2  $\mu\text{m}$  band is strictly due to  $\text{Fe}^{2+}$  in the M2 site. The 1 and 2  $\mu\text{m}$  absorptions shift to longer wavelengths with increasing total Fe or Ca contents (e.g., Adams 1974, Cloutis and Gaffey 1991, Klima et al. 2007). Pyroxene spectra exhibit another weaker absorption



band near  $1.2\ \mu\text{m}$ , caused by  $\text{Fe}^{2+}$  in the M1 site in high-Fe low-Ca orthopyroxenes with  $\geq 20\%$  of total iron (Klima et al. 2007, Klima and Pieters 2008). Orthopyroxenes are characterised by two major absorption bands situated between  $0.90\text{--}0.93\ \mu\text{m}$  and  $1.80\text{--}2.10\ \mu\text{m}$  which are of roughly equal intensity (Figure 1.9(d)). Clinopyroxene spectra are classified as type A and type B on the basis of their absorption bands. Type B spectra are similar to the orthopyroxenes but with absorption band positions between  $0.91\text{--}1.06\ \mu\text{m}$  and  $1.97\text{--}2.35\ \mu\text{m}$  (Figure 1.9(d)). Type A spectra exhibit two main absorption bands near  $0.9$  and  $1.15\ \mu\text{m}$  with a partially overlap. For type A spectrum, the M2 site is preferentially enriched with  $\text{Ca}^{2+}$  and the  $\text{Fe}^{2+}$  is restricted to the M1 site only (Cloutis and Gaffey 1991). An increase in the particle size results in a decrease in overall reflectance and an increase in the absorption band depth until the bands become saturated. This condition is true for both the orthopyroxenes and clinopyroxenes.

### 1.3.3 Feldspars

The feldspars have general formula  $\text{MT}_4\text{O}_8$  where M can be  $\text{Na}^+$ ,  $\text{K}^+$ ,  $\text{Rb}^+$ ,  $\text{Ca}^{2+}$ ,  $\text{Sr}^{2+}$  or  $\text{Ba}^{2+}$  and T can be Al and/or Si. The composition of most of the feldspars lie in the Albite-Anorthite-Orthoclase triangle (Figure 1.10(b)), in which the region separated by a line represents the extent of high temperature solid solution. Most lunar feldspars belong to the plagioclase series that comprise the continuous solid-solution series between albite and anorthite.

Apollo 15 anorthosite sample 15415 is shown in Figure 1.10(a). Sample 15415 is a unique sample, probably from the lunar highlands and made up of mostly (98%) calcic plagioclase ( $\text{An}_{96}$ ) and only mildly shocked. Spectral signature of the sample 15415 is shown in Figure 1.10(d).

Crystal structure of feldspars have a  $\text{SiO}_4$  and  $\text{AlO}_4$  tetrahedral linkage pattern which may undergo different kinds of distortions lowering the symmetry (Putnis 1992) (Figure 1.10(c)). The ratio of Al:Si varies from 1:1 when the large cations have divalent charge (e.g., Ca) to 1:3 when the large cations are monovalent (e.g., Na). Figure 1.10(c) shows tetrahedra (T1, T2) with oxygen atoms at the apices, combined with larger polyhedra. Spheres represent Ca atoms in anorthite, Na in albite, K in potassium feldspar, and Ba in celsian.

Plagioclase feldspar is the most abundant mineral of the lunar crust ( $> 90\%$ ) that dominates the crust as primary crystallization products of the lunar magma ocean. The spectral characteristics of plagioclase in the VIS-NIR wavelength range is not yet fully understood. Iron-bearing crystalline plagioclase exhibits a broad and weak absorption band around  $1.25\ \mu\text{m}$  due to electronic transitions of  $\text{Fe}^{2+}$  in the plagioclase structure if it has not been highly shocked by impacts (Adams and Goullaud 1978, Cheek et al. 2011). The laboratory studies of plagioclase reflectance spectra suggest that the band parameters may show composition dependencies, with band depth varying according to Fe content and band center position sensitive to plagioclase feldspar compositions (Adams and Goullaud 1978). Remote identification of plagioclase is challenging because pyroxenes can also exhibit a feature around  $1.25\ \mu\text{m}$  (Klima et al. 2007, Klima and Pieters 2008) and olivine can also mimic feldspar in absence of the high spectral resolution (Cheek et al. 2009, Lucey et al. 2006). However, indirect detection of the plagioclase is possible, based on spectra that lack a  $1\ \mu\text{m}$   $\text{Fe}^{2+}$  band and have a high albedo. Figure 1.10(d) shows spectral

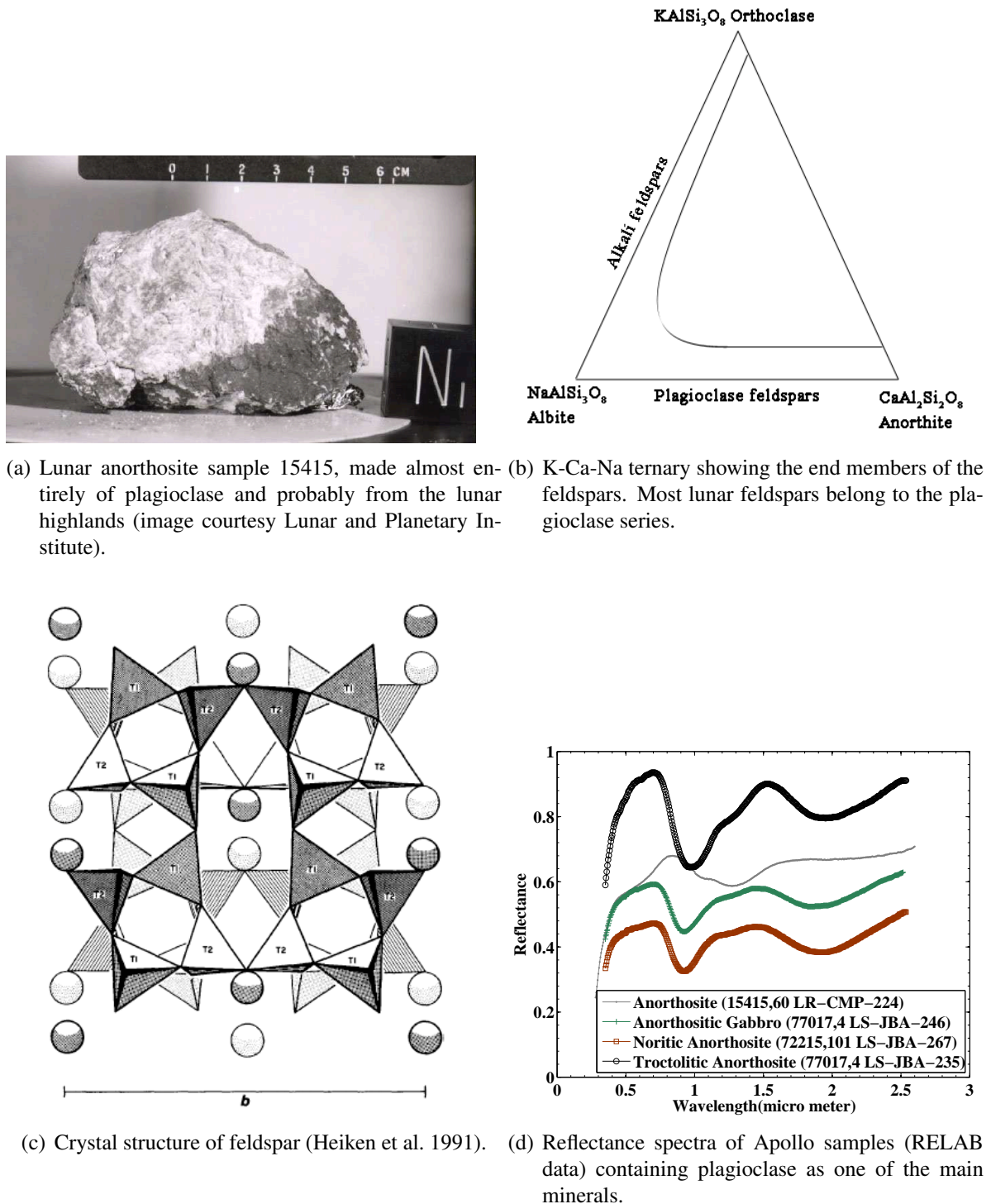


Figure 1.10: Feldspars.

signature of the Apollo samples containing plagioclase. Presence of the plagioclase was inspected in the VIS-NIR wavelength range using the Clementine data (Tompkins and Pieters 1999) and by using the MI and SP data collected by SELENE mission (Ohtake

et al. 2009a).

### 1.3.4 Oxides

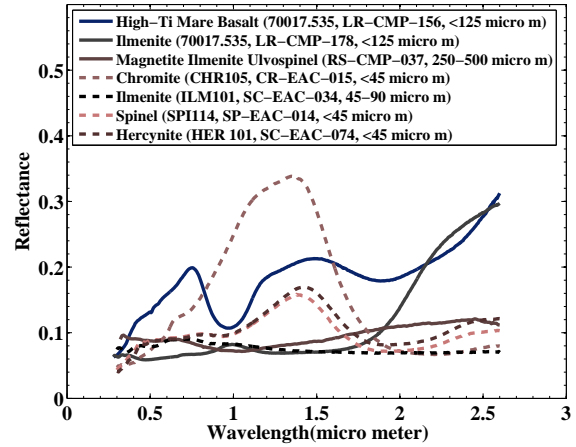
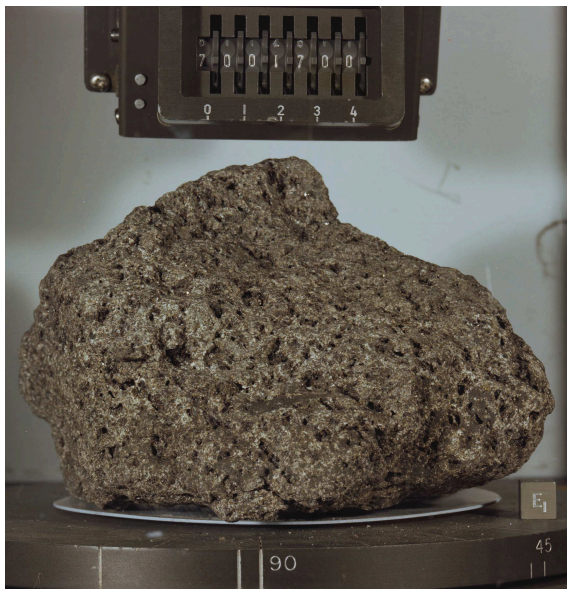
Several oxide minerals are present in the lunar rocks, the most abundant oxide mineral found in lunar rocks is, ilmenite ( $\text{FeTiO}_3$ ) varying between 0 to 24 vol%. The second most abundant oxide mineral on the Moon is spinel with extensive chemical variations,  $(\text{Fe, Mg})(\text{Cr, Al, Fe, Ti}_2)\text{O}_4$ . The spinels are found as high as 10 vol% in certain mare basalt samples collected from the Apollo 12 and 15 sites. The less abundant lunar oxide minerals include rutile, baddeleyite, and zirconolite (Heiken et al. 1991). We will discuss ilmenites and spinels in this section because these oxides are remotely detectable.

The ilmenite crystal structure is shown in Figure 1.11(c). The oxide ions are approximately hexagonally close-packed and the cations occupy octahedral sites. Ilmenite crystal structure forms alternating layers of Ti- and Fe. The cation-anion ratio indicates that only two-thirds of the octahedral sites are filled. The unit cell size is determined by the way octahedral sites are filled (Heiken et al. 1991, Putnis 1992).

The spinel group of minerals has general formula  $\text{AB}_2\text{O}_4$ , and is named after the mineral spinel,  $\text{MgAl}_2\text{O}_4$ . The basic crystal structure of the spinel is a cubic array of oxygen atoms with the 'A' and 'B' cations occupying one eighth of the tetrahedral sites and one half of the octahedral sites. Figure 1.11(d) shows the crystal structure of spinel, with two interstitial sites, a tetrahedral site 'A' coordinated with four oxygens and an octahedral site 'B' coordinated with six oxygens (Heiken et al. 1991, Putnis 1992).

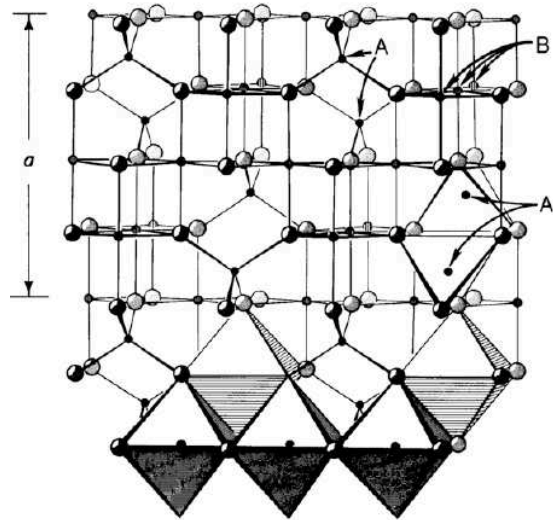
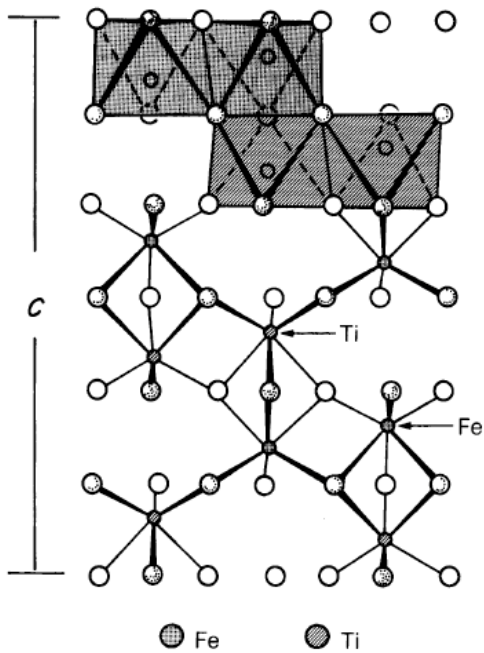
Figure 1.11(b) shows the spectral features of natural and synthetic oxides. Ilmenite is spectrally dark, neutral and exhibits broad absorptions centered near  $0.6 \mu\text{m}$ , a relative reflectance peak around  $1 \mu\text{m}$ , and significantly increased reflectance across NIR wavelengths (Riner et al. 2009, Isaacson et al. 2011b). Ilmenites and spinels commonly occur in mare basalts as bladed crystals. Although oxide minerals, mainly ilmenites and spinels are less abundant than silicates in lunar rocks, they have importance in interpreting lunar surface compositions from remote spectroscopy because they retain signatures of critical conditions of formation of rocks in which they occur. We know from the laboratory studies of the returned samples that most of the lunar spinels have the composition between chromite and ulvöspinel. The relations of the various members of the spinel group can be displayed in a diagram known as the Johnston compositional prism (Heiken et al. 1991). The end members represented include chromite ( $\text{FeCr}_2\text{O}_4$ ), ulvöspinel  $\text{Fe}_2\text{TiO}_4$ , hercynite ( $\text{FeAl}_2\text{O}_4$ ), and spinel  $\text{MgAl}_2\text{O}_4$ . The spectral signature of the spinel group endmembers is shown in Figure 1.11(b). Generally spinel has no detectable absorption feature near  $1 \mu\text{m}$  but exhibits a prominent absorption centered near  $2 \mu\text{m}$ . Mg-spinel lithologies have been detected remotely by Pieters et al. (2011), Dhingra et al. (2011) using the  $\text{M}^3$  data.

Ilmenites and spinels are present in mare basalts. As mentioned in the Section 1.2.2, the mare basalts are primarily classified based on their  $\text{TiO}_2$  contents. The  $\text{TiO}_2$  is largely hosted by spinels in low-Ti basalts and by ilmenite in high-Ti basalts (Neal and Taylor 1992). Therefore, identifying the abundance of ilmenite and spinels provide first order approximation of basalt type and thus clues to mare basalt source regions and their evolution over time.



(a) High-Ti basalt sample 70017 contains 22% of opaques and 50% of pyroxene (image courtesy Lunar and Planetary Institute).

(b) Reflectance spectra of Apollo rock samples (RELAB data) containing ilmenite (solid line) and synthetic spectra of some common oxides present on the Moon surface (dashed line).



(c) Crystal structure of ilmenite (Heiken et al. 1991). The unit cell dimension along the c-axis is shown as 'c'.

(d) Crystal structure of spinel (Heiken et al. 1991). The unit cell dimension along the a-axis is shown.

Figure 1.11: Ilmenites and Spinel.

Table 1.2: Key features of SIR-2 (Mall et al. 2009), HySI (Kumar et al. 2009) and M<sup>3</sup> (Pieters et al. 2009) for 100 km lunar polar orbit. The M<sup>3</sup> operated in two modes, target and global. The listed specifications are from global mode.

Key Features	SIR-2	HySI	M <sup>3</sup>
Type of spectrometer	point	Imaging	Imaging
Spatial Resolution (from 100 km altitude)	220 m	80 m/pixel	140 m/pixel
Spectral range ( $\mu\text{m}$ )	0.93-2.41	0.42-0.96	0.40-3.0
No. of spectral bands	256	64	86
Spectral bandwidth	6 nm	<20 nm	20-40 nm
Field of View	0.13°	13°	24°
Quantization	16 bit	12 bit	12 bit
Weight	3 kg	2.5 kg	8.3kg

## 1.4 Spectrometers on-board Chandrayaan-1

The key features of SIR-2, HySI, and M<sup>3</sup> on-board Chandrayaan-1 are given in Table 1.2. Figure 1.12 displays the flight models of the SIR-2, HySI and M<sup>3</sup>. The main scientific objective of these three spectrometers was the mineralogical study of the Moon with high spectral and spatial resolutions.

### 1.4.1 SIR-2 instrument description

The SIR-2 instrument was developed in a project led by Max-Planck Institute for Solar System Research, Germany, in collaboration with the University of Bergen (UiB), the Polish Academy of Sciences/Space Research Centre (PAS/SRC), and ESA. The SIR-2 instrument's working principle is the same as the SIR demonstrator instrument, flown on SMART-1 mission (Mall et al. 2009). However, the SIR-2 is redesigned with an actively cooled detector in order to have a consistent measurements of the lunar surface. The instrument consists of three parts: Electronics Box (E-Box), the Senser-Head-Radiator-Unit (SHRU) and the Front-End Optics also called Optical box (O-Box), and shown in Figure 1.12 (left sub-figure). The sub-untits of the SIR-2 are linked by an optical fibre connecting O-Box and SHRU and an electrical harness (ILH) connecting SHRU and E-Box. The SIR-2 mapped the Moon surface at an altitude of 100 km and 200 km, much lower than that mapped by the SIR on SMART-1. The lower altitude improved the spatial resolution from 300-3000 m in the case of SIR to 220 m (100 km altitude) for the SIR-2. Please refer to Chapter 2 for a detailed description of the SIR-2 instrument's working principle.

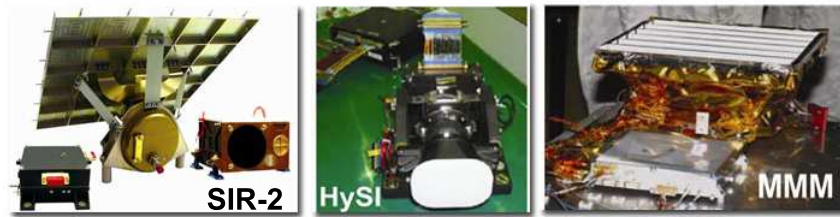


Figure 1.12: Instrument flight model of SIR-2, HySI and M<sup>3</sup> (Mall et al. 2009, Kumar et al. 2009, Pieters et al. 2009).

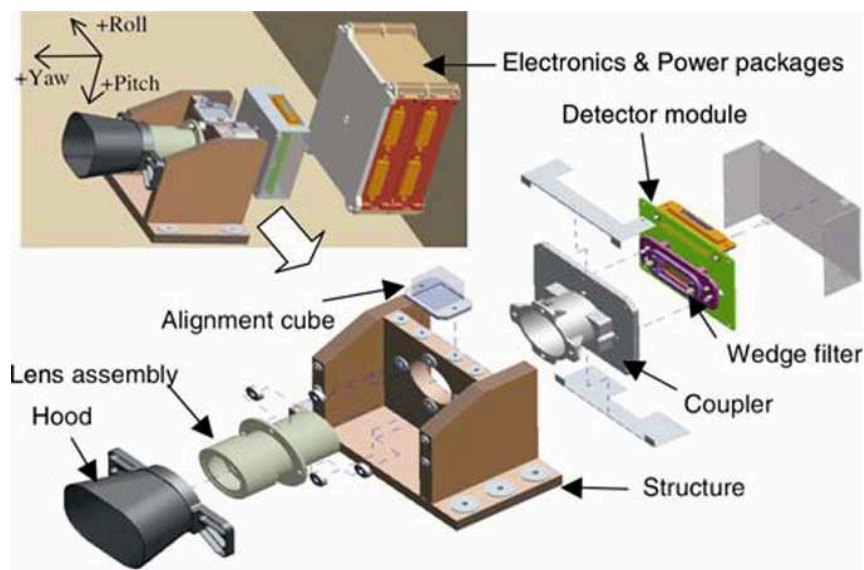


Figure 1.13: Schematic of HySI (Kumar et al. 2009).

### 1.4.2 HySI instrument description

The HySI instrument is developed by ISRO that mapped the lunar surface in 64 contiguous bands in the spectral range of 0.42 to 0.96  $\mu\text{m}$  (Kumar et al. 2009). The instrument worked in push-broom mode with a swath of 20 km from 100 km polar orbit of Chandrayaan-1. The HySI instrument is divided into two units, first unit comprising the focusing optics, a wedge filter for spectral separation, an Active Pixel Sensor (APS) area detector. The second unit is the camera and power electronics connected to the first unit through inter-connecting harness (Figure 1.13). The APS detector collect the reflected light from the Moon's surface through a focusing optics and wedge filter. Wedge filter has varying coating thickness which is responsible for spectral separation. The full spectrum of a target is obtained by acquiring image data in push broom mode, as the satellite moves along the column direction of the detector. Please refer to Kumar et al. (2009) for a detailed instrument description.

Initially the idea was to combine HySI and SIR-2 responses to get a complete coverage

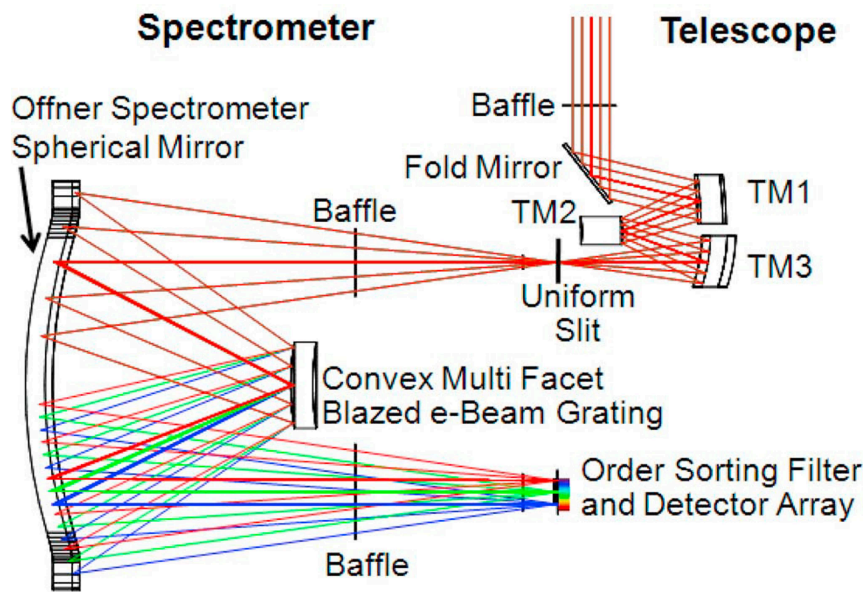


Figure 1.14: cross section of the  $M^3$  imaging spectrometer with telescope (Green et al. 2011).

from 0.42 to 2.41  $\mu\text{m}$  (Mall et al. 2009). However, inter-calibration of SIR-2 and HySI is challenging mainly due to only 60 nm of overlapping between the spectral channels. An approach to combine the SIR-2 and HySI reflectance data is discussed in detail in Chapter 3.

### 1.4.3 $M^3$ instrument description

The  $M^3$  is developed by the Brown University and the Jet Propulsion Laboratory. This is a pushbroom imaging spectrometer operating in the wavelength range of 0.43 to 3.0  $\mu\text{m}$  (Pieters et al. 2009). The data was recorded in two modes, a target mode with 260 spectral bands and 70 m/pixel spatial resolution, and a global mode with 86 spectral bands and 140 m/pixel spatial resolution and 40 km swath for images acquired from a 100 km spacecraft altitude. The  $M^3$  mapped over 95% of the Moon surface in global mode. Target data was only obtained for a limited number of locations on the Moon, mainly because of the early end of the Chandrayaan-1 mission.

The  $M^3$  has mainly two units, a three-mirror anastigmat (TMA) telescope and an Offner-type spectrometer, with a slit placed at the telescope focus (Mouroulis et al. 2007). The light enters  $M^3$  through TMA and directed to the slit. Light selected by the slit passes to the spectrometer and disperses in the spectral range between 0.43 and 3.0  $\mu\text{m}$ . This dispersed light is focused on the area array detector after transmitting through order sorting filter (Figure 1.14). Please refer to Green et al. (2011) for a detailed instrument description. The  $M^3$  data is available on-line from the NASA archive <sup>2</sup>.

<sup>2</sup><http://m3.jpl.nasa.gov/m3data.html>

## 1.5 Outline and thesis structure

The work presented in this thesis can be divided into two parts, (1) calibration of the SIR-2 data and integration of the datasets obtained by SIR-2, HySI, and M<sup>3</sup> instruments, and (2) development of the lunar iron abundance algorithm based on the 2- $\mu$ m absorption band parameters and application of this method to some specific sites of the Moon.

Chapter 2 describes the working principle of the SIR-2 instrument, its ground calibration, and in-flight calibration. the Apollo landing sites have been chosen as locations of the “ground truth” for the in-flight calibration of the SIR-2 instrument. Chapter 3 discuss about an attempt made to combine the datasets of the spectrometers SIR-2, HySI, and M<sup>3</sup>. The Moscoviense basin is considered as a case study because the three SIR-2 tracks and corresponding HySI and M<sup>3</sup> tracks are available. Chapter 4 presents the iron abundance estimation algorithm based on the 2- $\mu$ m absorption band parameters. The proposed method is based on an empirical calibration between the band parameters and the laboratory measured iron abundance of 68 lunar samples. The discrepancies observed between the iron abundance maps generated using the 1 and 2- $\mu$ m absorption band parameters are discussed. The iron abundance estimation method is applied to the four different sites on the Moon in Chapter 5. The SIR-2 and M<sup>3</sup> derived FeO maps are compared with the Clementine derived FeO abundance maps.



## 2 SIR-2 instrument, calibration and data reduction

The instruments on-board Chandrayaan-1 saw first light on 14 November 2008. The SIR-2 instrument recorded a total of 2076 orbits from the nominal 100 km spacecraft altitude between 19 November 2008 and 28 April 2009. One of the principal strengths of the SIR-2 instrument is the reliability of measurements made at a steady detector temperature ( $-55^{\circ}\text{C} \pm 0.5^{\circ}\text{C}$ ), that provided a consistent data-set of the lunar surface measurements.

This chapter discusses the SIR-2 instrument working principle (Section 2.1) and its calibration. The calibration of SIR-2 was divided into two phases: (1) Calibration of the integrated instrument before launch (preflight calibration). The test set-up and results from preflight calibration are described in Section 2.2. (2) In-flight calibration of the instrument after launch. The results of in-flight calibration are explained in Section 2.4. The data reduction steps are described in Section 2.3 to convert the SIR-2 raw spectra into reflectance spectra. The SIR-2 reflectance spectra are compared to the laboratory-measured reflectance spectra of Apollo landing sites in Section 2.5.

### 2.1 SIR-2 instrument working principle

The working principle of the SIR-2 instrument can be explained with the help of Figure 2.1. The SIR-2 collects the sunlight reflected by the Moon with the help of an optical box (O-Box), which houses a main front mirror and a secondary mirror. The diameter of the main front mirror is 72 mm (Mall et al. 2009) which defines the aperture of the optics. The incoming light is reflected by an off-axis parabolic mirror, onto a secondary mirror. The secondary mirror reflects the light into an optical quartz fiber, which transmits the light to the Sensor-Head/Radiator Unit (SHRU). The diameter of the fiber core is 400  $\mu\text{m}$ , which defines the field of view (FOV) of the instrument to be 2.22 mrad. The SHRU consists of the spectrometer and the radiator. The spectrometer part of the instrument contains a blocking filter, a holographic corrected concave grating, and the detector with its analogue electronics. The light enters the SHRU through the fiber, passes a filter, spectrometer slit, and reaches to the dispersing grating by passing through a quartz body. The light dispersed by the grating then passes through the quartz body again to reach a second order filter, which is glued onto the window of the detector holder. The light is detected by the detector after it passes through the window. The electrons released by individual pixel of the detector array are collected and a sequential readout is performed after every exposure time period. The analogue value representing the magnitude of the pixels is sampled by a 16 bit Analogue to Digital Converter (ADC) located in the Electronic Box (E-Box).

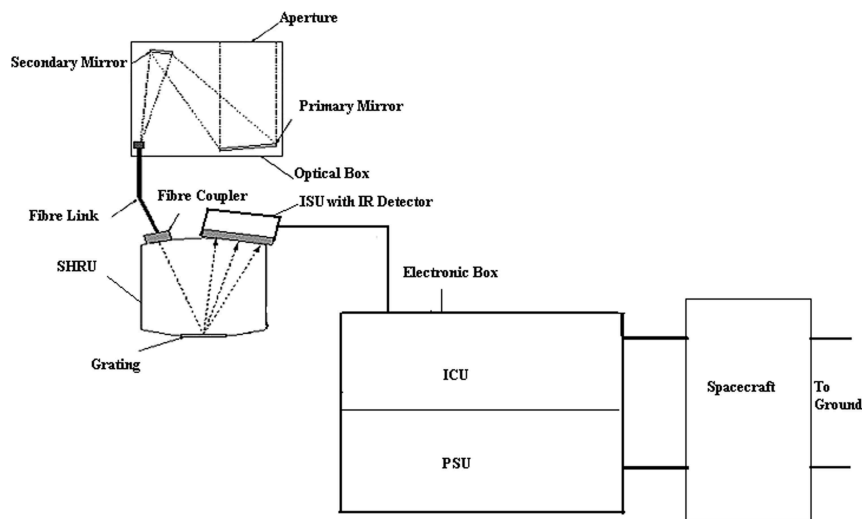


Figure 2.1: A schematic view of the SIR-2.

The E-box is connected to the SHRU through the instrument's local harness (ILH). To minimize electronic noise, the E-Box was split into two sections: the upper section is the Instrument Control Unit (ICU) and the lower is the Power Supply Unit (PSU). The ICU provides control instructions and communicates with the spacecraft. The computer architecture developed for the ICU and its operation is described by Torheim et al. (2009). The PSU supports the system's different voltage requirements. The PSU receives the power from the spacecraft's main power supply and redistributes it to the various components of the system according to their power requirements. The obtained digital values (counts) proportional to the electrons released by the individual pixels of the instrument's detector are finally embedded in the telemetry (TM) packages, in order to send them to the spacecraft's mass memory. The spacecraft communicates to and from on-board instruments and organizes it into a single data stream and transfers it to Earth data receiving station via the long range telemetry.

The detector of SIR-2 is a linear IR detector G9208-256W from Hamamatsu. The detector had 256 pixels with a pixel pitch of  $50\ \mu\text{m}$  arranged along a strip. It is a Photo Diode Array (PDA) type of detector and made of Indium Gallium Arsenide (InGaAs). The so-called cooling console inside the SHRU mechanically holds the detector. Among three IR detector of type G9208-256W, number 06C4546 was selected for the SIR-2 Flight Spare (FS) model that flown on Chandrayaan-1 mission. The detector was selected based on the tests described by Sitek et al. (2008). The temperature of the detector was stabilized by an embedded thermoelectric cooler. One heater was used for increasing the temperature of the cooling console of the detector to provide a suitable temperature range. The active temperature control of SIR-2 detector enabled us having a consistent data-set throughout the mission. The overall power consumption of the SIR-2 instrument was 11 W. The key characteristic parameters of the SIR-2 are listed in Table 1.2.

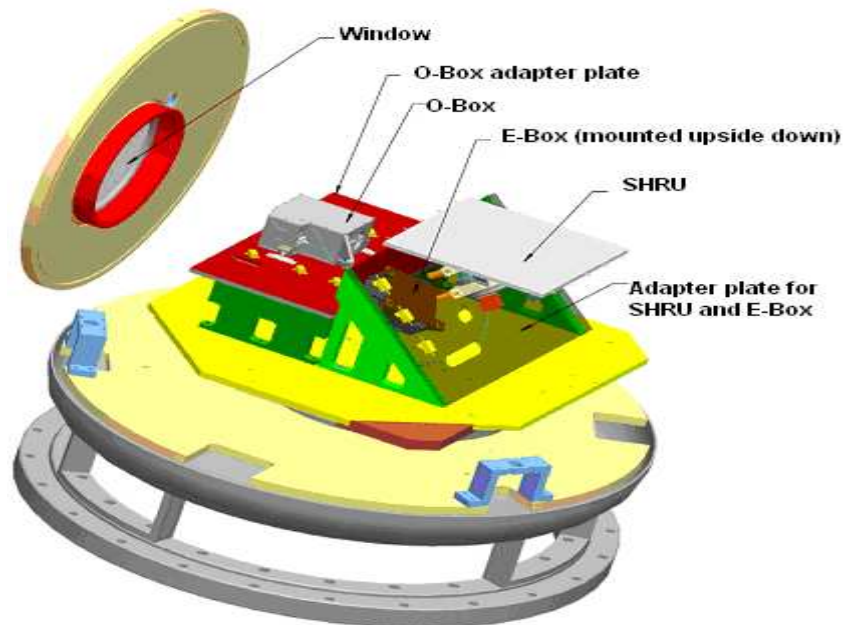


Figure 2.2: The SIR-2 subunits mounted on the thermal vacuum chamber's turn table. The chamber's diameter is 1 m, length is approximately 1.25 m and thickness is 4 mm. The aperture is 0.4 m (Image courtesy: R. Orlik).

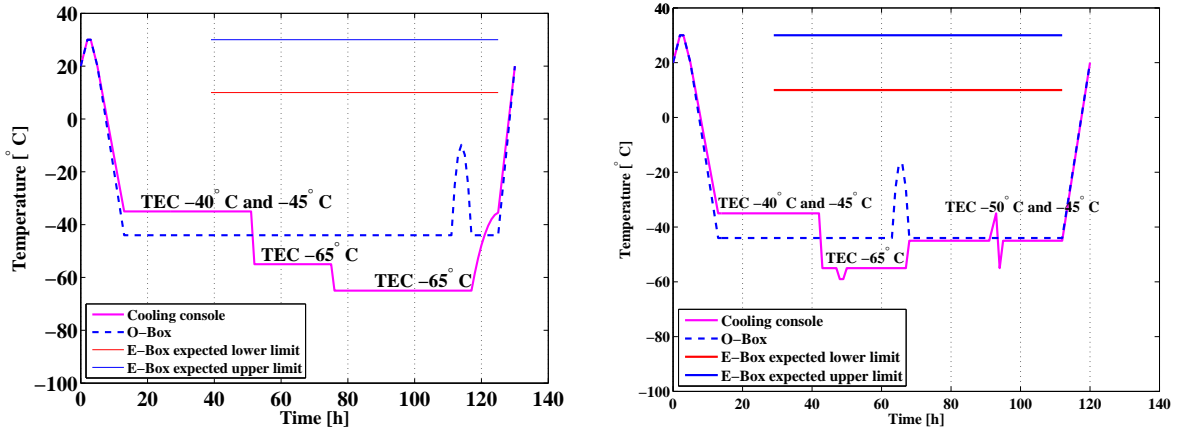
## 2.2 Preflight calibration

Understanding the instrument's behaviour and its limitations on-ground under known laboratory conditions is important in order to retrieve reliable information from remotely sensed data. The main aim of the preflight calibration is to find out the instrument's optical performance at different temperatures. The Thermal Vacuum (TV) qualification tests for the subunits of the SIR-2 were performed prior to the preflight calibration of the integrated instrument (Sitek 2008). The preflight calibration was divided into three parts:

- Bias and Dark count rate measurement, by covering the TV chamber window.
- Spectral calibration, using the monochromator (MS 257 from LOT Oriel).
- Radiometric calibration, using the integrating sphere (manufactured by PRC Krochmann, serial number 00430).

The SIR-2 FS was calibrated at Max Planck Institute for Solar System Research (MPS) clean room of class 10000 (Heizhaus). The SIR instrument which was flown on the SMART-1 mission was also calibrated in the same laboratory (Vilenius 2009). The other potential flight model of SIR-2 was calibrated in October 2007 at the Space Applications centre (SAC), Ahmedabad, India Vilenius (2009).

The preflight calibration of the SIR-2 proceeded through the collection of measurements from the spectral and radiometric sources. These measurements were acquired for five days starting from 28 April 2008 to 2 March 2008. The subunits of the SIR-2 FS



(a) Planned temperature cycle (Image courtesy: E. Vilenius). (b) Temperature cycle followed during preflight calibration.

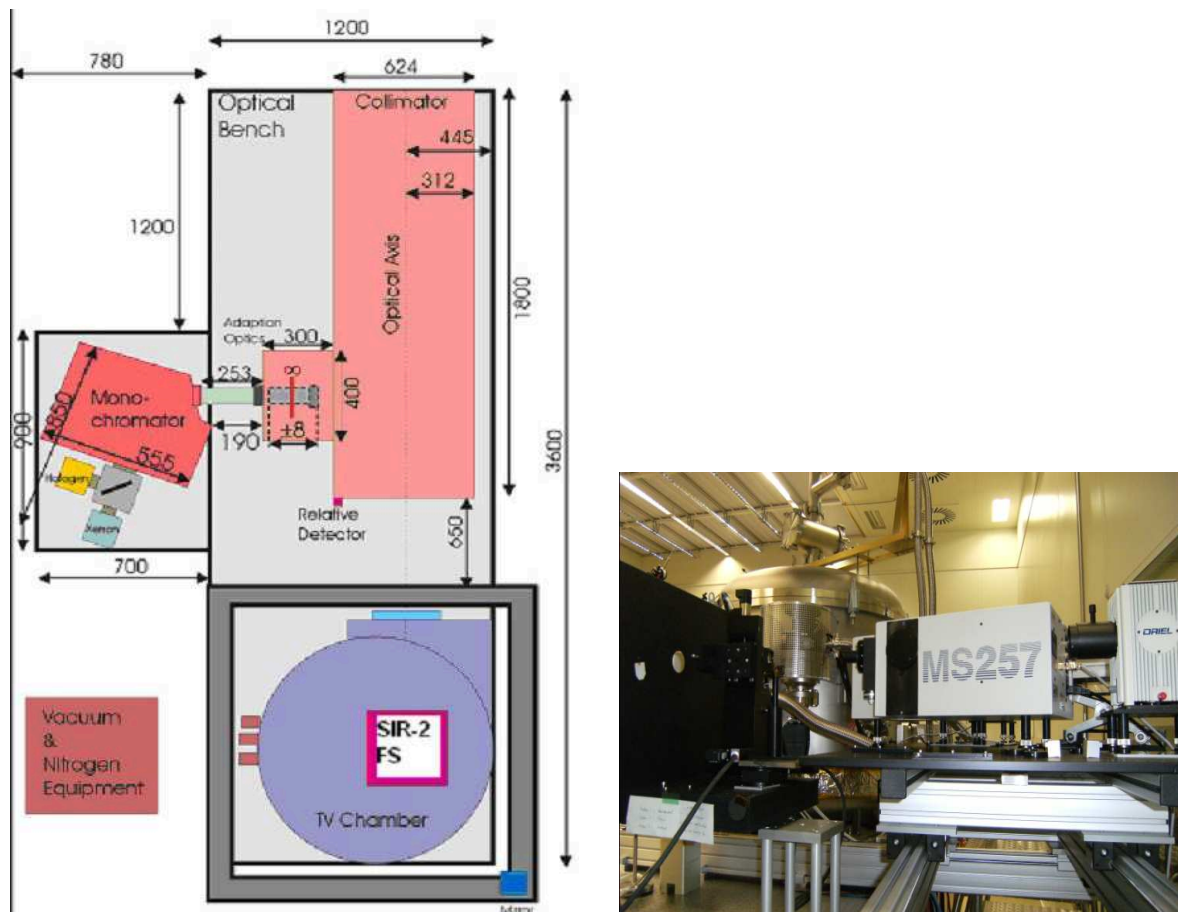
Figure 2.3: Temperatures of the SHRU’s cooling console, O-Box, and E-Box at the time of on-ground calibration.

were mounted on a turntable inside the TV chamber and co-aligned with respect to the optical axis of an illumination facility located outside the chamber. The SIR-2 subunits inside the TV chamber are shown in Figure 2.2. The SHRU and E-Box were attached on a plate however, that is not shown in Figure 2.2 to have a clear view of the SIR-2 subunits. The SIR-2 was illuminated through a 265 mm diameter optical window at the front of the TV chamber. The window is made of a specific type of quartz glass, Suprasil 1. The window’s thickness was not measured before starting the calibration and was considered to be 35 mm. The transmission curve of the TV chamber window was calculated using Equation 2.1. The transmission profile of the TV chamber’s window should be taken into account at the time of calculating the absolute sensitivity of the detector.

$$T(\lambda) = 10^{-l(\lambda)x} \quad (2.1)$$

where,  $\lambda$  is the wavelength,  $l$  is a decadic extinction coefficient and  $x$  is the thickness of the window.

One of the main goals of the calibration campaign was to determine the instrument’s performance at different temperatures. We prepared the temperature cycling procedure for the subunits of the SIR-2 instrument and tested the instrument’s response at the different detector temperatures. We started with a warming period of about 6 hours (Figure 2.3) before starting the calibration to ensure that no dew and condensed water is present in the chamber. Cooling was achieved by liquid nitrogen injection into the chamber’s shroud. The cooling of the first phase started by decreasing the cooling console temperature from 30 °C to -30 °C as shown in Figure 2.3. Our plan was to achieve the lowest cooling console temperature of -65 °C but we observed instability in the detector performance beyond -59 °C and decided not to go below -55 °C. Figures 2.3(a) and 2.3(b) show a comparison between the planned and achieved temperatures for the subunits of the SIR-2 instrument.



(a) A schematic diagram of the spectral calibration test set-up. The units are in millimeters. Figure adopted from Sebastian (2002). (b) Picture showing the TV chamber and the mono-chromator inside the clean room at the time of the spectral calibration of the SIR-2 FS.

Figure 2.4: Spectral calibration test set-up for the SIR-2 FS model

## 2.2.1 Preflight calibration set-up

### 2.2.1.1 Spectral calibration set-up

The spectral calibration test set-up is shown in the Figure 2.4. The O-Box was placed in front of the TV chamber's window. The mono-chromator was aligned to the optical axis of the collimator, and the exit slit spectrum was fed to the collimator through a biconvex lens. The effective focal length of the lens is 70 mm and the diameter of the lens is 30 mm. The entrance slit of the mono-chromator was illuminated by a halogen light source. The mono-chromator's spectral coverage is in the range 180 to 2,500 nm. This spectral range is achieved using three gratings on a rotatable turret. The mono-chromator has a motorized filter wheel equipped with 3 order sorting filters. The filter wheel is intended to be used with filters for blocking, order sorting, or for the spectral characterization. We checked the calibration status of the mono-chromator with the He-Ne laser at 632.8 nm. The He-Ne laser was aligned at the lateral input port of the mono-chromator and the output beam was checked at several slit width and wavelength adjustments. The mono-chromator

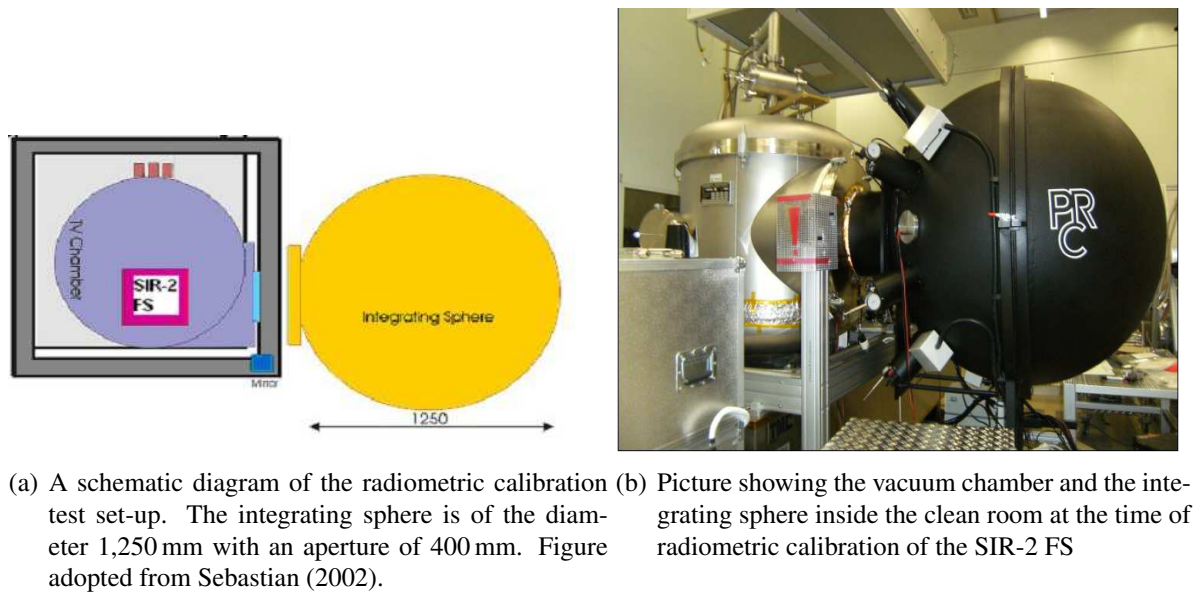


Figure 2.5: Radiometric calibration test set-up for the SIR-2 FS model

settings were fully accessible through the Optical Ground Support Equipment (OGSE) system. The monochromator settings used for the spectral calibration of the SIR-2 FS are : Grating: 3 (NIR grating, wavelength range: 600 – 2,500 nm), Filter: 3 (empty), Slit width: 460  $\mu\text{m}$ , Port: 8, and Shutter: Open.

The background current was measured by covering the filter of the filter wheel and the dark current was measured by covering the TV chamber’s window for the spectral calibration.

### 2.2.1.2 Radiometric calibration set-up

The radiometric calibration set-up is shown in Figure 2.5. The TV chamber was rotated so that the SIR-2 FS was in front of the integrating sphere. The PRC Krochmann sphere is equipped with four halogen lamps at a constant light level. The lamps can be moved mechanically that allow to adjust the output intensity. The integrating sphere’s response was measured during a calibration made by the Physikalisch-Technische Bundesanstalt (PTB 2001) and plotted in Figure 2.10(a) interpolated in the SIR-2 wavelength range.

### 2.2.2 Bias and Dark count rate detection

The first process in the spectral and radiometric calibration of the SIR-2 instrument is the removal of the background signal from the total detected signal. The background signal is a combination of the bias/offset and dark values. The bias value of a PDA type detector is the value that a pixel shows even when the integration time is zero. Dark values are dependent on the integration time and the detector temperature. Dark values are basically the thermal noise which needs to be subtracted as a first step in the data reduction process. The dark count rate is defined as the dark level in Digital Number (DN)

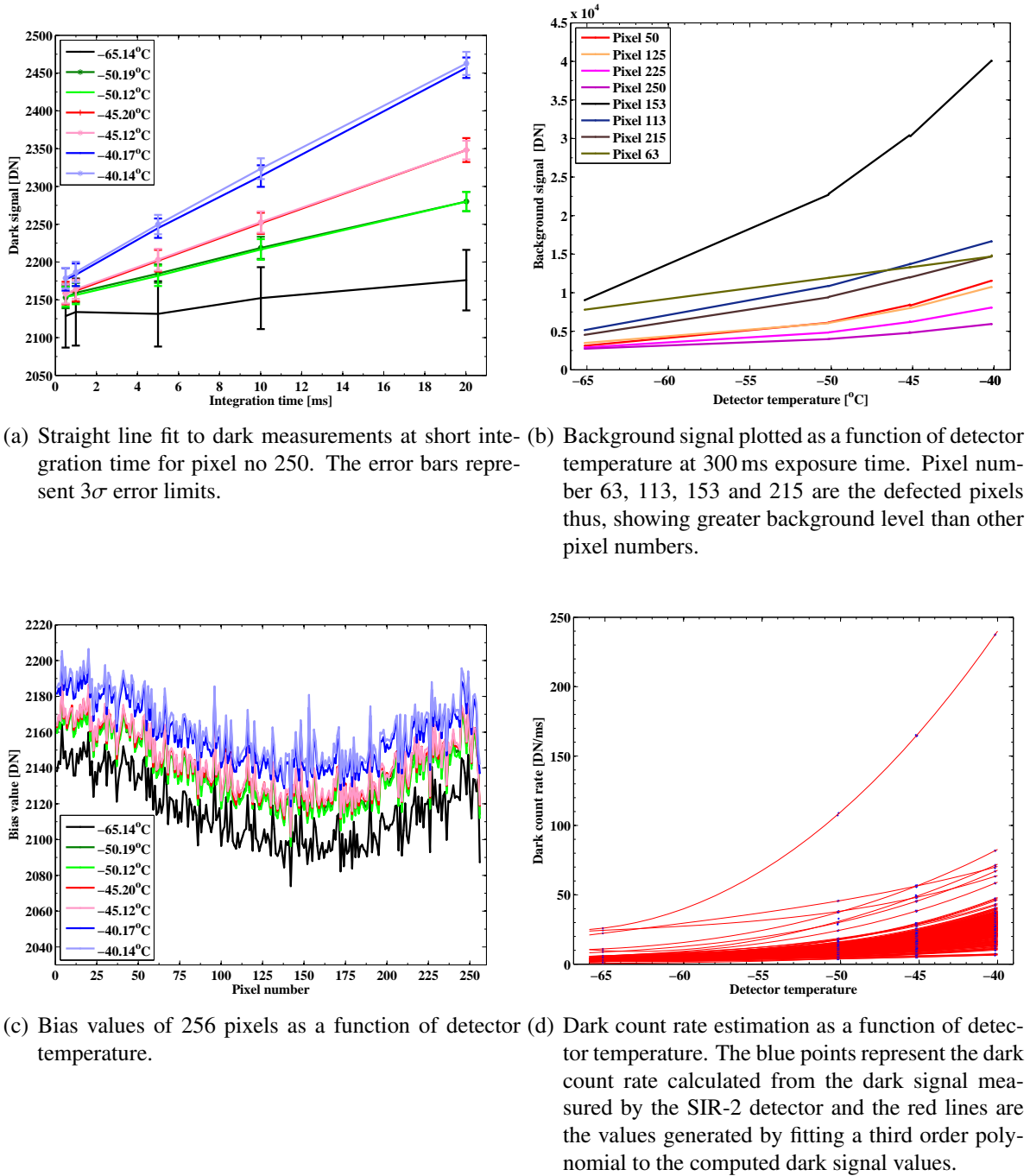


Figure 2.6: Dark and bias analysis results.

units per integration time.

Dark spectra were recorded at different detector temperatures and exposure/integration times by covering the TV chamber's window. The dark measurements are utilized in computing the bias value and the dark count rate of the SIR-2 FS detector. Table A.1 lists the dark measurement files recorded during the preflight calibration. The instrument was commanded for 12 different integration times (Table A.1) and about 100 dark spectra

were recorded for each integration time at a nearly constant detector temperature. The SIR-2 instrument had an active temperature control system that could maintain the detector's operating temperature approximately at a constant value. We observed a maximum deviation of 0.35 °C in the detector temperature values for a set of dark measurements.

Dark spectra were first inspected visually to eliminate any outliers. We observed that the dark output of the SIR-2 is dependent on both the exposure time and detector temperature, and increases by the rising of any of these two parameters. This dependency is shown in Figure 2.6(a) for pixel number 250. The bias level of the SIR-2 detector is calculated by fitting a straight line to the dark signal measured by changing the integration time between 0.5 and 20 ms for an approximately constant detector temperature. We selected the integration time shorter than 50 ms for the bias and dark count rate analysis because the dark signal versus integration time relationship starts to deviate from the straight line response at longer integration time periods. The intercept term of the fitted straight line represents the bias value. We observed from Figure 2.6(a) that the bias level is minimum at  $-65$  °C. However, larger error bars in this case demonstrates higher variations in the measured dark values. This could be due to higher thermal noise sensitivity of the instrument at the detector temperatures below  $-60$  °C. Pixel number 13, 63, 67, 113, 153, 182, and 215 are considered to be defect pixels that showed a more than 40% increase in the recorded background signal level in comparison to other pixels of the detector. The dark signal versus integration time response of defect pixels is similar to other pixels at short integration time intervals and therefore, they are not considered separately for computing the bias level of each pixel.

Figure 2.6(b) shows the effect of increasing the detector temperature on the background signal measured at a fixed exposure time of 300 ms. Defect pixels response are shown in dark colors in Figure 2.6(b) and "good" pixels are plotted in shades of red. Figure 2.6(c) shows the bias values computed for all pixels at different detector temperatures. Defect pixels show 20-30 DN higher bias values. The bias values are approximately the same for the detector temperatures  $-45$  °C and  $-50$  °C however, these values show wider spread for the detector temperatures  $-40$  °C and  $-65$  °C. The dark count rate is the slope of the straight line fitted to the dark signal measured by changing the integration time at a constant detector temperature. Figure 2.6(d) shows the dark count rate plotted as a function of the detector temperature for all 256 pixels of the detector. The dark count rate increases with increasing detector temperature. The dark count rate values at the detector temperatures other than measured was estimated by fitting a third order polynomial and shown in Figure 2.6(d). The seven defect pixels show a noticeable difference in the dark count rate compared to the good pixels response. The good pixels of the SIR-2 detector show the dark count rate lower than 50 DN/ms for the detector temperature range between  $-40$  °C and  $-65$  °C however, pixel number 153 shows abrupt increase in the dark count rate response and gives the highest dark count rate value higher than 200 DN/ms at  $-40$  °C.

### 2.2.3 Spectral calibration

The spectral calibration of the SIR-2 FS was done to characterize:

- The wavelength-pixel dependency and to determine the coverage of the spectral wavelength, by changing the monochromator wavelength range between 950 and 2,500 nm



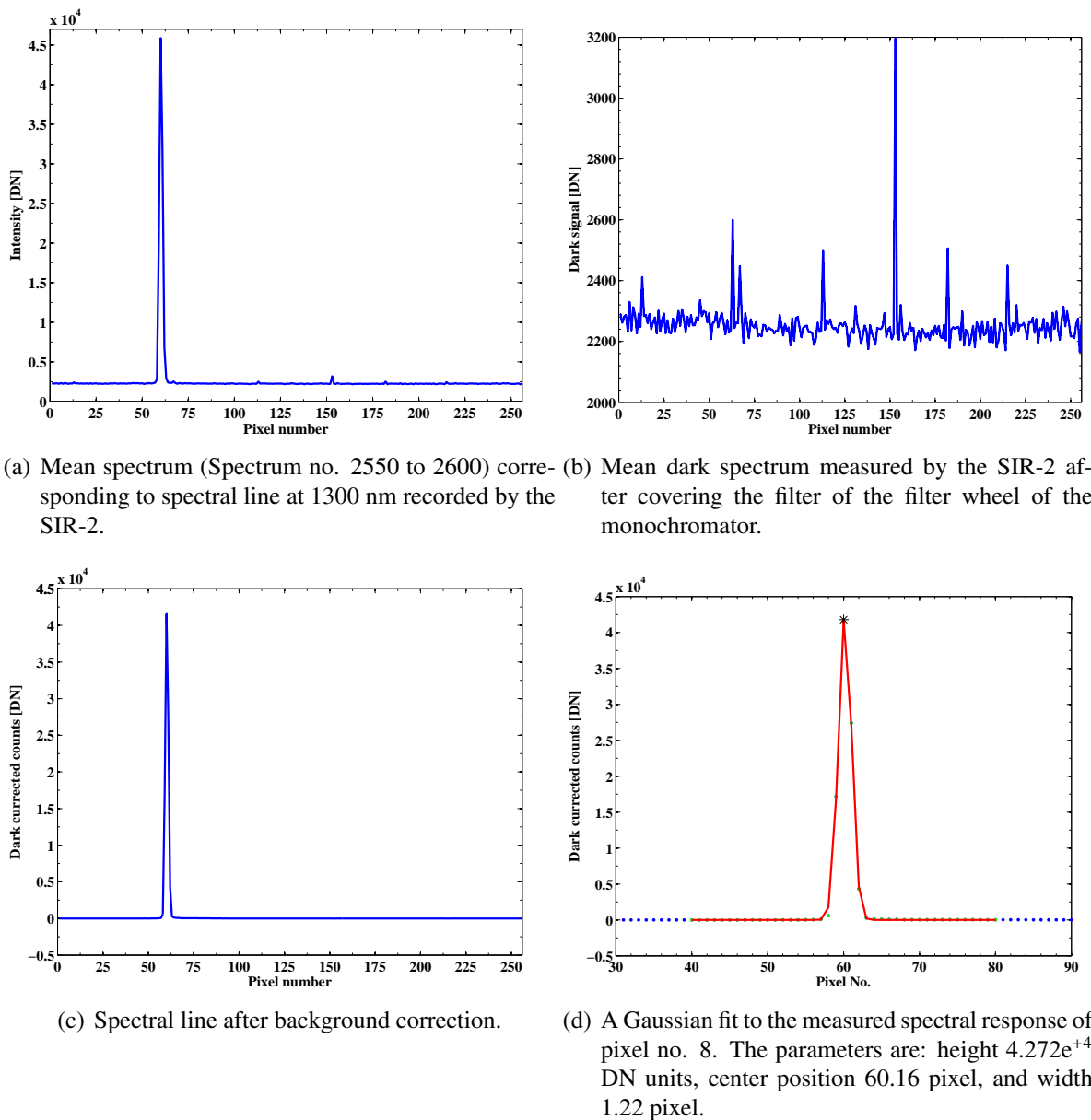


Figure 2.7: Spectral calibration of the SIR-2 instrument. Data presented here are from File number 13 and 15 of Table A.2

in step size of 50, 10 and 5 nm for different exposure time intervals. A 5 nm step size was used to scan shorter (925 – 950 nm) and longer (2,400 – 2,425 nm) wavelength ranges corresponding to the first few and the last few pixels of the detector.

- The spectral Point Spread Function (PSF) of four selected pixels : We selected the wavelength ranges; 1,415 – 1,447 nm, 1,810 – 1,861 nm, and 2,220 – 2,274 nm with a wavelength step size of 2 and 0.5 nm for this purpose.
- Stray-light and second order effects using out-of-band illumination : To test the stray light effects on the measured spectrum, the TV chamber was rotated by 5,

10 and 15 mm distances in clockwise and anticlockwise directions. However, we could not get measurements for a TV chamber rotation beyond 5 nm in clockwise direction due to the strong influence of background signal on the measured signal.

### 2.2.3.1 Spectral position and wavelength coverage determination

The spectral calibration test set-up is shown in Figure 2.4. The measurements taken during the preflight calibrations are listed in Table A.2.

Figure 2.7 demonstrates the procedure of finding the central wavelength corresponding to the pixel position. Figure 2.7(a) shows a spectral line (raw data) measured at 1,300 nm, commanded through the monochromator in a step size of 50 nm. We subtracted the mean dark signal from the raw measurements to minimize the background noise. Figure 2.7(b) shows the mean background signal recorded at a detector temperature of  $-50\text{ }^{\circ}\text{C}$  by closing the filter of the monochromator's filter wheel. Total seven peaks present in the mean background signal are corresponding to the seven defective pixel's position of the SIR-2 FS detector. Figure 2.7(c) shows a background corrected spectral line. The pixel position corresponding to the spectral channel peak is obtained by fitting a Gaussian curve to the background corrected signal as shown in Figure 2.7(d). Every spectral line had been measured for more than 20 times and data points in blue in Figure 2.7(d) show an average spectrum derived from all spectra measured at the same spectral line. We have selected 20 consecutive pixels in both side of the maximum spectral peak (total 40 pixels) to apply a Gaussian fit. These data points are shown in green color in Figure 2.7(d) and a Gaussian fit is shown by a red line. The location of pixel corresponding to the spectral line is shown as a black star. We applied a one dimensional Gaussian fit to the spectral lines detected by the SIR-2 instrument as given by Equation 2.2.

$$f(x) = A \times \exp(-((x - B)/C)^2) \quad (2.2)$$

where,  $A$  is the height of the curve's peak,  $B$  is the position of the centre of the peak and  $C$  is the width of the peak.

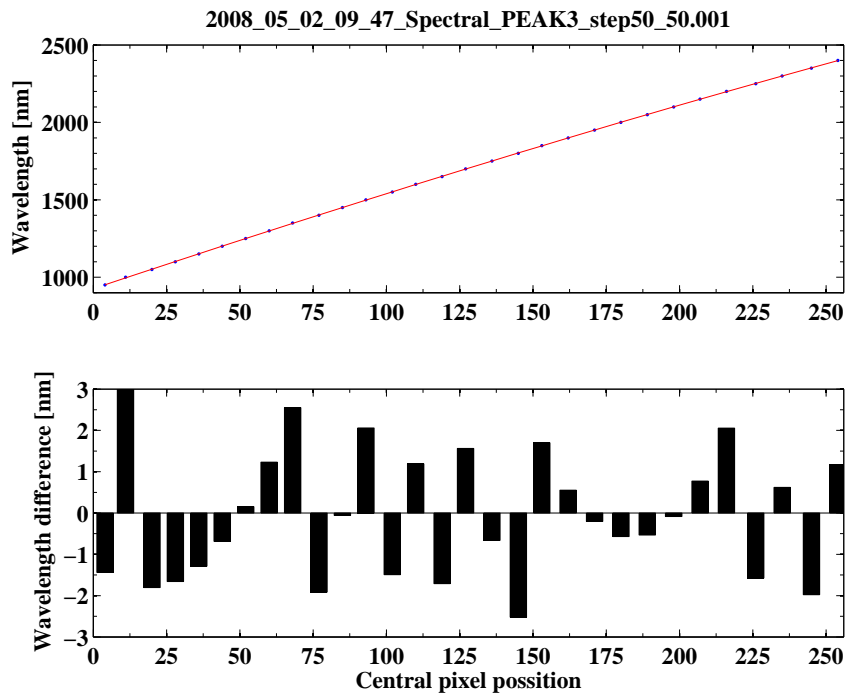
Figure 2.8 shows the results of the spectral calibration of the SIR-2 instrument derived for a detector temperature of  $-50\text{ }^{\circ}\text{C}$ . The spectral calibration analysis was done for different detector temperatures and monochromator wavelength step sizes. However, we did not observe any temperature dependency in pixel to wavelength conversion.

Figure 2.8(a) shows the extracted wavelength pixel number correlation for SIR-2. A third order polynomial could be fitted to the pixel-wavelength relation as given by Equation 2.3:

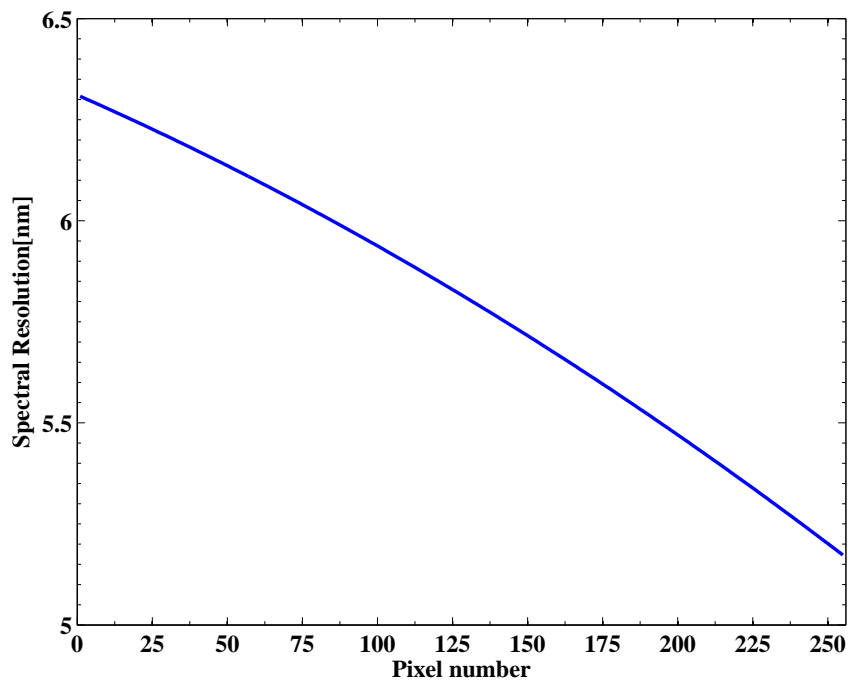
$$\lambda(\text{PIX}) = 927.73 + 6.2839 \times \text{PIX} - 0.0015338 \times \text{PIX}^2 - 1.49332e^{-6} \times \text{PIX}^3 \quad (2.3)$$

Where,  $\lambda$  is the wavelength and  $\text{PIX}$  is the number of pixels between 1 and 256.

The wavelength coverage range varies between 934 and 2,410.8 nm according to Equation 2.3. The maximum deviation we found in the wavelength range using the spectral measurements at other detector temperatures (Table A.2) is  $\pm 2$  nm, which is much lower than the SIR-2 spectral resolution (6 nm). The difference between the measured and polynomial fitted values is shown in lower panel of Figure 2.8(a). The residual errors are



- (a) The upper panel shows the third order polynomial fit (plotted as red line) to determine the wavelength versus pixel number relation. The lower panel shows the residual of the polynomial fit.



- (b) Spectral sampling as a function of pixel number. The residual is calculated by taking the difference between pixels in the third order polynomial.

Figure 2.8: Pixel to wavelength relation and spectral resolution computed for on-ground spectral calibration of the SIR-2.

lower than 2 nm for more than 95% of pixels, however some pixels such as pixel number 11 in Figure 2.8(a) (lower panel) shows a residual error larger than 3 nm. We observed the maximum residual error about 5 nm for spectral calibration files (Table A.2) with a sampling interval of 10 nm. However, this error is smaller than the average spectral resolution of 6 nm of the SIR-2 instrument.

The spectral resolution is computed by taking the difference between wavelength values of adjacent pixel from Equation 2.3 and plotted in Figure 2.8(b). The spectral resolution varies between 6.5 to 5 nm with an average spectral resolution of 6 nm. The spectral resolution is decreasing with increasing pixel number, this trend is observed for all the spectral calibration files analysed.

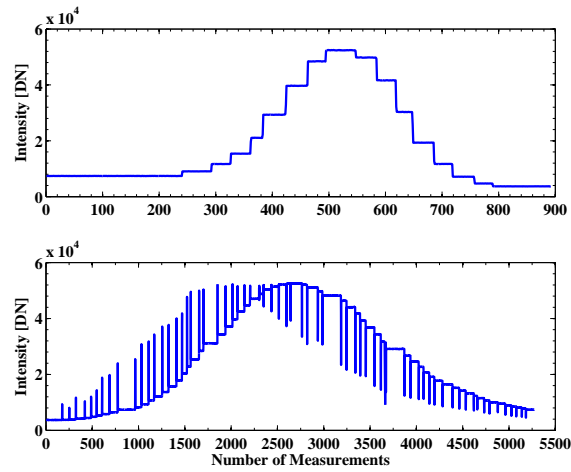
### 2.2.3.2 Point Spread Function (PSF)

We selected pixel number 14, 82, 152 and 226 for the PSF analysis. The PSF measurements were recorded at the detector temperatures  $-50^{\circ}\text{C}$  and  $-65^{\circ}\text{C}$  with two wavelength step sizes of 2 nm and 0.5 nm as listed in Table A.3. The monochromator wavelength was commanded in sub-pixel steps using the OGSE monochromator monitoring program. A 2 nm step is in-built while a 0.5 nm wavelength step was commanded each time manually.

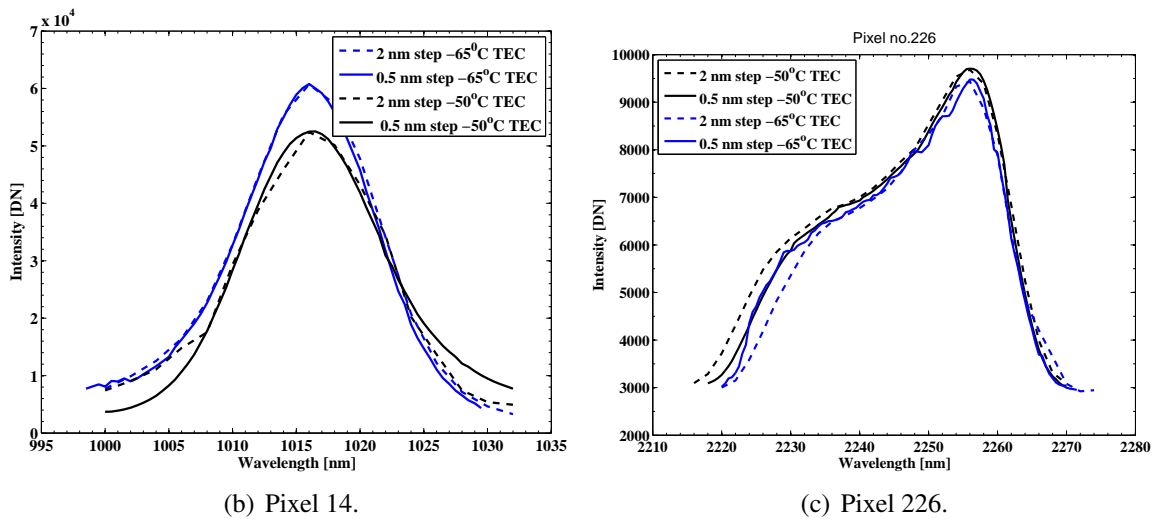
Figure 2.9 shows the PSF plots for measurements recorded at detector temperatures of  $-50^{\circ}$  and  $-65^{\circ}$  with different exposure time as listed in Table A.3. Figure 2.9(a) shows the raw data recorded with wavelength step size 2 nm and 0.5 nm for pixel number 14 in the wavelength range 1,000–1,032 nm. We observed that backward and forward spikes are present for a 0.5 nm wavelength step size in the measured raw data (Figure 2.9(a), lower panel). The spikes are observed for all four pixels selected for the PSF analysis. The presence of spikes in the measured raw data could be due to the monochromator's instability in its wavelength commanding because we manually changed wavelength step of 0.5 nm. We have removed these short duration spikes while computing PSF at 0.5 nm wavelength step. We have taken the average value of intensity (DN) at every commanded wavelength to generate PSF plots from the raw data.

The PSF plots for pixel number 14 and 226 are shown in Figure 2.9(b) and 2.9(c), respectively. The difference observed in the intensity level for pixel number 14 in Figure 2.9(b) could be due to a different exposure time. However, this difference is minor in the case of pixel number 226 in Figure 2.9(c) probably due to low sensitivity of the pixels located at the edge of the detector array. We observed 4 to 8 nm wavelength shift in central peak position between the two days of measurements. The reason for this shift could be either a mismatch in start and end values of the wavelength or presence of spikes in the case of 0.5 nm wavelength step which was difficult to correlate accurately to the wavelength position. To overcome this problem, we plotted intensity peaks for pixels with respect to the relative wavelength to compare the Full Width Half Minimum (FWHM) values and shape of the PSF curves. The intensity-wavelength relationship is approximately symmetric in the case of pixel 14 and 82 with FWHM of 2 to 3 pixels. However, pixel number 226 shows wider spread for wavelength range 2,220–2,272 nm with FWHM of 5 to 6 pixels.

We concluded from PSF analysis of pixel number 14, 82 and 226 that the FWHM is about 3 pixels for pixel number lower than 200 and at the edge of the detector it increases



(a) PSF measurements at 2 nm (top panel) and 0.5 nm (bottom panel) monochromator wavelength steps (File no. 9 and 10, Table A.3) for pixel number 14 at  $-50^\circ$  detector temperature.



(b) Pixel 14.

(c) Pixel 226.

Figure 2.9: PSF plots for Pixel No. 14 and 226 measured at  $-50^\circ$  and  $-65^\circ$  detector temperatures (Table A.3).

to 5-6 pixels. Our analysis shows that the Rayleigh resolution of the SIR-2 FS model is between 18 and 36 nm.

## 2.2.4 Radiometric calibration

The radiometric calibration of the SIR-2 FS has been done to characterize:

- The absolute spectral sensitivity and flat field of the instrument at the different integration time.
- The linearity with respect to the incident irradiance measured by changing the lamp position between 20 – 45 mm.

- The linearity with respect to the integration time measured by changing the integration time at a constant irradiance intensity of the integrating sphere.
- Dark signal linearity and Bias current measurements by changing the integration time (Discussed in Section 2.2.2).

Radiometric calibration is required in order to obtain the radiance  $I$  ( $\text{W}/(\text{m}^2 \text{sr } \mu\text{m})$ ) from the original spectrum recorded in DN. The radiometric measurements were acquired at  $-40^\circ\text{C}$ ,  $-45^\circ\text{C}$ ,  $-50^\circ\text{C}$ , and  $-65^\circ\text{C}$  detector temperatures with 12 different exposure time intervals and listed in Table A.4. The radiometric calibration test set-up is shown in Figure 2.5. The measured radiance by the SIR-2 detector can be written in equation form as given in Equation 2.4:

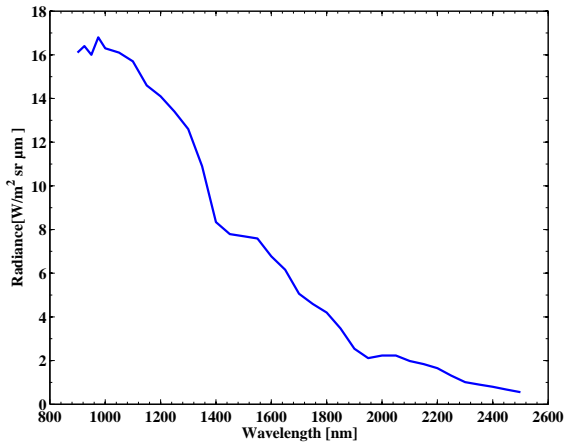
$$\text{Measured Spectrum} = (\text{Absolute Sensitivity} \times \text{Incident Radiance}) + \text{Dark Signal} \quad (2.4)$$

The incident radiance in Equation 2.4 represents the absolute spectral response of the integrating sphere viewed by SIR-2 through the Suprasil 1 window of the TV chamber. The integrating sphere response was measured in 2001 and is plotted after interpolating it to the SIR-2 wavelength range in Figure 2.10(a). We assumed that the sphere's emission response is not changed at the SIR-2 wavelength range for the radiometric calibration analysis.

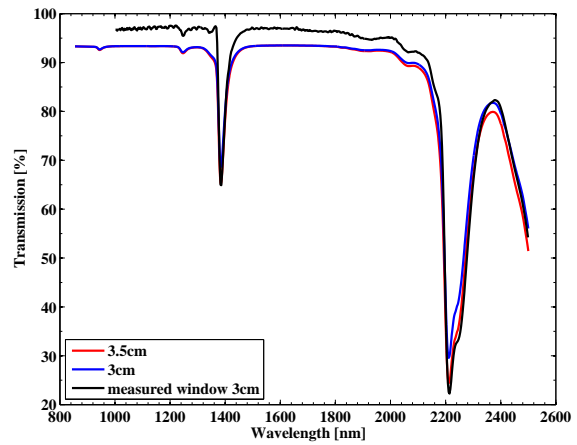
The transmission profile of the TV chamber's window is computed using equation 2.1 assuming a window thickness 3.5 cm. However, the window thickness measurements were done in the VIS-NIR wavelength range on 5<sup>th</sup> and 6<sup>th</sup> May 2009. The window thickness was measured as 3 cm instead of 3.5 cm. Figure 2.10(b) shows the transmission profiles of Suprasil 1 material computed using Equation 2.1 at 3 and 3.5 cm window thickness and the transmission profile measured on 5<sup>th</sup> May 2009 (window thickness 3 cm). We observed from Figure 2.10(b) that the TV chamber's window transmission is less than 40% at about 2  $\mu\text{m}$ . The overall transmission curve shape is comparable for calculated and measured window thicknesses. However, transmission values are about 5% higher for the measured window thickness in the wavelength range 1 – 2  $\mu\text{m}$ . The transmission response of the measured window thickness is very similar to the calculated window thickness of 3.5 cm mainly in the range 2 – 2.5  $\mu\text{m}$ . Figure 2.10(b) demonstrates that the TV chamber's window thickness has a significant effect on the transmission curve and therefore, may affect significantly the instrument's sensitivity function derivation. Figure 2.10(c) shows the total radiance incident on the instrument mounted inside the TV chamber. The absolute sensitivity of the detector is computed using Equation 2.5.

$$\text{Absolute Sensitivity} = \frac{(\text{Measured Spectrum} - \text{Dark Signal}) \text{ per Exposure Time}}{\text{Incident Radiance}} \quad (2.5)$$

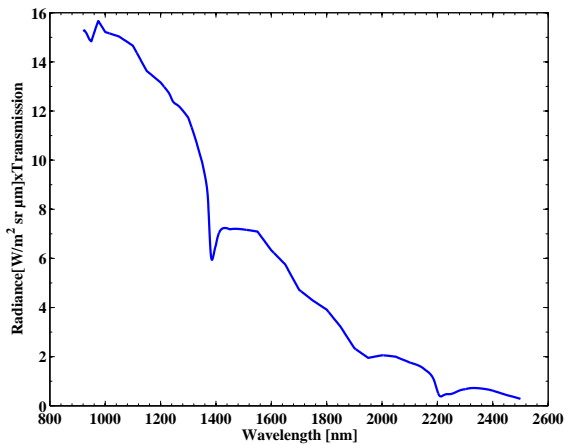
In order to calculate the absolute sensitivity, we followed the following steps: (1) removal of dark signal from the measured raw data. We took an average of approximately 100 dark spectra measured at the same integration time and approximately at the same detector temperature and subtracted it from the average raw spectrum; (2) pixel to wavelength conversion using equation 2.3; (3) dividing the dark corrected spectra by



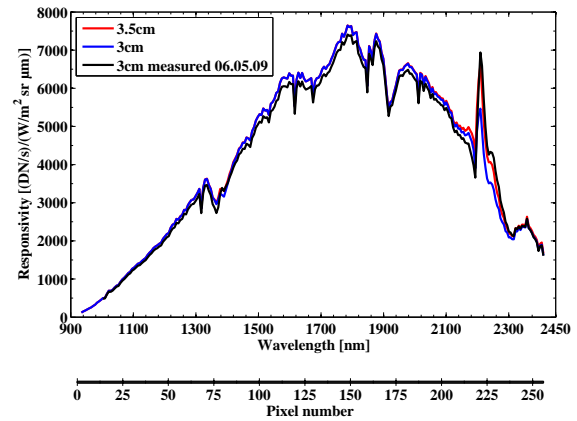
(a) Radiance output of the integrating sphere used for radiometric calibration. This graph is integrated to the SIR-2 wavelength range for calculating the original spectrum in equation 2.5.



(b) Transmission curve of thermal vacuum chamber window made of Suprasil 1 material. The measured transmission values have been compared with calculated one corresponding to window thickness 3 and 3.5 mm using equation 2.1.



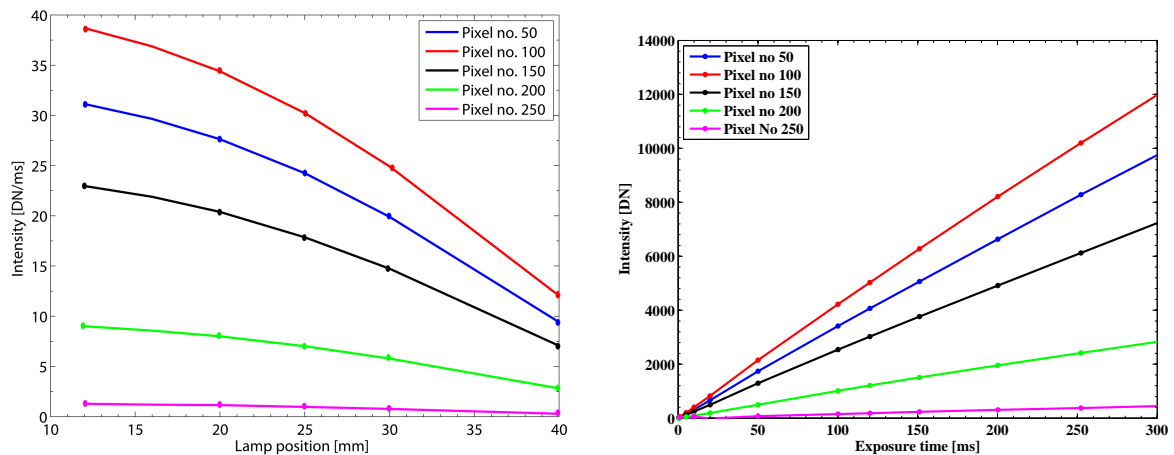
(c) Total radiance incident on the instrument is the multiplication of radiance output of the integrating sphere and transmission curve of TV chamber window.



(d) Absolute sensitivity/responsivity of 256 pixel computed using equation 2.5. Dependency of absolute sensitivity on the transmission window function is shown.

Figure 2.10: Stepwise description of the radiometric calibration of the SIR-2 instrument. Data presented here are from file number 19 of Table A.4.

the exposure time and by the total incident irradiance. An example of an absolute sensitivity curve derived using Equation 2.5 at the detector temperature  $-50\text{ }^{\circ}\text{C}$  is shown in Figure 2.10(d). The standard readout frequency is 1.54 MHz and the integration time is 300 ms (File number 19, Table A.4). Figure 2.10(d) shows that the absolute sensitivity response corresponding to three different window thickness values are approximately the same except for the 2,185 to 2,315 nm wavelength region. The absolute sensitivity is maximum at 2214 nm and the transmission curve of the TV chamber's window shows the maximum absorption at the same wavelength. The intensity recorded by the SIR-



(a) Linearity with respect to light intensity at detector temperature  $-50\text{ }^{\circ}\text{C}$ . (b) Linearity with respect to exposure time at detector temperature  $-50\text{ }^{\circ}\text{C}$ .

Figure 2.11: Linearity check at detector temperature  $-50\text{ }^{\circ}\text{C}$ .

2 in the wavelength range 2,214 to 2,410 nm (Pixel number 219 to 256) is between 200 to 1000 DN after dark signal correction at detector temperatures considered for radiometric calibration.

The radiometric calibration analysis suggest that the high absolute sensitivity at wavelength 2215 nm could be due to three main reasons: (1) low efficiency of the instrument after pixel number 200 due to low total transmission through the instrument (Please refer Figure 2.12 in Vilenius (2009)); (2) less than 40% transmission of the incident radiation through the thermal vacuum chamber window around 2,000 nm, which increases the repeatability error of radiometric calibration (Figure 2.10(b)), and (3) change in the integrating sphere response which was measured in 2001 and could not be verified before starting the radiometric calibration of the SIR-2 instrument. This feature of the absolute sensitivity curve is no longer present after after in-flight calibration (Figure 2.13(a)).

To examine the linearity with respect to the light intensity, we changed the lamp position of the integrating sphere from 12 mm to 40 mm (total 5 lamp positions). The linearity with respect to exposure time was measured by changing the exposure time from 0.5 ms to 300 ms (total 12 exposure time intervals). Figure 2.11 shows the result of linearity tested at the detector temperature  $-50\text{ }^{\circ}\text{C}$  for every  $50^{\text{th}}$  pixel of the SIR-2 detector array. Figure 2.11(a) shows that the incident irradiance is considerably low for pixel number greater than 200. We observed a slight deviation from a straight line for lamp position between 12 to 25 mm. We can assume a piecewise linear relationship between the measured intensity and the lamp positions for the SIR-2 detector. The linearity check at detector temperature of  $-45\text{ }^{\circ}\text{C}$  and  $-65\text{ }^{\circ}\text{C}$  gives the similar results as shown in Figure 2.11(a). The linearity with respect to the exposure time was measured by changing the exposure time at constant intensity of sphere (lamp position at 12 mm). Figure 2.11(b) shows the relationship between the exposure time and measured intensity. We found that except defective pixels, all other pixels show a linear relationship with respect to the exposure time intervals and the intensity increases linearly with increasing exposure time. This re-



relationship is temperature independent because the measurements on detector temperature  $-45\text{ }^{\circ}\text{C}$  and  $-65\text{ }^{\circ}\text{C}$  gives the same results as shown in Figure 2.11(b) at  $-50\text{ }^{\circ}\text{C}$ .

## 2.3 Data reduction steps

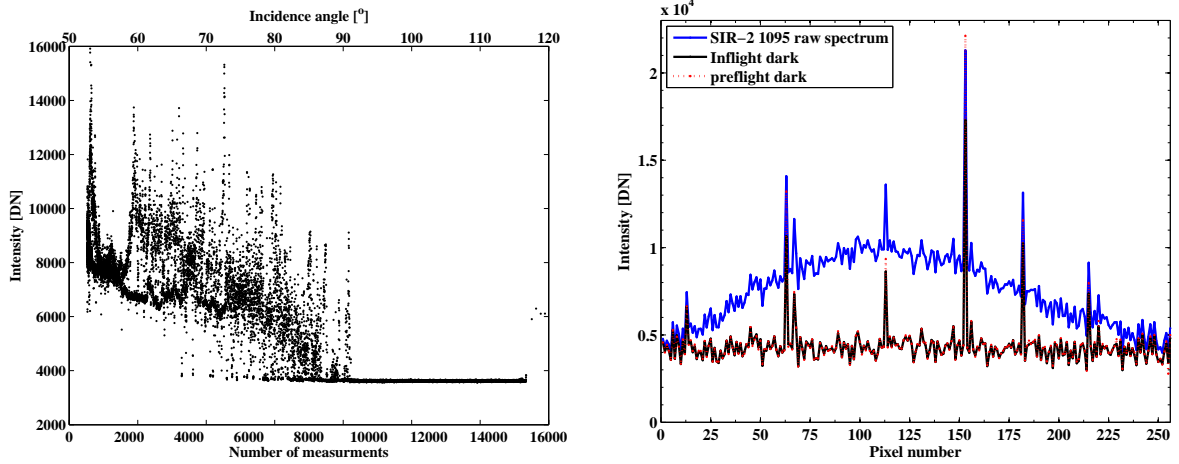
The remotely measured SIR-2 raw data are converted to the reflectance spectra by following the data reduction steps listed below:

- Removal of Dark and Bias.
- Obtain the radiance spectra ( $\text{W m}^{-2} \text{sr}^{-1} \mu\text{m}^{-1}$ ) from the dark corrected raw spectra by dividing them by the absolute sensitivity of the SIR-2 instrument.
- Division of radiance spectra by the solar irradiance at one Astronomical Unit (AU) and by cosine of incidence angle.
- Conversion of the reflectance spectra into standard viewing geometry by dividing them by a photometric function proposed by Shkuratov et al. (1999b).
- The defective pixel's response is replaced using the spline interpolation.

The bias level and dark count correction for preflight measurements are discussed in section 2.2.2. We used in-flight dark signal acquired in association with each SIR-2 orbit for dark correction in the case of in-flight SIR-2 measurements. We estimated the dark signal from the data obtained at the night side of the Moon. We determine the night side data when incidence angle  $i$  is  $> 90^{\circ}$ . The DN values at  $i$  is  $> 90^{\circ}$  remains nearly constant and rises abruptly for  $i$  is  $< 90^{\circ}$ . Figure 2.12(b) shows raw data measured by the SIR-2 and the dark signal extracted from the same orbit and the dark signal computed using preflight calibration. The overall dark signal shape is the same for the dark measured in-flight, and computed using preflight calibration however, we observed greater intensity (DN) for dark signal computed using preflight calibration at defective pixels.

To convert the dark corrected spectra into physical units; the spectra are first divided by the exposure time and then the absolute sensitivity of each pixel is corrected. The absolute sensitivity is derived from the radiometric calibration of the instrument during preflight measurements and is discussed in Section 2.2.4. However, the absolute sensitivity of the instrument may change after satellite launch and may require in-flight cross-calibration. We have used cross-calibrated absolute sensitivity of the SIR-2 instrument in the data reduction pipeline. We will discuss the in-flight calibration method in Section 2.4. The dark corrected spectrum is expressed in the units of radiance ( $\text{W m}^{-2} \text{sr}^{-1} \mu\text{m}^{-1}$ ) after correcting absolute sensitivity of pixels. The radiance spectra are converted into reflectance spectra by dividing them by the cosine of the incidence angle and by the solar irradiance spectrum. The solar irradiance spectrum used for converting radiance into reflectance is the newkUR spectrum of MODTRAN4 (Berk et al. 1999). The same solar irradiance spectrum was used to convert the  $M^3$  and HySI radiance profiles into reflectance profiles.

The measured radiance depends on the observation geometry, i.e., the solar incident angle  $i$ , the emission angle  $e$ , and the phase angle  $\alpha$  (Hapke 1993). The reflectance spectra



- (a) Intensity is plotted with respect to the incidence angle for pixel number 200. The average DN is  $\sim 3650$  for  $i$  is  $> 90^\circ$  and remains almost constant. The SIR-2 data correspond to  $i$  is  $> 90^\circ$  is considered as in-flight dark signal.
- (b) A comparison of in-flight dark and preflight dark along with the mean DN at every pixel of the SIR-2. The shape of dark signal computed from preflight measurements and dark signal from in-flight is similar.

Figure 2.12: The SIR-2 orbit 1095 raw data plotted for channel number 200 ( $\lambda = 2.1 \mu\text{m}$ ). The average dark signal is compared from preflight and in-flight measurements and plotted along with the average raw SIR-2 spectrum.

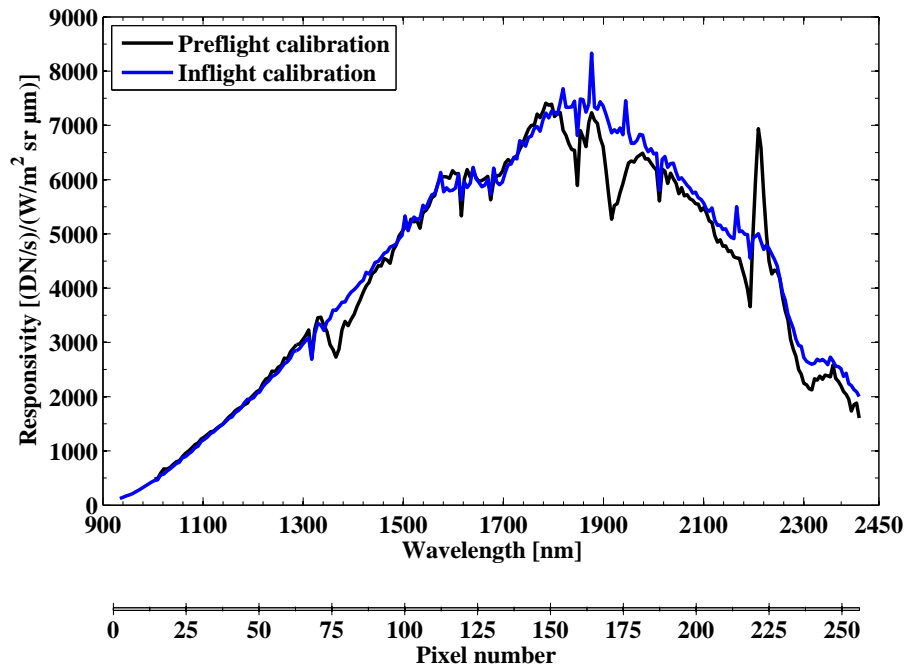
measured by the SIR-2 are converted in the standard geometry ( $i=30^\circ$ ,  $e=0^\circ$ , and  $\alpha=30^\circ$ ) by using the Semiempirical Shkuratov function (Shkuratov et al. 1999b) given by Equation 2.6.

$$f(\alpha, b, l) = H(\alpha)D(\alpha, b, l) \quad (2.6)$$

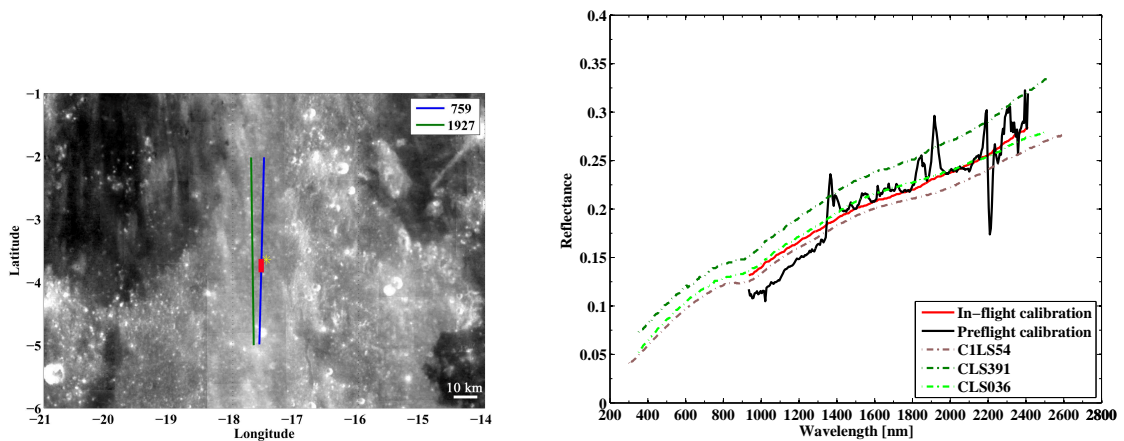
where,  $H$  is the phase function which depends on shadow-hiding and coherent backscattering,  $D$  describes the brightness distribution over the lunar disk and depends only on the observation geometry,  $\alpha$  is the phase angle,  $b$  and  $l$  are the photometric latitude and longitude, and, derived from phase, emergence and incidence angles. The phase function used for SIR and SIR-2 instruments is described in detail by Vilenius (2009).

## 2.4 In-flight calibration

Despite careful laboratory calibrations, space-born remote sensing instrumentation usually requires an in-flight cross-calibration of their data set. Validation of the on-orbit spectral and radiometric calibration is essential for science use of the SIR-2 measurements. We selected Apollo landing sites with known mineralogy as locations of the “ground-truth” to verify radiometric calibration of the SIR-2. The cross-calibration based on the Apollo samples may introduce errors in calculating coefficients necessary to convert the remotely measured reflectance comparable to the laboratory measured reflectance values if the location of the remotely measured spectra are several kilometres from the landing sites. We don’t have SIR-2 tracks passing exactly from the landing sites therefore, we assumed that



(a) Preflight and in-flight absolute sensitivity comparison.



(b) Apollo 14 landing site (Clementine image) and (c) SIR-2 and RELAB spectra comparison from SIR-2 orbits passing near by it.

Figure 2.13: Preflight and in-flight calibration comparison.

the compositional differences are negligible for the areas considered for on-orbit radiometric calibration.

The spectral calibration was assumed to be the same after launch due to the strong fixation between the entrance slit, the grating and the detector. We did not observe any discrepancies in the SIR-2 spectra when compared to the locations of broad spectral features such as the absorptions of pyroxene and olivine.

We compared the reflectance spectra measured by the SIR-2 near by the Apollo landing sites and the reflectance spectra of the lunar returned samples downloaded from RELAB to validate the radiometric calibration. We observed abrupt increase in reflectance

values at fixed wavelength positions while utilizing preflight absolute sensitivity calibration for converting the SIR-2 radiance in reflectance. The wavelength positions of the peaks present in the SIR-2 reflectance spectra were fixed for the SIR-2 orbits passing near by the Apollo landing sites. The presence and fixed location of these peaks in the SIR-2 reflectance spectra might be due to the change in the preflight radiometric calibration of the instrument.

The Apollo 14 ( $3.7^{\circ}S$ ,  $17.5^{\circ}W$ ) landing site was selected as a post-launch or in-flight calibration site. We selected the SIR-2 orbit 759 for finding any deviation if present in absolute sensitivity of individual pixels of the SIR-2 detector. The sampling points are selected very carefully from the SIR-2 orbit 759 which represents very similar geology as the Apollo 14 landing site (Figure 2.13(b)). The SIR-2 geometric coordinates have been compared and corrected according to the Clementine mission's (Nozette et al. 1994) geographic coordinate system. Clementine images are downloaded from the PDS imaging node <sup>1</sup>. The dark and photometric corrected SIR-2 spectra are divided by the reflectance factor of the Apollo 14 sample number 14156 to obtain the absolute sensitivity correction factor. A comparison between the preflight and in-flight calibration is shown in Figure 2.13(a). The shape of the absolute sensitivity generated using in-flight calibration is approximately similar to the absolute sensitivity curve generated using preflight calibration. The peak present at the wavelength 2214 nm in the preflight calibration is absent when corrections are applied based on in-flight calibration. We computed the correction factor for each Apollo landing site, however found the best match to the preflight calibration for the Apollo 14 landing site. We applied the correction to the preflight calibration based on in-flight calibration and have used it to retrieve reflectance spectra from SIR-2 raw spectra measured remotely. The reflectance spectra of the Apollo 14 returned samples analysed in laboratory are plotted along with the SIR-2 reflectance spectrum from approximately the same location in Figure 2.13(c). The peaks present in the SIR-2 reflectance spectrum considering absolute sensitivity from preflight calibration are minimized when the in-flight calibration is applied to the same spectrum.

## 2.5 Application of in-flight calibration to Apollo 12 and 15 landing sites

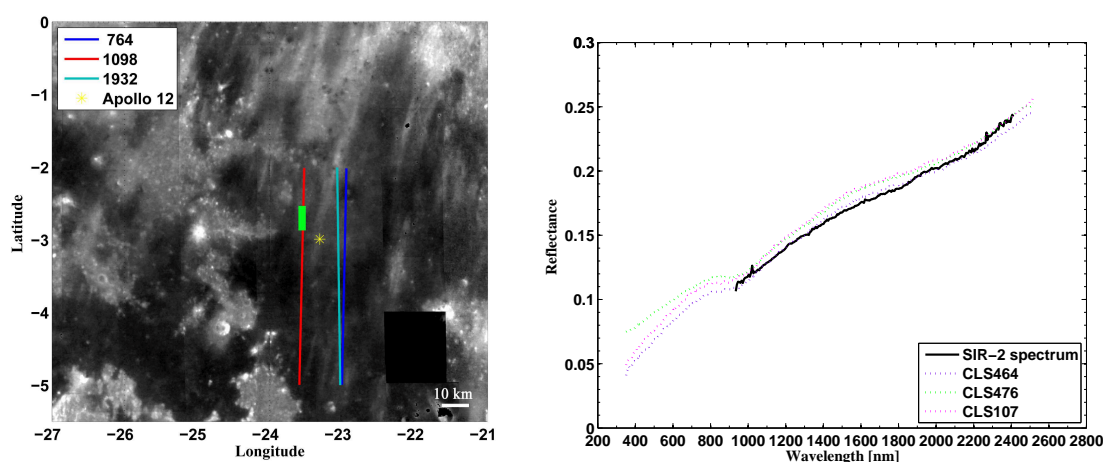
Figure 2.14 shows the SIR-2 tracks crossed nearby Apollo 12 and 15 landing sites and a comparison of the spectral shape between remotely measured reflectance spectra by SIR-2 and the laboratory measured reflectance spectra downloaded from RELAB. The spectral shape comparisons from Figures 2.14(b) and 2.14(d) illustrate a good match in the overall spectral shape and reflectance values.

Apollo 12 landing site ( $3.2^{\circ}N$ ,  $23.4^{\circ}W$ ) is in southeastern Oceanus Procellarum and sampled younger mare basalts than the Apollo 11 basalt. This landing site is less cratered (younger) and dominated by the ejecta of several craters as shown in Figure 2.14(a). Samples 12070 (LS-JBA-060-P2/CLS107) and 12042 (LS-JBA-036-P2/CLS476, LS-JBA-036-P4/CLS464) are selected as the best representative samples for bulk soil around the Apollo 12 landing site and plotted along with the remotely measured SIR-2 reflectance

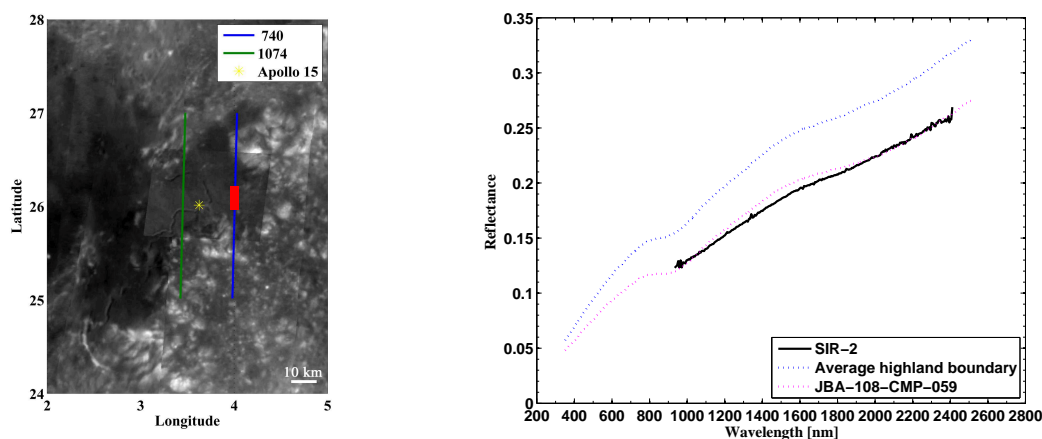
---

<sup>1</sup><http://www.mapaplanet.org/>

## 2.5 Application of in-flight calibration to Apollo 12 and 15 landing sites



(a) Apollo 12 landing site (Yellow star) located on the Clementine image and The SIR-2 orbits passing near by it. (b) SIR-2 and RELAB spectra comparison for the Apollo 12 landing site.



(c) Apollo 15 landing site (Clementine image) and The SIR-2 orbits passing near by it. (d) SIR-2 and RELAB spectra comparison for the Apollo 15 landing site.

Figure 2.14: Apollo 12 and 15 landing sites and comparison of RELAB and the SIR-2 reflectance spectra after apply in-flight calibration.

spectrum extracted from a similar geology as the Apollo 12 landing site in Figure 2.14(b). Sample 12070 is categorized as submature and sample 12042 is mature based on the maturity parameter ( $I_s/FeO$ ) values of 47 and 61 respectively (Morris 1978). The petrography studies (Morris et al. 1983) and absorption band parameters studies suggest that pyroxene and olivine are the main minerals present in these soil samples. Remotely measured SIR-2 spectra from the nearby area of the landing site confirm the presence of pyroxene based on the band parameters extracted for the 2- $\mu$ m absorption band region.

Apollo 15 landing site ( $26.1^\circ N$ ,  $3.7^\circ E$ ) is in the Hadley-Apennine region and sampled both mare and nonmare rocks of the Imbrium rim and of Hadley Rille. Figure 2.14(d) shows the Apollo 15 landing site and the SIR-2 tracks passing nearby it. We selected an average reflectance spectrum representing highland boundary from sample numbers

15091, 15211, 15101 and 15231. We selected sample numbers 15261 and 15081 to represent an average mare soil reflectance spectrum. Figure 2.14(d) shows comparative spectra chosen from the laboratory measurements of the returned samples and the SIR-2 reflectance spectrum from orbit 740 extracted from a similar geology as the Apollo 15 landing site. All the returned samples considered are categorized as mature with the maturity parameter ranging between 68 and 77 (Morris 1978). These samples consist mainly plagioclase, pyroxene, olivine and ilmenite. A comparison between the laboratory measured spectra and remotely measured SIR-2 spectra show similar absolute reflectance levels, however the 2- $\mu\text{m}$  absorption band is not easily recognized for the SIR-2 spectrum probably due to high maturity of this region.

The analysis and results of the SIR-2 data-sets from the Apollo landing sites provide an on-orbit assessment of the instrument's performance and demonstrates that the preflight calibration is important but not sufficient, and a in-flight cross-calibration is required for validation of the remotely measured data.

## 2.6 Spectral parameters definition

The two spectral parameters; band depth and continuum slope are mainly used to interpret results from the SIR-2, HySI, and M<sup>3</sup> spectrometers.

The strength of absorption bands is one of the diagnostic parameters of those VIS-NIR reflectance spectra related to a mineral's crystal structure and Fe abundance. The strength of absorption bands can be measured as the band depth at the band center. The band depth parameter is not only dependent on the chemical composition of a reflectance spectrum but it is also affected by the presence of strongly absorbing opaque minerals (such as ilmenite), the effects of space weathering, and observational conditions (Hapke 2001, Noble et al. 2007, Pieters et al. 2000). The band depth is evaluated using equation 2.7 (Clark and Roush 1984):

$$\text{Band depth} = 1 - \frac{R_b}{R_c} \quad (2.7)$$

where  $R_b$  is the reflectance value of a normalized spectrum at band center and  $R_c$  is the reflectance value of the continuum line at the band center.

The continuum to a near-infrared spectrum is defined as a convex hull to the reflectance spectrum, i.e. the continuum slope or spectral slope represents the slope of a straight line passing through the local maxima adjacent to the band center positions.

The selection of the continuum points is carried out in an automated way by connecting the spectrum's local maxima by segments of straight line to the normalized reflectance spectra (Clark 1988). This method ensures that all reflectance values are located below the continuum line. The automatic selection of the continuum points is sensitive to the noise present in the reflectance spectra, therefore we have used a Savitsky-Golay filter as proposed by Lillesand et al. (2008) as a preprocessing step in our band parameters extraction routine. The advantage of the Savitsky-Golay filter over a polynomial fit lies in its property of retaining the shape of the signal.

### **3 Comparing the SIR-2 response with HySI and M<sup>3</sup>**

The Chandrayaan-1 spacecraft carried HySI, SIR-2, and M<sup>3</sup> spectrometers operating in the UV-VIS-NIR wavelength region (0.4-3  $\mu\text{m}$ ). The primary objective of these three instruments was to carry out a high spectral and spatial resolution mineralogical survey of the lunar surface. All of the three instruments are capable of producing high quality reflectance spectra of the lunar surface and combining the three data sets provides maximum scientific return. The HySI instrument has a spectral range of 0.42-0.96  $\mu\text{m}$  and hence incapable of fully characterizing the 0.90  $\mu\text{m}$  pyroxene absorption band. The SIR-2 instrument has a spectral range of 0.94-2.4  $\mu\text{m}$  and can characterize the 2- $\mu\text{m}$  absorption band. Due to incomplete wavelength coverage the SIR-2 can not characterize the 0.90  $\mu\text{m}$  band. The overlapping wavelength range of the two instruments is approximately 0.30  $\mu\text{m}$  (HySI bands 60-64 and SIR-2 bands 1-4) between 0.93 and 0.95  $\mu\text{m}$  for the SIR-2 and the HySI instruments. At this wavelength range, the instrument's response is more sensitive to the noise due to drop in quantum efficiency of the detector. Therefore, we have used the M<sup>3</sup> data as a reference to compare the normalized combined reflectance spectra of the SIR-2 and HySI. However, M<sup>3</sup> could not always operate in its optimal temperature range (Green et al. 2011). A process of inter-calibration between these instruments is helpful to unlock their full diagnostic potential.

In this chapter, we compared the SIR-2 and HySI data from the Apollo 15 landing site in Section 3.2 and found that the two data sets required geographic coordinate adjustments. We selected the Mare Moscoviense region from the lunar far side in an attempt to combine the reflectance spectra from SIR-2, HySI, and M<sup>3</sup> because three HySI orbits and corresponding SIR-2 and M<sup>3</sup> orbits are available from this region (Section 3.3). Mare Moscoviense area has been mapped individually both by HySI (Bhattacharya et al. 2011), and M<sup>3</sup> (Thaisen et al. 2011, Pieters et al. 2011), allowing a comparison between the combined analysis and published research.

#### **3.1 Radiance to reflectance conversion of HySI and M<sup>3</sup> datasets**

The key features of HySI and M<sup>3</sup> instruments are listed in Table 1.2. We received HySI data as level 1b product that is radiometrically calibrated, dark corrected and band-to-band registered. HySI radiance data were then converted to reflectance using Relative Spectral Response (RSR) data of 64 HySI filters and convolving the solar irradiance values to

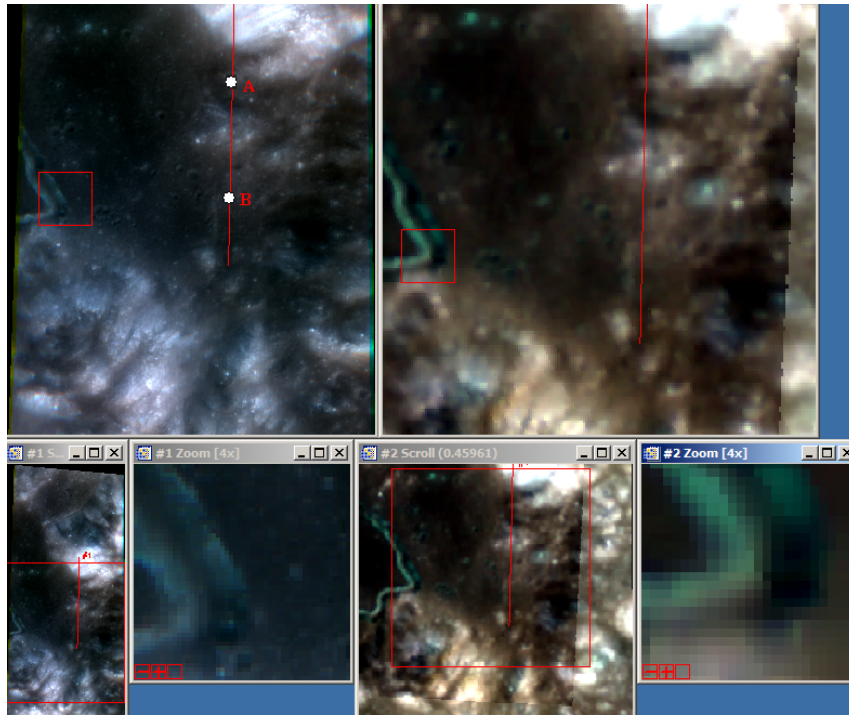


Figure 3.1: SIR-2 orbit number 740 plotted on HySI (left) and Clementine images (right). The two small windows just below the HySI and Clementine image show the full image considered for this analysis, and the zoomed area inside the small red box.

HySI RSR within the spectral range of 0.42-0.96  $\mu\text{m}$ . HySI images provided to us are not cross-calibrated based on in-flight calibration. Therefore, site specific correction has to be applied to these images in order to compare and combine their response with the SIR-2 data. We downloaded M<sup>3</sup> product IDs recorded at the same Coordinated Universal Time (UTC) as the SIR-2 from the NASA archive and obtained the “apparent reflectance” by dividing dark corrected radiance values by the standard solar irradiance and the cosine of the incidence angle. Equation 3.1 (Green et al. 2011) is used for both the HySI and M<sup>3</sup> radiance profiles to convert them to reflectance/apparent reflectance spectra.

$$\rho(\lambda) = \frac{L(\lambda)}{\cos(i) \times \frac{F_o(\lambda)}{\pi}} \times \left(\frac{1}{d_{AU}}\right)^2 \quad (3.1)$$

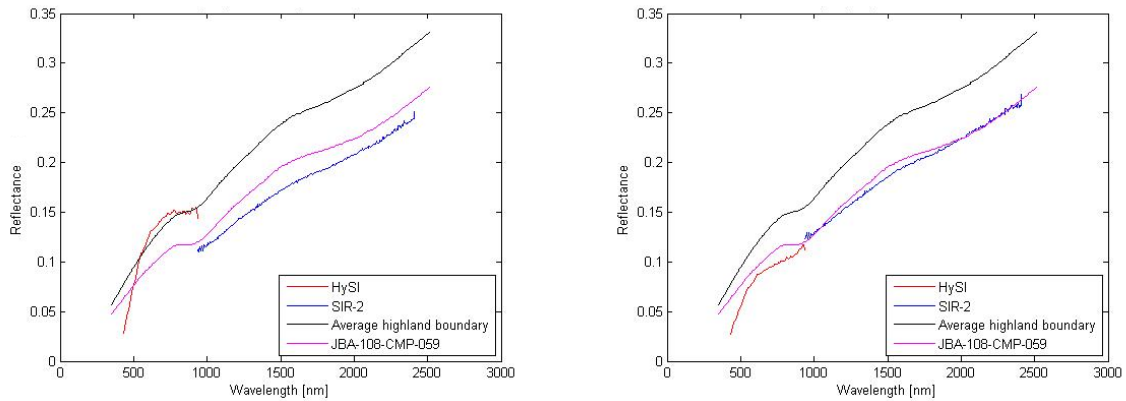
where,  $\rho(\lambda)$  is the reflectance or apparent reflectance in the case of M<sup>3</sup> data,  $\lambda$  is the wavelength,  $L$  is the calibrated radiance measured by HySI and M<sup>3</sup>,  $i$  is the solar zenith incidence angle,  $F_o$  is the solar irradiance at one AU, and  $d_{AU}$  is the distance from the surface to the sun in AU.

## 3.2 HySI and SIR-2 combined response at the Apollo 15 landing site

The SIR-2 orbit numbers 1074 and 740 sampled a nearby area of the Apollo 15 landing site (Figure 2.14(c)). The HySI orbit number 737 covered an area near the Apollo 15



### 3.2 HySI and SIR-2 combined response at the Apollo 15 landing site



(a) SIR-2 and HySI average reflectance spectra from a location marked as 'A' in Figure 3.1. In this case we took an average of three SIR-2 footprints and corresponding 20 HySI pixels response.

(b) SIR-2 and HySI spectra extracted from a location marked as 'B' in Figure 3.1. The real footprint shape of the SIR-2 is not considered in this case and the HySI pixel is selected based on the minimum difference between the geographic coordinates.

Figure 3.2: SIR-2 and HySI spectra extracted from the locations marked in Figure 3.1. HySI reflectance spectra deviate from the RELAB spectra for the wavelengths smaller than 530 nm.

landing site including small part of Rima Hadley Rille (Figure 3.1, left panel). A comparison between the HySI and Clementine images along with a subsection of the SIR-2 orbit number 740 plotted over these images is also shown in Figure 3.1. The SIR-2 track is plotted on the HySI and Clementine images based on its given longitude and latitude information (red line in Figure 3.1). The HySI and the Clementine images are geographically matched, this implies that the area within the “red square” shows the same projection area at the same longitude and latitude for both the images. The HySI images have a spatial resolution of 80 m/pixel and the Clementine images shown in Figure 3.1 has a spatial resolution of 200 m/pixel. A  $\pm 0.2^\circ$  shift was observed in given geographic coordinates between the HySI and Clementine images of the same regions.

We selected the SIR-2 footprints that sampled a mare and highland boundary from the Apollo 15 region and extracted the reflectance spectra based on given geographic coordinates from the HySI image. Figure 3.2 shows the combined response of the SIR-2 and HySI from the mare region and plotted along with the reflectance spectra of mature mare and highland soils as obtained from the Apollo 15 return samples (RELAB). The HySI reflectance spectrum is extracted from the location 'A' in Figure 3.1 and plotted in Figure 3.2(a). The SIR-2 spectrum is an average spectrum of the three consecutive SIR-2 footprints from the region 'A' in Figure 3.1 and the HySI spectrum is an average of 20 pixels that corresponds to the three SIR-2 footprints. Figure 3.2(b) shows the SIR-2 spectrum from the location 'B' in Figure 3.1 and corresponding HySI spectrum extracted from the pixel location based on the least difference in the geographic coordinates. We observed a sharp decrease in reflectance values for wavelengths smaller than 530 nm for HySI spectra. Although the absolute reflectance of the SIR-2 data is comparable to that of RELAB spectra, the HySI wavelength range shows a mismatch. We concluded from this

analysis that a comparison between the two datasets might be possible only after applying a site specific calibration to the HySI images. We need to compare the radiance profiles of the SIR-2 and HySI at an approximately common wavelength channel to locate the SIR-2 track on a HySI image in order to find the exact location of the SIR-2 track on the HySI image prior to the combined reflectance spectra analysis.

## 3.3 Comparing SIR-2, HySI, and M<sup>3</sup> responses: Mare Moscoviense

### 3.3.1 Regional setting

The Moscoviense basin (Figure 3.3, 27°N, 146°E) is located in the lunar farside Feldspathic Highland Terrane (FHT) within a 100 km thick anorthositic crust (Zuber et al. 1994) and has been reported as having the thinnest crust on the Moon among the measured basins (Ishihara et al. 2009). Mare Moscoviense covers an area of 35,000 km<sup>2</sup> (Gillis 1998) within a 445 km diameter well-developed, but asymmetric, ring system (Wilhelms et al. 1987). This basin is assumed to be the result of a major impact during the Nectarian Period (3.85-3.92 Ga) (Wilhelms et al. 1987) resulting in multiple ring basin. The basin experienced subsequent mare volcanism during the upper Imbrian epoch (3.2-3.8 Ga) (Gillis-Davis et al. 2006, Kramer et al. 2008), with the final basalt flows between 2.5-2.6 Ga (Haruyama et al. 2009, Morota et al. 2009). The unique geologic setting of the Moscoviense basin may provide information of the lunar mantle by a systematic study of the different basaltic mare units composition that are exposed across the basin and may help us in understanding the compositional heterogeneity of the basaltic source regions allowing to establish a compositional stratigraphy of the different mare units within the basin.

Recent observations by the M<sup>3</sup> instrument have identified several regions within the peak ring of the Moscoviense basin with olivine and magnesium-rich spinel (MgAl<sub>2</sub>O<sub>4</sub>) suggesting an exposure of crustal products from the cooling magma ocean (Pieters et al. 2011). A total of four distinct mare basalt compositions have been identified across the basin by analysing Clementine UVVIS data on the basis of variation in TiO<sub>2</sub> and FeO contents (Gillis-Davis et al. 2006, Kramer et al. 2008, Gillis 1998): (1) the oldest basaltic unit in the southern part with low Fe, low Ti mare (Im), (2) a northwestern basaltic unit with low Ti mare (Iltm), (3) an Imbrian low-Ti basaltic unit in the crater Komarov (Ikm), (4) an eastern unit with high Ti mare (Ihtm). Unit Im was dated at 3.9 Ga, unit Iltm was dated at 3.5 Ga, unit Ikm was dated as 3.3-3.5 Ga, and unit Ihtm was dated at 2.6 Ga and thus placed within the Eratosthenian system and refereed as Ehtm instead (Morota et al. 2009).

### 3.3.2 Data sets

We considered three SIR-2 tracks (orbit numbers 606, 610 and 614) recorded on 29 December 2008, M<sup>3</sup>, and HySI data sets recorded at the same Coordinated Universal Time (UTC) as the SIR-2 (Table 3.1). The location of the SIR-2 tracks and corresponding M<sup>3</sup> images are shown in Figure 3.3. The phase angle range is between 20° and 37° with an

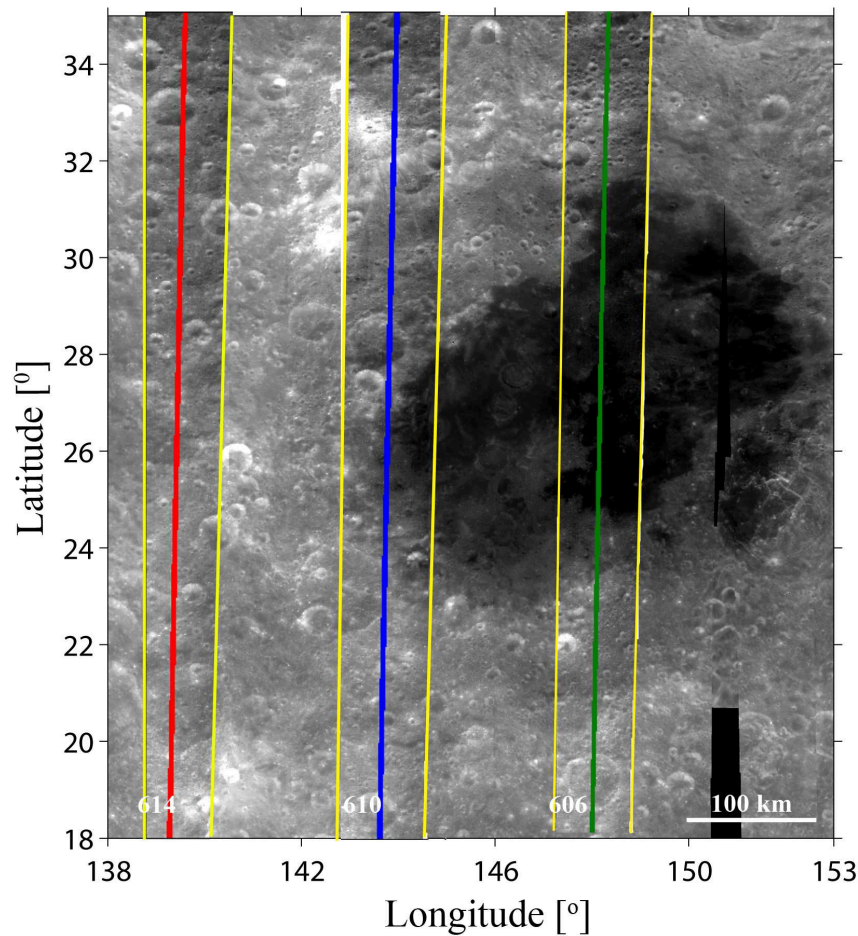


Figure 3.3: SIR-2 orbits 606, 610 and 614 and corresponding M<sup>3</sup> orbits (bounded by yellow box) superposed over Clementine image. The SIR-2 orbit's position is adjusted as explained in Section 3.3.3.

average phase angle of 30° for the data considered in this analysis. The SIR-2 tracks 606, 610 and corresponding M<sup>3</sup> and HySI products sampled a part of filled mare and the SIR-2 orbit 614 sampled the highly feldspathic highland material with very little amount of mafic minerals.

The HySI dataset includes a separate geometry, label, and satellite position file along with the radiance file in cube format. The latitude and longitude information for each HySI orbit is stored in the grid file at every 32<sup>nd</sup> line number and pixel number. This information is linearly interpolated to get the latitude and longitude of each HySI line and pixel number. The SIR-2 dataset includes a FITS file and a label file with the information for each column of the FITS file. The SIR-2 latitude, longitude, and UTC informations are provided by a SPICE kernel and stored within the FITS formatted data file for each sampling point. The M<sup>3</sup> radiance data has the longitude and latitude information of each pixel and line number in a separate 'LOC' file and UTC information in a separate 'TIM' file. The M<sup>3</sup> products are downloaded from the NASA archive <sup>1</sup> and listed in Table 3.1.

<sup>1</sup><http://m3.jpl.nasa.gov/m3data.html>

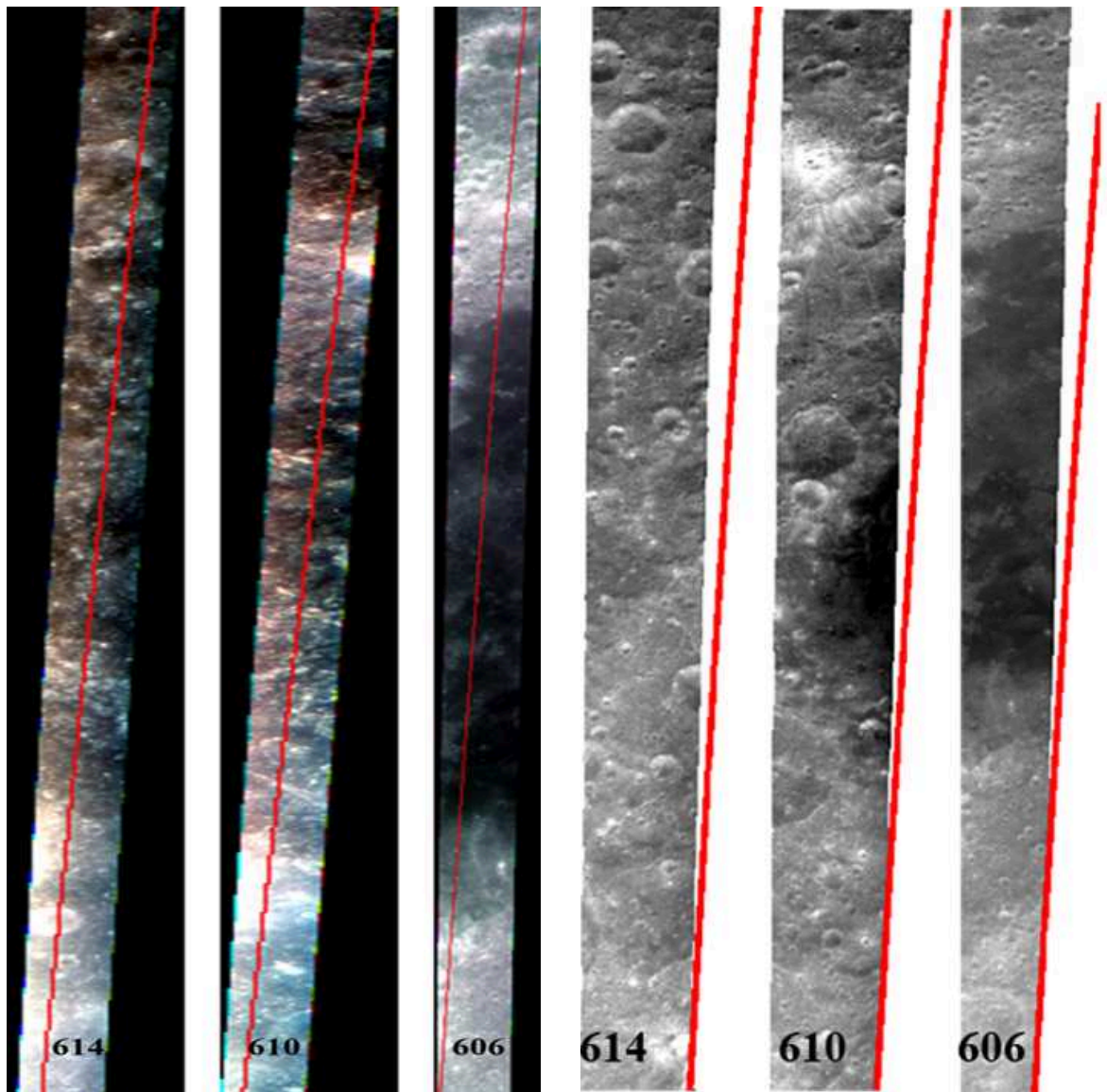
Table 3.1: SIR-2, HySI, and M<sup>3</sup> product IDs considered to analyse Mare Moscoviense region. The geographic shift calculated based on Radiance profile comparison is also given. The procedure of the radiance profile comparison is explained in Section 3.3.3.

SIR-2 Product ID	HySI Product ID	M <sup>3</sup> Product ID	UTC shift		Correlation (between M <sup>3</sup> and SIR-2) after shift (%)
			M <sup>3</sup> Pixel	M <sup>3</sup> Line	
CH1SIR2_NE2_SC_R00606	HySI orbit 607	M3G20081229T022350_V03_RDN	148	7	94
CH1SIR2_NE2_SC_R00610	HySI orbit 611	M3G20081229T101650_V03_RDN	148	3	96
CH1SIR2_NE2_SC_R00614	HySI orbit 613	M3G20081229T180950_V03_RDN	148	3	95

### 3.3.3 Alignment of SIR-2 tracks over HySI and M<sup>3</sup>

The location of the SIR-2 data on corresponding HySI and M<sup>3</sup> data is critical for integrating the three data sets. The three VIS-NIR spectrometers on-board the Chandrayaan-1 spacecraft were aligned in such a way that the SIR-2 tracks should fall in the middle of the HySI (pixel number 128) and M<sup>3</sup> (pixel number 154) images. However, we observed a clear deviation from the central position for the three SIR-2 orbits considered in this study when plotted based on their given latitude and longitude coordinates as shown in Figure 3.4. The discrepancy observed in geographic coordinates could be due to the use of different processing tools for the three instruments. In the case of SIR-2 and corresponding M<sup>3</sup> products, we observed a mismatch of an order of  $\pm 0.2^\circ$  in geographic coordinates for a total of 37 orbits considered between  $55^\circ N - 55^\circ S$ ,  $3^\circ E - 50^\circ W$  from west part of the nearside. However, the SIR-2 tracks only fall partially within the M<sup>3</sup> products for the orbits selected from the Mare Moscoviense region (Figure 3.4(b)). Our observation suggests that the inaccuracy in absolute coordinates is greater for the farside compared to the nearside. Study of other regions of farside may help to understand if any systematic geographic coordinates deviation is present between the SIR-2 and M<sup>3</sup> datasets. This work can be carried out once the fully calibrated M<sup>3</sup> products are available. A similar analysis could not be done for HySI products because only a limited dataset was available.

Figure 3.4 shows the need for an independent constraint on SIR-2 tracks to find the correct location on the HySI and M<sup>3</sup> image. Therefore, we considered the alignment of SIR-2 and HySI based on their UTC information. The start and end UTC information of every HySI image is provided in the label file. We linearly interpolated the HySI UTC values between the start and end times of the observation to get UTC for each line of the HySI image. The SIR-2 start and end UTC differ from HySI; thus the image line numbers which fall within the SIR-2 start and end UTC time are considered for the analysis. The HySI radiance profile was extracted in pixel direction by extracting the radiance values from HySI line numbers based on the UTC information. The nearest UTC value to the SIR-2 measurements was taken from HySI image. We did not consider the exact shape of SIR-2 footprints on the HySI images for this analysis. HySI channel number 62 corresponding to 939.4 nm and the SIR-2 channel number 2 corresponding to 940 nm were considered for radiance comparison. The HySI image was divided into 9 subsections. The extracted HySI radiance is scaled by subtracting it from its mean value and dividing by its standard deviation. The SIR-2 radiance is also scaled in the same way as the HySI radiance profile and a cross-correlation is computed for each subsection of



(a) SIR-2 orbits plotted on subsets of HySI products from Table 3.1. Only a part of HySI image shown where the SIR-2 tracks are within the image. (b) SIR-2 orbits plotted on M<sup>3</sup> products from Table 3.1. The latitude range is between 18° – 35°N. The M<sup>3</sup> sub-images are superimposed over the Clementine image in Figure 3.3.

Figure 3.4: SIR-2 orbits plotted on HySI and M<sup>3</sup> products based on the given latitude longitude informations. The SIR-2 track alignment is necessary prior to a combined analysis approach in order to extract spectral information from the approximately same geographic coordinates. The HySI and M<sup>3</sup> orbits corresponding to the SIR-2 orbit 614 and 610 do not show the same area because we considered only a subsection of HySI image that shows the SIR-2 track position within the image.

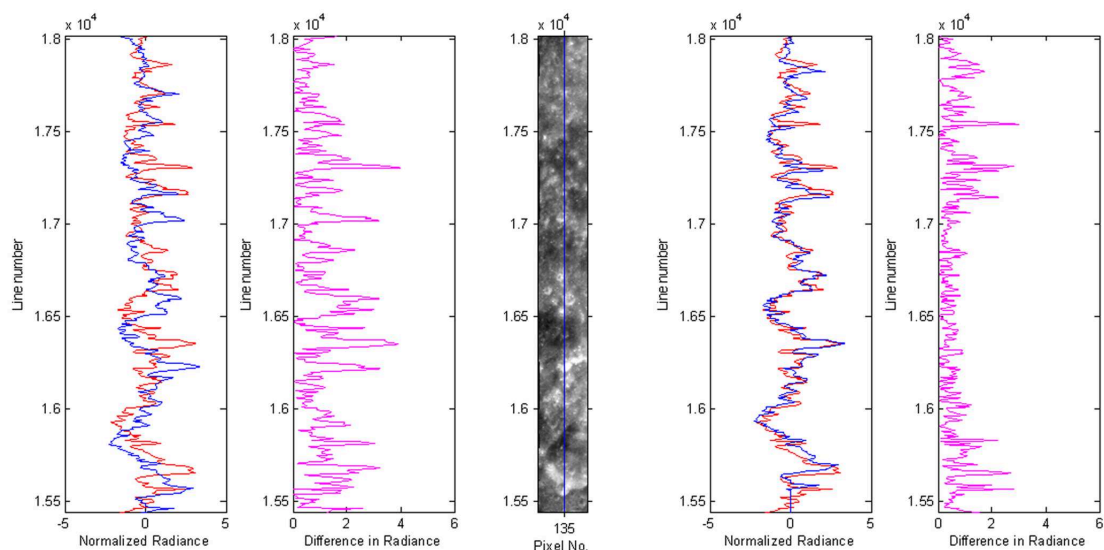


Figure 3.5: A subsection of HySI image corresponding to SIR-2 orbit 611 and scaled radiance profile comparison before (left side of image) and after (right side of image) applying 18 lines downward shift to get a cross-correlation greater than 70%. SIR-2 and HySI radiance profiles are plotted in red and blue respectively. The absolute difference between the two profiles are shown in magenta color.

the HySI image. The best pixel position for each subset is considered at the best cross-correlation obtained between the normalized radiance profiles for a UTC shift in upward or downward direction. Figure 3.5 shows a subsection of a HySI image and the SIR-2 track aligned at pixel number 135. We shifted the HySI radiance profile by 18 lines in downward direction to get a cross-correlation higher than 75% as shown in right panel of Figure 3.5. We observed that, if we fix the pixel position for all subsections of the HySI image, the UTC shift required to have the best correlation changes for each subsection. The UTC shift (line shift) calculated for each subsection of the HySI image corresponding to SIR-2 orbits 610 and 614 are listed in Table 3.2.

To study the misalignment problem and to find if the same problem exists between SIR-2 and HySI for other regions from the farside of the Moon, we requested a new calibrated HySI dataset from the Space Application Centre (SAC), India. We received the HySI orbit 1174 corresponding to the SIR-2 orbit 1173 which sampled a part of the crater Berkner (25.2°N, 105.2°W). Figure 3.6 shows the scaled radiance profile comparison and the original and optimized SIR-2 track positions over the HySI image. We observed in this case that the SIR-2 orbit’s geographic coordinates fall almost in the middle of the image at the pixel number 132. However, a comparison of the radiance profiles shows that a shift in longitude and latitude is required to match the two radiance profiles. We found the best match between the SIR-2 and HySI radiance profiles by shifting the SIR-2 track by 0.51°S and 0.12°W.

We concluded from this analysis that the geographic coordinates cannot be used directly in order to extract HySI radiance profiles from the SIR-2 footprints. We either require a calibrated HySI product or need to register HySI images to a known coordinate

Table 3.2: SIR-2 track alignment on corresponding HySI images. The line shift values are changing for subsets of the image.

SIR-2 orbit 610, HySI orbit 611			SIR-2 orbit 614, HySI orbit 613		
Image subset (line number)	line shift	Correlation (%)	Image subset (line number)	line shift	Correlation (%)
6-2578	32 upward	78	8-2585	37 upward	65
2579-5151	23 upward	67	2586-5164	28 upward	71
5152-7724	14 upward	72	5165-7742	20 upward	79
7725-10297	6 upward	77	7743-10320	12 upward	75
10298-12870	1 downward	92	10321-12899	3 upward	77
12871-15443	11 downward	89	12900-15477	5 downward	70
15444-18016	18 downward	70	15478-18055	13 downward	74
18017-20589	27 downward	73	18056-20634	20 downward	74
20590-23162	35 downward	58	20635-23212	30 downward	61

system like M<sup>3</sup> or Clementine. We used M<sup>3</sup> geographic coordinates as a reference because the viewing conditions for all the three instruments are similar and can be compared without applying any further corrections and the UTC information for each line is available in a similar way as the SIR-2 data, allowing us to locate the line number accurately on the M<sup>3</sup> image corresponding to SIR-2 footprints.

We applied the method of comparing the radiance profiles to the SIR-2 and M<sup>3</sup> data in a similar way as was applied to the SIR-2 and HySI data. M<sup>3</sup> channel number 49 corresponding to 1548.9 nm and the SIR-2 channel number 101 corresponding to 1545.2 nm were considered for radiance comparison. We found the best match at M<sup>3</sup> pixel number 148 for all the three orbits considered. The line shift required at the pixel number 148 for each SIR-2 orbits is given in Table 3.1 along with the cross-correlation between the M<sup>3</sup> and SIR-2 radiance profiles. The corrected SIR-2 track’s position with respect to the M<sup>3</sup> images is shown in Figure 3.3. The HySI images are georegistered to the M<sup>3</sup> coordinates by locating few common features in two subsets of the images and by wrapping the HySI image using method “polynomial” with degree 2 in ENVI software <sup>2</sup>. The radiance values from the M<sup>3</sup> and HySI images are extracted corresponding to the SIR-2 footprints and converted to “apparent reflectance” using Equation 3.1.

### 3.3.4 Spectral analysis of Mare Moscoviense region

Our analysis is focused mainly on the 2- $\mu$ m absorption band parameters; band depth, continuum slope (definitions are given in Section 2.6). We considered an additional spectral parameter Integrated Band Depth (IBD) for analysing M<sup>3</sup> images. The 2- $\mu$ m IBD is de-

<sup>2</sup><http://www.exelisvis.com/language/en-us/productservices/envi.aspx>

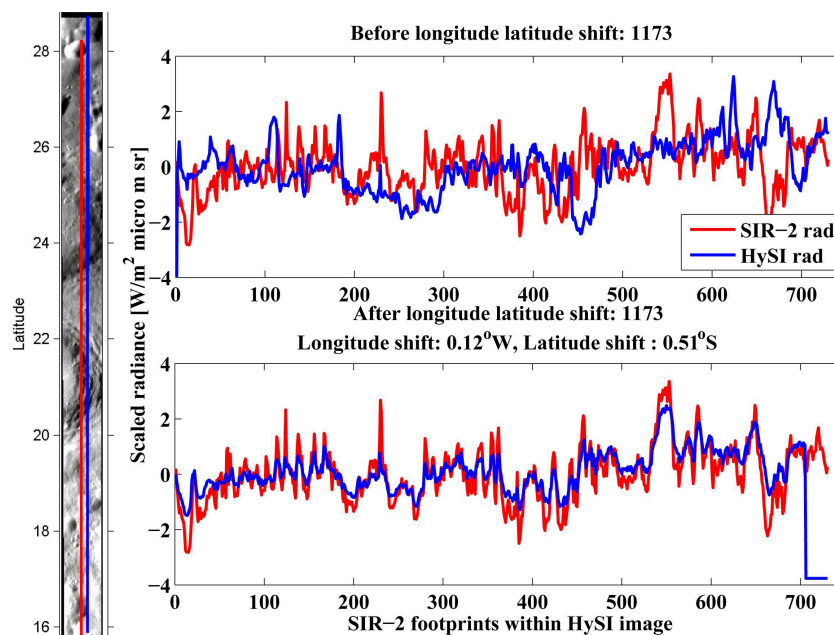


Figure 3.6: An example of optimization of geographic coordinates of SIR-2 based on scaled radiance profiles comparison for SIR-2 orbit 1173 and corresponding HySI orbit 1174. Left panel: A subset of the HySI orbit 1174 and SIR-2 orbit 1173 plotted over the image based on the coordinates provided by the mission (red line) and coordinates optimized based on the radiance profile comparison (blue). Total 732 SIR-2 footprints are within this subset of HySI image. Right panel: A shift in longitude and latitude direction is calculated by extracting the radiance profile from HySI pixels corresponding to the SIR-2 footprints and by finding the best correlation between the SIR-2 and HySI radiance profiles.

fined as the sum of band depths between 1.50 and 2.49  $\mu\text{m}$ . We considered IBD instead of the band depth mainly because IBD tends to be less sensitive to the noise and artifacts present in the spectra than a band depth parameter. Savitzky golay filter have been applied to the SIR-2 and M<sup>3</sup> data as a preprocessing step to avoid the spikes present in the reflectance spectra.

Figure 3.7 shows the 2- $\mu\text{m}$  IBD images of the M<sup>3</sup> orbits from Table 3.1. We assigned four colors; blue, green, red, and yellow to the M<sup>3</sup> 2- $\mu\text{m}$  IBD images in the order of weak (blue) to the strongest (yellow) IBD observed within the Mare Moscoviense region. The IBD range is between 0 and 3 as shown in Figure 3.10. The red and yellow areas in the Figure 3.7 indicate abundant mafic minerals in basalts with strong absorptions around 2- $\mu\text{m}$ , and areas with weak or no absorption band around 2- $\mu\text{m}$  is shown as blue indicating highly feldspathic nature of the basin.

The iron map of Mare Moscoviense and surroundings is derived using Lucey et al. (1998a) algorithm and shown in Figure 3.9.

The SIR-2 representative reflectance spectra (absolute and normalized) for the principal lithologies of the Moscoviense basin are shown in Figure 3.8 along with the corresponding M<sup>3</sup> and HySI spectra extracted from the SIR-2 footprints. The location of representative spectra is shown in Figure 3.7. M<sup>3</sup> spectra are not corrected thermally or



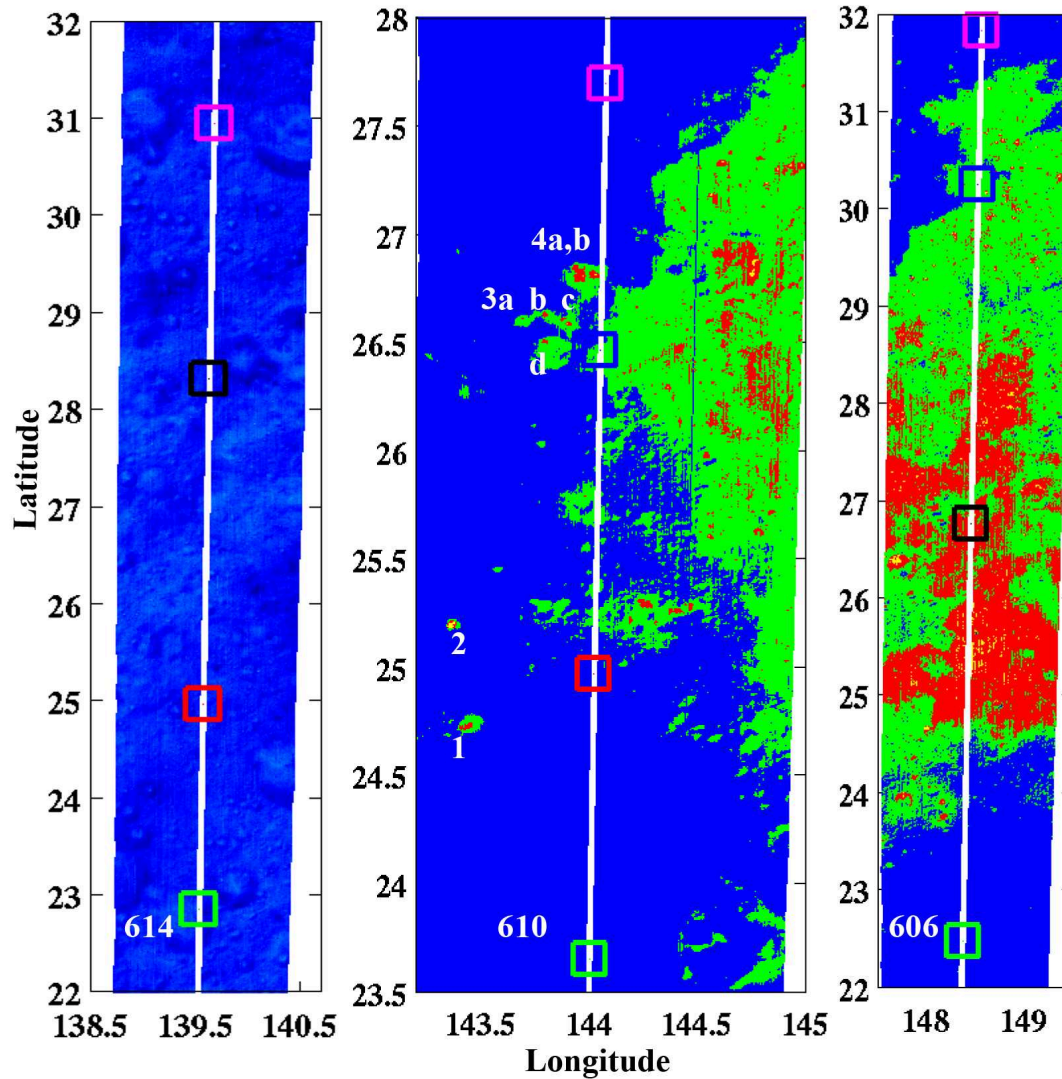


Figure 3.7: M<sup>3</sup> 2- $\mu$ m IBD images and the position of SIR-2 tracks. Blue color represents no or very weak 2- $\mu$ m absorption band and yellow represents the strongest absorption around 2- $\mu$ m. The middle image is zoomed in to show “OOS” areas marked as 1 to 4. The square areas show the location of representative spectra in Figure 3.8. Squares are centered across the SIR-2 footprint considered to extract M<sup>3</sup> and HySI representative spectra.

### 3 Comparing the SIR-2 response with HySI and M<sup>3</sup>

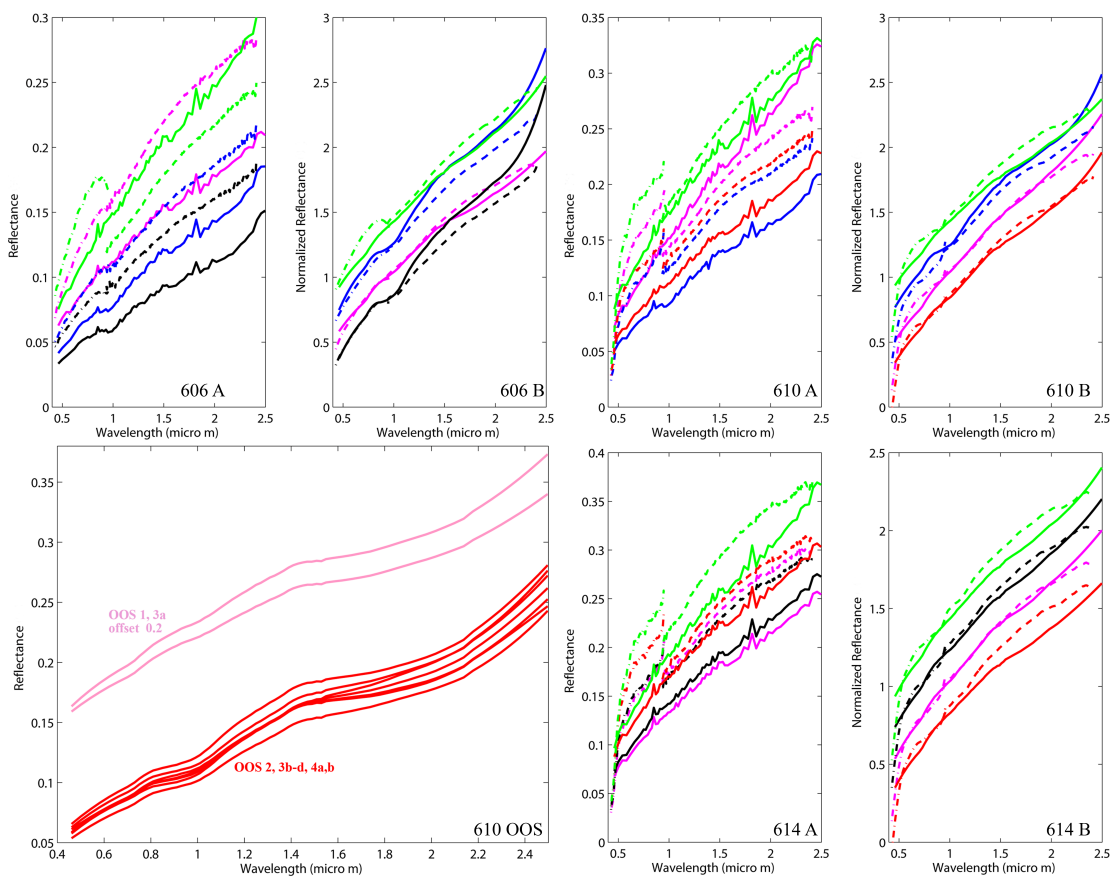


Figure 3.8: Representative spectra of SIR-2 orbits 606, 610 and 614 and corresponding M<sup>3</sup> and HySI spectra extracted from the location marked as square in Figure 3.7. SIR-2, M<sup>3</sup>, and HySI reflectance spectra are normalized at  $\sim 930$  nm. The “OOS” spectra are extracted from the locations marked as 1-4 in the middle image of Figure 3.7. Savitzky-golay filter of polynomial order 3 and frame size 19 is applied to normalized reflectance spectra as a preprocessing step. SIR-2 is plotted as dashed line, HySI as double dashed line and M<sup>3</sup> as solid line.

photometrically. HySI reflectance spectra are in a better match to the SIR-2 data from mare regions than highland soils. The shape of the HySI reflectance spectra is anomalous below 500 nm and above 930 nm. We normalized SIR-2, HySI and M<sup>3</sup> data at  $\sim 930$  nm in order to bring the reflectance response at the same level for the three instruments. We observed that the combined response of SIR-2 and HySI requires cross-calibration in order to compute the 1- $\mu$ m absorption band parameters accurately. The 1- $\mu$ m absorption band depth and continuum slope comparison between the combined HySI and SIR-2 response showed deviations when compared to the M<sup>3</sup> 1- $\mu$ m band parameters. Bhattacharya et al. (2011) suggested a site specific cross-calibration for the HySI orbit 607 using the Apollo 11 bulk soil reflectance spectrum and an average HySI spectrum from a dark mare region. However, we have not applied site specific corrections to HySI data because we have mainly concentrated on the analysis based on the 2- $\mu$ m absorption band.

Pieters et al. (2011) identified three unusual rock types along the inner basin ring from the area covered by M<sup>3</sup> product corresponding to the SIR-2 orbit 610 (Table 3.1). Pieters

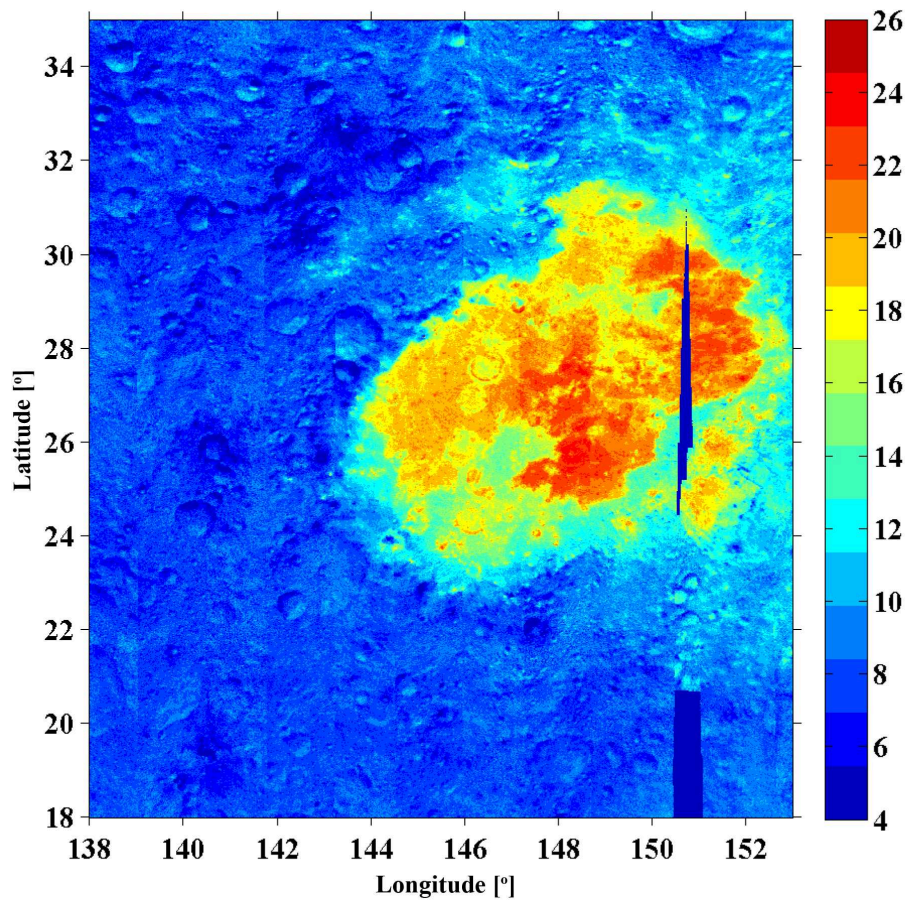


Figure 3.9: FeO distribution derived from the Clementine data using Lucey et al. (1998a) algorithm for Mare Moscoviense and surroundings. The SIR-2 and M<sup>3</sup> iron abundance maps from the same region is discussed in Chapter 5, Figure 5.10.

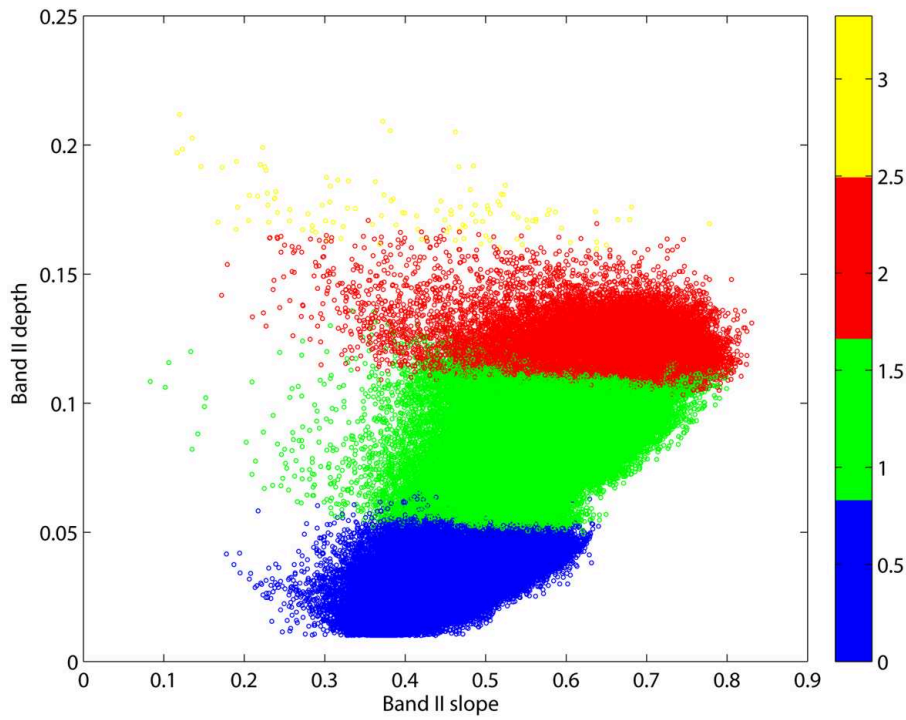
et al. (2011) denoted this distinctive new rock type as “OOS” since they are dominated by high concentration of orthopyroxene, olivine, and Mg-rich spinel, respectively. These unusual areas were identified using the 1- $\mu\text{m}$  IBD image and have been identified by their unusual high or low IBD values relative to surrounding materials. We analysed the presence of OOS rock types using the 2- $\mu\text{m}$  absorption band parameters of the M<sup>3</sup> image corresponding to the SIR-2 orbit 610. We identified four OOS locations at the same places as reported by Pieters et al. (2011). The reflectance spectra of OOS regions are shown in Figure 3.8. Pieters et al. (2011) identified total five OOS areas with three distinct lithologies however, we identified only two distinct lithologies from four area based on the 2- $\mu\text{m}$  IBD images. The fifth area is reported as olivine rich with very weak or no absorption band around 2- $\mu\text{m}$  region by Pieters et al. (2011) however, that area is observed with the band depth of the same order as the areas marked as 2 and 4 in Figure 3.7 in this analysis. No SIR-2 track is available for OOS areas from 100 km orbit, therefore OOS findings could not be verified using the SIR-2 data.

The area represented in blue color in Figure 3.7 is heavily cratered (Figure 3.3) and has 4 to 8 wt% FeO. The SIR-2 orbit 614 sampled only highland soils. Gillis-Davis et al. (2006) suggested the presence of cryptomare deposits between the inner and outer rings

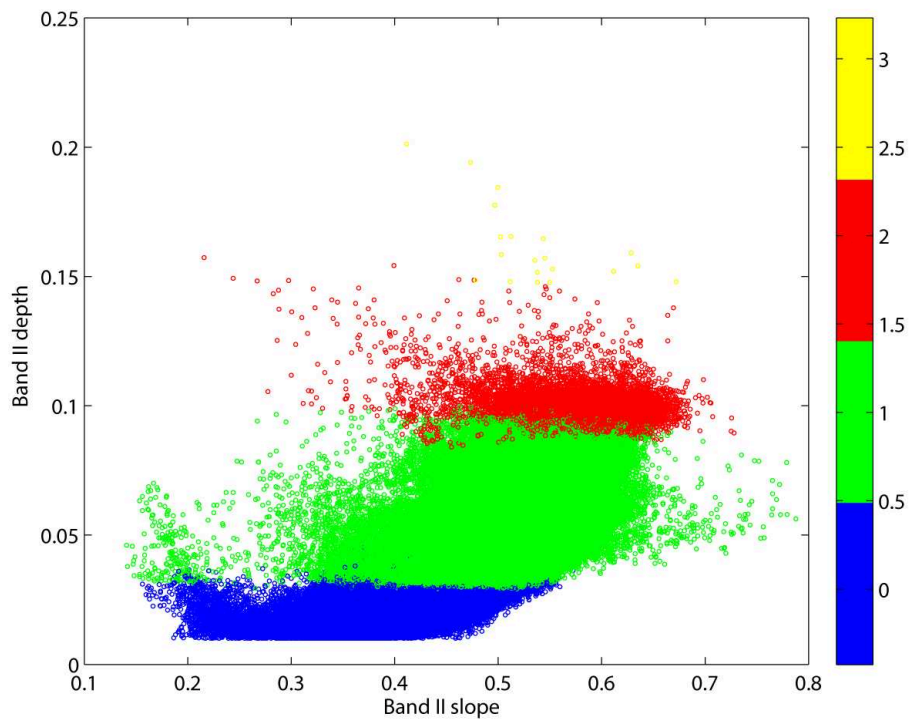
of the Mare Moscoviense basin. SIR-2 orbit 614 falls within the middle and outer rings. The reflectance spectrum plotted as green in Figure 3.8 from SIR-2 orbit 614 shows a narrow absorption bands around 1.3  $\mu\text{m}$  and 2.2  $\mu\text{m}$  however, these absorption bands are not detectable in the corresponding M<sup>3</sup> spectrum. The presence of an absorption band at 2 $\mu\text{m}$  might represent the presence of cryptomare in this region. The spectral shape of the spectra from highland soils are very similar to the ancient mature mare unit (Im), except the difference in albedo. The spectra from highland soils exhibits high albedo when compared to the Im unit. The Im unit appears as green in Figure 3.7 with the 2- $\mu\text{m}$  IBD in the range between 1 and 1.5. The representative spectra from unit Im is shown in Figure 3.8 in blue for SIR-2 orbit 606. The crater density of unit Im is less than highland soils and contains FeO in the range 10 to 13 wt%. The unit Im is characterised by a very weak feature at 1- $\mu\text{m}$  and 2- $\mu\text{m}$  absorption bands, the spectral characteristics are consistent with impact melt (Tompkins and Pieters 2010) thus can be interpreted as impact melt (Bhattacharya et al. 2011, Thaisen et al. 2011). Thaisen et al. (2011) suggested the origin of impact melt from melted and mixed feldspathic and mafic crustal materials and therefore, this unit can not be considered as a mare deposit.

Units Iltm and Ehtm are characterised by strong 1 and/or 2- $\mu\text{m}$  absorption bands and can be interpreted as basaltic units. The FeO wt% ranges are between 16 to 20, and 20 to 24, respectively for Iltm and Ehtm units. The unit Ehtm is mapped by SIR-2 orbit 606 and the representative spectra from this region is shown in black color in Figure 3.8. Unit Iltm is mapped by SIR-2 orbit 610 and the representative spectra of this unit is shown in red color in Figure 3.8. The unit Iltm has not assigned a unique color in Figure 3.7 because the IBD range for this unit is in the same range as the unit Im. However, based on the spectral shape comparison, units Im and Iltm are distinguishable in Figure 3.8. We observed that the fresh craters from units Iltm and Ehtm show deeper absorption band when compared to the surface soils. The change in band parameters within a unit may be due to space weathering effects and/or photometric effects. The unit Ehtm is the youngest mare unit present in the Mare Moscoviense and is exposed in the eastern part of the basin. The unit Ehtm has the lowest albedo among the studied mare units of this region. The low albedo can be due to presence of ilmenite because this area is reported as TiO<sub>2</sub> and FeO rich area using Clementine data (Gillis-Davis et al. 2006, Gillis 1998, Kramer et al. 2008). The crater density is much lower than in unit Im. Craters larger than 1 km in this unit may have excavated materials from relatively deeper layers and show mixed spectral characteristics. This kind of differences are visible in the derived iron map as yellow color (relatively low iron) within iron rich Ehtm unit.

The four colors assigned to the IBD images in the Figure 3.7 can also be shown as a scatter plot as shown in Figure 3.10 corresponding to SIR-2 orbits 606 and 610. Pixels with a strong band depth and low continuum slope represent fresh craters in Ehtm and Iltm units. Figure 3.10 is color-coded based on the IBD values from Figure 3.7. Figure 3.10 suggests that unit Im is compositionally intermediate between the basaltic unit Ehtm and the highland soil material. Figure 3.10 shows that the classification based on only one parameter IBD can be studied in detail considering band depth and band continuum parameters instead. The IBD values for the pair of lower band depth and higher continuum slope and vice versa are the same and thus the unit Im and Iltm could not be distinguish based on the IBD analysis. However, within the green section of the scatter plot; a subsection can be identified with low band depth and continuum slope that corresponds to



(a) Scatter plot for  $M^3$  image corresponding to SIR-2 orbit 606.



(b) Scatter plot for  $M^3$  image corresponding to SIR-2 orbit 611.

Figure 3.10: Scatter plot between 2- $\mu$ m absorption band depth and continuum slope colour-coded in IBD scale for  $M^3$  image subsets shown in Figure 3.3. The four colors represent four distinct units mapped in this study.

the unit Im.

## 3.4 Summary

We compared SIR-2 and HySI data from the Apollo 15 landing site and the Moscoviense basin and found that the geographic coordinate adjustments are required in order to locate the SIR-2 orbits on the M<sup>3</sup> and HySI images. Alignment of the SIR-2, HySI, and M<sup>3</sup> data was checked by comparing the radiance profiles at a common wavelength prior to extracting the reflectance spectra. A site specific cross-calibration is required for HySI data in order to combine the reflectance spectra with the SIR-2 response at absolute reflectance level.

Four distinct units have been mapped as Im, Ehtm, Iltm, and highland soils using spectral shape and band parameters from the SIR-2 and corresponding M<sup>3</sup> orbits. Bhattacharya et al. (2011) reported the same four units using HySI orbit 607. The match between the HySI and SIR-2 data is comparatively better for mare units than the highland soils. The 2- $\mu$ m absorption band parameters are computed for the SIR-2 and M<sup>3</sup> orbits. We observed that the M<sup>3</sup> spectra are relatively darker than the SIR-2 reflectance spectra. We identified “OOS” rock type at four places in the M<sup>3</sup> data corresponding to the SIR-2 orbit 610. These positions are at the same locations reported by Pieters et al. (2011). We don't have any SIR-2 track passing through the “OOS” locations.

## 4 Iron mapping algorithm based on SIR-2 band parameters

Reflectance spectra obtained in the visible/near-infrared (VIS-NIR) wavelength range at the lunar surface contain information regarding the mineralogical composition of the uppermost layer. The characteristics of the main lunar minerals are discussed in Section 1.3. The absorption features of the minerals present in the lunar soil are affected by space weathering (Section 1.2.4) thus making the detection and quantification of its constituent minerals (iron bearing silicates) challenging (Fischer and Pieters 1994, 1996, McKay et al. 1991). In order to estimate the FeO weight percentage (wt%) content remotely, the spectral alteration effects due to space weathering should be minimized.

First part of this chapter discusses different approaches of estimating iron abundances (Section 4.1 and 4.2) and the second part provides comparison between the iron estimation methods based on the 1 and 2- $\mu\text{m}$  absorption band parameters. The methods are applied to 68 lunar returned samples (Table B.1, Section 4.3). The M<sup>3</sup> data collected at the same UTC are used to verify the SIR-2 dataset. The proposed iron abundance estimation method is applied to the calibration site (crater Bonpland D and its surroundings) in mare region from nearside to highlight small scale variations present when compared to the iron abundance map derived using the Lucey et al. (1998a) algorithm (Section 4.10).

### 4.1 Direct and indirect measurement techniques of iron abundance estimations

Iron is a key element in aiding our understanding of the origin and evolution of planetary surfaces. The iron abundance in lunar soils can be measured either directly or indirectly. Direct measurement methods, such as: gamma-ray spectroscopy (e.g., Kobayashi et al. 2005, Lawrence et al. 2002, 1998); X-ray spectroscopy (e.g., Crawford et al. 2009, Swinyard et al. 2009, Yamamoto et al. 2008) and neutron spectroscopy (e.g., Elphic et al. 1998, 2002, Feldman et al. 1998), are able to measure elemental abundances independently of the molecular or mineralogical state of iron. An indirect measurement of the iron content in terms of the FeO weight percent (wt%) is possible by measuring the absorption band parameters of visible/near-infrared (VIS-NIR) reflectance spectra. These two different approaches give results that are not directly comparable. For instance, compared to VIS-NIR observation techniques which sample only the uppermost surface layer, gamma-ray signals originate from an average depth of 30 cm beneath the lunar surface with footprints, to date, usually in the region of tens of km. This means that the absolute

elemental abundances obtained with gamma-ray spectroscopic methods are relatively independent of ground-truth data. Therefore, the iron abundance estimates obtained from sampling over small-area landing sites may not necessarily be comparable to the larger areas sampled by gamma-ray spectrometers. Direct analytical techniques determining the bulk concentration of iron in lunar samples give the concentration of iron regardless of its oxidation state. By geochemical convention, this concentration is usually expressed as the percent oxide (wt%). Since very little Fe on the Moon exists as  $\text{Fe}^{+3}$ , iron concentrations in lunar samples are commonly reported as FeO wt%.

## 4.2 Iron abundance estimation methods: background

Various attempts have been made to decouple the spectral effects of mineral composition from surface maturity by utilizing the 1- $\mu\text{m}$  absorption band parameters, as was done for Clementine and telescopic datasets. The first global map of lunar iron abundance using Clementine data was produced by Lucey et al. (1995). Their empirical method for FeO wt% estimation is based on the reflectance value at 750 nm versus the 950/750 nm ratio for the laboratory spectra of the returned lunar soil samples. A number of publications based on the Lucey et al. (1995) approach show a high correlation between the spectral parameter derived from 750 nm versus the 950/750 nm ratio plot for Clementine data and the laboratory measured FeO wt%, although with a few outliers (Blewett et al. 1997b, Gillis et al. 2004, Lucey et al. 1998a, 2000). Lucey et al. (2006) noted that the comparison between multispectrally-derived Fe and Lunar Prospector's Gamma Ray Spectrometer (GRS) abundances shows three major regional anomalies: the Western Oceanus Procellarum, the South Pole-Aitken Basin, and Mare Tranquillitatis. The NIR/VIS ratio method (950/750 nm) suffers from the effects of changing topography affecting shading, especially at high incidence angles (Lucey et al. 1998a). To minimize topographic effects in the Clementine data set, Le Mouélic et al. (2000) included an NIR filter at 1500 nm to estimate the continuum slope along with the 750 and 950 nm filters in their study. They defined the band depth for the 1- $\mu\text{m}$  absorption band by considering a normalized ratio of reflectance values at 950, 750, and 1500 nm filters. They resultantly found a correlation for the 1- $\mu\text{m}$  band depth and continuum slope across a small fresh crater located near Aristarchus Plateau and proposed an equation for FeO wt% estimation based on a coefficient derived from the correlation plot of the band depth and continuum slope. This equation represents the total FeO wt% as the summation of iron in both silicates and oxides (i.e. with ilmenite, as the most common phase). The contribution of spectrally neutral ilmenite is given by the  $\text{TiO}_2$  wt% estimation based on the method of Lucey et al. (1998a). Shkuratov et al. (1999a) proposed a three dimensional correlation method for simultaneous prediction of FeO wt%,  $\text{TiO}_2$  wt%, and the maturity parameter ( $I_s/\text{FeO}$ ) utilizing albedo measurements from telescopic data. A more recent approach to the estimation of elemental abundances using Clementine data was given by Shkuratov et al. (2005) and Wöhler et al. (2011) taking Lunar Prospector (LP) data as reference. These methods rely on a regression model for the estimation of elemental abundances based on the extraction of spectral features from Clementine images.



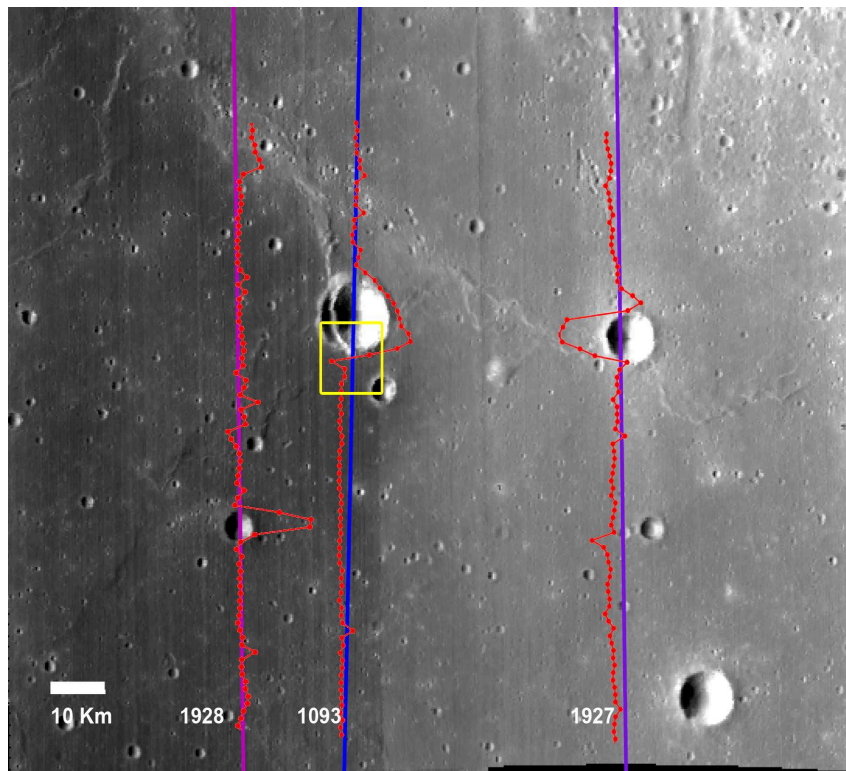


Figure 4.1: SIR-2 orbit 1093 sampled Bonpland D crater which is considered as a calibration site for mafic iron estimation method. The summed reflectance profiles are plotted on the  $M^3$  mosaics. The  $M^3$  mosaics are prepared from the  $M^3$  product IDs corresponding to the SIR-2 orbits given in Table 4.1. A shift in geometric coordinates was required for the SIR-2 orbits to match the summed reflectance profiles with crater positions in  $M^3$  mosaics and have listed in Table 4.1.

### 4.3 Data-sets and data preparation

We selected 68 laboratory-measured reflectance spectra from Apollo landing sites from the J. B. Adams collection available from RELAB. Table B.1 presents an extended list of samples from Le Mouélic et al. (2000). FeO ranges from 3 to 20 wt% and maturity index ( $I_s/FeO$ ) ranges from 3 (immature) to 92 (mature) for the selected dataset. We have included most of the available samples with varying FeO wt% and maturity indices collected at different locations including mare highland boundaries, highland, and mare soils. We have also included a few soil spectra from materials collected by the Luna 24 mission.

For calibrating the iron content estimation method we selected the SIR-2 orbits 1093, 1927, and 1928 (Figure 4.1). Orbit 1093 intersected crater Bonpland D, while orbits 1927 and 1928 lay outside the crater and are used for comparing the spectral response variations within and around the crater. Additionally, we have used  $M^3$  data (0.46-2.57  $\mu\text{m}$ ). To ensure that the SIR-2 and  $M^3$  data are photometrically comparable, we used only data which were taken at the same UTC. Figure 4.1 shows the SIR-2 tracks and their summed reflectance plotted on the  $M^3$  mosaic of Bonpland D and its surroundings.  $M^3$  images

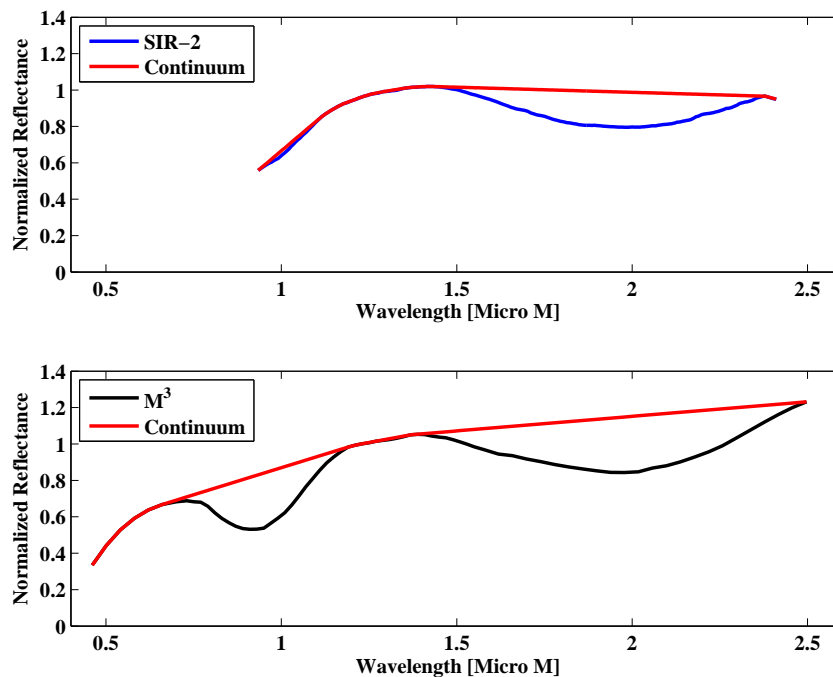


Figure 4.2: The continuum line for the SIR-2 and  $M^3$  reflectance spectra is segments of straight line to the normalized reflectance spectra. The reflectance spectra are extracted from the crater floor region from the square area drawn in Figure 4.1.

show brightness differences in the mosaics since the images are not corrected for the viewing geometry. We have adjusted the SIR-2 data relative to the  $M^3$  images by comparing the scaled radiance profiles (the radiance spectrum divided by its mean). The SIR-2 and  $M^3$  files used in this study along with the shift calculated are given in Table 4.1. We have used  $M^3$  data between channels 1-75 (0.46-2.57  $\mu\text{m}$ ) to avoid thermal emission effects as well as to be able to be comparable with laboratory measured data.

The RELAB spectra are interpolated to the SIR-2 wavelength range (0.93 to 2.4  $\mu\text{m}$ ) and the  $M^3$  wavelength range (0.46 to 2.47  $\mu\text{m}$ ). These datasets were normalized to unity at 1.5  $\mu\text{m}$ . The 1 and 2- $\mu\text{m}$  absorption band parameters are calculated by fitting a straight line continuum (Section 2.6).

We have applied a spectrum selection threshold based on the maximum absolute reflectance value. SIR-2 and  $M^3$  spectra that have a maximum absolute reflectance/apparent reflectance lower than 0.05 were excluded from the analysis. The 2- $\mu\text{m}$  absorption band parameters for the SIR-2 data are computed considering the short-wavelength end between 1.4 and 1.5  $\mu\text{m}$  and the long-wavelength end at 2.4  $\mu\text{m}$ . The 1- $\mu\text{m}$  absorption band parameters for the SIR-2 data are not computed in this analysis because the wavelength range of the SIR-2 instrument starts at 0.94  $\mu\text{m}$ . Figure 4.2 shows an example of continuum removal for the SIR-2 and  $M^3$  data.

Table 4.1: SIR-2 and M<sup>3</sup> product IDs used from calibration site and the geometric coordinate shifts calculated by comparing their scaled radiance profiles.

SIR-2 Product ID	M <sup>3</sup> Product ID	Geometric shifts	Correlation	
			Before(%)	After(%)
CH1SIR2_NE2_SC_R01093	M3G20090207T003331_V02_RDN	0.16°S,0.02°W	32	97
CH1SIR2_NE2_SC_R01927	M3G20090416T081001_V01_RDN	0.21°S,0.06°E	22	92
CH1SIR2_NE2_SC_R01928	M3G20090416T101921_V01_RDN	0.21°S,0.04°E	16	80

## 4.4 Band depth comparison between SIR-2 and M<sup>3</sup> orbits from Bonpland D and surroundings

Figure 4.3 shows a comparison between the 2- $\mu\text{m}$  (band II) band depth calculated using Equation 2.7 for SIR-2 orbits 1093, 1927, and 1928 and their corresponding M<sup>3</sup> orbits (Table 4.1). M<sup>3</sup> spectra are extracted from the nearest pixel to the SIR-2 footprints. Both the data-sets show similar variations in band II depth however, M<sup>3</sup> band depth values are greater than the SIR-2 in general. We applied Equation (2.7) to the M<sup>3</sup> images corresponding to the SIR-2 orbits (Table 4.1) to generate the band II band depth map for Bonpland D and its surroundings (Figure 4.4). The surrounding part of the craters show lower band depth values compared to the crater wall areas. Figure 4.4 shows a direct relationship between the band depth and the maturity of the surface. The small craters are relatively fresh and exhibit greater band depth values in the range 0.25 to 0.35 whereas, surround mare area is relatively older and exhibit band depth variations in the range 0.01 to 0.15. The band depth is a function of both the amount of the Fe<sup>2+</sup> present and the spectral alteration due to the space weathering effects. Any mineralogy interpretation based on the band depth analysis first requires an evaluation of the spectral alteration due to the space weathering.

## 4.5 Correlation between continuum slope and concentration of nanophase metallic iron

Figure 4.5 shows a comparison between the continuum slope (as defined in section 2.6) for the 1 and 2- $\mu\text{m}$  absorption bands and the parameter  $I_s$ . Parameter  $I_s$  is proportional to the amount of nanophase metallic iron particles (Morris 1978). Nanophase metallic iron particles are produced by hypervelocity micrometeorite impacts (Pieters et al. 2000, Taylor et al. 2001) and/or deposition of atoms in lunar soil grains by solar wind sputtering (Hapke 2001). We observed a positive correlation between the continuum slope and the parameter  $I_s$  for both the absorption bands. Similar results have been shown by Hiroi et al. (1997) and Le Mouélic et al. (2000) for the 1- $\mu\text{m}$  continuum slope and parameter  $I_s$  (Figure 4.5, sub-figure C) for a subset of the lunar samples. Hiroi et al. (1997) suggested that the parameter  $I_s$  is correlated to the continuum slope since maturity processes affect the continuum slope by reddening and darkening the reflectance spectra. The relationship between the parameter  $I_s$  and the continuum slope is important to understand because

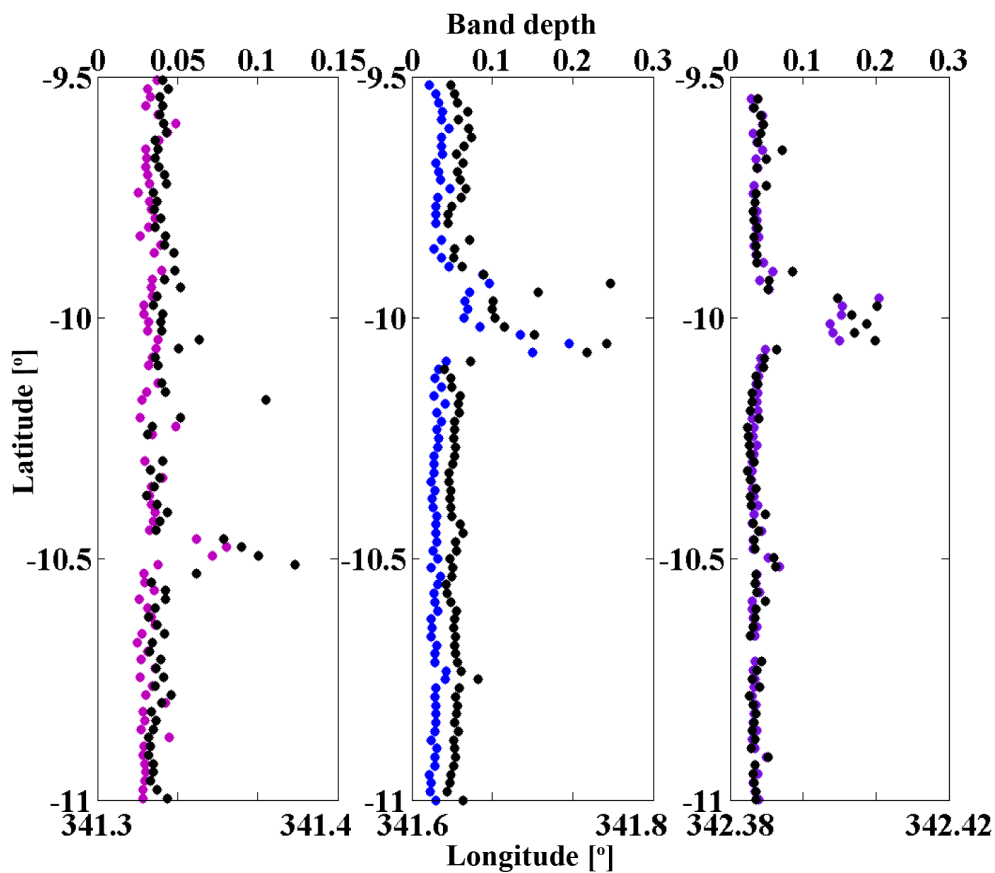


Figure 4.3: Band II depth estimated for M<sup>3</sup> from SIR-2 footprints is higher than SIR-2. M<sup>3</sup> band depth is shown by black dots for SIR-2 orbits 1928 (left), 1093 (center) and 1927 (right).

the continuum slope increases with both the iron content (FeO wt%) and the parameter  $I_s$ . The continuum slope shows a direct correlation to the composition and parameter  $I_s$  whereas the band depth parameter increases with increasing iron abundance but decreases with increasing maturity (Fischer and Pieters 1996, 1994, Lucey et al. 1995). The band parameters (continuum slope and band depth) can be employed to decouple the maturity and iron content information from a NIR spectrum because these parameters respond inversely to maturity. This relationship is exploited by Le Mouélic et al. (2000) and Lucey et al. (1995) for deriving iron abundance maps using Clementine data.

Figure 4.5 shows a comparison between the continuum slope (for band I and band II) and FeO wt% for the samples listed in Table B.1. We also show a comparison between the band I slope and the Optical Maturity Parameter (OMAT) as defined by Lucey et al. (1998b) in Figure 4.5. A comparison between the top two sub-figures of Figure 4.5 shows that the relationship between the continuum slope and the parameter  $I_s$  is similar for both the 1- $\mu$ m and 2- $\mu$ m absorption bands. However, band II continuum slope shows a narrow range of variation in comparison to the 1- $\mu$ m absorption band which may introduce uncertainties in our iron abundance estimation algorithm. The spectral slope values saturate for

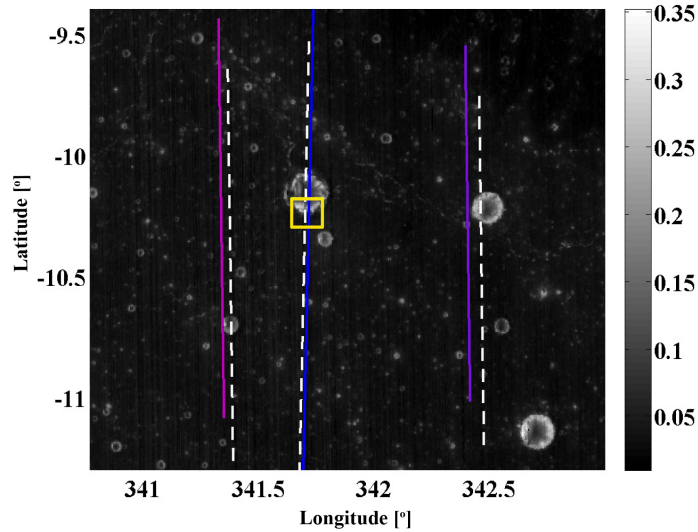


Figure 4.4: Band II depth mosaic from M<sup>3</sup> product IDs given in Table 4.1 with SIR-2 orbit's positions, absolute coordinates by solid lines and shifted coordinates by dashed lines. The deep band depths are found at crater walls for Bonpland D and all small craters in the image.

the parameter  $I_s$  above 900 for both the absorption bands and the relationship becomes non-linear. Hiroi et al. (1997) suggested that the deviation from the linear relationship may occur at high  $I_s$  values due to the presence of dark minerals such as ilmenite. The band I continuum slope shows a high anti-correlation with the OMAT parameter as shown in figure 4.5(d).

## 4.6 Comparison of SIR-2 and M<sup>3</sup> spectra from Bonpland D

Figure 4.6(a) compares the SIR-2 and M<sup>3</sup> apparent reflectance spectra from crater floor to the surrounding mare from the square area drawn in Figure 4.1. The M<sup>3</sup> apparent reflectance spectra are extracted from the pixel position nearest to the SIR-2 geometric coordinates. The spectra in Figure 4.6 demonstrate the spectral effects of the space weathering processes, present in a small region around a fresh crater. We assume that the variations in the mineralogical composition within the small region marked in Figure 4.1 are minor but with varying exposures to space weathering due to the excavation of the fresh material at the time of impact. Spectrum 1 is extracted from the southern crater wall (showing the highest band depth), whereas spectrum 4 is extracted from the surrounding mare material. Spectra 2 and 3 are from the intermediate locations between 1 and 4. No filtering is applied to the spectra from either instrument. Although we observe some offset in absolute levels, the shapes of the spectra are broadly comparable. Figure 4.6(b) shows the apparent reflectance spectra divided by a continuum line. The overall reflectance and the absorption band depth increases from the surrounding mare material (spectrum 4) to the fresh material exposed on the crater wall (spectrum 1) while the continuum slope

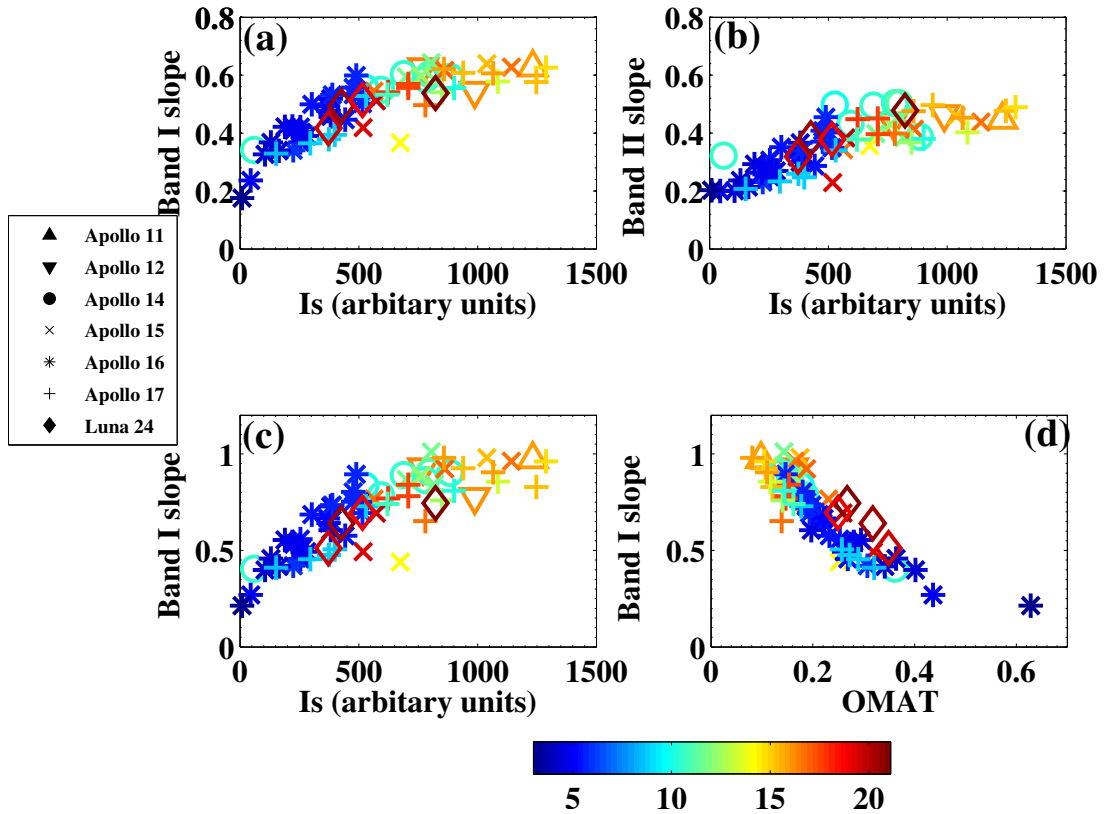


Figure 4.5: Correlation plots of the continuum slope and the parameter  $I_s$  for the 68 samples listed in Table B.1. The samples are color-coded according to their FeO wt%. The continuum slope increases with increasing FeO and  $I_s$ . The continuum slope is computed in an automated way using convex hull method (Section 2.6) for sub-figures (a) and (b). Sub-figure (c) uses a continuum slope definition from Le Mouélic et al. (2000) and the OMAT is calculated from Lucey et al. (1998b).

features an inverse relationship to the band depth.

## 4.7 Method

Figure 4.7 shows the relationship between the band depth and the continuum slope for three ideal sample series. We assume that only maturity is changing for each series and that FeO wt% remains the same. Each sample series with a fixed FeO wt% falls along a so-called maturity line (dashed lines in Figure 4.7), showing higher maturity at the upper left corner and fresh materials at the lower right corner. Samples with a fixed maturity show an increase in FeO wt% in the direction indicated in Figure 4.7. The absolute slope calculated from different sample series is similar and thus can be used as a multiplier in computing an empirical calibration between the band parameters and the laboratory-measured FeO wt%. This unique multiplier term minimizes the maturity effects from a sample series in such a way that all samples show the same FeO content. The remotely

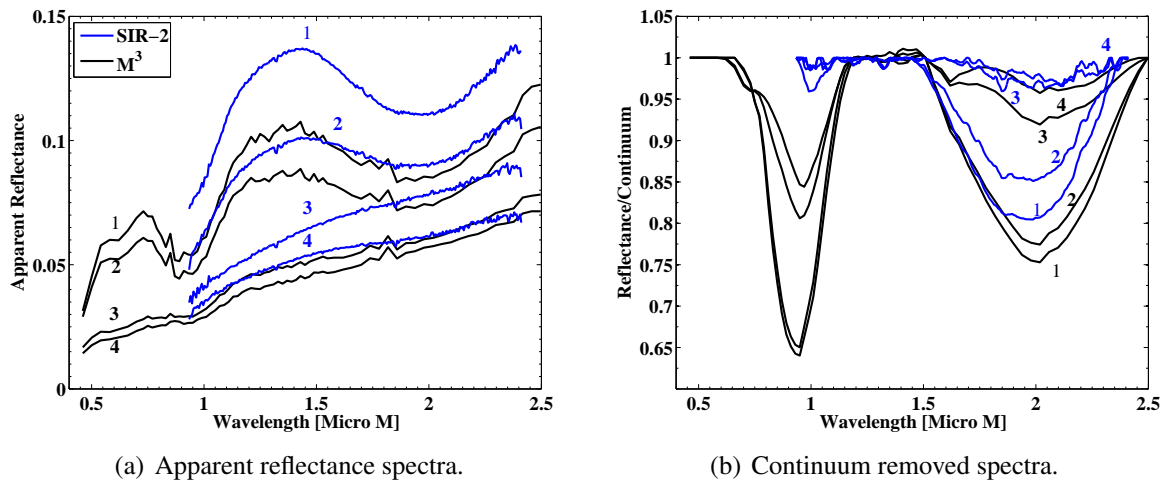


Figure 4.6: A comparison of SIR-2 and M<sup>3</sup> spectra extracted from the square marked in Figure 4.1, M<sup>3</sup> spectra are extracted from the pixels closest to the SIR-2 footprints. Spectra are marked as 1 from the interior of the crater to 4 in the outer mature surrounding mare. The band depth decreases with increasing maturity.

measured FeO wt% sensitive parameter is given by Equation 4.1:

$$\text{FeO(wt\%)}\text{ sensitive parameter} = BD + \text{absolute slope coefficient} \times CS \quad (4.1)$$

where  $BD$  represents the band depth and  $CS$  represents the continuum slope.

However, the task of separating mineralogy and space weathering effects is complicated due to the presence of opaque minerals, such as ilmenite ( $\text{FeTiO}_3$ ). Ilmenite is mainly present in mare regions along with pyroxenes (Papike et al. 1976) (Section 1.3.4). Therefore, corrections for the presence of ilmenite may be needed when estimating FeO wt% remotely. We will illustrate this issue with an example of returned samples in Section 4.9.

## 4.8 Derivation of the absolute slope coefficient for SIR-2 and M<sup>3</sup> data-sets

The selection of a suitable target for derivation of the absolute slope coefficient was dependent on a SIR-2 track crossing a small crater and the availability of at least two adjacent tracks for comparing the effect of spectral alteration due to soil maturity. Bonpland D crater ( $10.1^\circ\text{S } 18.2^\circ\text{W}$ , Figure 4.1) meets all of these requirements and it was selected as a calibration site.

Figure 4.8 illustrates the band depth-continuum slope relationship for the 2- $\mu\text{m}$  absorption band for the SIR-2 and M<sup>3</sup> data. A total of twelve SIR-2 footprints lie within the crater and they show deeper band depth and lower continuum slope values than the footprints located outside the crater. SIR-2 footprints outside the crater represent mature mare materials and are clustered in the upper left part of Figure 4.11(a) whereas the footprints from inside crater show a gradual decrease in continuum slope and increase in band

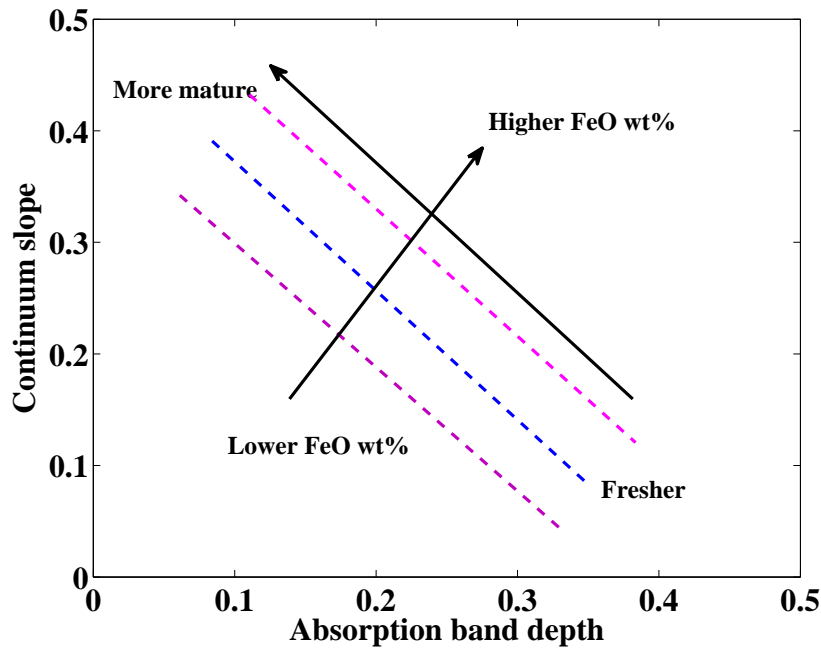
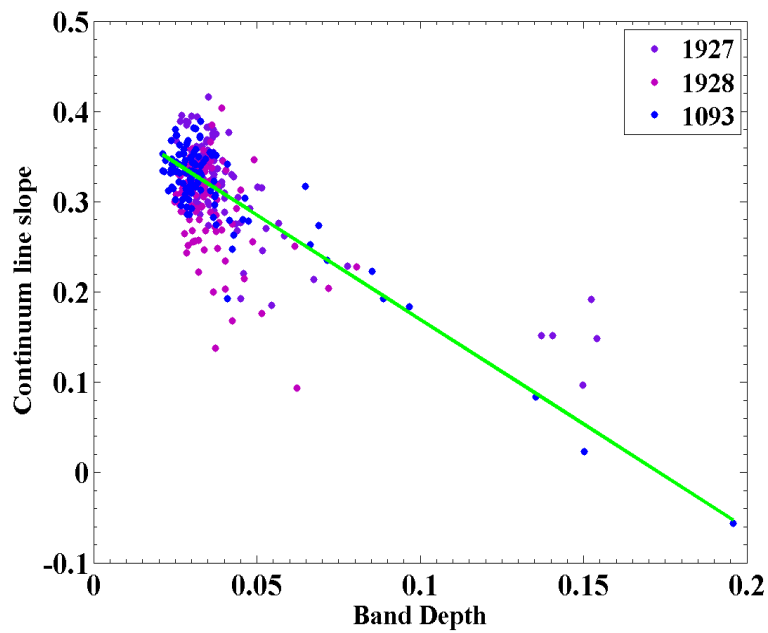


Figure 4.7: Conceptual band depth and continuum slope relationship for sample series with particular FeO content and varying maturity.

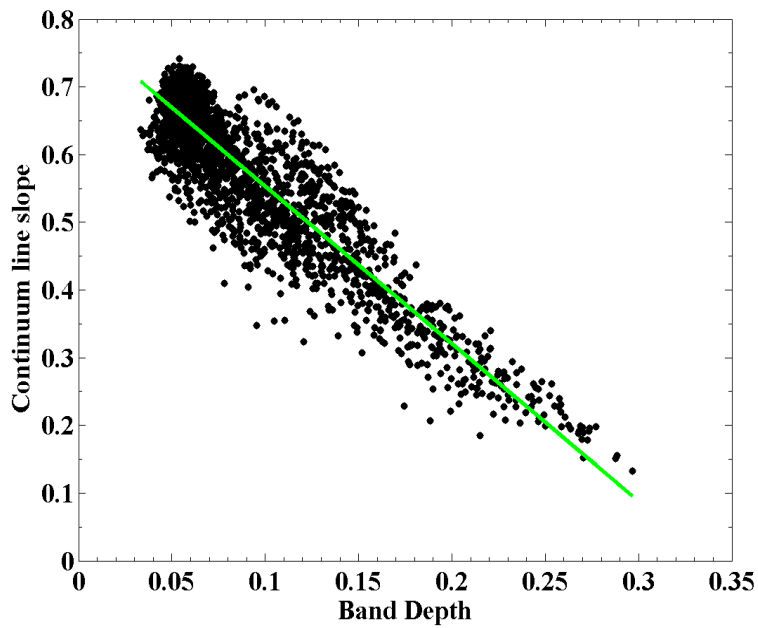
depth moving towards the lower right part of Figure 4.11(a). A similar linear relationship was observed by Le Mouélic et al. (2000) for a small fresh mare crater area located near Aristarchus Plateau utilizing 1- $\mu\text{m}$  absorption band parameters from the Clementine mission. We observe negative continuum slope values for the crater wall region, probably due to the cutoff point at 2.4  $\mu\text{m}$  of the SIR-2 wavelength range. The line passing through the data points in Figure 4.8 represents the best regression line fit. The absolute slope coefficient of the line is calculated by dividing the absolute difference of the band depth by the absolute difference of the continuum slope.

Figure 4.8(b) illustrates the band depth-continuum slope relationship for the  $M^3$  data points extracted from Bonpland D and its surroundings. The  $M^3$  data have been used to verify our results and to compensate for the small sample of SIR-2 footprints within the crater. The slope of the best regression line for  $M^3$  data from Figure 4.8(b) is 0.297 while for the SIR-2 data is 0.456. We observe that the continuum slope and the band depth values are higher for the  $M^3$  data sets than are those from SIR-2 data. Therefore, the slope of the best regression line is less than that of the SIR-2 line. However, this should not affect the final iron abundance maps because we compute iron abundances based on separate calibrations for the SIR-2 and  $M^3$  data-sets.





(a) For SIR-2 orbits 1093, 1927 and 1928



(b) For M<sup>3</sup> product id M3G20090207T003331\_V02\_RDN

Figure 4.8: Correlation plots of the continuum slope versus the 2- $\mu$ m absorption band depth for Bonpland D crater and its surrounding areas for the SIR-2 and M<sup>3</sup> data.

## 4.9 Empirical calibration based on the lunar returned samples

### 4.9.1 Iron abundance estimation based on 1- $\mu\text{m}$ absorption band parameters

In order to compare our results with the Lucey et al. (1998a) and Le Mouélic et al. (2000) algorithms, we first applied equation 4.1 using the absolute continuum slope parameter derived from the Bonpland D crater to the 1- $\mu\text{m}$  absorption band parameters calculated for the 68 samples listed in Table B.1 (section 4.3), followed by application of the same method to the 2- $\mu\text{m}$  absorption band parameters. Figure 4.9(a) shows a clear correlation between the FeO wt% sensitive parameter calculated through equation 4.1 for the 1- $\mu\text{m}$  absorption band parameters and the laboratory measured values of FeO wt% listed in Table B.1. The correlation (68%) between the FeO wt% sensitive parameter and the laboratory-measured FeO wt% shows however, a bias of an average of 5 wt%. Le Mouélic et al. (2000) suggested correlating the difference between FeO wt% measured in the laboratory and the values calculated through the use of equation 4.1 with the iron contained in the ilmenite in the samples. The iron content in ilmenite in the samples can be estimated using the  $\text{TiO}_2$  wt% values measured in the laboratory. This relationship is shown in Figure 4.9(b). One can see that certain samples from the Apollo 16, Apollo 15, Apollo 14 and Luna 24 data do not follow a simple linear relationship. Assuming the relationship from Figure 4.9(b) to be linear may introduce an error in estimating the total iron abundance. The total iron content is given by equation 4.2 after including the ilmenite correction in terms of a best regression line equation fitted to the data in Figure 4.9(b) and plotted in Figure 4.9(c).

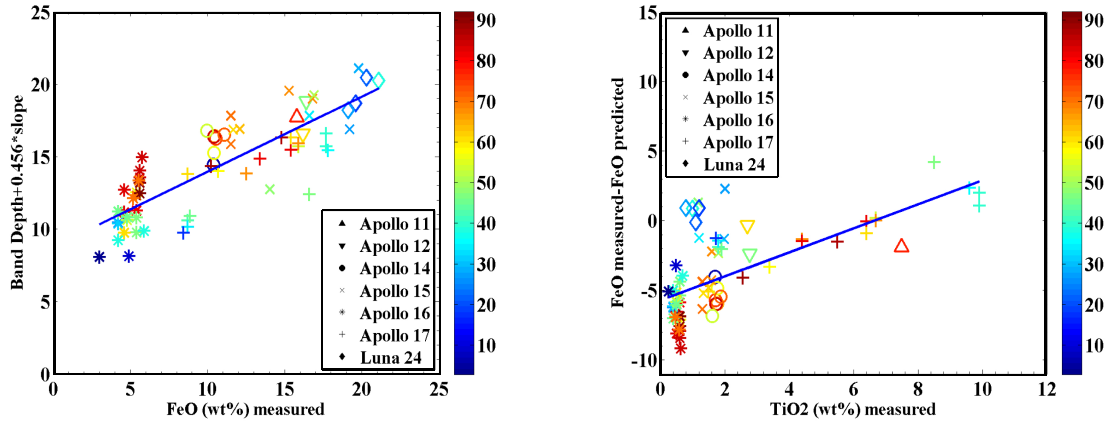
$$\text{FeO}_{SIR}(\text{wt}\%) = 47.86 \times (BD1 + 0.456 \times CS1) - 5.72 + 0.86\text{TiO}_2 \quad (4.2)$$

where  $BD1$  is the band depth for the 1- $\mu\text{m}$  absorption band calculated using equation 2.7 and  $CS1$  is the continuum slope evaluated using the convex hull continuum removal method.

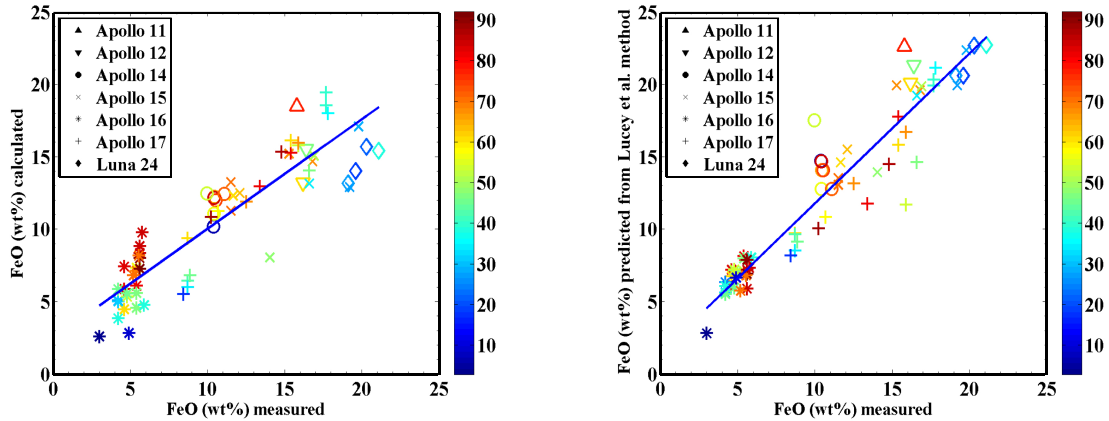
From Figure 4.9(c) we observe a 90% correlation between the iron content estimated using equation 4.2 and the iron content measured in the laboratory. The difference between estimated and measured values of FeO wt% has a standard deviation of 2.3 wt%. If we apply the Le Mouélic et al. (2000) equation of iron abundance estimation to the 68 samples listed in Table B.1, we get a standard deviation of 2.8 wt% whereas the Lucey et al. (1998a) method shows a standard deviation of 1.8 wt% for the same dataset. The total iron content estimation using the Lucey et al. (1998a) equation is shown for comparison in Figure 4.9(d).

A comparison of Figures 4.9(c) and 4.9(d) shows greater inaccuracy in the iron estimation derived using equation 4.2 for the highland soils (FeO >6 wt%). One of the reasons for this increased inaccuracy can be attributed to the selection of the mare region as a calibration site (Le Mouélic et al. 2000). Figures 4.9(c) and 4.9(d) demonstrate that both methods show inaccuracy in iron abundance estimation for some of the samples from Apollo 16, 14 and 17. Additionally iron estimation from Figure 4.9(c) shows inaccuracy for Luna 24 samples. Both methods show some advantages with respect to the

## 4.9 Empirical calibration based on the lunar returned samples



(a) The correlation between the FeO wt% sensitive parameter computed from equation 4.1 and laboratory measured iron content. (b) Difference between measured and derived iron content is correlated to the titanium content.



(c) Total iron content derived from equation 4.2 (correlation 90%). (d) Total iron content derived from Lucey et al. (1998a) ratio method (correlation 95%).

Figure 4.9: Empirical calibration of FeO wt% for the 1- $\mu$ m absorption band parameters from Table B.1. The Samples are color-coded according to their maturity index ( $I_s/FeO$ ).

other. Equation 4.2 is derived in a similar way to that used by Le Mouélic et al. (2000) for the Clementine data and it is aimed at minimizing topographic effects; however, this method needs a separate evaluation of iron contained in ilmenite. The determination of the iron content in ilmenite through remotely sensed data is dependent on the detection of the  $TiO_2$  abundance in the UV-VIS wavelength range. The most common methods of estimating  $TiO_2$  abundance are based on an empirical calibration between laboratory-measured  $TiO_2$  wt% and the spectral slope across the ultraviolet to visible wavelengths (Blewett et al. 1997a, Lucey et al. 1998a, Charette et al. 1974, Lucey et al. 2000). However, this empirical calibration suffers from low precision and accuracy of the order of 5 wt% in comparison to  $TiO_2$  estimates from the Lunar Prospector's neutron-spectrometer (Elphic et al. 2002, 1998, Gillis et al. 2003). The empirical relation of estimating  $TiO_2$  based on the UV/VIS color ratio shows a complex relation and it cannot be directly correlated to the iron content present in ilmenite (Lucey et al. 2006). Despite these difficulties il-

menite corrections have been applied to the calibrated Clementine data by Le Mouélic et al. (2002, 2000) by deriving 415/750 nm ratio from Lucey et al. (1998a) for the mare regions. Ilmenite corrections for titanium-poor regions like highlands can be neglected.

#### 4.9.2 Iron abundance estimation based on 2- $\mu\text{m}$ absorption band parameters

The band depth of the 2- $\mu\text{m}$  absorption band is shallower than the 1- $\mu\text{m}$  absorption band and we discussed in section 4.5 that the continuum slope values of the 2- $\mu\text{m}$  absorption band decrease by 50% for samples from Table B.1 when compared to the 1- $\mu\text{m}$  absorption band's continuum slope. However, the same relation between FeO wt% measured and estimated should exist for both the absorption bands. equation 4.1 has been applied to RELAB data from Table B.1 to correlate 2- $\mu\text{m}$  absorption band parameters to the laboratory-measured FeO wt% in a similar way to that described in section 4.9.1 for the 1- $\mu\text{m}$  absorption band. In order to support the iron estimation based on the 2- $\mu\text{m}$  absorption band parameters for SIR-2 data, we applied the same method to the M<sup>3</sup> dataset (i.e. RELAB data were interpolated into the SIR-2 and M<sup>3</sup> wavelength ranges) and Equations 4.3 and 4.4 employed for the estimation of the FeO wt% in the SIR-2 and M<sup>3</sup> data-sets:

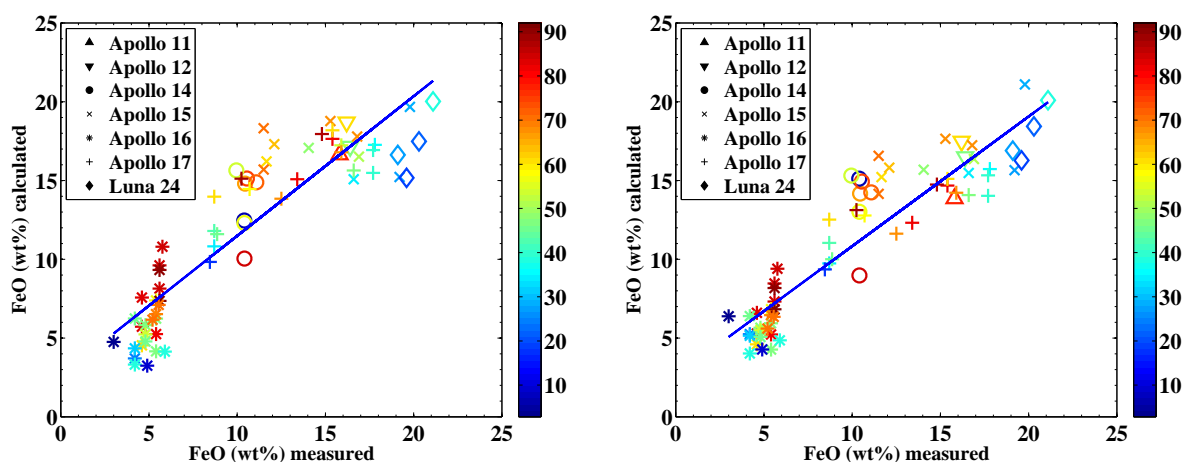
$$\text{FeO}_{SIR}(\text{wt}\%) = 85.08 \times (BD2 + 0.456 \times CS2) - 6.87 + 0.88\text{TiO}_2 \quad (4.3)$$

$$\text{FeO}_{M^3}(\text{wt}\%) = 95.33 \times (BD2 + 0.297 \times CS2) - 5.30 + 0.90\text{TiO}_2 \quad (4.4)$$

where *BD2* represents the band depth for the 2- $\mu\text{m}$  absorption band calculated using equation 2.7 and *CS2* the continuum slope for the 2- $\mu\text{m}$  absorption band computed using a convex hull continuum removal method.

The iron abundance derived from equation 4.3 shows a correlation of 77% between the estimated and measured FeO wt%. This correlation is lower than those FeO wt% estimations based on the 1- $\mu\text{m}$  absorption band parameters. However, we found the FeO wt% sensitive parameter (equation 4.3) to show a direct correlation to the laboratory measured FeO wt% for all samples listed in Table B.1 except for Apollo 14 and 16. Applying this condition to equation 4.3 improves the correlation between the measured and estimated FeO wt% to 90%. This result for RELAB data interpolated to the SIR-2 wavelength range is shown in Figure 4.10(a). Similarly, equation 4.4 is used to derive iron abundance estimations for RELAB data interpolated into the M<sup>3</sup> wavelength range. In this case, a correlation of 86% is obtained. The difference between estimated and measured FeO wt% has a standard deviation of 2.7 wt%. If we apply condition of an additional contribution of FeO wt% from ilmenite only to Apollo 14 and 16 samples in equation 4.4, the correlation between the measured and estimated FeO wt% reaches 91% (Figure 4.10(b)), with a standard deviation of 2.0 wt%. The standard deviation computed for equation 4.3 on applying the condition of an FeO wt% contribution from ilmenite only to Apollo 14 and 16 samples is 2.4 wt%.

We observed that the correlation between measured and estimated FeO wt% is comparable to that shown by RELAB data considering the 1- $\mu\text{m}$  and 2- $\mu\text{m}$  absorption bands independently. However, iron abundance estimations based on 2- $\mu\text{m}$  absorption band



(a) Total iron content derived from equation 4.3 for RE-LAB data interpolated in the SIR-2 wavelength range (correlation 90%). (b) Total iron derived from equation 4.4 for RELAB data interpolated in the  $M^3$  wavelength range (correlation 91%).

Figure 4.10: Empirical calibration of FeO wt% for the 2- $\mu\text{m}$  absorption band parameters from Table B.1. The Samples are color-coded based on their maturity index ( $I_s/\text{FeO}$ ).  $\text{TiO}_2$  wt% is correlated only for the highland samples.

parameters need an additional condition for highland soils in order to improve the accuracy of iron abundance estimations for RELAB data interpolated in the SIR-2 wavelength range. RELAB data interpolated in the  $M^3$  wavelength range show an insignificant improvement in the correlation between estimated and measured iron abundances when the additional condition of an FeO wt% contribution from ilmenite is applied. This discrepancy between the two data-sets could be due to the fact that the SIR-2 data is cross-calibrated with the Apollo 14 landing site whereas no cross-calibration was applied to the  $M^3$  data.

### 4.9.3 Limitations of the proposed iron abundance method based on 2- $\mu\text{m}$ absorption band

We derived the absolute slope coefficient from bidirectional reflectance data and have applied it to the hemispherical laboratory measurements. This approach can be one of the reasons for the deviation we observed between the measured and estimated FeO wt% using equations 4.2 and 4.3. We could improve our algorithm by selecting SIR-2 orbits that passed through the lunar sample return sites and then calculating the band parameters directly from the remotely sensed spectra, rather than using RELAB data for deriving an empirical relation between the band parameters and laboratory measured FeO wt%. This approach was helpful to improve the iron abundance estimations based on multispectral data from the Clementine mission (Blewett et al. 1997a). However, due to the premature end of the Chandrayaan-1 mission, we do not have enough SIR-2 tracks passing over the sample return sites at 100 km altitude to fully carry out this task. We observed negative continuum slope values for the SIR-2 data-sets from fresh materials (for example crater walls and central peak areas). Fresh materials exhibit stronger absorption band depth and

lower continuum slope values that may show a negative value in the absence of full spectral wavelength coverage up to 2.5  $\mu\text{m}$ . This problem needs rectification for an accurate estimation of FeO wt% based on the SIR-2 data. The negative continuum slope problem is absent in the M<sup>3</sup> data-set due to its full wavelength coverage. Nevertheless, an accurate estimation of FeO wt% for the M<sup>3</sup> data-set requires corrections since the wavelength range beyond 2  $\mu\text{m}$  is affected by the thermal emission problem.

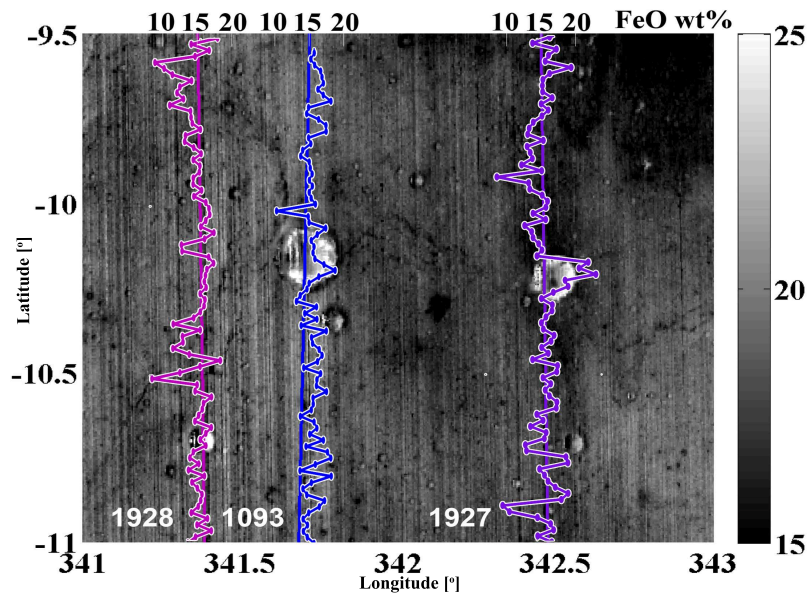
Adjustments relating to the iron contained in ilmenite is only required to be added to Apollo 14 and 16 samples to improve the accuracy of the proposed algorithm. Our algorithm is based on detecting pyroxene absorption bands in the 2- $\mu\text{m}$  region and does not account for the iron contained in minerals with prominent absorption bands that occur only in the 1- $\mu\text{m}$  region. Hence, our iron abundance estimation algorithm may show low accuracy in olivine rich areas such as the South Pole-Aitken Basin.

## 4.10 Iron map of calibration site

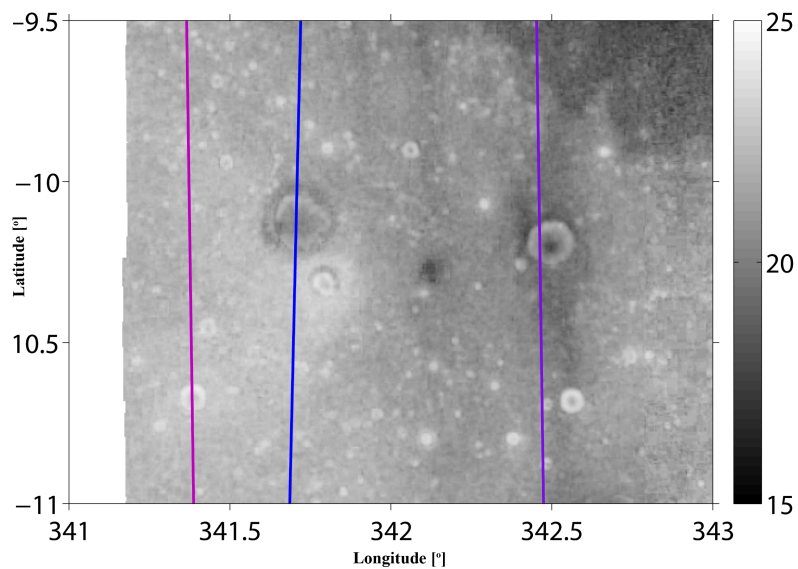
Figure 4.11 displays the iron abundance maps generated for a subsection of the SIR-2 orbits 1093, 1927 and 1928 crossing Bonpland D and their corresponding M<sup>3</sup> and Clementine data. Our aim is to highlight small scale variations and compare the iron abundance estimation maps derived for SIR-2 and M<sup>3</sup> orbits utilizing 2- $\mu\text{m}$  absorption band parameters with Clementine iron abundance maps based on the Lucey et al. (1998a) algorithm. Figure 4.11(a) shows the iron abundance estimation derived from SIR-2 data (using equation 4.3) as a line plotted over the iron abundance map from M<sup>3</sup> data. In equation 4.3, we excluded the term representing the iron contained in ilmenite. The FeO wt% estimate ranges between 10 to 20 wt% for the SIR-2 data with an average of 17 wt%. The average FeO wt% within Bonpland D is 18 wt% with a variation within the crater of 2.5 wt%. This variation is within the range of the standard deviation computed for the lunar returned samples (section 4.9). This result is important because it shows that our algorithm can successfully decouple spectral alterations due to space weathering and absorption features linked directly to FeO wt% content.

The average FeO wt% corresponding to SIR-2 footprints derived from M<sup>3</sup> data is 20 wt%. The FeO wt% range varies between 15 and 25 on the M<sup>3</sup> iron abundance map. This map was derived by applying equation 4.4 to the M<sup>3</sup> data from Table ?? corresponding to SIR-2 orbits 1093, 1927 and 1928. By comparing the iron abundance map of SIR-2 and M<sup>3</sup> in Figure 4.11(a) we can conclude that the M<sup>3</sup> data predicts 2-3 wt% higher FeO than the SIR-2 orbital data. However, both data-sets show similar trends and appear comparable. The differences in iron abundance estimates derived from SIR-2 and M<sup>3</sup> using the same calibration method needs to be investigated in more detail. Our next step will be to include topographic corrections to both data-sets. The SIR-2 data-sets are converted to standard viewing geometry while the M<sup>3</sup> data-set is not corrected photometrically. This may represent one of the reason for the mismatch between the SIR-2 and M<sup>3</sup> derived iron abundance maps. Figure 4.11(a) shows an increase of 2-4 wt% of FeO for the illuminated part of the craters in the M<sup>3</sup> derived iron abundance map. This artifact also needs to be taken into account.

Figure 4.11(b) shows a Clementine derived iron abundance map using the Lucey et al. (1998a) algorithm. The calibrated Clementine images were obtained from the Planetary



(a) SIR-2 orbits 1093, 1027 and 1928 and corresponding  $M^3$  orbits from Table 4.1. The average FeO wt% within Bonpland D crater is about 18 wt% using SIR-2 data and about 20 wt% using  $M^3$  data.



(b) Clementine iron abundance map based on Lucey et al. (1998a) algorithm. The average FeO wt% for Bonpland D is about 20wt%.

Figure 4.11: Iron abundance maps for crater Bonpland D and surroundings.

Data System (PDS) node <sup>1</sup>. In Figure 4.11(b) we have scaled the iron abundance map derived from Clementine data to match the iron abundance map derived using M<sup>3</sup> data. The average FeO wt% within the Bonpland D crater is around 20 wt%. The “white part” in Figure 4.11(b) represents an area with data missing from at least one of the filters at 750 or 950 nm. A comparison between SIR-2, M<sup>3</sup>, and Clementine data shows the variations observed to be similar; however, SIR-2 data indicate an approximately 2 wt% lower FeO in Bonpland D than that derived using M<sup>3</sup> and Clementine data. The average iron abundance in Bonpland D is in good agreement between M<sup>3</sup> and Clementine iron abundance maps. However, M<sup>3</sup> predicts 3-5 wt% higher FeO at the crater walls than the crater floor. In Clementine’s iron abundance map Bonpland D’s surrounding area is in the range 23-25 wt%. Most of the small craters appears artificially enriched in iron since the Lucey et al. (1998a) algorithm is sensitive to local slopes that play a major role in the variation of reflectance at 750 nm (Le Mouélic et al. 2002). These artifacts are minimized in abundance maps derived from in SIR-2 and M<sup>3</sup> data.

Our comparative analysis shows that the FeO content estimated using the 2- $\mu$ m absorption band parameters shares the same trend as the FeO wt% map derived using the band ratio method from Clementine data and thus it can be employed to generate global FeO wt% maps of the lunar surface.

---

<sup>1</sup><http://www.mapaplanet.org/>



# 5 Application of the iron mapping algorithm

We selected a total of four locations (three from nearside and one from farside) and applied our iron abundance estimation method proposed in Chapter 4. We compared the results derived using the method based on the 2- $\mu\text{m}$  absorption parameters with the the FeO wt% abundance maps derived using the Lucey et al. (1998a) algorithm. We have employed M<sup>3</sup> data recorded at the same UTC for a comparative study. The SIR-2 and M<sup>3</sup> product IDs used to study Tycho, Copernicus and Mare Moscoviense regions are given in Table 5.1 and the FeO abundance maps are discussed in Section 5.1 to Section 5.3. In Section 5.4, we generated a SIR-2 FeO abundance low resolution image covering the longitude range between 5 °E and 40 °W, and the latitude range between 55 °N and 55 °S. The SIR-2, M<sup>3</sup> and Clementine derived FeO maps are compared.

## 5.1 Crater Tycho

Tycho (43.4 °S 11.1 °W) is an impact crater of Copernican age (~100 Ma. old) (Arvidson et al. 1976). It represents a textbook example of a fresh complex crater featuring a conspicuous ray pattern, part of which extends to the limbs of the Moon. The SIR-2 orbit footpaths that sampled Tycho are shown in Figure 5.1, along with their summed

Table 5.1: SIR-2 and M<sup>3</sup> files used for Tycho, Copernicus and Mare Moscoviense regions.

	Product IDs	
	SIR-2	M <sup>3</sup>
Tycho	CH1SIR2_NE2_SC_R01085	M3G20090206T092112_V02_RDN
	CH1SIR2_NE2_SC_R01086	M3G20090206T105850_V02_RDN
	CH1SIR2_NE2_SC_R01087	M3G20090206T124510_V02_RDN
Copernicus	CH1SIR2_NE2_SC_R01096	M3G20090207T065039_V03_RDN
	CH1SIR2_NE2_SC_R01095	M3G20090207T044515_V03_RDN
Mare Moscoviense	CH1SIR2_NE2_SC_R0606	M3G20081229T022350_V03_RDN
	CH1SIR2_NE2_SC_R0610	M3G20081229T101650_V03_RDN
	CH1SIR2_NE2_SC_R0614	M3G20081229T180950_V03_RDN

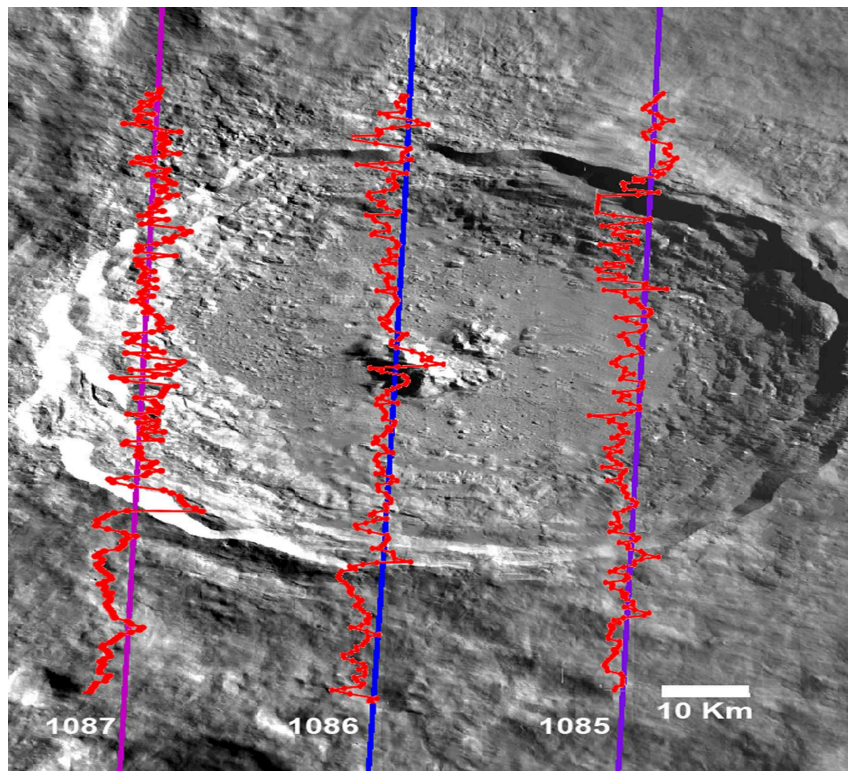


Figure 5.1: The SIR-2 orbits along with their summed reflectance profiles are plotted on the  $M^3$  mosaics of crater Tycho. SIR-2 orbit 1086 is crossing the central peak region of the Tycho crater, and orbit no. 1085 and 1087 are crossing over crater wall.

reflectance profiles. The average phase angle for SIR-2 footprints within Tycho and  $M^3$  data is  $64^\circ$ . SIR-2 Orbit 1086 flew directly over the crater's central peak. A total of 168 sampling points covered the crater interior of which 17 are within the central peak region (Figure 5.3(a)).  $M^3$  product IDs corresponding to SIR-2 orbits 1085, 1086 and 1087 are listed in Table 5.1.

### 5.1.1 2- $\mu\text{m}$ absorption band depth variations

The 2- $\mu\text{m}$  absorption band depth mosaic of three  $M^3$  images recorded at the same UTC as SIR-2 orbits (Table 5.1) along with the SIR-2 tracks positions is shown in Figure 5.2. The band depth range varies between 0 and 0.32 for SIR-2 orbits 1087 and 1086 and between 0 and 0.06 for SIR-2 orbit 1086. The band depth range for  $M^3$  mosaics corresponding to the SIR-2 orbits 1085, 1086 and 1087 ranges between 0 and 0.2 (Figure 5.2). The band depth values at the eastern crater wall and floor are as high as at the central peak in-contrast to the low (0-0.06) band depth range of SIR-2 orbit 1085. We have excluded pixels with band depth smaller than 0.01 in deriving FeO abundance estimations based on the 2- $\mu\text{m}$  absorption band parameters.

The geographic shifts of the SIR-2 tracks with respect to the  $M^3$  data are calculated by comparing the scaled radiance profiles at a common wavelength channel as explained in Section 3.3.3. Figure 5.2 displays the SIR-2 absolute coordinates (solid lines) along

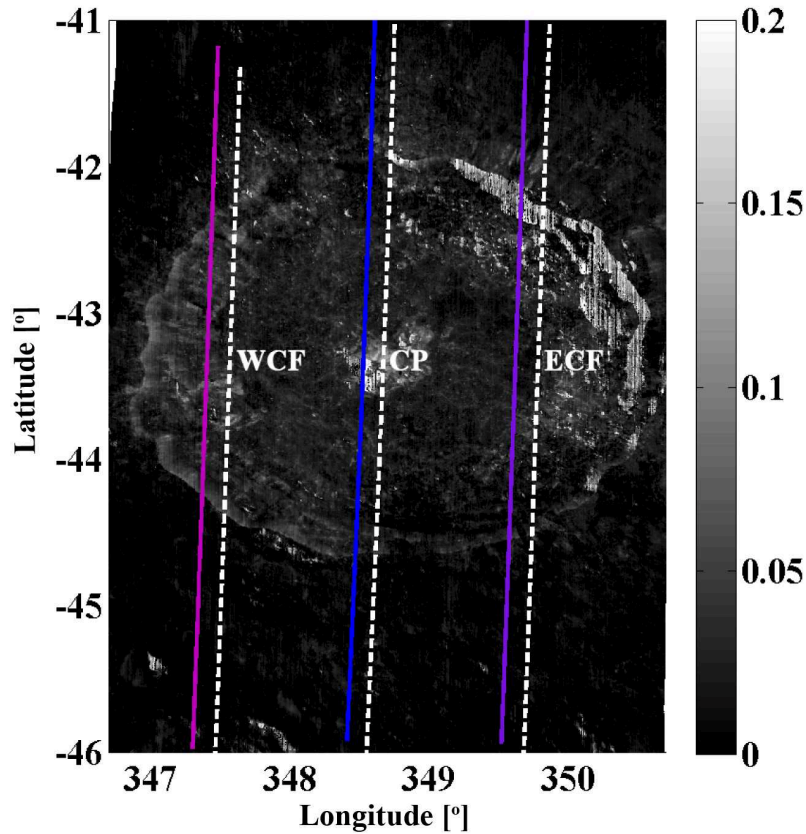
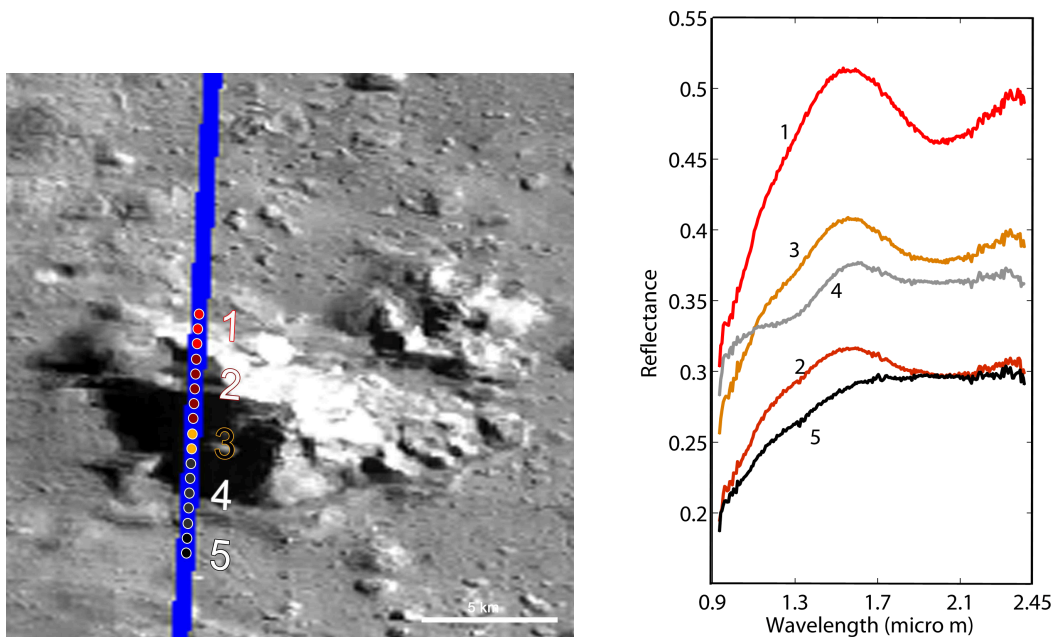


Figure 5.2: 2- $\mu\text{m}$  absorption band depth for  $M^3$  orbits from Tycho region with SIR-2 orbit's positions, absolute coordinates by solid lines and shifted coordinates by dashed lines.

with the shifted coordinates (dashed lines) plotted on the band II  $M^3$  image. The longitudinal shift computed for the SIR-2 orbits 1085, 1087 is  $0.16^\circ E$ , and for orbit 1086 is  $0.14^\circ E$ . The latitudinal shift computed for the SIR-2 orbits 1085, 1086 and 1087 are  $0.07^\circ S$ ,  $0.09^\circ S$ , and  $0.11^\circ S$  respectively.

### 5.1.2 SIR-2 and $M^3$ spectra from central peak region of Tycho

The SIR-2 footprints have been divided into 5 representative groups of spectra based on their spectral shape as shown in Figure 5.3(b) (Bhatt et al. 2011). The representative spectra are the average spectrum of SIR-2 sampling points falling within that group. We observe a systematic change in spectral signature as we move downward from spectrum number 1 to spectrum number 17 (Figure 5.3(a)). Groups 1 and 2 show a high-Ca pyroxene absorption band with the band center between 2.00 and 2.07  $\mu\text{m}$ . This finding is consistent with previous published results (Pieters 1982, Hawke et al. 1986, Ohtake et al. 2009b). In groups 2 and 3, the 2- $\mu\text{m}$  absorption feature is broader and shallower than that of group 1 and also the absolute reflectance is weaker than group 1. The higher absorption band depth for group 1 spectra indicates exposure of fresh materials in the area corresponding to the group 1 footprints. Groups 2 and 3 are possibly a mixture of high



(a) SIR-2 footprints plotted on a  $M^3$  image of Tycho central peak. (b) Representative SIR-2 spectra from the central peak region. Grouping is based on spectral variations of 17 sampling points. The group colors correspond to the SIR-2 footprint colors in Figure 5.3(a).

Figure 5.3: SIR-2 orbit 1086 sampled the central peak of Tycho and representative SIR-2 spectra from this region.

and low-Ca pyroxenes. A prominent absorption feature around  $1.25 \mu\text{m}$  is observed in the spectra belonging to group 4 which indicates the probable presence of iron bearing crystalline plagioclase. This group also shows a very broad and shallow  $2\text{-}\mu\text{m}$  absorption band which could be due to low-Ca pyroxene. Featureless spectra of group 5 represent mature soil materials. This spectral analysis hints towards the probable anorthositic and noritic compositions for the Tycho region. Detection of crystalline plagioclase in the central peak also supports the LMO hypothesis; nevertheless, we have not detected the pure anorthosite signature described by Ohtake et al. (2009a).

Figure 5.4 shows a comparison between the absolute and continuum-removed spectra of SIR-2 and  $M^3$ . These spectra are extracted from the Central Peak (CP), Eastern Crater Floor (ECF), and Western Crater Floor (WCF) regions of Tycho between latitude  $43.3^\circ\text{S}$  and  $43.5^\circ\text{S}$  (Figure 5.2). Although the absolute scale differs, the SIR-2 and  $M^3$  reflectance spectra show comparable spectral shapes. The spectra from CP and WCF have a broad  $2\text{-}\mu\text{m}$  absorption band confirming the presence of pyroxene in crater Tycho; however, the spectra from ECF are featureless probably due to shadowing effects.

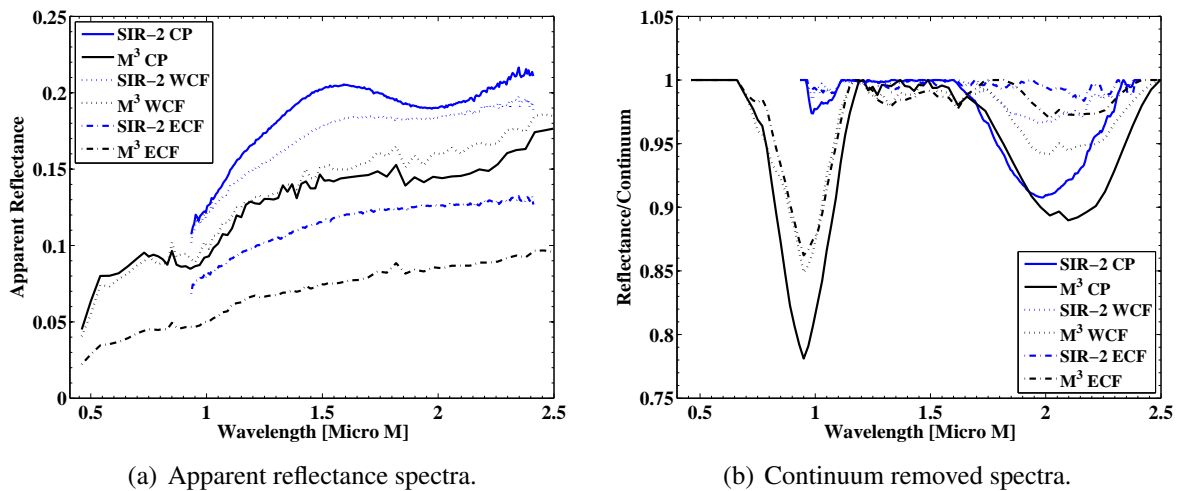


Figure 5.4: A comparison of SIR-2 and  $M^3$  spectra extracted from the area marked as ECF, WCF and CP in Figure 5.2.

### 5.1.3 The FeO abundance map of crater Tycho

Figure 5.5 shows the FeO abundance maps derived from the SIR-2,  $M^3$  and Clementine data obtained from crater Tycho. The FeO abundance maps for SIR-2 and  $M^3$  are derived using Equations 4.1 and 4.4 and shown in Figure 5.5(a). The SIR-2 FeO wt% map is plotted over the  $M^3$  FeO wt% map. FeO wt% could not be computed for the area marked 'x' in SIR-2 data because the band depth values were smaller than 0.01 and thus excluded according to our selection criteria. The average FeO wt% derived from the SIR-2 orbits crossing the Tycho crater is 6 wt% and the FeO wt% range varies between 2 and 10 wt%. The iron map produced using SIR-2 orbits appears homogeneous around the crater rim, the crater wall (CW), the crater floor (CF), and the central peak (CP). However, the same method when applied to the  $M^3$  data, shows 14 wt% FeO for an area of the central peak (Figure 5.5(a)).  $M^3$  FeO abundance map predicts high FeO (14 wt%) for part of the ESW, while SIR-2 orbit 1085 crossing ECW does not show a similar increase in FeO wt%. Topographic effects could be one of the reasons for the high FeO prediction in part of the  $M^3$  image and not an actual reading.  $M^3$  FeO abundance estimation ranges between 6 and 8 wt% and appears homogeneous in Figure 5.5(a) except in parts of CP and ECW. The discrepancies between the SIR-2 orbit 1085 and the corresponding  $M^3$  product ID can be addressed and studied in detail when a fully calibrated data-set becomes available. Figure 5.5(b) shows a Clementine derived FeO abundance map with the same area as that shown in Figure 5.5(a) to support comparing our results with the Lucey et al. (1998a) method. The average FeO wt% for the Tycho region is estimated to be in the range 7-8 wt% using Lucey et al. (1998a) algorithm, whereas the same region was mapped in the range 6-7 wt% by Le Mouélic et al. (2002). In Figure 5.5(b) the northern crater rim is shown to be richer in FeO than the southern crater rim. This suggests a clear dependency on the topography. This effect is minimized in Figure 5.5(a) for SIR-2 and  $M^3$  FeO abundance estimations.

Tycho's central peak composition is thought to range between gabbroic and gabbro-noritic (Tompkins and Pieters 1999). This petrology appears to include the crater

floor and walls suggesting that the FeO wt% content does not vary within the crater diameter. Our results from Figure 5.5(a) confirm these previous findings by showing no major variations in the FeO abundance derived from SIR-2 orbit 1087 and 1086 data and their corresponding M<sup>3</sup> FeO abundance map.

## 5.2 Crater Copernicus

The crater Copernicus is located within a highly complex geological region with pre-Imbrium ejecta overlain by thin mare basalts, an extended impact melt sheet, olivine rich central peak and anorthositic ejecta (Pieters 1982, Sunshine and Tompkins 2001). Copernicus central peak is identified as olivine rich from previous studies (e.g., Pieters 1982, Lucey et al. 1991, Mouélic and Langevin 2001, Matsunaga et al. 2008, Bugiolacchi et al. 2011). Although it is classified as a highland crater, impact melts and localized abundance of iron-bearing minerals are detected inside crater and its surroundings (Pinet et al. 1993, Pieters et al. 1994).

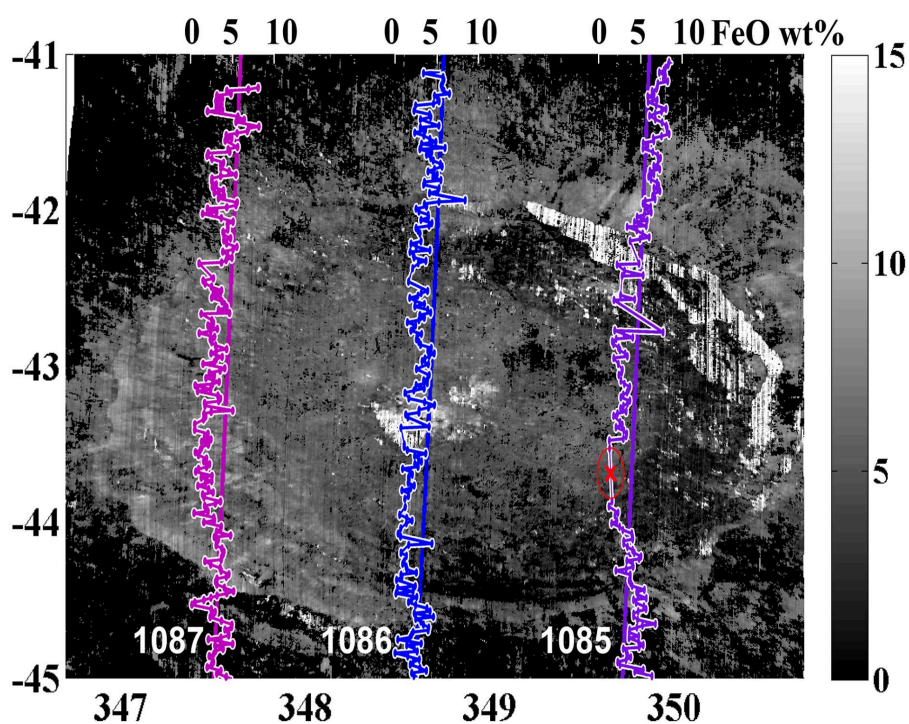
Copernicus crater was sampled by SIR-2 orbits 1095 and 1096 with orbit 1096 crossing the crater's central peak. The M<sup>3</sup> orbits corresponding to SIR-2 orbits are given in Table 5.1.

### 5.2.1 SIR-2 and M<sup>3</sup> spectra from central peak region of Copernicus

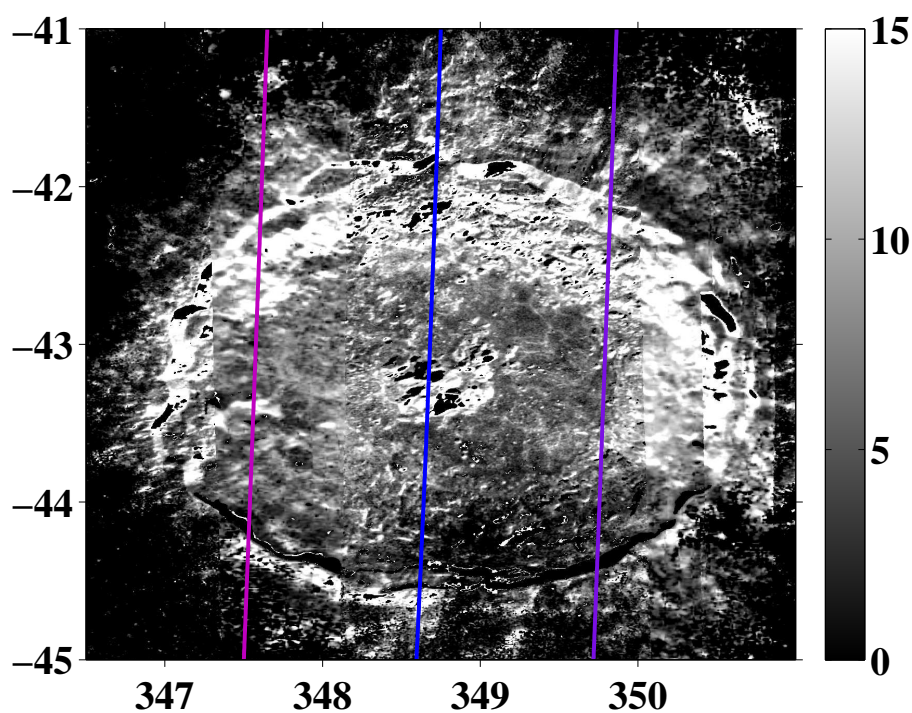
A total of six spectral groups have been identified by Bugiolacchi et al. (2011) utilizing the SIR-2 data for spectral analysis of the crater Copernicus. Figure 5.7 shows the SIR-2 and M<sup>3</sup> spectra normalized at 1.5  $\mu\text{m}$  and extracted from the locations marked in M<sup>3</sup> image in Figure 5.7. The spectrum from one of the central peaks of Copernicus is shown in light green color in Figure 5.7. We observed the 2- $\mu\text{m}$  absorption band in the M<sup>3</sup> spectrum from the central peak region, however SIR-2 shows very weak/negligible 2- $\mu\text{m}$  band from the same location. The SIR-2 spectra from the central peak region are shape-wise similar to the spectra collected from the northern rim of the crater, but are distinguishable based on absolute reflectance level. The spectra from central peak are brighter than the northern crater rim. The southern rim is characterised by a deep 2- $\mu\text{m}$  absorption feature and the band center position suggest that this area is clinopyroxene rich. In contrast, the northern rim is characterised by flat and a very weak 2- $\mu\text{m}$  absorption band. The spectra from northern rim are dark probably due to presence of opaque materials. The difference in mineralogy between the northern and southern part of the rim may be related to the topography effects which should be taken into account. The SIR-2 representative spectra from the Copernicus show a downward trend around 1- $\mu\text{m}$  region suggesting the presence of olivine as suggested by several previous studies.

### 5.2.2 Band depth variation comparison between SIR-2 orbit 1095 and corresponding M<sup>3</sup> orbit

Figure 5.8(a) is a 2- $\mu\text{m}$  absorption band depth M<sup>3</sup> image of the Copernicus region. The areas which possess deep 2- $\mu\text{m}$  absorption bands, due to presence of pyroxene appear as shades of yellow to red. Several small craters from the north and south side of the



(a) SIR-2 orbits 1085, 1086, 1087 and corresponding  $M^3$  orbits from Table 5.1. The FeO abundance map is derived from Equation 4.1 for SIR-2 orbits and Equation 4.4 for  $M^3$  data.



(b) Clementine FeO abundance map with SIR-2 orbits position. The FeO abundance is derived using the Lucey et al. (1998a) method.

Figure 5.5: The FeO abundance maps for Tycho. The X-axis is longitude and Y-axis is latitude. The color bar is the range of FeO wt% of the  $M^3$  and the Clementine FeO abundance maps

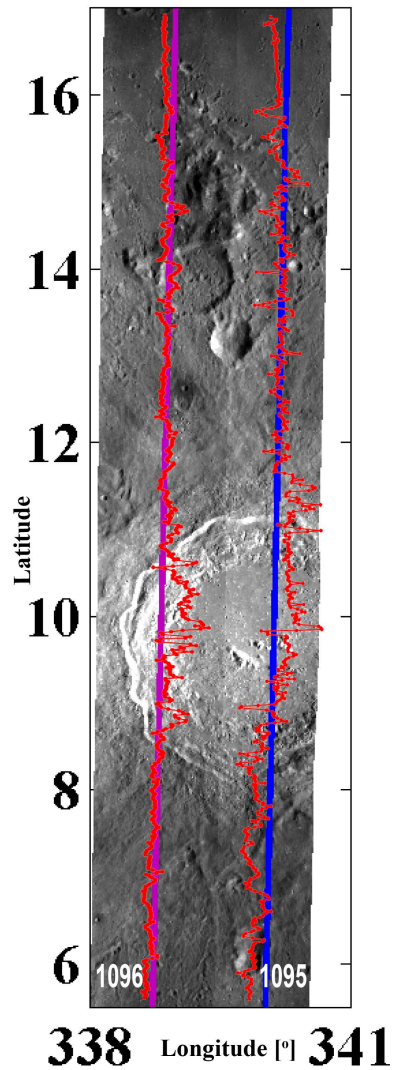


Figure 5.6: Summed reflectance of SIR-2 orbits 1095 and 1096 of the Copernicus and surroundings plotted on the  $M^3$  mosaic prepared from  $M^3$  orbits listed in Table 5.1. The SIR-2 orbit 1095 crossed the central peak region of the Copernicus. The SIR-2 tracks are plotted based on the given geographic coordinates.



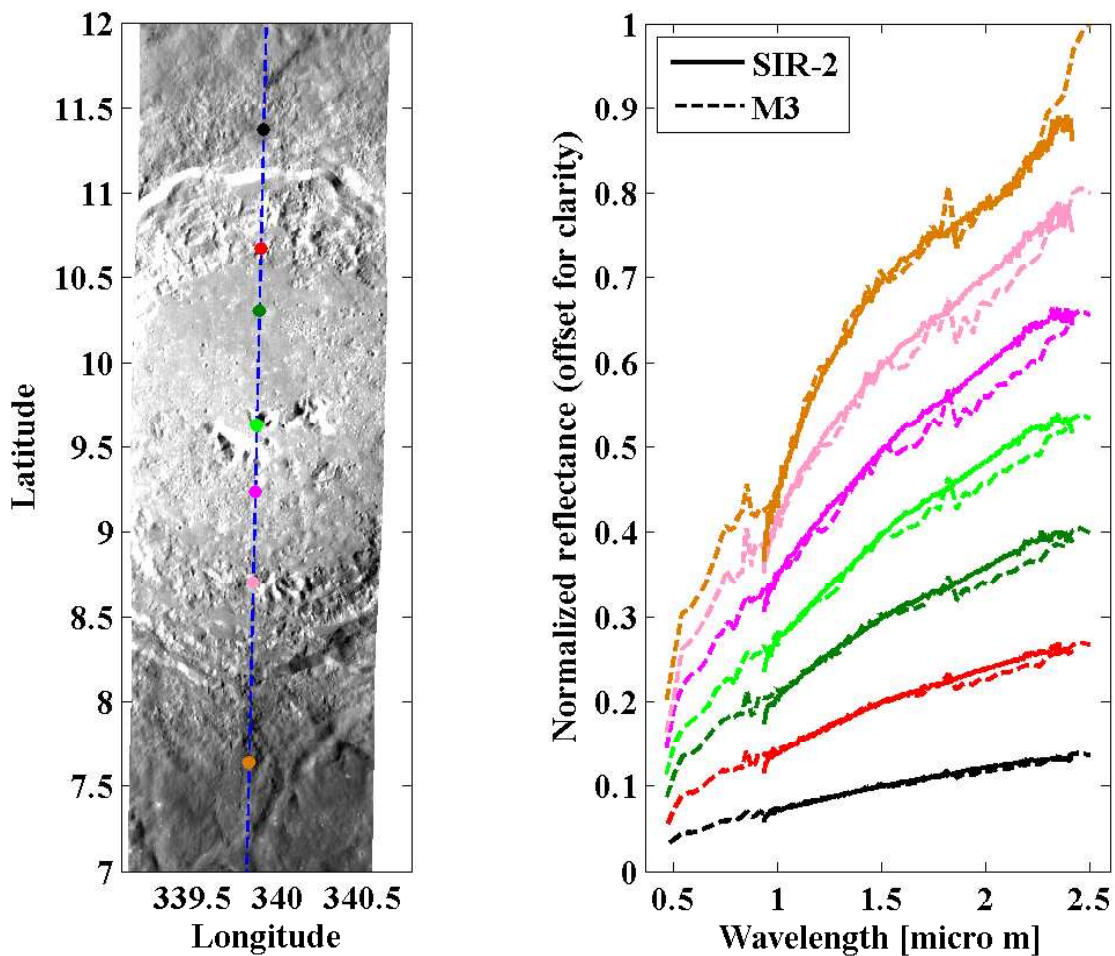


Figure 5.7: Left panel is the  $M^3$  orbit corresponding to SIR-2 orbit 1095. The SIR-2 footprints are shown from specific geographical region. Right panel shows the normalized reflectance spectra of SIR-2 and  $M^3$  extracted from the regions marked in the left panel and color coded for comparing spectral signatures.

crater Copernicus and the walls and rim of Copernicus have generally band depth higher than 0.1 consistent with pyroxene absorption features. The central part of the Copernicus appears in shades of blue in Figure 5.8(a) with band depths lower than 0.04. This low value of 2- $\mu\text{m}$  absorption band depth suggests that the central peaks have very weak 2- $\mu\text{m}$  absorption bands consistent with the olivine known to be present. The variation in band depth observed between northern and southern crater rim may be due to the topography effects for which the  $M^3$  data have not been corrected. The SIR-2 track positions based on radiance profile comparison are shown as dashed lines in Figure 5.8(a) along with the absolute coordinates.

In order to understand the central peak characteristics, we have compared the  $M^3$  band I and band II depths extracted from the pixels corresponding to the SIR-2 tracks and have plotted in Figure 5.8(b). We observed from the scatter plot in Figure 5.8(b) that most of the sample points lie along an elongated trend. Some footprints show a second, less elongated trend extending from the lower part of the main trend in the direction of olivine

with 3 times higher band I depth than the band II. These sampling points belong to the central peak region. Most of the footprints exhibit both the band I and band II band depths which correspond to the presence of pyroxene outside of the central peak and crater wall.

In Figure 5.8(c) we compared the SIR-2 band II depth versus the M<sup>3</sup> band II depth. We found that both the instrument's response are comparable however, SIR-2 band depth range is about half of the M<sup>3</sup> range.

### 5.2.3 FeO map of crater Copernicus

Our FeO wt% abundance estimation algorithm is based on detecting pyroxene absorption bands in the band II region and does not account for iron contained in minerals with prominent absorption bands only in the band I region. Therefore, our method may show low accuracy for olivine rich areas. We selected Copernicus crater to check for the discrepancies present between FeO abundance estimation maps derived for SIR-2 and M<sup>3</sup> orbits utilizing 2- $\mu$ m absorption band parameters with Clementine FeO abundance map based on Lucey et al. (1998a) and Lucey et al. (2000) algorithms. We compared our results with the Lucey et al. (1998a) algorithm first and found a difference of more than 10 wt%, mainly for the areas outside the crater. We applied a modified algorithm from Lucey et al. (2000) instead and found that although both the algorithms (Lucey et al. (1998a) and Lucey et al. (2000)) show more than 90% correlation with the returned samples, the overall result significantly differ. Figure 5.9 presents a comparison between the methods based on band I and band II parameters. The SIR-2 FeO abundance estimations are plotted as a line over the FeO abundance estimation map of the M<sup>3</sup>. Our method is comparable to the Lucey et al. (2000) algorithm. However, several areas from northern region are 2-4 wt% higher in FeO according to our method in comparison to the Lucey et al. (2000) algorithm. The central peak is estimated in the range 10-12 wt%, but the same area is estimated within 4-8 wt% using the Lucey et al. (2000) algorithm. The SIR-2 orbit 1095 predicts 2-4 wt% higher FeO than the M<sup>3</sup> and Clementine derived FeO abundance map and need to be inspected carefully. We observed that all the three datasets give the average FeO wt% for Copernicus crater in the same range; however, overall FeO wt% range varies significantly. A ~10 km diameter crater in north side of the Copernicus shows 4 wt% higher FeO in sub-figure 'A' in comparison to sub-figure 'C' of Figure 5.9. Our analysis shows that although the overall FeO variation range is comparable but the absolute values do not match.

## 5.3 Mare Moscoviense

SIR-2 orbits 606, 610 and 614 sampled the Moscoviense basin. A detailed spectral analysis of the Moscoviense basin using the SIR-2 and corresponding HySI, and M<sup>3</sup> data is described in Chapter 3 (Section 3.3) along with the Clementine derived FeO abundance map of the Mare Moscoviense and surroundings. In this section we will discuss the FeO abundance maps derived using the SIR-2 and M<sup>3</sup> data.

### 5.3.1 FeO maps of Mare Moscoviense

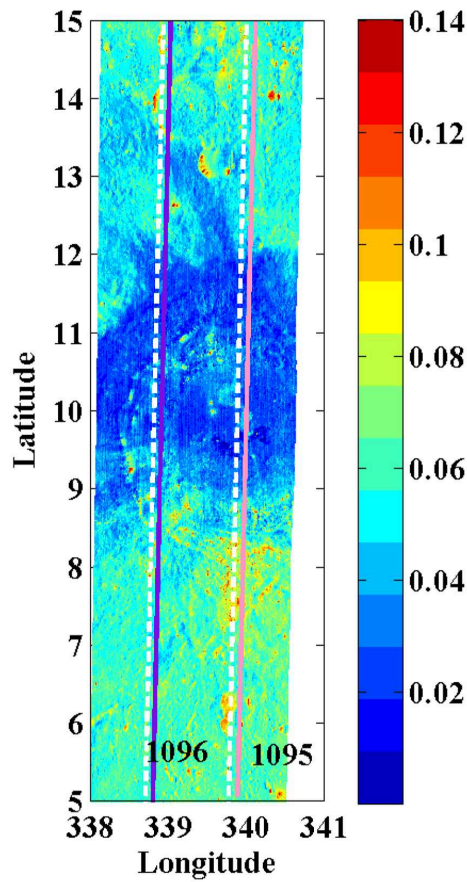
A total of four major compositional units have been identified from the Mare Moscoviense region (Kramer et al. 2008, Gillis 1998) and at least three different volcanic eruptive events observed. The different volcanic units show variations in their FeO and TiO<sub>2</sub> wt%. A wide variation in TiO<sub>2</sub> and FeO contents has been observed in the soils from different flows by Gillis-Davis et al. (2006) using Clementine derived FeO map. Figure 5.10 shows these variations in terms of FeO wt% estimation maps of the SIR-2 and M<sup>3</sup> data. The youngest mare unit (Ehtm) in the basin exhibits the highest FeO wt% between the range 22-25 and mapped by the SIR-2 orbit 606 and corresponding M<sup>3</sup> orbits. The second unit has a surface composition with FeO wt% ranging between 15-20 and overlain by the youngest unit. This unit represents highland contaminated mare soil. The ancient mare unit (Im) is mapped at southern part of the SIR-2 orbits 606 and 610. This unit is more heavily cratered and shows low FeO wt% in the range 10-12. The highland soils from this region shows FeO wt% below 8. The SIR-2 orbit 614 sampled highland soil from the Moscoviense basin showing FeO wt% range between 10-15 with an average value of about 12.

Our results identify the different volcanic events in a comparable way to the Clementine derived FeO abundance map shown in Figure 3.9 (Section 3.3). However, FeO wt% ranges are higher by 2-4 wt% when compared to the Clementine FeO abundance map of the same region. In this study, we have applied Equation 4.1 to derive the SIR-2 FeO abundance maps and have not considered the TiO<sub>2</sub> contribution which might be one of the reasons of observed discrepancies.

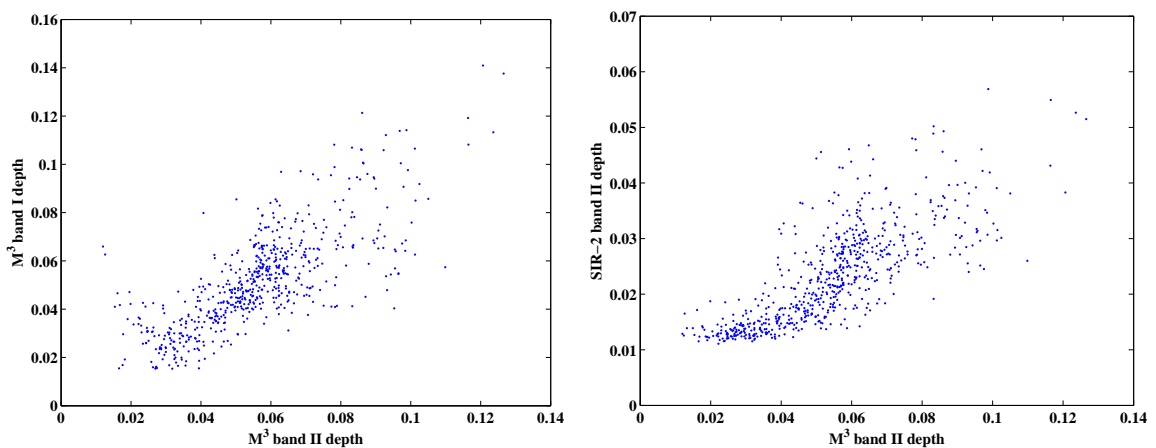
## 5.4 Western nearside FeO abundance map of the Moon

We presented the SIR-2 FeO abundance maps as a line plot over the M<sup>3</sup> images in previous sections because the Chandrayaan-1 mission unfortunately terminated short of its planned two years, thus preventing the garnering of the SIR-2 data at a high spatial resolution. As shown in previous sections, we have only 3-5 SIR-2 tracks available, from ~100 km surface area on the Moon. We observed that the FeO abundance variations between the SIR-2, M<sup>3</sup>, and Clementine data are difficult to compare because the SIR-2 covers two pixels from the M<sup>3</sup> image and one pixel from the Clementine image. To overcome this difficulty we applied our FeO abundance estimation method to the SIR-2 dataset collected from the western nearside of the Moon (55°N – 55°S, 3°E – 50°W), and generated a coarse resolution FeO abundance map using the SIR-2 data for the first time. We selected a total of 37 SIR-2 tracks in this analysis, and have plotted them on the Clementine image based on the given geographic coordinates as shown in Figure 5.11. We selected the western nearside because this side of the Moon is studied in detail and has been of immense interest since many decades. Western mare regions are interpreted as olivine rich and iron rich based on Clementine data analysis. Recently this area was mapped for more detailed mineralogy investigation using the M<sup>3</sup> data (Staid et al. 2011). Figure 5.11 shows that we have equidistant SIR-2 tracks from the Imbrium basin, extending to the crater Copernicus, the Apollo 12 and 14 landing locations, Mare Nubium, and the crater Tycho in the south. Some of the interesting targets of this region are marked in Figure 5.11.

We downloaded total 22 M<sup>3</sup> orbits measured at the same UTC for a comparative study. We applied the Lucey et al. (2000) FeO abundance estimation algorithm to the Clementine image from the same area and compared the FeO abundance maps generated using the SIR-2, M<sup>3</sup>, and Clementine data in Figure 5.12. The FeO abundance range for the SIR-2 and M<sup>3</sup> maps is between 4 and 24 however, the highest FeO wt% value from the Clementine derived FeO abundance map is about 20 wt%. The colorbar and the latitude and longitude ranges are the same for all the three datasets. We observed that the general trends are comparable in all the three datasets, for example, the basaltic regions are iron rich and the feldspathic highland regions are iron poor. We have marked four areas in Figure 5.12 showing the areas 'A' and 'B' in a good agreement for all the three data sets and the areas marked as 'C' and 'D' show discrepancies. The area 'C' shows the maximum deviations in FeO abundance estimation based on the 2- $\mu$ m absorption band parameters and the Lucey et al. (2000) algorithm. The area 'D' covers the crater Plato and shows 2 wt% increase in FeO for the eastern side of the crater in comparison to the western side in the Clementine derived FeO map. In contrast we observed the similar variations in the FeO abundance for the SIR-2 and M<sup>3</sup> maps in the middle of the crater plato with no such sharp boundary between the east and west side of the crater. The FeO content variation range within the crater Plato is between 15 and 18 in all the three maps. We do not see sharp boundaries between the basaltic region and the highland region in the SIR-2 and M<sup>3</sup> maps as seen in the Clementine FeO map. The western side of the crater Tycho shows 10 to 12 wt% FeO in the case of SIR-2 and M<sup>3</sup> derived maps while the Clementine map shows approximately the same FeO content as within the Tycho. Several individual higher values are visible from the mare region in the SIR-2 and M<sup>3</sup> maps which are absent in the Clementine map.



(a) 2- $\mu\text{m}$  absorption band depth image for  $M^3$  orbits from the Copernicus region with SIR-2 orbit's positions, absolute coordinates by solid lines and shifted coordinates by dashed lines.



(b) Band I (1- $\mu\text{m}$ ) vs. Band II (2- $\mu\text{m}$ ) depth measured for  $M^3$  orbit corresponding to SIR-2 orbit 1095. (c) Band II (2- $\mu\text{m}$ ) depth comparison between SIR-2 orbit 1095 and corresponding  $M^3$  orbit from Table 5.1

Figure 5.8: Band depth variation comparison from Copernicus region.

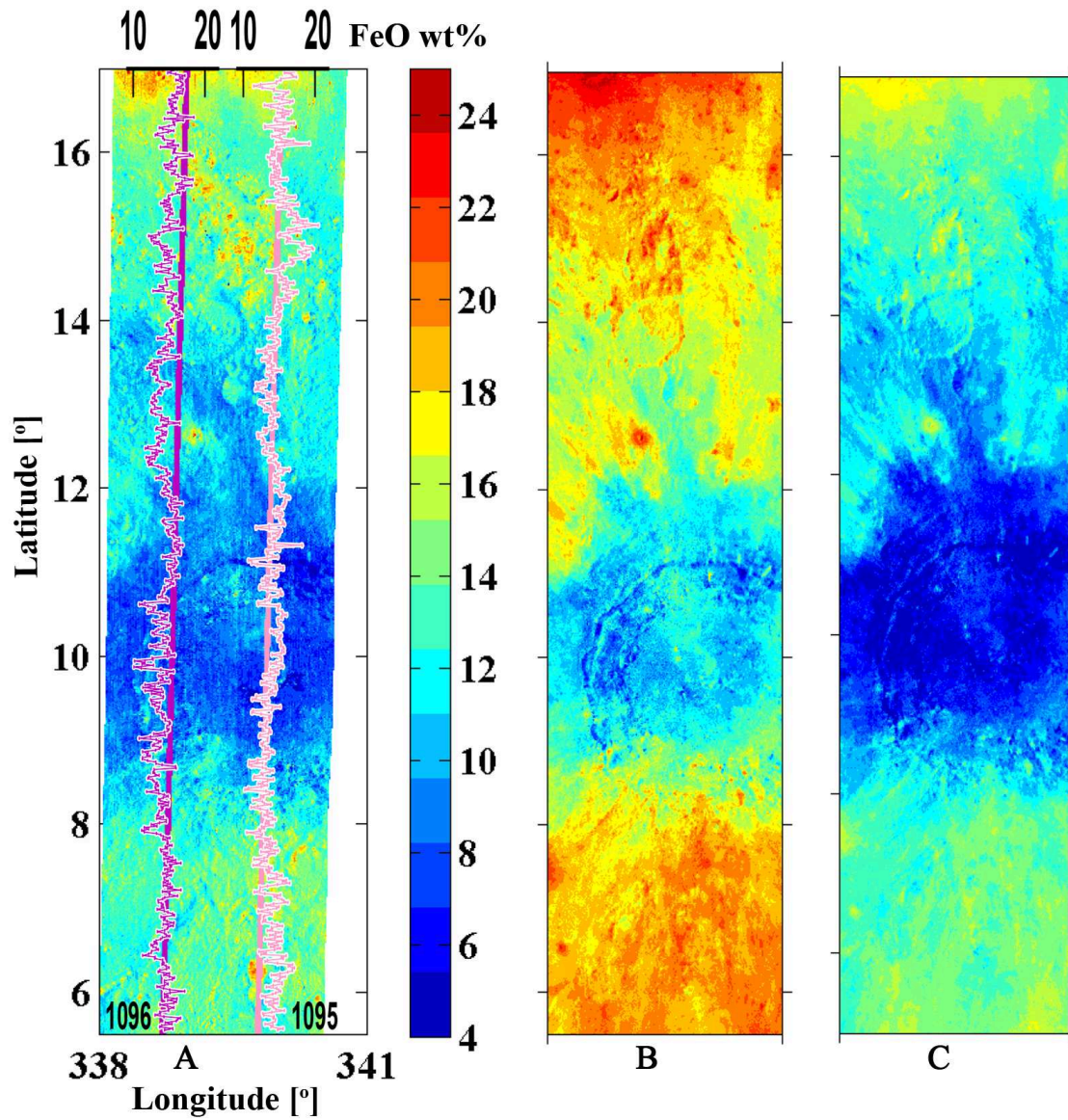


Figure 5.9: The FeO abundance maps for Copernicus. A: The SIR-2 and M<sup>3</sup> maps based on 2- $\mu$ m absorption band parameters. B: Clementine FeO abundance map based on the Lucey et al. (1998a) algorithm. C: The Clementine FeO abundance map based on the Lucey et al. (2000) algorithm.

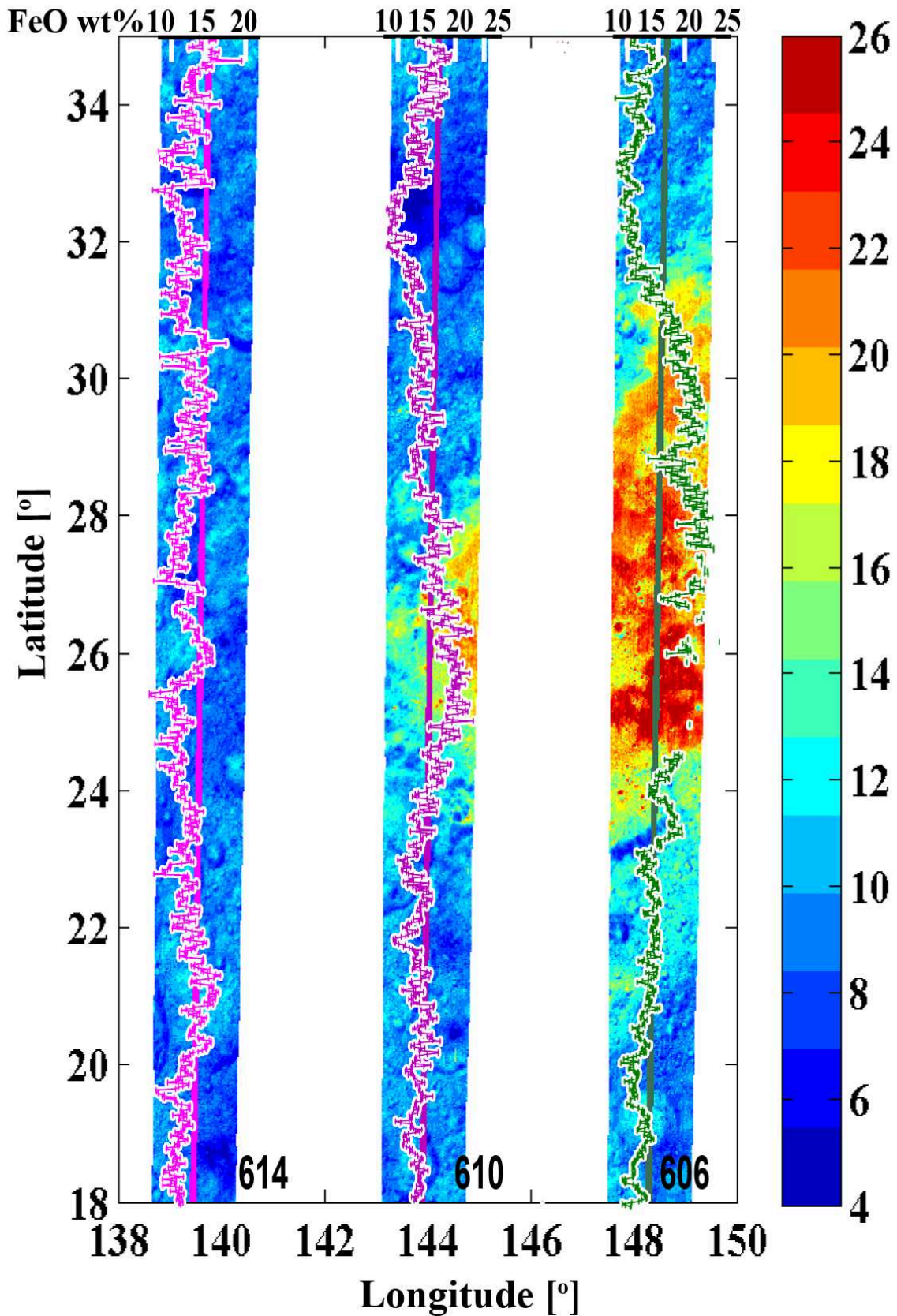


Figure 5.10: FeO abundance maps for the Mare Moscoviense and surroundings, derived from SIR-2 and M<sup>3</sup> orbits from Table 3.1.

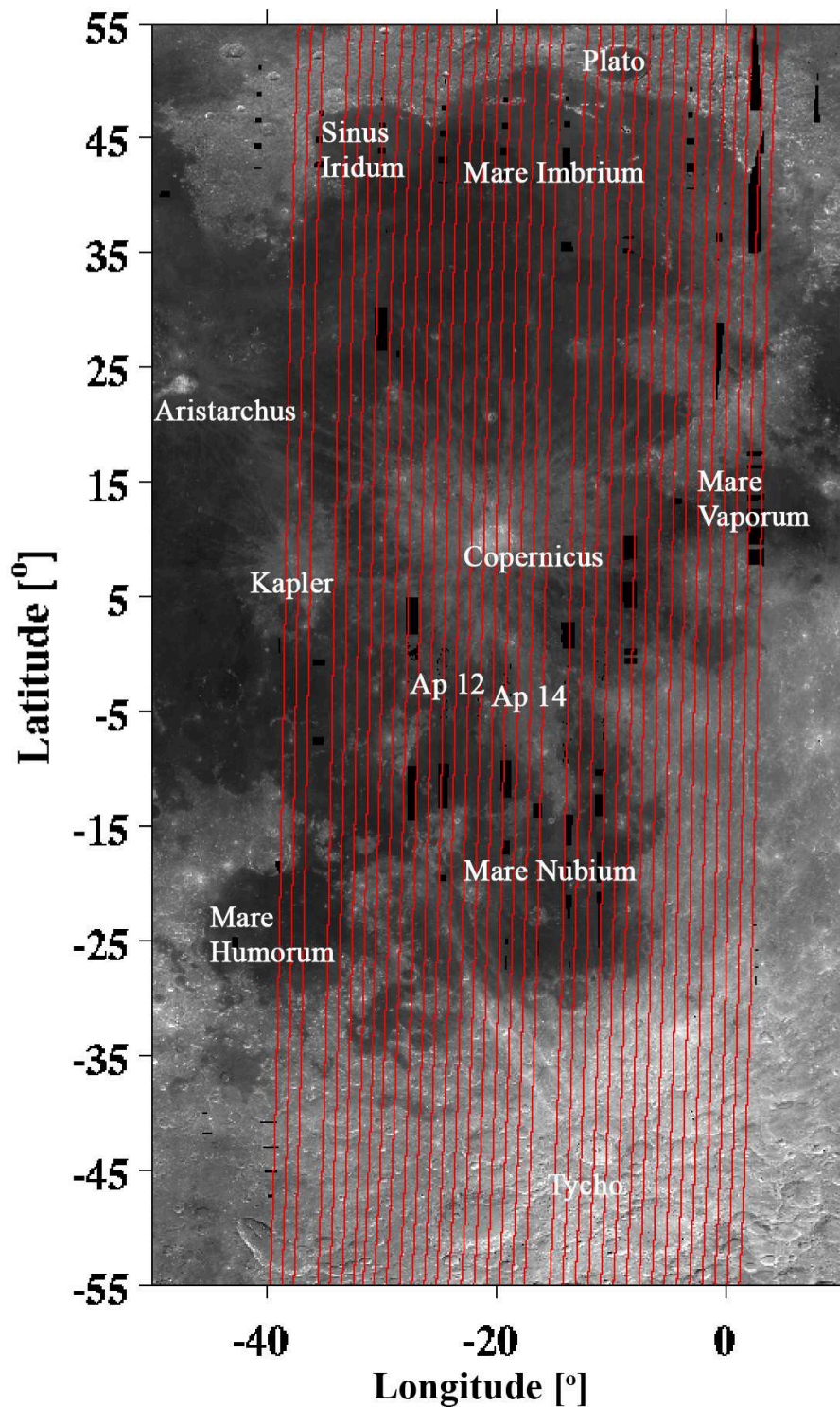


Figure 5.11: The SIR-2 tracks plotted on the Clementine image of the west nearside of the Moon between  $55^{\circ}N - 55^{\circ}S$ ,  $3^{\circ}E - 50^{\circ}W$ .



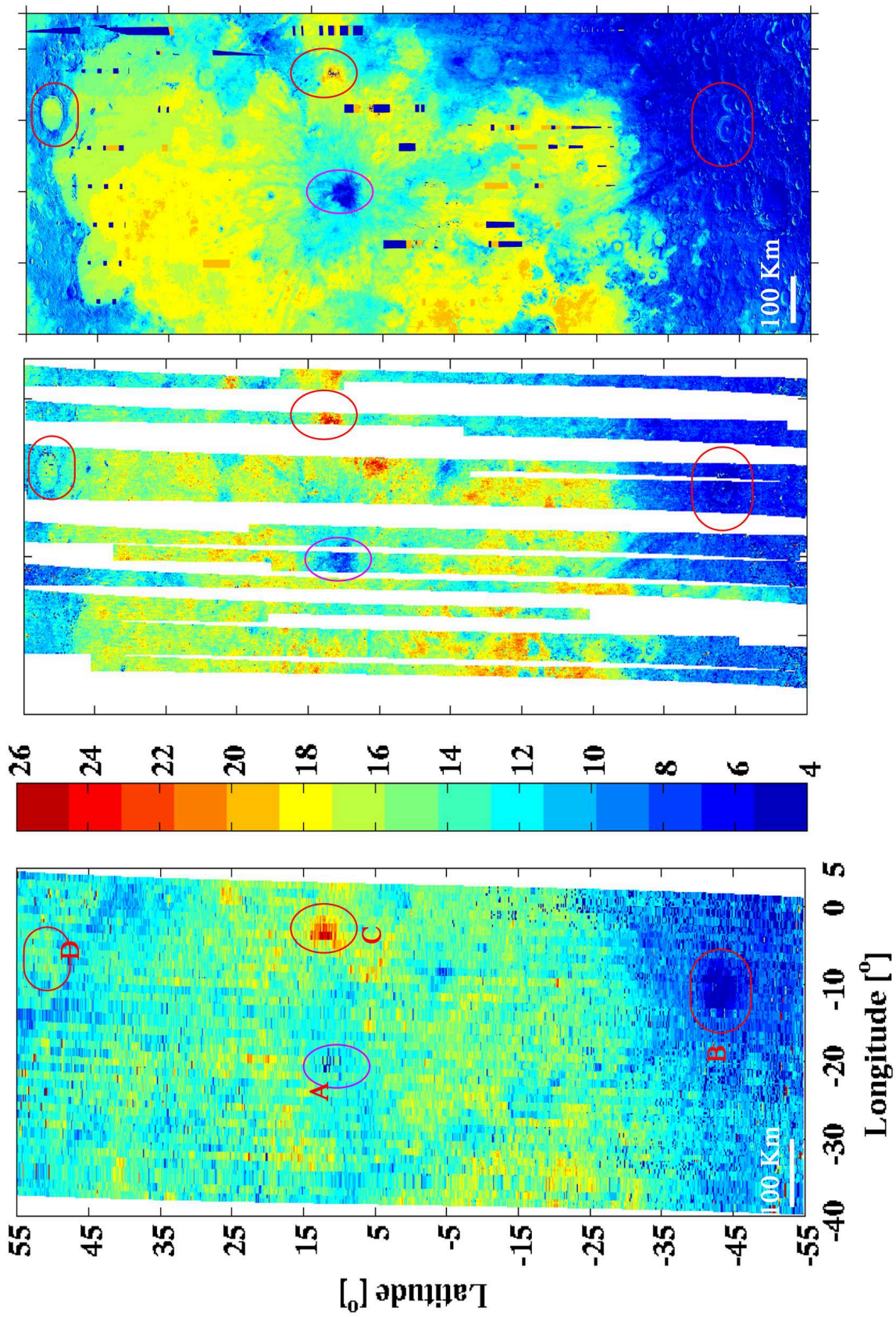


Figure 5.12: The FeO abundance maps of western nearside of the Moon derived for the SIR-2, M<sup>3</sup> using the method based on the 2- $\mu$ m absorption band, and for Clementine data using the Lucey et al. (2000) algorithm.



## 6 Conclusion and future work

In this thesis, data from the three spectrometers SIR-2, HySI, and M<sup>3</sup> on-board of the Chandrayaan-1 is used to develop the lunar iron abundance algorithm and have discussed the SIR-2 data calibration and data reduction methods.

The SIR-2 instrument was spectrally and radiometrically calibrated in the laboratory between 29<sup>th</sup> April and 2<sup>nd</sup> May 2008. After Chandrayaan-1 launch, in-flight calibration was done by comparing remotely measured SIR-2 response with Apollo soil samples reflectance spectra. The SIR-2 data is cross-calibrated by comparing the reflectance spectra from the Apollo 14 landing site detected by the SIR-2 and measured in laboratory from returned samples. In-flight calibration showed a good match between the overall reflectance level and the spectral shape when applied to reflectance spectra from the other Apollo landing sites.

Remote detection of main lunar minerals requires characterization of both band I (0.9-1.2  $\mu\text{m}$ ) and band II (1.9-2.2  $\mu\text{m}$ ) absorption bands in NIR wavelength range. The SIR-2 spectral range does not cover the complete band I and requires to be used in combination with other datasets. We used the HySI images from the Apollo 15 and the Mare Moscoviense regions and combined the SIR-2 and HySI datasets as our first attempt to cover the full wavelength range between 0.4 and 2.4  $\mu\text{m}$ . However, we found that inter-calibration of these two instruments is necessary in order to compare the spectral response at the absolute level. The SIR-2 positions have been adjusted on the HySI images by comparing the radiance profiles of these two instruments at a common wavelength channel. The SIR-2 track adjustment on the HySI image was challenging because the SIR-2 and the HySI had only four common channels and the detector sensitivity was low in this overlapping region for both the instruments. We utilized M<sup>3</sup> data instead for a comparative study after the data was released for public access. A comparison between the geographic coordinates and the radiance profiles extracted from the SIR-2 and M<sup>3</sup> data suggested that the SIR-2 tracks should be located on the M<sup>3</sup> images based on their radiance profile comparison independent of given geographic information. The comparison of SIR-2 and M<sup>3</sup> spectra extracted from the same location showed that the shapes of the spectra are broadly comparable but the absolute levels differ. The SIR-2 data has the advantage of high spectral resolution, and stable response due to active detector temperature control, whereas the M<sup>3</sup> data has the advantage of complete wavelength coverage from visible to NIR range and a 40 km swath. The two datasets are therefore, used in combination for a comparative study.

The remotely measured bidirectional reflectance spectra contain absorption features that are characteristic of the mineral's presence on the uppermost layer of the planetary surface. However, remote measurements in NIR wavelength range are affected by the space weathering effects and significantly weaken the absorption bands. Instead of detect-

ing the presence of individual minerals in a reflectance spectrum, we focused on mapping FeO abundance based on the band II spectral parameters. The method developed in this thesis relies on the successful minimization of maturity effects from the mineralogical absorption features that characterize a remotely measured bidirectional reflectance spectrum. The SIR-2 data was used for the first time to derive the iron content of the Moon's surface. We found that the correlation between the measured and estimated FeO wt% obtained using band II parameters can be improved on and made comparable to results based on the band I parameters by including the spectral contribution of ilmenite for highland-type soils only. We applied the same iron abundance estimation approach to the M<sup>3</sup> data to compare results. We applied the iron abundance estimation algorithm based on the band II parameters to a total of 49 SIR-2 tracks and corresponding M<sup>3</sup> images and compared the results with the Clementine derived iron abundance maps. We observed similar trends in the iron abundance maps derived for SIR-2, M<sup>3</sup>, and Clementine datasets. The major differences are observed in mare regions between the three datasets.

Our first attempt to correlate SIR-2, M<sup>3</sup>, and Clementine iron maps can be deemed successful and further refinements will be carried out when fully calibrated datasets become available. We found that the ilmenite corrections are required only for the highland soils in the case of laboratory data, however we have not applied such corrections to the remotely sensed data. We have to understand the effect of ilmenite on the band II region in order to understand this problem in detail as a next step to refine our method. The iron abundance estimations based on the band II parameters may differ for olivine rich areas since olivine exhibits prominent absorption bands only in the band I region of the VIS-NIR reflectance spectra. We should apply our method to the olivine rich areas from the near and far sides of the Moon to estimate the deviations in the FeO estimation using methods based on the band I and band II parameters. A spectral parameter sensitive to the shape of the spectrum between 1 and 1.5  $\mu\text{m}$  can be computed to detect the presence of iron-bearing minerals in this wavelength region and can be included in our iron abundance estimation algorithm as a correction factor. In our first effort we did not introduce topographic corrections in the SIR-2 and M<sup>3</sup> data-sets. However, we observed 2-3 wt% higher FeO for the illuminated side of the M<sup>3</sup> images which confirms that the topographic corrections are necessary for accurate calculations. Thermal corrections are not applied to the M<sup>3</sup> data but will be included in further studies. Our next task will be to apply the iron abundance estimation algorithm to all SIR-2 orbits from the 100 km spacecraft altitude survey to generate a FeO wt% map. Further, we will integrate the topographic corrected SIR-2 and M<sup>3</sup> datasets to investigate any eventual differences or systematic variations. This method will also allow us to generate maturity maps for these datasets. The laboratory study of the lunar returned samples suggest that the iron abundance is inversely proportional to the aluminum abundance, we can utilize this relationship in future to compute the aluminium abundances using the SIR-2 data.

The main advantage of the SIR-2 instrument are the Moon's surface measurements at an almost constant detector temperature, which enables us to obtain a well calibrated and consistent dataset. The SIR-2 data can be utilized in many different ways such as; for both quantitative and qualitative mineralogical analysis using linear and non-linear mixing models, for phase function derivation employing the measurements at different phase angles, and the effect of phase function on the band parameters such as continuum slope.

# A Preflight calibration: List of the SIR-2 files recorded

## A.1 Dark current measurements

Dark current was measured by covering the Thermal Vacuum (TV) chamber's window for the spectral calibration. Dark measurements were taken at each detector temperature (TEC) and at exposure time periods of 0.5, 1, 5, 10, 20, 50, 100, 120, 151, 200, 252 and 300 ms. Approximately 100 dark spectra were recorded for each TEC and exposure time.

Table A.1: Dark measurement files recorded during preflight calibration of the SIR-2 Flight Spare (FS) model.

Detector Temperature (°C)	Cooling Console Temperature (°C)	File Name
-40.16	-36.18	2008_04_29_15_23_Dark_40_1.001
-45.17	-34.27	2008_04_29_15_30_Dark_45_1.001
-40.15	-33.49	2008_04_29_19_26_Dark_40_2.001
-65.13	-51.95	2008_04_30_10_03_Dark_65_1.001
-50.12	-45.44	2008_05_01_09_37_Dark_50.001
-45.20	-44.28	2008_05_01_09_43_Dark_45.001
-45.12	-43.85	2008_05_02_09_29_Dark_45.001
-50.18	-43.00	2008_05_02_10_06_Dark_50.001

## A.2 Spectral calibration measurements

Table A.2: Spectral calibration measurement files

SN.	Detector Temperature (°C)	Cooling Console Temperature (°C)	Quartz Body Temperature (°C)	Wavelength Step (nm)	File Name	Remarks
1	-40.13	-34.98	-26.25	50	2008_04_29_14_05_Spectral_PEAK_50ms_step50_40.001	950-2400 nm
2	-40.16	-35.44	-26.32	10	2008_04_29_15_04_Spectral_PEAK2_step10_40.001	940-2410 nm
3	-40.12	-35.59	-26.27	5	2008_04_29_14_36_Spectral_PEAK_100ms_step5_40.001/002	950 nm downwards 2400 nm upwards
4	-39.78	-34.96	-26.01	-	2008_04_29_13_25_Spectral_BG_40_lin.001	Monochromator dark
5	-65.15	-52.94	-31.07	10	2008_04_30_14_50_Spectral_PEAK2_step10_65.001/002	940-2410 nm
6	-65.18	-53.38	-30.69	5	2008_04_30_17_35_Spectral_PEAK_step5_65.001	950 nm downwards 2400-2420 nm upwards
7	-65.16	-51.53	-30.73	-	2008_04_30_17_25_BG_Spectral_65_lin.001	Monochromator dark
8	-45.14	-43.11	-27.96	10	2008_05_02_08_52_Spectral_PEAK2_step10_45.001	940-2410 nm
9	-45.15	-44.30	-27.88	50	2008_05_02_09_39_Spectral_PEAK3_step50_45.001	950-2400 nm
10	-45.18	-43.46	-27.89	5	2008_05_02_08_26_Spectral_PEAK_edges_step5_45.001	950 nm downwards 2350 nm upwards
11	-45.14	-44.31	-27.96	-	2008_05_02_09_11_BG_Spectral_45.001	Monochromator dark
12	-50.16	-43.32	-27.93	10	2008_05_02_08_39_Spectral_PEAK2_step10_50.001	940-2410 nm
13	-50.16	-42.00	-27.84	50	2008_05_02_09_47_Spectral_PEAK3_step50_50.001	950-2400 nm
14	-50.10	-43.28	-27.94	5	2008_05_02_08_32_Spectral_PEAK_edges_step5_50.001	950 nm downwards 2350 nm upwards
15	-50.11	-42.94	-27.82	-	2008_05_02_09_5_BG_Spectral_50.004	Monochromator dark

## A.3 Point Spread Function (PSF) measurement files

Table A.3: Point Spread Function measurement files

SN.	Detector Temperature(°C)	Cooling console Temperature (°C)	Quarts Body Temperature (°C)	Exposure Time(ms)	File Name	Pixel	Wavelength Range(nm)	Wavelength Step (nm)
1	-65.18	-53.23	-31.01	200.2	2008_04_30_15_38_Spectral_PSF_step05_65.001	14	1000-1032	0.5
2	-65.15	-52.95	-30.96	100.1	2008_04_30_16_03_Spectral_PSF2_step05_65.001	152	1810-1862	0.5
3	-65.15	-53.07	-30.89	300.3	2008_04_30_16_25_Spectral_PSF3_step05_65.001	226	2220-2274	0.5
4	-65.18	-51.84	-30.85	300.3	2008_04_30_16_45_Spectral_PSF1b_step2_65.001	14	1000-1032	2
				100.1,200.2				
5	-65.18	-52.47	-30.83	100.1	2008_04_30_16_48_Spectral_PSF2b_step2_65.001	152	1810-1862	2
6	-65.18	-53.06	-30.82	300.3	2008_04_30_16_50_Spectral_PSF3b_step2_65.001	226	2220-2274	2
7	-65.09	-53.82	-30.86	50.05	2008_04_30_16_57_Spectral_PSF4b_step2_65.001	82	1415-1447	2
8	-65.15	-51.48	-30.81	50.05	2008_04_30_17_01_Spectral_PSF4_step05_65.001	82	1415-1447	0.5
9	-50.16	-43.44	-27.64	50.05	2008_05_02_10_31_Spectral_PSF_Step2_50.001	14	1000-1032	2
10	-50.12	-41.85	-27.68	50.05	2008_05_02_10_31_Spectral_PSF_Step05_50.001	14	1000-1032	0.5
11	-50.11	-42.64	-27.63	20.02	2008_05_02_10_44_Spectral_PSF_Step2_50.001	152	1810-1862	2
12	-50.15	-43.09	-27.55	20.02	2008_05_02_10_44_Spectral_PSF_Step05_50.001	152	1810-1862	0.5
13	-50.13	-44.40	-27.51	10.01	2008_05_02_11_08_Spectral_PSF_Step2_50.001	82	1415-1447	2
14	-50.14	-42.65	-27.47	10.01	2008_05_02_11_08_Spectral_PSF_Step05_50.001	82	1415-1447	0.5
15	-50.12	-42.21	-27.40	100.17	2008_05_02_11_21_Spectral_PSF_Step2_50.001	226	2220-2274	2
16	-50.15	-43.02	-27.35	100.17	2008_05_02_11_30_Spectral_PSF_Step05_50.001	226	2220-2274	0.5

## A.4 Radiometric calibration measurement files

Table A.4: Radiometric calibration measurement files

SN.	Detector Temperature (°C)	Cooling Console(°C) Temperature (°C)	Exposure Time(ms)	File Name	Remark
1	-40	-36	0.5, 1, 5, 10, 20, 50 100, 120, 151, 200, 252, 300	2008_04_29_15_23_Dark_40_1.001	Dark, Closed chamber
2	-45	-35	0.5, 1, 5, 10, 20, 50 100, 120, 151, 200, 252, 300	2008_04_29_15_30_Dark_45_1.001/002	Dark, Closed chamber
3	-40	-35	120, 151, 200, 252	2008_04_29_17_23_Radio_40.001	Absolute sensitivity, lamps at 12 mm readout frequency standard 1.54 MHz
4	-40	-35	120, 151, 200, 252	2008_04_29_17_31_Radio_40f.001	Absolute sensitivity, lamps at 12 mm readout frequency 1.00 MHz
5	-40	-35	0.5, 1, 5, 10, 20, 50	2008_04_29_17_41_Radio_40lin.001	Linearity w.r.t. int. time, lamps at 12 mm

## A Preflight calibration: List of the SIR-2 files recorded

SN.	Detector	Cooling Console(°C)		Exposure	File Name	Remark
	Temperature (°C)	Temperature (°C)	Time(ms)			
6	-45	-35	120, 151, 200, 252, 300	2008_04_29_17_51_Radio_45.001	readout frequency standard 1.54 MHz Absolute sensitivity, lamps at 12 mm	
7	-45	-35	120, 151, 200, 252, 300	2008_04_29_18_08_Radio_45f.001	readout frequency standard 1.54 MHz Absolute sensitivity lamps at 12 mm	
8	-45	-35	0.5, 1, 5, 10, 20, 50 100, 120, 151, 200, 252, 300	2008_04_29_18_18_Radio_45lin.001	readout frequency 1.00 MHz Linearity w.r.t. int. time lamps at 12 mm	
9	-65	-53	0.5, 1, 5, 10, 20, 50 100, 120, 151, 200, 252, 300	2008_04_30_10_03_Dark_65_1.001	readout frequency standard 1.54 MHz Dark, Closed TV chamber	
10	-65	-55	120, 151, 200, 252, 300	2008_04_30_10_16_Radio_65.001	Absolute sensitivity, lamps at 12 mm	
11	-65	-55	120, 151, 200, 252, 300	2008_04_30_10_26_Radio_65f.001	readout frequency standard 1.54 MHz Absolute sensitivity, lamps at 12 mm	
12	-65	-55	0.5, 1, 5, 10, 20, 50 100, 120, 151, 200, 252, 300	2008_04_30_10_35_Radio_65lin.001	readout frequency 1.00 MHz Linearity w.r.t. int. time, lamps at 12 mm	
13	-65	-55	120, 151, 200, 252, 300	2008_04_30_11_19_Radio_65_Jamp20mm.002	readout frequency standard 1.54 MHz Absolute sensitivity, lamps at 20 mm	
14	-65	-55	120, 151, 200, 252, 300	2008_04_30_12_17_Radio_65_Jamp30mm.001	readout frequency standard 1.54 MHz Absolute sensitivity, lamps at 30 mm	
15	-65	-55	151, 252, 300, 524	2008_04_30_13_37_Radio_65_Jamp40mm.001	readout frequency standard 1.54 MHz Absolute sensitivity, lamps at 40 mm	
16	-50	-45	0.5, 1, 5, 10, 20, 50 100, 120, 151, 200, 252, 300	2008_05_01_09_37_Dark_50.001	readout frequency 1 MHz Dark, Closed TV chamber	
17	-45	-45	0.5, 1, 5, 10, 20, 50 100, 120, 151, 200, 252, 300	2008_05_01_09_43_Dark_45.001	Dark, Closed TV chamber	
18	-45	-45	120, 151, 200, 252, 300	2008_05_01_10_13_Radio_45.001	Absolute sensitivity, lamps at 12 mm	
19	-50	-45	120, 151, 200, 252, 300	2008_05_01_10_22_Radio_50.001	readout frequency standard 1.54 MHz Absolute sensitivity lamps at 12 mm	
20	-50	-45	0.5, 1, 5, 10, 20, 50 100, 120, 151, 200, 252, 300	2008_05_01_10_31_Radio_50lin.001	readout frequency standard 1.54 MHz Linearity w.r.t. int. time, lamps at 12 mm	
21	-45	-45	0.5, 1, 5, 10, 20, 50 100, 120, 151, 200, 252, 300	2008_05_01_10_38_Radio_45lin.001	readout frequency standard 1.54 MHz Linearity w.r.t. int. time, lamps at 12 mm	
22	-45	-45	151, 252, 300, 524	2008_05_01_10_46_Radio_45_Jamp_12mm.001	readout frequency 1 MHz Absolute sensitivity, lamps at 12 mm	
23	-45	-45	120, 151, 200, 252, 300	2008_05_01_11_13_Radio_45f.001	readout frequency 1 MHz Absolute sensitivity, lamps at 12 mm	
24	-50	-45	120, 151, 200, 252, 300	2008_05_01_11_20_Radio_50f.001	readout frequency 1 MHz Absolute sensitivity, lamps at 12 mm	
25	-50	-45	151, 252, 300, 524	2008_05_01_11_30_Radio_50_Jamp_12mm.001	readout frequency 1 MHz Absolute sensitivity, lamps at 12 mm	
26	-50	-45	151, 252, 300, 524	2008_05_01_12_02_Radio_50_Jamp_16mm.001	readout frequency 1 MHz Absolute sensitivity, lamps at 16 mm	



## A.4 Radiometric calibration measurement files

SN.	Detector	Cooling Console( $^{\circ}$ C)		Exposure	File Name	Remark
	Temperature ( $^{\circ}$ C)	Temperature ( $^{\circ}$ C)	Time(ms)			
27	-45	-45	151, 252, 300, 524	2008_05_01_12_30_Radio_45_Jamp_16mm.001	Absolute sensitivity, lamps at 16 mm readout frequency 1 MHz	
28	-45	-45	151, 252, 300, 524	2008_05_01_12_30_Radio_45_Jamp_20mm.001	Absolute sensitivity, lamps at 20 mm readout frequency 1 MHz	
29	-50	-45	151, 252, 300, 524	2008_05_01_13_26_Radio_50_Jamp_20mm.001	Absolute sensitivity, lamps at 20 mm readout frequency 1 MHz	
30	-50	-45	151, 252, 300, 524	2008_05_01_14_08_Radio_50_Jamp_25mm.001	Absolute sensitivity, lamps at 25 mm readout frequency 1 MHz	
31	-45	-45	151, 252, 300, 524	2008_05_01_14_39_Radio_45_Jamp_25mm.001	Absolute sensitivity, lamps at 25 mm readout frequency 1 MHz	
32	-45	-45	151, 252, 300, 524	2008_05_01_15_10_Radio_45_Jamp_30mm.001	Absolute sensitivity, lamps at 30 mm readout frequency 1 MHz	
33	-50	-45	151, 252, 300, 524	2008_05_01_15_41_Radio_50_Jamp_30mm.001	Absolute sensitivity, lamps at 30 mm readout frequency 1 MHz	
34	-50	-45	151, 252, 300, 524	2008_05_01_16_11_Radio_50_Jamp_40mm.001	Absolute sensitivity, lamps at 40 mm readout frequency 1 MHz	
35	-45	-45	151, 252, 300, 524	2008_05_01_16_38_Radio_45_Jamp_40mm.001	Absolute sensitivity, lamps at 40 mm readout frequency 1 MHz	
36	-45	-45	151, 252, 300, 524	2008_05_01_17_06_Radio_45_Jamp_45mm.001	Absolute sensitivity, lamps at 45 mm readout frequency 1 MHz	
37	-50	-45	151, 252, 300, 524	2008_05_01_17_22_Radio_50_Jamp_45mm.001	Absolute sensitivity, lamps at 45 mm readout frequency 1 MHz	
38	-58	-45	0.5, 1, 5, 10, 20, 50	2008_05_02_12_13_Dark_58.001	Darks, Closed chamber	



## B Lunar samples used for iron mapping method

All the reflectance spectra listed in Table B.1 are taken from the Reflectance Experiment Laboratory (RELAB) and have been measured through using a Directional-Hemispherical Visible-NIR (DHC-VNIR) spectrometer. The wavelength for the selected RELAB data ranges from 0.35 to 2.51  $\mu\text{m}$ . FeO wt%,  $I_s/\text{FeO}$ , and  $\text{TiO}_2$  wt% values for selected samples are taken from Morris (1978) and Morris et al. (1983) and a short description of the samples is taken from RELAB.

Table B.1: List of the lunar samples used in iron mapping algorithm.

Sample	Site	RELAB File Name	Description	FeO (wt%)	$I_s/\text{FeO}$	$\text{TiO}_2$ (wt%)
10084	Apollo 11	LS-JBA-006-P1/CLS052	Soil Mare Breccia Bulk	15.8	78	7.5
12042	Apollo 12	LS-JBA-036-P2/CLS476	Soil Mare Bulk	16.2	61	2.7
12070	Apollo 12	LS-JBA-060-P1/CLS531	Soil Mare Bulk	16.4	47	2.8
14003	Apollo 14 LM	LS-JBA-070-P/CLS237	Soil Highland Bulk	10.5	66	1.8
14141	Apollo 14 SC	LS-JBA-076-P1/CLS271	Soil Highland Bulk	10.4	5.7	1.7
14148	Apollo 14 SG	LS-JBA-081-P/CLS391	Soil Highland Bulk	10.6	74	1.7
14149	Apollo 14 SG	LS-JBA-084-M/CLS016	Soil Highland Magnetic	10.0	53	1.6
14163	Apollo 14 LM	LS-JBA-088-P/CLS174	Soil Highland Bulk	10.4	57	1.8
14259	Apollo 14 LM	LS-JBA-091-P4/CLS036	Soil Highland Bulk	10.4	85	1.7
14260	Apollo 14 LM	LS-JBA-092-PX/CLS428	Soil Highland Bulk Mixture	11.1	72	1.9
15081	Apollo 15 S1	LS-JBA-108/CLS294	Soil Highland Boundary	15.3	68	1.6
15081	Apollo 15 S1	LS-JBA-108/CLS295	Soil Highland Boundary	16.8	68	1.6
15101	Apollo 15 S2	LS-JBA-111-P2/CLS232	Soil Highland Boundary Bulk	11.5	70	1.3
15211	Apollo 15 S2	LS-JBA-113/CLS087	Soil Highland Boundary Bulk	11.7	60	1.3
15231	Apollo 15 S2	LS-JBA-116-P2/CLS254	Soil Highland Boundary Bulk	11.5	71	1.3
15471	Apollo 15 S4	LS-JBA-125-P3/CLS467	Soil Mare Bulk	16.6	34	1.2
15271	Apollo 15 S6	LS-JBA-119-P2/CLS260	Soil Highland Bulk	12.1	63	1.5
15501	Apollo 15 S9	LS-JBA-127-P2/CLS408	Soil Mare Bulk	16.9	51	1.8
15531	Apollo 15 S9	LS-JBA-128-P1/CLS286	Soil Mare Bulk	19.2	27	2.0
15301	Apollo 15 S7	LS-JBA-120-P1/CLS279	Soil Highland Bulk	14.1	48	1.2
15601	Apollo 15 S9a	LS-JBA-130-P/CLS086	Soil Mare Bulk	19.8	29	2.0
61221	Apollo 16 S1	LS-JBA-154-P/CLS429	Soil Highland Bulk	4.9	9.2	0.5
61141	Apollo 16 S1	LS-JBA-152-P/CLS357	Soil Highland Bulk	5.4	56	0.6
61161	Apollo 16 S2	LS-JBA-153-P/CLS183	Soil Highland Bulk	5.4	82	0.6
61241	Apollo 16 S2	LS-JBA-155-P2/CLS044	Soil Highland Bulk	5.4	47	0.6
61241	Apollo 16 S2	LS-JBA-155-P3/CLS438	Soil Highland Bulk	5.4	47	0.6
61281	Apollo 16 S2	LS-JBA-156-P/CLS182	Soil Highland Bulk	5.4	69	0.6
64421	Apollo 16 S4	LS-JBA-162-P3/CLS252	Soil Highland Bulk	4.6	83	0.5
64421	Apollo 16 S4	LS-JBA-162-P2/CLS243	Soil Highland Bulk	4.6	83	0.5
64501	Apollo 16 S4	LS-JBA-163-P/CLS029	Soil Highland Bulk	4.6	61	0.5
64801	Apollo 16 4b	LS-JBA-164-P/CLS023	Soil Highland Bulk	5.2	71	0.5

## B Lunar samples used for iron mapping method

Sample	Site	RELAB File Name	Description	FeO (wt%)	$I_s/FeO$	TiO <sub>2</sub> (wt%)
65501	Apollo 16 S5	LS-JBA-166-P/CLS401	Soil Highland Bulk	5.9	38	0.7
68501	Apollo 16 S8	LS-JBA-178/CLS430	Soil Highland Bulk	5.6	85	0.6
68841	Apollo 16 S8	LS-JBA-180-P/CLS392	Soil Highland Bulk	5.5	70	0.6
69921	Apollo 16 S9	LS-JBA-181-P/CLS341	Soil Highland Bulk	5.6	90	0.6
69941	Apollo 16 S9	LS-JBA-182-M/CLS017	Soil Highland Magnetic	5.7	85	0.6
69961	Apollo 16 S9	LS-JBA-183-P/CLS398	Soil Highland Bulk	5.6	92	0.6
60601	Apollo 16 S10	LS-JBA-151-P/CLS393	Soil Highland Bulk	5.6	85	0.6
67461	Apollo 16 S11	LS-JBA-172-P/CLS056	Soil Highland Bulk	4.2	25	0.4
67481	Apollo 16 S11	LS-JBA-173-P2/CLS276	Soil Highland Bulk	4.2	31	0.4
67601	Apollo 16 S11	LS-JBA-174-P/CLS390	Soil Highland Bulk	4.2	45	0.4
67701	Apollo 16 S11	LS-JBA-175-P/CLS031	Soil Highland Bulk	4.2	39	0.4
67711	Apollo 16 S11	LS-JBA-176/CLS304	Soil Highland Nonmagnetic	3.0	2.8	0.3
63321	Apollo 16 S13	LS-JBA-159-P2/CLS043	Soil Highland Bulk	4.8	47	0.5
63341	Apollo 16 S13	LS-JBA-160-PX/CLS419	Soil Highland Bulk Mixture	4.8	54	0.5
63501	Apollo 16 S13	LS-JBA-161-P/CLS399	Soil Highland Bulk	4.8	46	0.5
70181	Apollo 17 LM	LS-JBA-202-P/CLS840	Soil Mare Bulk	16.6	47	8.5
71501	Apollo 17 S1	LS-JBA-208-P/CLS011	Soil Mare Bulk	17.8	35	9.6
72701	Apollo 17 S2	LS-JBA-217-P1/CLS385	Soil Highland Boundary	8.7	61	1.5
73221	Apollo 17 S3	LS-JBA-220-P2/CLS785	Soil Highland/Mantle Bulk	8.7	43	1.8
73241	Apollo 17 S3	LS-JBA-221/CLS002	Soil Highland/Mantle Bulk	8.5	18	1.7
73261	Apollo 17 S3	LS-JBA-244/CLS635	Soil Highland/Mantle Bulk	8.8	45	1.9
73281	Apollo 17 S3	LS-JBA-222-P/CLS193	Soil Highland/Mantle Bulk	8.7	34	1.8
75081	Apollo 17 S5	LS-JBA-230-P1/CLS061	Soil Mare Bulk	17.7	40	9.9
75081	Apollo 17 S5	LS-JBA-230-P1/CLS250	Soil Mare Bulk	17.7	40	9.9
76261	Apollo 17 S6	LS-JBA-234-P1/CLS048	Soil Highland Boundary Bulk	10.7	58	3.4
78121	Apollo 17 S8	LS-JBA-237/CLS198	Soil Highland Boundary Bulk	12.5	68	4.4
79221	Apollo 17 S9	LS-JBA-241-P/CLS235	Soil Mare Bulk	15.4	81	6.4
79511	Apollo 17 S9	LS-JBA-242-P/CLS375	Soil Mare Bulk	15.4	61	6.4
72141	Apollo 17 LRV2	LS-JBA-210/CLS374	Soil Highland/Mantle Bulk	13.4	81	4.4
72161	Apollo 17 LRV3	LS-JBA-211-P/CLS196	Soil Mare Bulk	14.8	87	5.5
75111	Apollo 17 LRV7	LS-JBA-231/CLS194	Soil Mare Bulk	15.9	54	6.7
75121	Apollo 17 LRV7	LS-JBA-232-P2/CLS195	Soil Mare/Mantle Bulk	15.9	67	6.7
74121	Apollo 17 LRV6	LS-JBA-247/CLS656	Soil Highland/Mantle Bulk	10.2	88	2.6
24077	Luna 24	LS-JBA-141/CLS334	Mare Bulk Core Sample	21.1	39	1.0
24182	Luna 24	LS-JBA-145/CLS175	Soil Mare Bulk Core Sample	19.6	19	1.2
24149	Luna 24	LS-JBA-143/CLS321	Soil Mare Bulk Core Sample	20.3	21	1.1
24174	Luna 24	LS-JBA-144/CLS342	Soil Mare Bulk Core Sample	19.1	27	0.8

# Bibliography

- Adams, J. B., 1974, Visible and near-infrared diffuse reflectance spectra of pyroxenes as applied to remote sensing of solid objects in the solar system, *J. Geophys. Res.*, 79, 4829–4836
- Adams, J. B., Goullaud, L. H., 1978, Plagioclase feldspars: Visible and near infrared diffuse reflectance spectra as applied to remote sensing, in *Lunar Planet. Sci. Conf.*, vol. 9, pp. 1–3
- Arvidson, R., Drozd, R., Guinness, E., Hohenberg, C., Morgan, C., Morrison, R., Oberbeck, V., 1976, Cosmic ray exposure ages of Apollo 17 samples and the age of TYCHO, in *Lunar Planet. Sci. Conf. Proceedings*, (Ed.) D. C. Kinsler, vol. 7, pp. 2817–2832
- Berk, A., Anderson, G., Acharya, P., Chetwynd, J., Bernstein, L., Shettle, E., Matthew, M., Adler-Golden, S., 1999, *Modtran4 user's manual*, Air Force Research Laboratory, Space Vehicles Directorate
- Bhatt, M., Mall, U., Bugiolacchi, R., Lehmann, B., 2011, Study of spectral characteristics of the central peak region of Tycho crater using the SIR-2 data on-board Chandrayaan-1, vol. 42 of *Lunar Planet. Sci. Conf.*, p. 2390
- Bhattacharya, S., Chauhan, P., Rajawat, A. S., Ajai, Kumar, A. S. K., 2011, Lithological mapping of central part of Mare Moscoviense using Chandrayaan-1 Hyperspectral Imager (HySI) data, *Icarus*, 212, 470–479
- Binder, A. B., 1998, Lunar Prospector: Overview, *Science*, 281, 1475–1476
- Blewett, D. T., Lucey, P. G., Hawke, B. R., Jolliff, B. L., 1997a, FeO mapping of the moon - Refinement using images of the sample-return stations, in *Lunar Planet. Sci. Conf.*, vol. 28
- Blewett, D. T., Lucey, P. G., Hawke, B. R., Jolliff, B. L., 1997b, Clementine images of the lunar sample-return stations: Refinement of FeO and TiO<sub>2</sub> mapping techniques, *J. Geophys. Res.*, 102, 16 319–16 326
- Borg, L. E., Connelly, J. N., Boyet, M., Carlson, R. W., 2011, Chronological evidence that the Moon is either young or did not have a global magma ocean, *Nature*, 477, 70–72
- Boss, A., 1986, The origin of the Moon, *Science*, 231, 341–345

- Bugiolacchi, R., Mall, U., Bhatt, M., McKenna-Lawlor, S., Banaszkiewicz, M., Brønstad, K., Nathues, A., Søråas, F., Ullaland, K., Pedersen, R. B., 2011, An in-depth look at the lunar crater Copernicus: Exposed mineralogy by high-resolution near-infrared spectroscopy, *Icarus*, 213, 43–63
- Burns, R. G., 1993, *Mineralogical applications of crystal field theory*, Cambridge University Press, New York, 2nd edn.
- Burns, R. G., 1993, Origin of electronic spectra of minerals in the visible to near-infrared region, in *Remote Geochemical Analysis: Elemental and Mineralogical Composition*, Cambridge University Press., New York
- Cameron, A. G. W., 1997, The Origin of the Moon and the Single Impact Hypothesis V, *Icarus*, 126, 126–137
- Cameron, A. G. W., Ward, W. R., 1976, The Origin of the Moon, vol. 7 of *Lunar Planet. Sci. Conf.*, p. 120
- Charette, M. P., McCord, T. B., Pieters, C., Adams, J. B., 1974, Application of remote spectral reflectance measurements to lunar geology classification and determination of titanium content of lunar soils, *J. Geophys. Res.*, 79, 1605–1613
- Cheek, L. C., Pieters, C. M., Dyar, M. D., Milam, K. A., 2009, Revisiting plagioclase optical properties for lunar exploration, in *Lunar Planet. Sci. Conf.*, vol. 40 of *Lunar and Planetary Inst. Technical Report*, p. 1928
- Cheek, L. C., Pieters, C. M., Boardman, J. W., Clark, R. N., Combe, J. P., Head, J. W., Isaacson, P. J., McCord, T. B., Moriarty, D., Nettles, J. W., Petro, N. E., Sunshine, J. M., Taylor, L. A., 2011, Goldschmidt crater and the Moon's north polar region: Results from the Moon Mineralogy Mapper (M<sup>3</sup>), *J. Geophys. Res. (Planets)*, 116, E00G02
- Chin, G., Brylow, S., Foote, M., Garvin, J., Kasper, J., Keller, J., Litvak, M., Mitrofanov, I., Paige, D., Raney, K., Robinson, M., Sanin, A., Smith, D., Spence, H., Spudis, P., Stern, S. A., Zuber, M., 2007, *Lunar Reconnaissance Orbiter Overview: The Instrument Suite and Mission*, *Space Sci. Rev.*, 129, 391–419
- Clark, R. N., 1988, Automated analysis of reflectance spectra., *NASA Tech. Memo.*, NASA TM-4041, p. 143 - 145, 4041, 143–145
- Clark, R. N., Roush, T. L., 1984, Reflectance spectroscopy - Quantitative analysis techniques for remote sensing applications, *J. Geophys. Res.*, 89, 6329–6340
- Cloutis, E. A., Gaffey, M. J., 1991, Pyroxene spectroscopy revisited - Spectral-compositional correlations and relationship to geothermometry, *J. Geophys. Res.*, 96, 22 809–22 826
- Crawford, I. A., Joy, K. H., Kellett, B. J., Grande, M., Anand, M., Bhandari, N., Cook, A. C., D'Uston, L., Fernandes, V. A., Gasnault, O., Goswami, J., Howe, C. J., Huovelin, J., Koschny, D., Lawrence, D. J., Maddison, B. J., Maurice, S., Narendranath, S., Pieters, C., Okada, T., Rothery, D. A., Russell, S. S., Sreekumar, P., Swinyard, B.,

- Wieczorek, M., Wilding, M., 2009, The scientific rationale for the C1XS X-ray spectrometer on India's Chandrayaan-1 mission to the moon, *Planet. Space Sci.*, 57, 725–734
- Darwin, G., 1878, On the precession of a viscous spheroid, and on the remote history of the Earth, *Proceedings of the Royal Society of London*, 28, 184
- Dhingra, D., Pieters, C. M., Boardman, J. W., Head, J. W., Isaacson, P. J., Taylor, L. A., 2011, Compositional diversity at Theophilus Crater: Understanding the geological context of Mg-spinel bearing central peaks, *Geophys. Res. Lett.*, 38, L11 201
- Elphic, R. C., Lawrence, D. J., Feldman, W. C., Barraclough, B. L., Maurice, S., Binder, A. B., Lucey, P. G., 1998, Lunar Fe and Ti Abundances: Comparison of Lunar Prospector and Clementine Data, *Science*, 281, 1493–1496
- Elphic, R. C., Lawrence, D. J., Feldman, W. C., Barraclough, B. L., Gasnault, O. M., Maurice, S., Lucey, P. G., Blewett, D. T., Binder, A. B., 2002, Lunar Prospector neutron spectrometer constraints on TiO<sub>2</sub>, *J. Geophys. Res. (Planets)*, 107(E4),5024
- Feldman, W. C., Barraclough, B. L., Maurice, S., Elphic, R. C., Lawrence, D. J., Thomsen, D. R., Binder, A. B., 1998, Major compositional units of the Moon: Lunar Prospector thermal and fast neutrons, *Science*, 281, 1489–1493
- Fischer, E. M., Pieters, C. M., 1994, Remote determination of exposure degree and iron concentration of lunar soils using VIS-NIR spectroscopic methods, *Icarus*, 111, 475–488
- Fischer, E. M., Pieters, C. M., 1996, Composition and exposure age of the Apollo 16 Cayley and Descartes regions from Clementine data: Normalizing the optical effects of space weathering, *J. Geophys. Res.*, 101, 2225–2234
- Foing, B. H., Heather, D. J., Almeida, M., Science Technology Working Team, S.-., 2001, The Science Goals Of Esa's Smart-1 Mission To The Moon, *Earth Moon and Planets*, 85, 523–531
- Gaffey, M. J., 2010, Space weathering and the interpretation of asteroid reflectance spectra, *Icarus*, 209, 564–574
- Gillis, J., 1998, The composition and geologic setting of mare deposits on the far side of the Moon, Ph.D. thesis, PhD thesis, Rice University, Houston
- Gillis, J. J., Jolliff, B. L., Elphic, R. C., 2003, A revised algorithm for calculating TiO<sub>2</sub> from Clementine UVVIS data: A synthesis of rock, soil, and remotely sensed TiO<sub>2</sub> concentrations, *Journal of Geophysical Research (Planets)*, 108, 5009
- Gillis, J. J., Jolliff, B. L., Korotev, R. L., 2004, Lunar surface geochemistry: Global concentrations of Th, K, and FeO as derived from lunar prospector and Clementine data, *Geochimica et Cosmochimica Acta*, 68, 3791 – 3805, ISSN 0016-7037

- Gillis-Davis, J. J., Lucey, P. G., Hawke, B. R., 2006, Mare Moscoviense a window into the interior of the Moon, in 37th Annual Lunar and Planetary Science Conference, (Ed.) S. Mackwell & E. Stansbery, vol. 37 of Lunar and Planetary Institute Science Conference Abstracts, p. 2454
- Goswami, J., Annadurai, M., 2009, Chandrayaan-1: India's first planetary science mission to the Moon, *Current Science*, 96, 486–491
- Green, R. O., Pieters, C., Mouroulis, P., Eastwood, M., Boardman, J., Glavich, T., Isaacson, P., Annadurai, M., Besse, S., Barr, D., Buratti, B., Cate, D., Chatterjee, A., Clark, R., Cheek, L., Combe, J., Dhingra, D., Essandoh, V., Geier, S., Goswami, J. N., Green, R., Haemmerle, V., Head, J., Hovland, L., Hyman, S., Klima, R., Koch, T., Kramer, G., Kumar, A. S. K., Lee, K., Lundeen, S., Malaret, E., McCord, T., McLaughlin, S., Mustard, J., Nettles, J., Petro, N., Plourde, K., Racho, C., Rodriguez, J., Runyon, C., Sellar, G., Smith, C., Sobel, H., Staid, M., Sunshine, J., Taylor, L., Thaisen, K., Tompkins, S., Tseng, H., Vane, G., Varanasi, P., White, M., Wilson, D., 2011, The Moon Mineralogy Mapper (M<sup>3</sup>) imaging spectrometer for lunar science: Instrument description, calibration, on-orbit measurements, science data calibration and on-orbit validation, *Journal of Geophysical Research (Planets)*, 116, E00G19
- Hapke, B., 1993, *Introduction to the Theory of reflectance and Emittance Spectroscopy*, Cambridge University Press, New York
- Hapke, B., 2001, Space weathering from Mercury to the asteroid belt, *J. Geophys. Res.*, 106, 10 039–10 074
- Hartmann, W. K., Davis, D. R., 1975, Satellite-sized planetesimals and lunar origin, *Icarus*, 24, 504–514
- Haruyama, J., Ohtake, M., Matsunaga, T., Morota, T., Honda, C., Yokota, Y., Abe, M., Ogawa, Y., Miyamoto, H., Iwasaki, A., Pieters, C. M., Asada, N., Demura, H., Hirata, N., Terazono, J., Sasaki, S., Saiki, K., Yamaji, A., Torii, M., Josset, J., 2009, Long-lived volcanism on the lunar farside revealed by SELENE Terrain Camera, *Science*, 323, 905–908
- Hawke, B. R., Lucey, P. G., Bell, J. F., Jaumann, R., Neukum, G., 1986, Spectral reflectance studies of TYCHO crater: Preliminary results, in *Lunar Planet. Sci. Conf.*, vol. 17 of Lunar and Planetary Inst. Technical Report, pp. 999–1000
- Heiken, G. H., Vaniman, D. T., French, B. M., 1991, *Lunar sourcebook - A user's guide to the Moon*, Cambridge Univ. Press, New York
- Hiesinger, H., Head III, J., 2006, New views of lunar geoscience: An introduction and overview, *Reviews in mineralogy and geochemistry*, 60, 1–85
- Hiroi, T., Pieters, C. M., Morris, R. V., 1997, New considerations for estimating lunar soil maturity from VIS-NIR reflectance spectroscopy, in *Lunar Planet. Sci Conf.*, vol. 28 of Lunar and Planetary Inst. Technical Report



- Isaacson, P. J., Pieters, C. M., Besse, S., Clark, R. N., Head, J. W., Klima, R. L., Mustard, J. F., Petro, N. E., Staid, M. I., Sunshine, J. M., Taylor, L. A., Thaisen, K. G., Tompkins, S., 2011a, Remote compositional analysis of lunar olivine-rich lithologies with Moon Mineralogy Mapper ( $M^3$ ) spectra, *J. Geophys. Res. (Planets)*, 116, E00G11
- Isaacson, P. J., Pieters, C. M., Hiroi, T., Liu, Y., Dhingra, D., Klima, R. L., Taylor, L. A., 2011b, Reflectance spectroscopy of ilmenite: New constraints from Apollo sample measurements, in *Lunar Planet. Sci. Conf.*, vol. 42, p. 2130
- Ishihara, Y., Goossens, S., Matsumoto, K., Noda, H., Araki, H., Namiki, N., Hanada, H., Iwata, T., Tazawa, S., Sasaki, S., 2009, Crustal thickness of the Moon: Implications for farside basin structures, *Geophys. Res. Lett.*, 36, L19202
- Jutzi, M., Asphaug, E., 2011, Forming the lunar farside highlands by accretion of a companion moon, *Nature*, 476, 69–72
- Kato, M., Sasaki, S., Takizawa, Y., 2010, The Kaguya mission overview, *Space Sci. Rev.*, 154, 3–19
- King, T. V. V., Ridley, W. I., 1987, Relation of the spectroscopic reflectance of olivine to mineral chemistry and some remote sensing implications, *J. Geophys. Res.*, 921, 11 457–11 469
- Klima, R. L., Pieters, C. M., 2008, MGM analysis of pyroxene mineral separates from Apollo 15 and 17, in *Lunar Planet. Sci. Conf.*, vol. 39 of Lunar and Planetary Inst. Technical Report, p. 1756
- Klima, R. L., Pieters, C. M., Dyar, M. D., 2007, Spectroscopy of synthetic Mg-Fe pyroxenes I: Spin-allowed and spin-forbidden crystal field bands in the visible and near-infrared, *Meteoritics and Planetary Science*, 42, 235–253
- Kobayashi, M.-N., Berezhnoy, A. A., D'Uston, C., Fujii, M., Hasebe, N., Hiroishi, T., Kaneko, H., Miyachi, T., Mori, K., Maurice, S., Nakazawa, M., Narasaki, K., Okudaira, O., Shibamura, E., Takashima, T., Yamashita, N., 2005, Global mapping of elemental abundance on lunar surface by SELENE gamma-ray spectrometer, in *Lunar Planet. Sci. Conf.*, (Ed.) S. Mackwell & E. Stansbery, vol. 36, p. 2092
- Korotev, R. L., Jolliff, B. L., Zeigler, R. A., 2010, On the origin of the Moon's feldspathic highlands, pure anorthosite, and the feldspathic lunar meteorites, in *Lunar Planet. Sci. Conf.*, vol. 41, p. 1440
- Kramer, G. Y., Jolliff, B. L., Neal, C. R., 2008, Distinguishing high-alumina mare basalts using Clementine UVVIS and Lunar Prospector GRS data: Mare Moscoviense and Mare Nectaris, *Journal of Geophysical Research (Planets)*, 113, E01002
- Kumar, A., Chowdhury, A., Banerjee, A., Dave, A., Sharma, B., Shah, K., Murali, K., Mehta, S., Joshi, S., Sarkar, S., 2009, Hyper spectral imager for lunar mineral mapping in visible and near infrared band, *Current Science*, 96, 496

- Lawrence, D. J., Feldman, W. C., Barraclough, B. L., Binder, A. B., Elphic, R. C., Maurice, S., Thomsen, D. R., 1998, Global elemental maps of the Moon: The lunar prospector gamma-ray spectrometer, *Science*, 281, 1484–1489
- Lawrence, D. J., Feldman, W. C., Elphic, R. C., Little, R. C., Prettyman, T. H., Maurice, S., Lucey, P. G., Binder, A. B., 2002, Iron abundances on the lunar surface as measured by the Lunar Prospector gamma-ray and neutron spectrometers, *J. Geophys. Res. (Planets)*, 107, 5130
- Le Mouélic, S., Langevin, Y., Erard, S., Pinet, P., Chevrel, S., Daydou, Y., 2000, Discrimination between maturity and composition of lunar soils from integrated Clementine UV-visible/near-infrared data: Application to the Aristarchus Plateau, *J. Geophys. Res.*, 105, 9445–9456
- Le Mouélic, S., Lucey, P. G., Langevin, Y., Hawke, B. R., 2002, Calculating iron contents of lunar highland materials surrounding Tycho crater from integrated Clementine UV-visible and near-infrared data, *J. Geophys. Res. (Planets)*, 107, 5074
- Lillesand, T., Kiefer, R., Chipman, J., 2008, Remote sensing and image interpretation, John Wiley and Sons Inc., New York, NY, 6th edition edn., ISBN 9780470052457
- Longhi, J., 1980, A model of early lunar differentiation, in *Lunar Planet. Conf. Proceedings*, (Ed.) S. A. Bedini, vol. 11, pp. 289–315
- Lucey, P., Korotev, R., Gillis, J., Taylor, L., Lawrence, D., Campbell, B., Elphic, R., Feldman, B., Hood, L., Hunten, D., et al., 2006, Understanding the lunar surface and space-Moon interactions, *Reviews in mineralogy and geochemistry*, 60, 83–219
- Lucey, P. G., Hawke, B. R., Pieters, C. M., Head, J. W., McCord, T. B., 1986, A compositional study of the Aristarchus region of the Moon using near-infrared reflectance spectroscopy, *J. Geophys. Res.*, 91, D344–D350
- Lucey, P. G., Hawke, B. R., Horton, K., 1991, The distribution of olivine in the crater Copernicus, *Geophys. Res. Lett.*, 18, 2133–2136
- Lucey, P. G., Taylor, G. J., Malaret, E., 1995, Abundance and Distribution of Iron on the Moon, *Science*, 268, 1150–1153
- Lucey, P. G., Blewett, D. T., Hawke, B. R., 1998a, Mapping the FeO and TiO<sub>2</sub> content of the lunar surface with multispectral imagery, *J. Geophys. Res.*, 103, 3679–3699
- Lucey, P. G., Taylor, G. J., Hawke, B. R., 1998b, Global Imaging of Maturity: Results from Clementine and Lunar Sample Studies, in *Lunar Planet. Sci. Conf.*, vol. 29, p. 1356
- Lucey, P. G., Blewett, D. T., Jolliff, B. L., 2000, Lunar iron and titanium abundance algorithms based on final processing of Clementine ultraviolet-visible images, *J. Geophys. Res.*, 105, 20 297–20 306

- Mall, U., Banaszkiwicz, M., Bronstad, K., McKenna-Lawlor, S., Nathues, A., Soraas, F., Vilenius, E., Ullaland, K., 2009, Near infrared spectrometer SIR-2 on Chandrayaan-1, *Current Science*, 96, 506–511
- Matsunaga, T., Ohtake, M., Haruyama, J., Ogawa, Y., Nakamura, R., Yokota, Y., Morota, T., Honda, C., Torii, M., Abe, M., Nimura, T., Hiroi, T., Arai, T., Saiki, K., Takeda, H., Hirata, N., Kodama, S., Sugihara, T., Demura, H., Asada, N., Terazono, J., Otake, H., 2008, Discoveries on the lithology of lunar crater central peaks by SELENE Spectral Profiler, *Geophys. Res. Lett.*, 35, L23 201
- McKay, D., Heiken, G., Basu, A., Blanford, G., Simon, S., Reedy, R., French, B., Papike, J., 1991, The lunar regolith, in *Lunar Sourcebook*, (Ed.) G. H. Heiken, D. T. Vaniman & B. M. French, pp. 285–356, Cambridge Univ. Press, New York
- McKay, D. S., Fruland, R. M., Heiken, G. H., 1974, Grain size and the evolution of lunar soils, in *Lunar and Planetary Science Conference Proceedings*, vol. 5 of Lunar Planet. Sci. Conf. Proceedings, pp. 887–906
- Melosh, H. J., Sonett, C. P., 1986, When worlds collide - Jetted vapor plumes and the Moon's origin, in *Origin of the Moon*, (Ed.) W. K. Hartmann, R. J. Phillips, & G. J. Taylor, pp. 621–642
- Morota, T., Haruyama, J., Honda, C., Ohtake, M., Yokota, Y., Kimura, J., Matsunaga, T., Ogawa, Y., Hirata, N., Demura, H., Iwasaki, A., Miyamoto, H., Nakamura, R., Takeda, H., Ishihara, Y., Sasaki, S., 2009, Mare volcanism in the lunar farside Moscoviense region: Implication for lateral variation in magma production of the Moon, *Geophys. Res. Lett.*, 36, L21202
- Morris, R., Score, R., Dardano, C., Heiken, G., 1983, *Handbook of Lunar Soils*, NASA Planetary Materials Branch, publication No. 67, NASA/Johnson Space Center, Houston
- Morris, R. V., 1976, Surface exposure indices of lunar soils - A comparative FMR study, in *Lunar Planet. Sci. Conf. Proceedings*, (Ed.) D. C. Kinsler, vol. 7, pp. 315–335
- Morris, R. V., 1978, The surface exposure (maturity) of lunar soils - Some concepts and  $I_s/FeO$  compilation, in *Lunar Planet. Sci. Conf. Proceedings*, vol. 9, pp. 2287–2297
- Mouélic, S. L., Langevin, Y., 2001, The olivine at the lunar crater Copernicus as seen by Clementine NIR data, *Planet. Space Sci.*, 49, 65–70
- Mouroulis, P., Sellar, R. G., Wilson, D. W., Shea, J. J., Green, R. O., 2007, Optical design of a compact imaging spectrometer for planetary mineralogy, *Optical Engineering*, 46, 063 001,1–063 001,9
- Neal, C. R., Taylor, L. A., 1992, Petrogenesis of mare basalts - A record of lunar volcanism, *Geochim. Cosmochim. Acta*, 56, 2177–2211
- Noble, S. K., Pieters, C. M., Keller, L. P., 2007, An experimental approach to understanding the optical effects of space weathering, *Icarus*, 192, 629–642

- Nozette, S., Rustan, P., Pleasance, L. P., Horan, D. M., Regeon, P., Shoemaker, E. M., Spudis, P. D., Acton, C. H., Baker, D. N., Blamont, J. E., Buratti, B. J., Corson, M. P., Davies, M. E., Duxbury, T. C., Eliason, E. M., Jakosky, B. M., Kordas, J. F., Lewis, I. T., Lichtenberg, C. L., Lucey, P. G., Malaret, E., Massie, M. A., Resnick, J. H., Rollins, C. J., Park, H. S., McEwen, A. S., Priest, R. E., Pieters, C. M., Reisse, R. A., Robinson, M. S., Simpson, R. A., Smith, D. E., Sorenson, T. C., Vorder Breugge, R. W., Zuber, M. T., 1994, The Clementine Mission to the Moon: Scientific Overview, *Science*, 266, 1835–1839
- Ohtake, M., Matsunaga, T., Haruyama, J., Yokota, Y., Morota, T., Honda, C., Ogawa, Y., Torii, M., Miyamoto, H., Arai, T., Hirata, N., Iwasaki, A., Nakamura, R., Hiroi, T., Sugihara, T., Takeda, H., Otake, H., Pieters, C. M., Saiki, K., Kitazato, K., Abe, M., Asada, N., Demura, H., Yamaguchi, Y., Sasaki, S., Kodama, S., Terazono, J., Shirao, M., Yamaji, A., Minami, S., Akiyama, H., Josset, J., 2009a, The global distribution of pure anorthosite on the Moon, *Nature*, 461, 236–240
- Ohtake, M., Matsunaga, T., Yokota, Y., Haruyama, J., Miyamoto, H., Arai, T., Hirata, N., Takeda, H., Nakamura, R., Morota, T., Honda, C., Ogawa, Y., Kitazato, K., Lism Team, 2009b, Anorthosite with 100% Plagioclase on the Moon Detected by the SELENE Multiband Imager, in *Lunar Plane. Sci. Conf.*, vol. 40, p. 1557
- Papike, J., Ryder, G., Shearer, C., 1998, Lunar samples, in *Planetary Materials*, vol. 36 of *Reviews in Mineralogy & Geochemistry*, p. 501–534, Mineralogical Society of America, Washington, D.C.
- Papike, J. J., Hodges, F. N., Bence, A. E., Cameron, M., Rhodes, J. M., 1976, Mare basalts - Crystal chemistry, mineralogy, and petrology, *Reviews of Geophysics and Space Physics*, 14, 475 – 540
- Pieters, C., Boardman, J., Buratti, B., Chatterjee, A., Clark, R., Glavich, T., Green, R., Head III, J., Isaacson, P., Malaret, E., et al., 2009, The Moon Mineralogy Mapper (M<sup>3</sup>) on Chandrayaan-1, *Current Science*, 96, 500–505
- Pieters, C. M., 1982, Copernicus crater central peak - Lunar mountain of unique composition, *Science*, 215, 59–61
- Pieters, C. M., Staid, M. I., Fischer, E. M., Tompkins, S., He, G., 1994, A sharper view of impact craters from Clementine Data, *Science*, 266, 1844–1848
- Pieters, C. M., Taylor, L. A., Noble, S. K., Keller, L. P., Hapke, B., Morris, R. V., Allen, C. C., McKay, D. S., Wentworth, S., 2000, Space weathering on airless bodies: Resolving a mystery with lunar samples, *Meteoritics and Planetary Science*, 35, 1101–1107
- Pieters, C. M., Goswami, J. N., Clark, R. N., Annadurai, M., Boardman, J., Buratti, B., Combe, J., Dyar, M. D., Green, R., Head, J. W., Hibbitts, C., Hicks, M., Isaacson, P., Klima, R., Kramer, G., Kumar, S., Livo, E., Lundeen, S., Malaret, E., McCord, T., Mustard, J., Nettles, J., Petro, N., Runyon, C., Staid, M., Sunshine, J., Taylor, L. A., Tompkins, S., Varanasi, P., 2009, Character and Spatial Distribution of OH/H<sub>2</sub>O on the Surface of the Moon Seen by M<sup>3</sup> on Chandrayaan-1, *Science*, 326, 568–572

- Pieters, C. M., Besse, S., Boardman, J., Buratti, B., Cheek, L., Clark, R. N., Combe, J. P., Dhingra, D., Goswami, J. N., Green, R. O., Head, J. W., Isaacson, P., Klima, R., Kramer, G., Lundeen, S., Malaret, E., McCord, T., Mustard, J., Nettles, J., Petro, N., Runyon, C., Staid, M., Sunshine, J., Taylor, L. A., Thaisen, K., Tompkins, S., Whitten, J., 2011, Mg-spinel lithology: A new rock type on the lunar farside, *J. Geophys. Res. (Planets)*, 116, E00G08
- Pinet, P. C., Chevrel, S. D., Martin, P., 1993, Copernicus - A regional probe of the lunar interior, *Science*, 260, 797–801
- Putnis, A., 1992, *An Introduction to Mineral Sciences*, Cambridge University Press, Cambridge
- Riner, M. A., Lucey, P. G., Desch, S. J., McCubbin, F. M., 2009, Nature of opaque components on Mercury: Insights into a Mercurian magma ocean, *Geophys. Res. Lett.*, 36, L02201
- Schmidt, O., Hanna, G., 1959, *A Theory of the Origin of the Earth*, Lawrence and Wishart
- Sebastian, I., 2002, Sir calibration plan., s1-sir-pl-3006
- Shkuratov, Y. G., Kaydash, V. G., Opanasenko, N. V., 1999a, Iron and Titanium Abundance and Maturity Degree Distribution on the Lunar Nearside, *Icarus*, 137, 222–234
- Shkuratov, Y. G., Kreslavsky, M. A., Ovcharenko, A. A., Stankevich, D. G., Zubko, E. S., Pieters, C., Arnold, G., 1999b, Opposition Effect from Clementine Data and Mechanisms of Backscatter, *Icarus*, 141, 132–155
- Shkuratov, Y. G., Kaydash, V. G., Stankevich, D. G., Starukhina, L. V., Pinet, P. C., Chevrel, S. D., Daydou, Y. H., 2005, Derivation of elemental abundance maps at intermediate resolution from optical interpolation of lunar prospector gamma-ray spectrometer data, *Planet. Space Sci.*, 53, 1287–1301
- Singer, R. B., 1981, Near-infrared spectral reflectance of mineral mixtures - Systematic combinations of pyroxenes, olivine, and iron oxides, *J. Geophys. Res.*, 86, 7967–7982
- Singer, S., 1986, Origin of the moon by capture, in *Origin of the Moon*, vol. 1, pp. 471–485
- Sitek, P., 2008, Thermal vacuum test of space equipment: tests of sir-2 instrument chandrayaan-1 mission, in *Proceedings of SPIE*, vol. 7124, p. 71240G
- Sitek, P., Vilenius, E., Mall, U., 2008, Performance comparison and selection criteria: an assessment for choosing the best flight detector for the SIR-2 NIR-spectrometer on Chandrayaan-1, in *Society of Photo-Optical Instrumentation Engineers (SPIE) Conference Series*, vol. 6937 of *Society of Photo-Optical Instrumentation Engineers (SPIE) Conference Series*
- Spudis, P. D., 2005, *The Geology of Multi-Ring Impact Basins*, Cambridge Univ. Press, New York

- Spudis, P. D., Bussey, D. B. J., Baloga, S. M., Butler, B. J., Carl, D., Carter, L. M., Chakraborty, M., Elphic, R. C., Gillis-Davis, J. J., Goswami, J. N., Heggy, E., Hillyard, M., Jensen, R., Kirk, R. L., LaVallee, D., McKerracher, P., Neish, C. D., Nozette, S., Nylund, S., Palsetia, M., Patterson, W., Robinson, M. S., Raney, R. K., Schulze, R. C., Sequeira, H., Skura, J., Thompson, T. W., Thomson, B. J., Ustinov, E. A., Winters, H. L., 2010, Initial results for the north pole of the Moon from Mini-SAR, Chandrayaan-1 mission, *Geophys. Res. Lett.*, 37
- Staid, M. I., Pieters, C. M., Besse, S., Boardman, J., Dhingra, D., Green, R., Head, J. W., Isaacson, P., Klima, R., Kramer, G., Mustard, J. M., Runyon, C., Sunshine, J., Taylor, L. A., 2011, The mineralogy of late stage lunar volcanism as observed by the Moon Mineralogy Mapper on Chandrayaan-1, *Journal of Geophysical Research (Planets)*, 116, E00G10
- Sunshine, J. M., Pieters, C. M., 1998, Determining the composition of olivine from reflectance spectroscopy, *J. Geophys. Res.*, 1031, 13 675–13 688
- Sunshine, J. M., Tompkins, S., 2001, Yet Another New Look at Copernicus: Projecting Telescopic Spectra onto Clementine Multispectral Images Through Spectral Mixture Analysis, in *Lunar Planet. Sci. Conf.*, vol. 32 of *Lunar Planet. Inst. Technical Report*, p. 1324
- Swinyard, B. M., Joy, K. H., Kellett, B. J., Crawford, I. A., Grande, M., Howe, C. J., Fernandes, V. A., Gasnault, O., Lawrence, D. J., Russell, S. S., Wiczorek, M. A., Foing, B. H., The SMART-1 team, 2009, X-ray fluorescence observations of the moon by SMART-1/D-CIXS and the first detection of Ti  $K\alpha$  from the lunar surface, *Planet. Space Sci.*, 57, 744–750
- Taylor, L. A., Pieters, C., Keller, L. P., Morris, R. V., McKay, D. S., Patchen, A., Wentworth, S., 2001, The effects of space weathering on Apollo 17 mare soils: Petrographic and chemical characterization, *Meteoritics and Planetary Science*, 36, 285–299
- Thaisen, K. G., Head, J. W., Taylor, L. A., Kramer, G. Y., Isaacson, P., Nettles, J., Petro, N., Pieters, C. M., 2011, Geology of the Moscoviense Basin, *J. Geophys. Res. (Planets)*, 116, E00G07
- Tompkins, S., Pieters, C. M., 1999, Mineralogy of the lunar crust: Results from Clementine, *Meteoritics and Planetary Science*, 34, 25–41
- Tompkins, S., Pieters, C. M., 2010, Spectral characteristics of lunar impact melts and inferred mineralogy, *Meteoritics and Planetary Science*, 45, 1152–1169
- Tonks, W. B., Melosh, H. J., 1990, *Origin of the Earth*, chap. The physics of crystal settling and suspension in a turbulent magma ocean., pp. 151–174
- Torheim, O., Bronstad, K., Heerlein, K., Mall, U., Nathues, A., Nowosielski, W., Orleanski, P., Pommeresche, B., Reimundo, V., Skogseide, Y., Solberg, A., Ullaland, K., 2009, Development of an Embedded CPU-Based Instrument Control Unit for the SIR-2 Instrument Onboard the Chandrayaan-1 Mission to the Moon, *IEEE Transactions on Geoscience and Remote Sensing*, 47, 2836–2846

- Urey, H., 1966, The capture hypothesis of the origin of the Moon, in *The Earth-Moon System*, vol. 1
- Vilenius, E., 2009, On the analysis of near-infrared point spectrometer data for the investigation of lunar surface mineralogy, ISBN 978-3-936586-92-3
- Warren, P. H., 1985, The magma ocean concept and lunar evolution, *Annual Review of Earth and Planetary Sciences*, 13, 201–240
- Wiese, M., 2009, *Lunar Mineralogy with SIR-1 and Clementine UVVIS/NIR*, ISBN 978-3-942169-00-4
- Wilhelms, D. E., McCauley, J. F., Trask, N. J., 1987, *The geologic history of the Moon*
- Wöhler, C., Berezhnoy, A., Evans, R., 2011, Estimation of elemental abundances of the lunar regolith using Clementine UVVIS+NIR data, *Planet. Space Sci.*, 59, 92–110
- Wood, J. A., 1986, Moon over Mauna Loa - A review of hypotheses of formation of Earth's Moon, in *Origin of the Moon*, (Ed.) W. K. Hartmann, R. J. Phillips, & G. J. Taylor, pp. 17–55
- Wood, J. A., Dickey, Jr., J. S., Marvin, U. B., Powell, B. N., 1970, Lunar anorthosites and a geophysical model of the Moon, *Geochimica et Cosmochimica Acta Supplement*, 1, 965–990
- Yamamoto, S., Nakamura, R., Matsunaga, T., Ogawa, Y., Ishihara, Y., Morota, T., Hirata, N., Ohtake, M., Hiroi, T., Yokota, Y., Haruyama, J., 2012, Olivine-rich exposures in the South Pole-Aitken Basin, *Icarus*, 218, 331–344
- Yamamoto, Y., Okada, T., Shiraishi, H., Shirai, K., Arai, T., Ogawa, K., Hosono, K., Arakawa, M., Kato, M., 2008, Current status of X-ray spectrometer development in the SELENE project, *Advances in Space Research*, 42, 305–309
- Zheng, Y., Ouyang, Z., Li, C., Liu, J., Zou, Y., 2008, China's Lunar Exploration Program: Present and future, *Planet. Space Sci.*, 56, 881–886
- Zuber, M. T., Smith, D. E., Lemoine, F. G., Neumann, G. A., 1994, The Shape and Internal Structure of the Moon from the Clementine Mission, *Science*, 266, 1839–1843





# Publications

## Papers

- **Bhatt, M.**, Mall, U., Bugiolacchi, R., McKenna-Lawlor, S., Banaszekiewicz, M., Nathues, A., Ullaland, K., Lunar iron abundance determination using the 2- $\mu\text{m}$  absorption band parameters, *submitted to Icarus*, 2012.
- Bugiolacchi, R., Mall, U., **Bhatt, M.**, McKenna-Lawlor, S., Banaszekiewicz, M., Brønstad, K., Nathues, A., Søråas, F., Ullaland, K., Pedersen, R. B., An in-depth look at the lunar crater Copernicus: Exposed mineralogy by high-resolution near-infrared spectroscopy, *Icarus*, 2011, volume 213, pp 43-63.
- U. Mall, R. Bugiolacchi, **M. Bhatt**, J.-P. Combe, S. Bhattacharya, S. McKenna-Lawlor, Investigating Lunar Central Crater Peaks with the SIR-2 NIR Reflectance Spectrometer on Chandrayaan-1, *Advances in Geosciences*, 2010, volume 25, pp 87-108.

## Talks and posters

- **Bhatt, M.**, Mall, U., Bugiolacchi, R., Iron Abundance Estimation of the Lunar Surface Using VIS-NIR Spectrometers On-Board Chandrayaan-1, (poster), LPSC, 2012, volume 43, pp 1409.
- **Bhatt, M.**, Mall, U., Bugiolacchi, R., Application of iron abundance estimation method to Tycho and Copernicus craters, VII<sup>th</sup> Chandrayaan-1 Meet, 2011.
- **Bhatt, M.**, Mall, U., Bugiolacchi, R., Bhattacharya, S., Investigating mare Moscoviense using VIS-NIR spectrometers on-board Chandrayaan-1, (poster), VII<sup>th</sup> Chandrayaan-1 Meet, 2011.
- **Bhatt, M.**, Mall, U., Bugiolacchi, R., Iron mapping method based on 2- $\mu\text{m}$  absorption parameters using SIR-2 data on-board Chandrayaan-1, EPSC-DPS Joint Meeting 2011, pp 441.
- **Bhatt, M.**, Mall, U., Bugiolacchi, R., Lehmann, B., Study of Spectral Characteristics of the Central Peak Region of Tycho Crater Using the SIR-2 Data On-Board Chandrayaan-1, (poster), LPSC, 2011, volume 42, pp 2390.

- **Bhatt, M.,** Mall, U., Bugiolacchi, R., Bhattacharya, S., Towards an understanding of the lunar surface composition by combining near-infrared spectrometer SIR-2 and Hyper Spectral Imager (HySI) data from Chandrayaan-1, VI<sup>th</sup> Chandrayaan-1 Meet, 2010.
- **Bhatt, M.,** Mall, U., Bugiolacchi, R., Bhattacharya, S., Study of the central part of Mare Moscoviense by combining near-infrared spectrometer, SIR-2 and Hyper Spectral Imager (HySI) data on-board Chandrayaan-1, (poster), EGU General Assembly, 2010.
- **Bhatt, M.,** Mall, U., Bugiolacchi, R., Vilenius, E., On-orbit cross-calibration of SIR-2 using Apollo landing sites, (poster), EPSC, 2009, pp. 685.

# Acknowledgements

I am very thankful to Dr. Urs Mall, my supervisor at MPS, for his support and help throughout my stay in Lindau. Your constructive criticism of my work have been the most helpful to learn, think deeper, and to improve my presentation skills. Thanks for providing me the opportunities to attend various conferences and Chandrayaan-1 meetings to get into contact with renowned scientists in the same field.

I am grateful to Prof. Bernd Lehmann, my supervisor at the Technical University Clausthal, for accepting me as a PhD student and for always being helpful. Thanks for showing me thin sections of some of the main minerals present on the Moon. Your suggestions in the Thesis Advisory Committee (TAC) meetings were always very constructive and helpful.

Many thanks to Prof. Christian Wöhler from the Technical University Dortmund, for being in my Thesis Advisory Committee. The discussions about the various iron abundance estimation algorithms and topography effects on such calculations were very helpful.

The financial support from the Max Planck Research School is thankfully acknowledged. Many thanks to Dr. Dieter Schmitt and Dr. Julia Thalmann, coordinators of the Solar System School. The yearly student retreats provided a good chance to interact with fellow students and to learn some additional skills like paper writing, art of presentation etc. I thank sincerely to our group secretaries, Mrs. Fahlbusch and Claudia for their help in administrative work. Thanks to the computer centre for help in case of technical problems.

The SIR-2 project was funded through the Max Planck Society, and ESA. I acknowledge ESA and ISRO for this collaborative opportunity. I gratefully acknowledge the valuable input to this thesis by the public release of M<sup>3</sup> data and thanks to Space Application Centre (SAC), ISRO for providing some of the HySI images for the combined analysis.

Special thanks to the SIR-2 team members for their advice and help. Especially I would like to thank Dr. Roberto Bugiolacchi for almost daily discussions and your help with Photoshop. Thanks to Dr. Manuela Wiese and Dr. Esa Vilenius for their help in initial time of my PhD work. Dr. Borys Dabrowski, thanks for your help with MATLAB.

I am also indebted to Mr. C. M. Nagarani, Mr. Senthil Kumar, Mrs. Arti Sarkar, and Prof. L. Pandey for their continuous encouragement and friendly advices.

I express my gratitude to Sasha Basilevsky, Satadru Dada and Vishnu Ji for broad discussions about the Moon mineralogy and referring me some basic books on the planetary mineralogy. Very special thanks to my officemates Li and Zhenya for a good company, open discussions on science and life in general, and for help with L<sup>A</sup>T<sub>E</sub>X.

My friends at MPS have helped me a lot to make my life enjoyable in this quiet place. Thanks to Anne, Wieland, Peter, and Karsten for helping me with German to English

translation. Thanks Oksana, Zhenya, Neda, Lucia, Yeon Joo, and Li for the parties and weekend get-togethers. I wonder about the ideas you all have for a surprise party! Every birthday was a surprise for me in Lindau. Thanks Philippe and Ramy for sharing some basic knowledge of Salsa! Thanks to swimming, tennis, badminton, table tennis and skating mates for your company and for encouraging me to learn new sports.

I express thanks to my “Lindau family”, Indian community at Lindau from bottom of my heart. We celebrated most of the Indian festivals here in a traditional way with the same spirit and joy as in India. Wherever I am in future, I am going to miss you all. Nagaraju, Latha, and Jayant thanks for your open invitation for dinner at the critical time of thesis writing. Girjesh, thanks for passing by my office room, and sometimes asking for coffee breaks. Navdeep, Sanjiv, Gautam, Jisesh, Chaitanya, and Guneshwar thanks for your friendly nature and company. Supriya, thanks for your support, care, and organizing many parties together. I can not imagine life in Lindau without all of you! I am very thankful to Prasanta bhaiya and Manika didi for helping me to settle in a new country at the beginning. My college friends Anshu, Aparajita, Leena, Jagrati, Abha, Dolli, Shweta, Harish, and Amit deserve special thanks for lively discussions on many aspects of life.

Support from my family gave me strength to stay focused throughout my PhD. I express my deepest gratitude to my mother-in-law and father-in-law for their extremely supportive nature and blessings. Thanks to my brother-in-law Avinash bhaiya, Anurag bhaiya, Abhishek bhaiya, Ashish and my sister-in-law Astha bhabhi for their moral support, refreshing short tours and many cheerful moments. I lack words to express thanks to my elder sister Purvi and brother Tarang. You both played equal role in shaping my future. Bhagini, I simply followed your way, it would be hard for me to enter in research without your initiative. Bhai, your suggestions helped me throughout my scientific career, I learnt to be patient from you. A special thanks to Maitraya Jijaji and Ruchi Bhabhi for making my short trips to India all time memorable. I have no words to express my thanks to my mother and father. Being from a small village of India, it would not be possible to aim for a PhD from outside India without your encouragement, love, care and teachings. Mummy, thanks for travelling to Lindau whenever I requested despite extreme differences in weather. Pappa, wherever you are in other world of God, I want to tell you that the main motivation behind my PhD was your wish to see one of us with a PhD degree. You both are my internal power since beginning and will be throughout my life.

Aditya, my husband deserves a special thanks for being always available to share my happiness and my hurdles. You have been responsible for everything good in my life in the past four years. This PhD would not be possible without your unconditional support, love, and understanding.

# Curriculum Vitae

## Personal Details

**Date of Birth :** 19-Nov-1981

**Nationality :** Indian

**Languages :** English, Hindi, Gujarati

**Marital Status :** Married

## Education

**1999-2002 :** B.Sc (Electronics), Rani Durgavati Vishwavidyalaya, Jabalpur, India.

**2002-2004 :** M.Sc (Electronics), Rani Durgavati Vishwavidyalaya, Jabalpur, India.

**2009-Apr 2012:** PhD student, International Max-Planck Research School (IMPRS) on Physical Processes in the Solar System and Beyond, Katlenburg-Lindau, Germany.

## Scientific Experience

**Dec 2007-Dec 2008 :** Guest Scientist in the Planets and Comets group at Max Plank Institute for Solar System Research (MPS), Katlenburg-Lindau, Germany.

**Sep 2006-Nov 2007 :** Research Scholar at the Space Applications Centre (SAC), Indian Space Research Organization (ISRO), Ahmedabad, India.